

**DEVELOPMENT OF AN INTEGRATED
HYDRO-ENVIRONMENTAL MODEL AND ITS
APPLICATION TO A MACRO-TIDAL ESTUARY**

Dekui Yuan

Thesis submitted for the degree of
Doctor of Philosophy

Division of Civil Engineering, Cardiff School of Engineering
Cardiff University

March 2007

UMI Number: U584942

All rights reserved

INFORMATION TO ALL USERS

The quality of this reproduction is dependent upon the quality of the copy submitted.

In the unlikely event that the author did not send a complete manuscript and there are missing pages, these will be noted. Also, if material had to be removed, a note will indicate the deletion.



UMI U584942

Published by ProQuest LLC 2013. Copyright in the Dissertation held by the Author.
Microform Edition © ProQuest LLC.

All rights reserved. This work is protected against
unauthorized copying under Title 17, United States Code.



ProQuest LLC
789 East Eisenhower Parkway
P.O. Box 1346
Ann Arbor, MI 48106-1346

ACKNOWLEDGEMENTS

I would like to express my gratitude and appreciation to my supervisors Dr Binliang Lin and Professor Roger A. Falconer for their continued helpful advice, support and encouragement throughout the period of this research project.

I would like to thank all my teachers, present and past, for instilling the proper knowledge in me, which has enabled me to pursue this path.

I am also indebted to my friends in Cardiff University and Tianjin University for the arrangement of many technical matters and continuous support.

Finally, I owe a great deal to my family for their continuous love, encouragement and support.

Abstract

A two-dimensional depth-integrated hydro-environmental model has been refined to predict the hydrodynamic characteristics, solute and sediment transport processes and the fate and transport of trace metals in estuarine and coastal waters.

The mathematical basis of the governing equations for the hydrodynamic processes and solute and mass transport is first discussed in detail. Then the discretization of the hydrodynamic and transport equations is introduced, with particular attention being paid to simulating the moving boundary, or flooding and drying, problem. A new implicit method is developed to simulate the interaction between surface and ground water flows, in which the governing equations for these two types of flows are discretized in the same form. This method has shown to be particularly suited for dealing with the moving boundary problem.

The sediment transport model is then introduced, with the key coefficients used in the model being discussed in detail. The trace metal transport model is refined based on the concept of total trace metal transport, including both dissolved and particulate metals. In order to verify the trace metal transport model, two new test cases are designed and the corresponding analytical solutions are derived. In this study model verification has been undertaken systematically for each process sub-model, as well as the integrated model. Analytical solutions, experimental data and field survey data are used in the model verification. Numerical tests show that: a) the linked surface water and groundwater flow method is efficient and accurate, b) the new analytical solutions are useful to verify numerical models and c) all of the sub-process models are capable of providing accurate and reliable results.

The integrated hydro-environment model is applied to a practical case study to estimate the residence time and the behaviour of trace metals in a macro-tidal estuary, namely the Mersey Estuary, located in the north-western England. It has been found that: a) the integrated model is able to give reasonably accurate predictions for the flow field and salinity, sediment and trace metal concentration distributions for an estuary with complex geometry and bathymetry and, b) generally, the average residence time for the whole Mersey Estuary is affected more by the tidal level change than the river discharge. However, if the tidal range is small, then the freshwater discharge can significantly affect the average residence time. Because of the sorption and de-sorption processes, trace metals have shown to be more difficult to be flushed out of the estuary, thus they will have a long term impact on the aquatic environment of the estuary.

Keywords: Numerical model, hydro-environment, sediment transport, trace metal transport, moving boundary, residence time

CONTENTS

Declaration.....	i
Acknowledgements.....	ii
Abstract.....	iii
Contents.....	iv
List of Figures.....	xi
List of Tables.....	xvi
Notations.....	xvii
Abbreviations.....	xxii

CHAPTER 1

INTRODUCTION.....	1
1.1 Introduction.....	1
1.2 Aims and Objectives of this Study.....	2
1.3 Outline of the Thesis.....	4
1.4 Introduction to Application Study Area.....	5

CHAPTER 2

LITERATURE REVIEW.....	6
2.1 Introduction.....	6
2.2 Hydrodynamic and Solute and Mass Transport Models.....	6
2.2.1 Vertical profile and dispersion coefficient.....	7
2.2.2 Grid systems.....	7
2.2.3 Numerical methods.....	8
2.3 Moving Boundary Problem.....	9
2.4 Sediment Transport Model.....	11
2.4.1 Non-cohesive sediment.....	12
2.4.2 Cohesive sediment.....	13

2.5 Trace Metal Transport Model.....	14
2.5.1 Studies of partitioning coefficient.....	15
2.5.2 Development of numerical models.....	16
2.6 Residence Time.....	17
2.7 Summary.....	18

CHAPTER 3

GOVERNING EQUATIONS OF HYDRODYNAMIC AND SOLUTE TRANSPORT PROCESSES.....

3.1 Introduction.....	19
3.2 Basic Three Dimensional Governing Equations.....	19
3.2.1 Solute and mass transport processes.....	20
3.2.2 Governing equations for hydrodynamic processes.....	21
3.2.2.1 Continuity equation.....	22
3.2.2.2 Momentum equation.....	23
3.3 Three Dimensional Governing Equations for Turbulent Flow.....	26
3.3.1 Continuity equation.....	27
3.3.2 Momentum equation.....	27
3.3.2.1 <i>Reynolds stresses</i>	28
3.3.2.2 <i>Body forces and Coriolis acceleration</i>	30
3.3.3 Solute and mass transport processes.....	30
3.4 Depth Integrated Governing Equations.....	32
3.4.1 Hydrodynamic governing equations for surface water flow.....	32
3.4.1.1 <i>Continuity equation</i>	32
3.4.1.2 <i>Momentum equation</i>	34
3.4.2 Hydrodynamic governing equations for groundwater flow.....	39
3.4.2.1 <i>Continuity equation</i>	39
3.4.2.2 <i>Momentum equation</i>	40
3.4.3 Depth integrated governing equations for solute transport.....	43
3.5 Summary.....	44

CHAPTER 4

DISCRETIZATION OF GOVERNING EQUATIONS AND NUMERICAL SOLUTION

PROCEDURE.....	45
4.1 Introduction.....	45
4.2 Discretization of the Hydrodynamic Governing Equations.....	46
4.2.1 Discretization of the continuity equation.....	47
4.2.2 Discretization of the momentum equations for surface water flow.....	48
4.2.3 Discretization of the momentum equations for groundwater flow.....	51
4.2.4 Linked discretized momentum equations.....	52
4.2.5 Solving discretized equations.....	54
4.3 Discretization of Solute Transport Equation.....	55
4.4 Boundary Conditions.....	57
4.4.1 Closed boundary.....	57
4.4.2 Open boundary.....	59
4.4.3 Moving boundary.....	60
4.5 Summary.....	62

CHAPTER 5

VERIFICATION AND CALIBRATION OF HYDRODYNAMIC AND SOLUTE TRANSPORT MODEL.....

5.1 Introduction.....	63
5.2 Flow and Solute Transport in Surface Water.....	63
5.2.1 Tidal flow in a semi-closed open channel.....	63
5.2.1.1 <i>The exact solution</i>	64
5.2.1.2 <i>Computational parameters, initial and boundary conditions</i>	65
5.2.1.3 <i>Repeatability and symmetry</i>	66
5.2.1.4 <i>Comparison between numerical results and exact solutions</i>	68
5.2.2 Tidal flow in a laboratory model harbour.....	69
5.2.3 Solute transport in a uniform flow field.....	73

5.3 Ground Water Flow in Coastal Aquifer.....	76
5.3.1 Water table fluctuation in a laboratory model aquifer.....	76
5.3.2 Tidal water table fluctuation in a coastal aquifer.....	79
5.4 Moving Boundaries.....	81
5.4.1 Oscillating flow in a circular lake with paraboloidal bottom.....	82
5.4.1.1 <i>Description of test case</i>	82
5.4.1.2 <i>Results and discussions</i>	83
5.4.2 One dimensional uniformly sloping basin.....	88
5.4.3 One dimensional basin with bottom convexity.....	89
5.5 Summary.....	91

CHAPTER 6

RESIDENCE TIME OF THE MERSEY ESTUARY.....	93
6.1 Introduction.....	93
6.2 Model Calibration and Verification.....	93
6.2.1 Description of study area, field survey data and computational parameters.....	93
6.2.2 Water elevations.....	95
6.2.3 Salinity.....	97
6.3 Method for Evaluating Residence Time.....	99
6.4 Results and Discussions.....	101
6.4.1 Convergence of calculation.....	102
6.4.2 Sensitivity to initial condition.....	104
6.4.3 Effect of tidal range and freshwater discharge.....	105
6.5 Summary.....	108

CHAPTER 7

DEVELOPMENT AND VERIFICATION OF SEDIMENT TRANSPORT MODEL....	110
7.1 Introduction.....	110
7.2 Sediment Properties.....	110

7.2.1 Density and porosity.....	111
7.2.2 Shape.....	112
7.2.3 Size.....	113
7.2.4 Angle of Repose.....	114
7.2.5 Flocculation.....	115
7.2.6 Settling velocity.....	115
7.3 Initiation of Motion and Suspension.....	117
7.3.1 Initiation of motion.....	117
7.3.2 Initiation of suspension.....	118
7.4 Governing Equations for Sediment Transport Processes.....	119
7.4.1 Bed load transport.....	119
7.4.2 Suspended load transport.....	122
7.4.3 Cohesive sediment transport.....	129
7.5 Bed Evolution.....	130
7.5.1 Depth integrated mass balance equation.....	130
7.5.2 Numerical algorithm.....	131
7.6 Model Verification against Experimental Data.....	132
7.6.1 Sediment transport over a porous bed.....	133
7.6.2 Bed evolution in a sloping flume.....	134
7.6.3 Bed evolution over a dredged trench.....	136
7.7 Verification and Calibration of Model for the Mersey Estuary.....	138
7.7.1 Description of field data and computational parameters.....	138
7.7.2 Results and discussions.....	139
7.8 Summary.....	142

CHAPTER 8

TRACE METAL TRANSPORT MODEL AND ITS APPLICATION.....	143
8.1 Introduction.....	143
8.2 Transport and Fate of Trace Metal in Estuarine and Coastal Waters.....	143
8.2.1 Basic concepts and general processes.....	143

8.2.2 Basic definitions.....	145
8.2.3 Sorption and de-sorption.....	147
8.2.4 Partitioning coefficient.....	147
8.2.5 Mass exchange between water column and bed sediments.....	149
8.3 Trace Metal Transport Governing Equations.....	151
8.3.1 Governing equations for particulate and dissolved phases.....	151
8.3.2 Governing equation for total trace metal load.....	152
8.4 New Cases and Their Analytical Solutions.....	152
8.4.1 Case1: Deposition process.....	153
8.4.2 Case2: Erosion process.....	156
8.5 Verification of Model against Analytical Solutions.....	157
8.5.1 Case1: Deposition process.....	157
8.5.2 Case2: Erosion process.....	160
8.6 Model Application to the Mersey Estuary.....	161
8.6.1 Introduction of field survey.....	161
8.6.2 Partitioning coefficients and computational parameters.....	162
8.6.3 Comparisons between model results and field data.....	163
8.6.4 Trace metal behaviour in the Mersey Estuary.....	169
8.6.4.1 Case1: Trace metal released from contaminated bed sediment.....	170
8.6.4.2 Case2: Trace metal released due to accidental discharges.....	173
8.6.4.3 Case3: Trace metal released continuously from an outfall with clean initial water and bed sediment.....	178
8.7 Summary.....	184

CHAPTER 9

CONCLUSIONS AND RECOMMENDATIONS.....	185
9.1 Conclusions.....	185
9.1.1 Model development.....	185
9.1.2 Model application.....	187
9.1.2.1 Residence time.....	187

9.1.2.2 Behaviour of trace metal.....	187
9.2 Recommendations for Further Study.....	188
REFERENCES.....	190

LIST OF FIGURES

CHAPTER 3

- Figure 3-1 Schematic illustration of control volume for solute and mass transport
- Figure 3-2 Schematic illustration of control volume for momentum equation
- Figure 3-3 Schematic illustration of definition of stress components
- Figure 3-4 Coordinate system for depth integrated equations
- Figure 3-5 Schematic illustration of unconfined aquifer
- Figure 3-6 Experimental apparatus to demonstrate Darcy's law

CHAPTER 4

- Figure 4-1 Schematic illustration of space staggered grid system
- Figure 4-2 Demonstration of variables at f^{th} row
- Figure 4-3 Description of closed boundary condition
- Figure 4-4 Description of flow boundary
- Figure 4-5 Description of water elevation boundary
- Figure 4-6 Schematic illustration of moving boundary on a beach slope

CHAPTER 5

- Figure 5-1 Schematic illustration of semi-closed open channel
- Figure 5-2 Temporal distribution of water elevation at three points
- Figure 5-3 Temporal distribution of x-component of velocity at three points
- Figure 5-4 Spatial distribution of water elevation at three cross sections
- Figure 5-5 Comparison between numerical results and analytical solutions (a) amplitude of water elevation and (b) amplitude of x-velocity
- Figure 5-6 Comparison between numerical results and analytical solutions (a) evolution of water elevation and (b) evolution of x-velocity (T: tidal cycle)
- Figure 5-7 Schematic illustration of tidal basin
- Figure 5-8 Velocity profile across axis BOD at Time=1.25T (T: tidal cycle)
- Figure 5-9 Evolution of the velocity distribution in model harbour (T: tidal cycle)
- Figure 5-10 Schematic illustration of test case for verifying solute transport model

- Figure 5-11 Comparison of numerical results and exact solutions along Section A-C and Section B-D (Figure 5-10) at selected times
- Figure 5-12 3D plot of concentration distribution at three selected times
- Figure 5-13 Schematic illustration of experiment layout
- Figure 5-14 Water elevation along x-direction: a) for a wave period with time interval being 1.75s and b) for two selected time
- Figure 5-15 Water table in porous media at $x=0\text{m}$, 0.05m , 0.18m and 0.335m
- Figure 5-16 Sketch of tidal water table fluctuation in a coastal aquifer
- Figure 5-17 Water elevation along x-direction: a) for a tidal period with time interval being 0.5hr and b) for two selected times
- Figure 5-18 Upper and lower limits of water elevation along x-axis
- Figure 5-19 Water table in coastal aquifer at $x=0\text{m}$, 10m , 50m and 100m
- Figure 5-20 Sketch of paraboloidal basin and initial free water surface
- Figure 5-21 Comparison of spatial distribution of water elevations along x-axis for a period with time interval being $T/12$ (T : period)
- Figure 5-22 Detailed comparison of spatial distribution of water elevations along x-axis for two selected times
- Figure 5-23 Comparison of distribution of x-velocities along x-axis for a period with time interval being $T/12$ (T : period)
- Figure 5-24 Detailed comparison of spatial distribution of x-velocity along x-axis for two selected times
- Figure 5-25 Water elevations predicted by linked model and Falconer's model for a tidal period (T : period, $n_e=0.1$, $K=0.01$)
- Figure 5-26 x-velocity components predicted by linked model and Falconer's model for (a) $t=0$ to $t=5/12T$ and (b) $t=T/2$ to $t=T$ (T : period)
- Figure 5-27 Comparison of predicted water elevations with Falconer's model results in a 1D mild uniformly sloping basin
- Figure 5-28 Comparison of x-velocities with Falconer's model results in a 1D mild uniformly sloping basin for (a) $t=0$ to $t=5T/12$ and (b) $t=T/2$ to $t=T$ with time interval being $T/12$ (T : period)
- Figure 5-29 Comparison of predicted water elevations with Falconer's model results in a 1D mild uniformly sloping basin with convexity
- Figure 5-30 Comparison of x-velocities with Falconer's model results in a 1D mild uniformly sloping basin with convexity for (a) $t=0$ to $t=5T/12$ and (b) $t=T/2$ to $t=T$ with time interval being $T/12$ (T : period)
- Figure 5-31 Comparison of temporal distributions of x-velocities with Falconer's model results at four selected points

CHAPTER 6

- Figure 6-1 Mersey Estuary bathymetry showing location of sampling sites
- Figure 6-2 Comparison of predicted and measured water elevations on 18 March, 1991
- Figure 6-3 Comparison of predicted and measured salinity on 18 March, 1991
- Figure 6-4 Evolution of flow current circulation and salinity distribution at Runcorn (Date: 18 March, 1991)
- Figure 6-5 Relative residual PDCM, cumulative average residence time and relative error of accumulative average residence time for the Mersey Estuary (Case 8 in Table 6-2, with PDCM initialised at high water)
- Figure 6-6 Sensitivity of ARTME to release time of PDCM
- Figure 6-7 a) Relationship between ARTME and freshwater discharge and b) Relationship between ARTME and tidal range for freshwater discharge $Q = 0$
- Figure 6-8 Distribution of intensity of residual tidal current

CHAPTER 7

- Figure 7-1 Schematic illustration of variables referred in depth integrated mass balance equation
- Figure 7-2 A control volume for discretization of sediment mass balance
- Figure 7-3 Schematic illustration of Wang and Ribberink's (1986) experiment
- Figure 7-4 Depth-averaged concentration over a porous bed
- Figure 7-5 Comparison of predicted water surface and bed elevation against measured data ($t = 30$ mins)
- Figure 7-6 Initial dimensions of DHL dredged trench
- Figure 7-7 Comparison of predicted bed elevation against measured data
- Figure 7-8 Comparison of predicted and measured sediment concentrations at sampling points (see Figure 6-1) for Case1 in Table 7-4
- Figure 7-9 Distribution of predicted suspended sediment concentrations for a tidal cycle (Case1 in Table 7-4)

CHAPTER 8

- Figure 8-1 Schematic diagram of transport and fate of trace metal
- Figure 8-2 Schematic illustration of sorption and de-sorption of trace metal
- Figure 8-3 Schematic illustration of test cases

- Figure 8-4 Distribution of trace metal concentration (P_b) in bed sediment (a) Spatial distribution at three selected times and (b) Temporal distributions at three selected locations
- Figure 8-5 Temporal distribution of concentration of (a) suspended sediment (C_{SPM}), (b) total trace metal (C_T), (c) dissolved trace metal (C_d), and (d) particulate trace metal (C_p) in water body at $x = 9000\text{m}$ for Case 1
- Figure 8-6 Temporal distribution of concentration of (a) suspended sediment (C_{SPM}), (b) total trace metal (C_T), (c) dissolved trace metal (C_d) and (d) particulate trace metal (C_p) in water body at $x = 9000\text{m}$ for Case 2
- Figure 8-7 Comparison of predicted and field measured partitioning coefficients of (a) zinc and (b) cadmium in the Mersey Estuary
- Figure 8-8 Comparison of predicted and field measured axial salinity distributions
- Figure 8-9 Comparison of predicted and field measured axial suspended sediment distributions
- Figure 8-10 Comparison of predicted and field measured axial dissolved zinc distributions
- Figure 8-11 Comparison of predicted and field measured axial dissolved cadmium distributions
- Figure 8-12a Evolution of distributions of Salinity in the Mersey Estuary during a tidal cycle (25 June, 1998)
- Figure 8-12b Evolution of distributions of suspended sediment in the Mersey Estuary during a tidal cycle (25 June, 1998)
- Figure 8-12c Evolution of distributions of total zinc in the Mersey Estuary during a tidal cycle (25 June, 1998)
- Figure 8-12d Evolution of distributions of dissolved zinc in the Mersey Estuary during a tidal cycle (25 June, 1998)
- Figure 8-13 Spatial distributions of concentration of trace metal in bed sediment at (a) $t=0$ and (b) $t=100\text{hour}$ for Case 1
- Figure 8-14 Spatial distributions of concentration of dissolved trace metal in water body during 8th tidal cycle for Case 1
- Figure 8-15 Spatial distributions of concentration of particulate trace metal in water column during 8th tidal cycle for Case 1
- Figure 8-16 Temporal distributions of R_d , R_p , R_b and R_e for Case 1
- Figure 8-17 Spatial distributions of concentration of trace metal in bed sediment at (a) $t=0$ and (b) $t=100\text{hour}$ for Case 2

- Figure 8-18 Spatial distributions of concentration of dissolved trace metal in water column during 8th tidal cycle for Case 2
- Figure 8-19 Spatial distributions of concentration of particulate trace metal in water column during 8th tidal cycle for Case 2
- Figure 8-20 Temporal distributions of R_d , R_p , R_b and R_e for Case 2
- Figure 8-21 Temporal distributions of R_e and R_a for Case 1, Case 2 and Case2-P
- Figure 8-22 Spatial distributions of concentration of trace metal in bed sediment at (a) t=0 and (b) t=100hour for Case 3
- Figure 8-23 Spatial distributions of concentration of dissolved trace metal in water column during 8th tidal cycle for Case 3
- Figure 8-24 Spatial distributions of concentration of particulate trace metal in water column during 8th tidal cycle for Case 3
- Figure 8-25 Temporal distributions of R_d , R_p , R_b and R_e for Case 3
- Figure 8-26 Comparison of temporal distributions of R_e and R_a between Case 3 and Case 3-P
- Figure 8-27 Comparison of the temporal distributions of R_{up} and R_{dn} among Case 1, Case 2 and Case 3

LIST OF TABLES

CHAPTER 5

- Table 5-1 Coordinates of three sampling points and sections
Table 5-2 Relative errors of total mass and peak value
Table 5-3 Porosity and hydraulic conductivity in model simulations

CHAPTER 6

- Table 6-1 Six sets of field data for model calibration
Table 6-2 Additional cases studied for evaluating average residence time

CHAPTER 7

- Table 7-1 Grain size scale defined by American Geophysical Union
Table 7-2 Comparison of prediction of settling velocity
Table 7-3 Parameters used in DHL dredged trench experiment
Table 7-4 Three sets of field data for model calibration

CHAPTER 8

- Table 8-1 Values of coefficients for K_D and concentrations in bed sediment

NOTATIONS

a	reference distance
c_a	reference sediment concentration at a reference distance above bed
c_b	volumetric concentration
C	Chezy's bed roughness coefficient
C_d	porosity corrected dissolved trace metal concentration
C_D	drag coefficient
C_e	eddy viscosity coefficient
C_p	concentration of particulate trace metal
C_{SPM}	concentration of suspended particulate matter
C_T	total concentration of trace metal
C'	Chezy coefficient related to grain size
C'_d	concentration of dissolved trace metal
dt	computational time step
dx	computational spatial step in x -direction
dy	computational spatial step in y -direction
D	sieve diameter of grains
D	second order tensor of molecular diffusion coefficient
D_{16}	sediment diameter for which 16% of bed material being finer
D_{50}	sediment diameter for which 50% of bed material being finer
D_{84}	sediment diameter for which 84% of bed material being finer
D_{90}	sediment diameter for which 90% of bed material being finer
D_l	longitudinal dispersion constant
D_t	depth averaged turbulent diffusion constant
D_w	wind-induced dispersion-diffusion coefficient
D_{lx}	turbulent diffusion coefficients in x -direction
D_{ly}	turbulent diffusion coefficients in y -direction
D_{lz}	turbulent diffusion coefficients in z -direction
D_{xx}	longitudinal dispersion coefficient in x -direction
D_{xy}	depth averaged turbulent diffusion coefficient in x -direction
D_{yx}	depth averaged turbulent diffusion coefficient in y -direction
D_{yy}	longitudinal dispersion coefficient in y -direction

D_*	dimensionless grain size
E	depth averaged turbulent eddy viscosity
E	net erosion or deposition per unit area of bed
f	Coriolis parameter
f	Darcy-Weisbach friction coefficient
f_d	fraction of total trace metal that is dissolved
f_p	fraction of total trace metal that is particulate
\vec{f}	body force acting on fluid
\vec{F}	resultant force
g	gravitational acceleration
h	water depth below datum
H	total depth of water column
k_s	Nikuradse equivalent sand roughness size
k_u	sorption rate
K	hydraulic conductivity
K	desertion rate
K_D	partitioning coefficient
l	Prandtl's mixing length
M_b	mass of bed sediment per unit area
M_s	mass of solid phase in sediments
\vec{M}	momentum
\vec{n}	outward normal direction of surface
n_e	porosity of media
p	discharges per unit width in x -direction
\vec{p}	surface force acting on control volume
P	trace metal concentration expressed on a dry weight solid basis
\mathbf{P}	stress tensor
P_a	atmospheric pressure
P_b	concentration of trace metals adsorbed on bed sediments expressed on a dry weight solid basis
q	discharges per unit width in y -direction
q_b	volumetric bed-load transport rate
q_m	source or sink discharge per unit horizontal area
q_s	depth-integrated suspended load transport rate

$r(\tau)$	remnant function
R	hydraulic radius
R_e	Reynolds numbers
R_e^*	shear Reynold's number
s	specific density of sediment
s_b	sediment concentration near bed
S	depth-averaged suspended sediment concentration in mass
S_e	depth-averaged equilibrium concentration
S_F	Corey shape factor
S_b^p	particulate trace metal flux from or to bed
S_o^d	source or sink of dissolved trace metal
S_o^p	source or sink of adsorbed particulate trace metal
S_i^d	transformation term defining adsorbed or desorbed particulate fluxes to or from sediments
S_i^p	transformation term defining metal flux from, or to, dissolved phase in water column
T	transport stage parameter
u	instantaneous fluid velocity components in x-direction
u_b	particle velocity in bed sediment
u_d	Darcy velocity
\bar{u}	temporal average velocity component in x-direction
u'	fluctuating velocity component in x-direction
u_*	boundary shear velocity
$u_{*,cr}$	critical bed-shear velocity
u'_*	effective bed-shear velocity
U	depth average velocity components in x-direction
v	instantaneous fluid velocity components in y-direction
V	depth average velocity components in y-direction
\vec{V}	flow velocity vector
V_p	volume of solid or particulate phase of sediment
\vec{V}_r	velocity of the substance relative to the flow
V_v	non-solid volume of sediment
w	instantaneous fluid velocity components in z-direction
w_s	settling velocity of sediment

w_{sm}	hindered settling velocity
w'	vertical velocity component of the eddy
W_s	wind speed
W_x	wind velocity component in x-direction,
W_y	wind velocity component in y-direction
z_b	bed level
Z	suspension number
α	sediment concentration profile parameter
β	momentum correction factor
γ	air-water resistance coefficient,
γ	sediment concentration profile parameter
γ_1	sediment concentration profile parameter
γ_2	sediment concentration profile parameter
δ_b	thickness of bed load layer
ΔS	total surface of control volume
ΔV	total volume of control volume
ε	kinematic eddy viscosity
ε_s	mixing coefficient of sediment
τ_b	boundary shear stress
τ_r	average residence time
τ_{xb}	bed shear stress component
τ_{xw}	surface wind shear stress component
φ	concentration of substance
φ_o	source or sink item
$\bar{\varphi}$	temporal average concentration
φ'	fluctuating concentration
ϕ	depth-averaged solute concentration
η	absolute eddy viscosity
θ	mobility parameter
θ_{cr}	critical Shields' parameter
κ	von Karman's constant
μ	kinetic viscosity coefficient
ν	kinematic viscosity
ζ	water surface elevation above datum

ρ	density of the fluid
ρ_a	air density
ρ_s	sediment density
ω	speed of earth's rotation

ABBREVIATIONS

ADI	Alternating Direction Implicit
ARTME	Average Residence Time for whole Mersey Estuary
DHL	Delft Hydraulics Laboratory
DIVAST	Depth Integrated Velocities and Solute Transport
MWL	Mean Water Level
PDCM	Passive Dissolved Conservative Matter
PDE	Partial Differential Equation
QUICK	Quadratic Upstream Interpolation for Convective Kinematics
SPM	Suspended Particulate Matter
TOASOD	Third Order Advection and Second Order Diffusion
TRIVAST	ThRee dimensional layer Integrated Velocities and Solute Transport

CHAPTER 1

INTRODUCTION

1.1 INTRODUCTION

As the result of the recent rapid development of economy in estuarine and coastal areas, increasing attention has been paid to the water environment in estuarine and coastal regions. In order to effectively protect the environment, it is necessary to understand the transport and dispersion of toxic substances, sediment particles, dissolved oxygen etc. in estuarine and coastal waters under different dynamic conditions. In general, estuarine and coastal waters provide a unique ecological environment for a vast variety of mixed freshwater and marine life. The common features of these water bodies are that they normally have a shallow water depth, a complicated bathymetry and high biochemical activity.

Environmental pollution by trace metals has become a global phenomenon. Because of the growing apprehension about the potential effects of the metallic contaminants on various fauna and flora, the research on fundamental, applied and health aspects of trace metals in the environment has mushroomed to the point that it has become difficult to keep track of recent developments in particular fields. The quantities of trace metals entering coastal waters is of concern, for their impact on the coastal fish population and on the health of those who consume fish caught in coastal seas.

Sediment characteristics are morphologically and biologically important for estuaries. The movement of sediments can cause deposition to occur in waterways and harbour docks, or erosion of estuarine and coastal banks etc. To deal with these problems, expensive dredging operations or bank protection are generally needed. Usually, sediments are the main fate of trace metals in aquatic ecosystems, but under some conditions, they can also act as a source of these elements (Izquierdo et al, 1997). Fine sediments act as a source (or sink) for the organic chemicals and trace metals entering (or leaving) the water column with sediments contaminated by

trace metals being a potential threat to the aquatic environment. Re-suspension of contaminated bed sediments caused by strong tidal currents, short waves, wind or dredging operations may release a significant amount of trace metals into the water column, and the de-sorption of contaminants from their particulate phase can have a pronounced impact on the aquatic environment and ecosystem. Therefore, understanding and being able to determine the sediment dynamics in estuarine and coastal waters is of vital importance to the environmental management of estuarine and coastal waters.

In recent years the water residence time has been increasingly investigated in estuarine and coastal water quality studies, because the rate of water exchange between an estuary/sea bay and the open sea plays a critical role in controlling the chemical and biological processes within the estuary/sea bay.

The interaction between the fluid flow, sediment transport and therefore the bed level change has great importance with regard to some water quality problems, such as the transport of trace metals and the decay of bacteria micro-organism indicators. In the past, this complex behaviour would be investigated by a physical model, which could prove to be costly and time consuming. As a result of the rapid development of computer technology and numerical methods, many numerical models have been developed to predict the hydro-environmental processes in estuarine and coastal waters. Depending on the features of the phenomena studied, one-, two- or three-dimensional numerical models have been developed. However, it is important that numerical models are computationally efficient, and easily implemented with satisfactory levels of accuracy for practical applications.

In estuarine and coastal waters the horizontal scale is usually much larger than the vertical scale, so that the water motion can usually be assumed to be nearly horizontal. Depth-integrated two-dimensional models have been successfully used in many studies to predict the flow fields and pollutant distributions.

1.2 AIMS AND OBJECTIVES OF THIS STUDY

The primary aim of this research study is to develop an integrated hydro-environmental model to predict hydrodynamic, solute, sediment and trace metal transport processes in estuarine and coastal waters. The main objectives and key problems can be summarised as follows:-

1) To refine an existing hydrodynamic and solute transport model

As the basis for further study on the hydro-environment, a refinement of an existing numerical model for simulating the hydrodynamic and general solute transport process is necessary. Based on the understanding of the theoretical basis of the hydrodynamic and general solute transport process in three- and two-dimensional forms, a two-dimensional depth-integrated numerical model will be refined to improve its capacity for predicting the hydrodynamic and general solute transport process in estuarine and coastal water.

2) To develop a new method for linking surface and groundwater flow and apply the method for simulating moving boundaries

A moving boundary (wetting and drying processes) is a very important phenomenon in estuarine and coastal zones with large tidal flats. Usually it is conceptually complicated in simulating moving boundaries using an explicit method. Considering the natural linkage between the surface water and groundwater flows in estuarine and coastal zones, a new implicit method will be developed in this study to simulate the moving boundary phenomenon.

3) To develop a numerical approach to estimate residence time

Residence time is an important measure for evaluating the environmental impact assessment for estuarine and coastal waters. For natural water bodies, it is generally impossible to determine the residence time analytically. Thus, a numerical method is developed to determine the residence time of estuaries and sea bays based on model predicted concentration distributions.

4) To improve sediment and trace metal transport modelling

The sediment and trace metal transport processes have a vital impact on the quality of estuarine and coastal waters. Based on the refined models for the hydrodynamic and general transport processes, improved models for simulating the sediment and trace metal transport processes will be developed.

5) To develop analytical solutions for trace metal transport

In order to verify the trace metal transport model analytical solutions will be needed, because: a) there is no available measured data from well controlled experiments, b) the field measured data is usually not very accurate due to the complexity of the environment. Thus, new test cases will be designed to obtain suitable analytical solutions for verifying the trace metal transport model.

6) To test the refined numerical model and apply it to the Mersey Estuary

A numerical model needs to be rigorously tested and validated before being applied to any real cases. In this study, every sub-model will be verified systematically against analytical solutions, experimental and field measured data. In order to check the reliability and performance of the integrated model, the model will be applied to study the hydro-environmental characteristics of a macro-tidal estuary, namely the Mersey Estuary in the UK.

1.3 OUTLINE OF THE THESIS

The details of the remaining chapters can be summarized as follows:

Chapter 2 reviews the recent development in the general field of hydro-environment modelling, with the emphasis being given to methods for simulating the moving boundaries, sediment transport, trace metal transport and water exchange related problems.

Chapter 3 provides the details of the governing equations employed for fluid flow and mass and solute transport modelling. Certain assumptions and simplifications made in the model are explained.

Chapter 4 outlines the discretization of the hydrodynamic and solute transport equations, and the solution procedure for the discretized governing equations. The new method for treating the moving boundary implicitly is explained in detail.

Chapter 5 demonstrates the verification of the hydrodynamic and general solute transport model. The performance of the new method for treating the moving boundary implicitly is discussed in detail.

Chapter 6 presents the details of the study of water exchange of the Mersey Estuary using the hydrodynamic and general solute transport model, based on the concept of residence time.

Chapter 7 demonstrates the theoretic basis of the sediment transport model. Details of the verifications of the model against three sets of experimental data are provided, as well as the verification and calibration of the model against the measured data in the Mersey Estuary.

Chapter 8 outlines the governing equations of the trace metal transport model. The verification of the model are presented in detail, with two new analytical solutions being described in detail. Trace metal behaviour in the Mersey Estuary is investigated

via simulations for three scenarios.

Chapter 9 provides a summary of the study and the main conclusions drawn from this research, followed by recommendations for further studies.

1.4 INTRODUCTION TO APPLICATION STUDY AREA

The Mersey Estuary is one of the largest estuaries in the UK, with a catchment area of about 5,000 square kilometres over the north western part of England, and including the major conurbations of Liverpool and Manchester. This is a macro tidal estuary, with typical spring-neap cycle tidal ranges varying between about 3.5 m (extreme neap) to 10.5 m (extreme spring). Historically, this estuary has been seriously polluted by industrial discharges and adjacent sea dumping (Jones, 2000). The Mersey Basin Campaign has been focusing on improving the water quality in the rivers and waterways of the Northwest of England for almost 20 years, with the aim being to encourage high quality waterfront regeneration in the region, with a comprehensive programme of actions currently being undertaken to improve water quality (Burton, 2003). The Mersey Estuary has been widely studied because of its vital role in shipping transport, and the designation of parts of the inner estuary as nature reserves and 'Sites of Special Scientific Interest'. Sediment transport and bathymetric evolution have always been key drivers for studying this estuary (e.g., Thomas et al., 2002; Lane, 2004). In recent years, the re-suspension, reactivity and recycling of trace metals entering the Mersey Estuary have also become a concern, because of their potential impact on the estuarine ecosystem and on the health of those citizens living in the adjacent areas (Comber et al., 1995; Cole and Whitelaw, 2001; Falconer and Lin, 2003; Turner et al., 2004).

The main reasons for selecting the Mersey Estuary as the application site are: a) this estuary is a site of special scientific interest, and b) a set of measured data is available for this estuary.

CHAPTER 2

LITERATURE REVIEW

2.1 INTRODUCTION

Numerical modelling has become an important method to study flow and aquatic environment in estuarine and coastal waters, due to recent rapid progress in computer science and numerical methods. Many numerical models have been developed and applied to practical engineering problems. Generally an integrated hydro-environment model consists of a number of sub-models, including the hydrodynamic model, sediment transport model, toxic substance transport model, etc. These models can be classified according to different criteria. For example, they can be classified according to the numerical method deployed, or the dimension of the governing equations used in the model. One of the most suitable classifications is the dimensional classification of the model. The wide range of hydro-environmental problems encountered in practical studies has led to numerous researches in this area. In this chapter the development of different numerical models and the related numerical techniques involved in this study will be reviewed.

2.2 HYDRODYNAMIC AND SOLUTE AND MASS TRANSPORT MODELS

Many hydrodynamic models have been developed for modelling flows in estuarine and coastal waters in recent years. In general, these models can be divided into two types: a) baroclinic, i.e. models with density effects, and b) barotropic, i.e. models without density effects. In estuarine and coastal waters where the water column depth is relatively shallow then it is appropriate to assume that the flow is well mixed and therefore models without density effects are used. The advective-diffusion equation has been widely used to describe the solute and mass transport processes

in one-, two- and three-dimensions. Solute and mass transport models are usually dynamically linked to hydrodynamic models, and are the basis for simulating sediment transport, trace metal transport, etc.

Hydrodynamic and general solute transport models can be classified into one-, two- and three-dimensional models. One-dimensional models, such as HEC-RAS (USACE, 2004), two-dimensional models, such as DIVAST (Falconer, et al, 1999) and three-dimensional models, such as TRIVAST (Lin and Falconer, 1997) have already been applied extensively for research and practical purposes. Considering the characteristics of the bathymetry of estuarine zones, some linked one- and two-dimensional models have also be developed (e.g. Lin et al, 2001). Due to the rapid increasing of computer power, increasing attentions has being paid on three-dimensional models. However, it is still costly and time consuming to use a real three-dimensional model for most of the practical studies.

2.2.1 Vertical profile and dispersion coefficient

The vertical structure of the flow fields are not explicitly represented in the depth-integrated hydrodynamic models. Thus, it is necessary to assume a vertical velocity profile in this type of model. The logarithmic profile is used widely (van Rijn, 1993, Falconer et al, 1999). To improve the treatment of the wind stress effect, Falconer and Chen (1991) assumed a parabolic vertical velocity profile. Due to the assumption of the vertical distribution of velocity, it is only suitable to apply the depth-integrated models in the cases with a continuous bed level.

Due to the vertical distribution of concentration is represented by depth averaged concentration, the dispersion coefficient arise in the depth-integrated general solute transport model (Fisher et al, 1979). This coefficient is one of the most important parameters for depth-integrated solute transport models. A number of studies have been undertaken on this topic. A comprehensive account of flow and dispersion in rivers, estuaries and coasts is given in the book by Fisher et al. (1979). Chatwin and Allen (1985) provided a good review of the mathematical models of dispersion in rivers and estuaries. In practice, the dispersion coefficient is usually obtained from calibration against field measured data.

2.2.2 Grid systems

Generally the grid systems used in numerical modelling can be divided into two types: a) structured grid systems and b) unstructured grid systems. Structured grid systems

offer a simple and efficient approach for the solution of the governing transport equations using the finite difference scheme. Whilst unstructured grid systems provide geometric flexibility and simplicity in which the grid can be adapted according to the local topographic and flow features.

The most widely used structured grid is rectangular grid, such as that used in DIVAST (Falconer et al., 1999). Numerical models based on rectangular grid systems are often unable to resolve local features of a complicated geometric domain resulting in poor accuracy in model predictions. Moreover, numerical problems may arise at flow boundaries because of the poor resolution, producing excessive diffusion and vortex. In order to improve the resolution of the model based on rectangular grid system, nested grids have been developed (e.g. Nece and Falconer, 1989 and Wang, 2000). The simplest nested model involves the use of two sets of grid in which a fine mesh is embedded inside a coarse mesh. The coarser grid is imposed over the entire model domain while the finer mesh is located at regions of interest, for instance, at regions of high velocity gradient or complex geometry. Boundary fitted curvilinear grid system is another type of structured grid system, which provides a better representation of complicated geometry and bathymetry (e.g. Lin, 1997, Bao et al, 2000). However, the governing equations and the related numerical method will become more complicated under a curvilinear coordinate system.

Different types of unstructured grid systems exist including the classical triangular or tetrahedral grids, quadrilateral or hexahedral grids, prismatic grids or mixed grids. Among them, the triangular grid system is the most widely used unstructured grids (e.g. Anastasiou and Chan, 1997, Casulli and Walters, 2000). Wang (2000) noted that mixed type grids were recognised as more efficient than other grids by many researchers. Compared to the structured grids, the indexing system of the unstructured grids is more complicated, and searching neighbour grids or cells during the computations is generally time consuming.

2.2.3 Numerical methods

Over the years, various numerical methods and schemes have been developed and applied to solve the governing equations of hydrodynamic and solute and mass transport processes. The most common numerical methods, which have been applied to fluid flow and solute transport, are the finite difference method, the finite element method and the finite volume method. All of the methods have advantages

and disadvantages when compared to one another. The finite difference method, either explicit or implicit, is more efficient than the finite element method and also the approximations of the differential equations are relatively straightforward. It is not very convenient to fit irregular boundaries with the finite difference method, while the finite element method is more suitable for modelling irregular boundaries. Usually, the finite difference method uses less computer time for the same level of grid resolution than the finite element method. On the other hand the finite volume method is the integral formulation of the governing equations, which can be discretized directly and transformed to an algebraic system of equations (Roache, 1998).

For the finite difference method, consistency, stability and convergence are the three most important concepts. Consistency deals with the extent to which the finite difference equations approximate the corresponding partial differential equations. Numerical stability is a concept applicable in the strict sense only to unsteady problems. A stable numerical scheme is one for which errors from any source are not permitted to grow in the sequence of numerical procedures as the calculation proceeds from one step to the next. Convergence means that the solution to the finite difference equation approaches the true solution to the partial differential equation having the same initial and boundary conditions as the space and time steps are reduced. Any finite difference method should be consistent, stable and convergent. In addition, an optimal balance should be kept between accuracy and computing cost (Abbott and Basco, 1997).

In the frame of rectangular structured grid system, the particular finite difference method based upon the Alternating Direction Implicit technique (ADI technique) has been widely used for solving both hydrodynamic and solute transport governing equations (e.g. Leendertse, 1970, Falconer et al, 1999, Tao et al, 2001). According to the ADI technique, each time step is split up into two half time steps. Thus a two-dimensional problem can be solved considering only one dimension implicitly for each half time step, without the solution for a full two-dimensional matrix. Thus, the ADI method keeps a good balance between efficiency and stability.

2.3 MOVING BOUNDARY PROBLEM

Tidal flats are the extent of some estuarine and coastal areas with shallow water subjected to alternating wetting and drying due to experiencing tidal oscillation of the

free surface. Moving boundary (wetting and drying processes) is a common and important phenomenon of the estuarine and coastal zones and in some cases the area of the tidal flats can be of the same order of magnitude as the constantly submerged areas (e.g. in the Mersey Estuary). Most of the tidal flats in the estuaries and coasts play an important role in the ecosystem with their productivities being maintained by the periodic flooding and drying processes. Thus it is necessary for a numerical model to be capable of simulating wetting and drying processes.

The approaches to deal with the moving boundary problems can be broadly classified into two categories: a) moving mesh approach and b) fixed mesh approach. The fixed mesh approach can be divided into two sub-categories: a) the earlier explicit method suggested by Leendertse (1970) and b) the "porosity method" (Tao, 1984, Tao et al, 2001, Ip et al, 1998).

The moving mesh approach is based on spatially deforming computational meshes. The nodes at the boundary are front-tracking with the coordinates of the nodes varying with time. This approach is rather time-consuming because the mesh is re-generated with the moving boundary every time step.

Leendertse (1970) developed an explicit approach for treating the moving boundary problems in his two dimensional model using an ADI finite difference method. This type of approach turns on/off the computational cells when the water depth is greater/less than a threshold water depth, imposes a zero value to the velocity components at dry cells, and sets the water level to the bed elevation at the drying process. When it comes to the flooding process the water level at the moving boundary is determined by extrapolating the water level values at the adjacent wet cells. Falconer (1984, 1986), Falconer and Owens (1987), and Falconer and Chen (1991) improved the wetting and drying method of Leendertse (1970) and applied their refined wetting and drying methods to practical applications. Lin and Falconer (1997), in their three dimensional layer-integrated model, developed a refined wetting and drying algorithm based on the previous method (Falconer and Chen, 1991), tested widely for the two dimensional model. Zhang and Sun (2001, 2002) introduced a wetting and drying method to the ECOM model, and applied the modified model to the Jiaozhou Bay and the Bohai Bay, respectively. Oey (2005) proposed a wetting and drying scheme and applied it to the Princeton Ocean Model (POM). Detailed comparison amongst different wetting and drying methods can be found in Balzano (1998).

Tao (1984) suggested a “Slot Method” which is one type of porosity approach to simulate the moving boundary in short wave models based on Boussinesq equation. Then He (1986) and Wang et al (1998) expanded this method to tidal flows. Porosity approach is based on modifying the governing equations to include a cell “size factor”. In this approach, all of the dry and wet cells are computed by assuming that there is water flow in the porous layer below the bed elevation, and the water level can fall below this elevation. With this method it is not necessary to check every cell is wet or dry at every time step, i.e. this is an implicit method for simulating the wetting and drying processes. However, because of the existence of the porosity, the mass and momentum are not completely conserved in this approach. Some efforts have been taken to reduce the error due to the artificial porosity, e.g. Kennedy (2000) and Tao et al (2001) pointed out that the error can be reduced by adjusting the shape of the slot; Ip et al (1998) modified the momentum equation by adding a hydraulic conductivity in the porous medium; Heniche et al (2000) increased the bottom shear stress in the dry cells to reduce the fictitious flow between wet and dry cells.

2.4 SEDIMENT TRANSPORT MODEL

For several decades researchers have tried to measure and calculate the sediment transport in rivers, estuaries and coasts. As early as 1879 Duboys published his sediment transport formula (see van Rijn, 1993).

In modelling the sediment transport processes in estuarine and coastal waters, the sediment is generally classified as being either cohesive (mud) or non-cohesive (sand and silt) in nature, and with these two types of sediment being described by different formulations. In general, sediment is described as being cohesive if the particle (or grain) diameter is less than $62\mu\text{m}$, with the particles having cohesive properties due to electrostatic forces comparable with gravity forces active between the particles (van Rijn, 1993). The mechanism of cohesive sediment transport is different from that of non-cohesive sediment. In this thesis both cohesive and non-cohesive sediments are taken into account, with the main effort being focused to the non-cohesive sediment, because the sediments in the practical study area (the Mersey Estuary) is mainly non-cohesive.

Depending upon the size and density of the bed material and the flow conditions, sediment particles can be transported by the flow in either the form of bed load or

suspended load. The bed load is defined as that part of the total load where the sediment is almost continuously in contact with the bed, being carried by rolling, sliding or hopping, whereas the suspended load is that part of the total load which is maintained in suspension for considerable periods of time by the turbulence of the flow (van Rijn, 1993). These two components of total load transport are usually represented by different formulations, since the transport mechanisms are different.

2.4.1 Non-Cohesive Sediment

Today, a wide variety of relationships are available in the literature that consider sediment transport as a function of flow parameters and sediment characteristics. Many investigators, notably DuBoys (1879), Schoklitsch (1930), Einstein (1942), Kalinske (1947), Yalin (1972), Engelund and Hansen (1967) and van Rijn (1984a, b) have proposed various mechanisms causing the transport of bed and suspended loads and have suggested formulae to predict them. In recent model developments, especially in Europe, the formulations outlined by van Rijn (1984a, b) have been widely accepted for both suspended and bed load transport. In China, the study on sediment transport has developed quickly in the past 40 years mainly due to the very serious problems associated with sediment transport in several large rivers (e.g. the Yangtze River, Yellow River and Pearl River). Many new theories and empirical formulations were developed, refined and applied to practical studies successfully (see Chien et al (1999), Dou (2003), Lin (2001) and Li et al (2001) et al.).

Due to the complexity of the mechanism of sediment transport, it is generally difficult to derive an analytical solution for this problem. Most of the solutions for practical problems are based upon empirical formulae. Since the sediment transport processes are very complex, the numerical models are generally parameterizations of the elaborated mathematical-physical descriptions. This is still a common practice to make the computer codes cost and time efficient in order for the model to be applicable to practical managerial problems.

It is widely accepted that the concentration of sediment in suspension can be described by an advective-diffusion equation. When the concentration field is solved by the advective-diffusion equation the sediment transport flux can be determined by integration. However, Owens (1986) pointed out that due to the difficulty in defining a bed boundary condition theoretically, suspended load formulae such as given by van Rijn (1984b) tend to rely heavily on empirical coefficients.

Garcia and Parker (1991) studied methods for predicting the entrainment of uniform sediment into suspension by comparing seven different sediment formulae, including that of Einstein (1950), Engelund and Fredsoe (1976), Smith and Mclean (1977), Itakura and Kishi (1980), van Rijn (1984b), Celik and Rodi (1984), Akiyama and Fukushima (1986). They concluded that the formulae given by van Rijn (1984b) and Smith and McLean (1977) performed best when tested against a standard set of data. Van Den Berg and Van Gelder compared three equilibrium sand transport formulae for the prediction of suspended bed material transport rates in the Yellow River, where they found that van Rijn's (1984a) formulation gave the best results.

2.4.2 Cohesive Sediment

Cohesive sediment, or mud, is a mixture of clay particles, silt, (fine) sand, organic material, sometimes gas, and water. This sediment mixture has cohesive properties because of low permeability and electrochemical attraction of clay particles and organic material. Mud is therefore encountered in the form of aggregates (flocs), both in the water column and in the bed.

Cohesive sediment is one of the controlling factors for ecological development in the water system. It is often beneficial as an agent for nutrient transport. On the other hand, high turbidity limits the penetration of sunlight into the water and hinders the growth of water plants by inhibiting photosynthesis and affects the sight of foraging aquatic animals. Furthermore, clay particles in the soil change the erosion and consolidation properties of the soil and therefore the long-term morphodynamic development of the system.

To model cohesive sediment transport, several model parameters given by semi-empirical closure equations are used as input parameters. The settling velocity of flocs, the eddy diffusivity and the sediment flux at the bed (deposition, erosion) are among the most important parameters.

Krone (1962) showed that the deposition process is predominant when the bed-shear stress (τ_b) falls below a critical value for deposition (τ_d). Krone (1962) performed a series of deposition experiments in a flume at low sediment concentrations. He found that the flocculation effect appeared to be of major importance. Metha and Partheniades (1975) performed experiments with cohesive materials under steady flow conditions with bed-shear stresses smaller and larger than the critical bed shear stress for full deposition. Based on the experimental

results of Metha and Partheniades (1975), the following processes can be distinguished as: a) full deposition, b) hindered or partial deposition, and c) no deposition (van Rijn, 1993). Metha (1984) and Winterwerp et al. (1991) tested various natural muds from lakes, rivers and estuaries. Based on these experiments, the critical bed-shear stress (τ_d) was estimated for several sites. Until now, there is not yet an analytical method that can be used to determine the value of τ_d , thus the value of τ_d is usually estimated either with field measured data or by trial and error in numerical modelling studies.

Sediment particles, flocs of the bed surface will be eroded when the applied bed-shear stress (τ_b) exceeds a critical value for erosion (τ_e), which depends on the bed material characteristics (mineral composition, organic materials, salinity, density etc.) and bed structures. Experimental results show that the critical bed-shear stress for erosion is strongly dependent on the deposition and consolidation history. The critical bed-shear stress for erosion was found to be larger than the critical bed-shear stress for full deposition (van Rijn, 1993). At present, a generally accepted formulation to determine the value of τ_e is not yet available, thus this value is usually estimated based on laboratory tests using natural mud or on in-situ field test.

2.5 TRACE METAL TRANSPORT MODEL

Environmental pollution with toxic metals has become a global phenomenon. Because of the growing apprehension about the potential effects of the metallic contaminants on various fauna and flora, the research on fundamental, applied and health aspects of trace metals in the environment has mushroomed to the point that it has become difficult to keep track of recent developments in particular fields (Vernet, 1991). Because of their impact on coastal fish population and on the health of those who eat fish caught in coastal seas, the quantities of trace metals entering coastal waters are of concern. An awareness of the need to quantify such inputs was heightened in the late 1970s with the implementation of the Dangerous Substances Directive (Council of European Communities, 1976). In this study, the focus is placed on modelling the trace metal transport in estuarine and coastal waters.

Sediments are the main fate of heavy metals in aquatic ecosystems, but under several conditions, they can also act as a source of these elements (Izquierdo et al,

1997). Fine sediments act as a source (or sink) for the organic chemicals and trace metals entering (or leaving) the water column with sediments contaminated by trace metals being a potential threat to the aquatic environment. The re-suspension of contaminated bed sediments caused by strong tidal currents or dredging operations may release a significant amount of trace metals into the water column, and the de-sorption of contaminants from their particulate phase can have a pronounced impact on the aquatic environment and ecosystem.

2.5.1 Studies of Partitioning Coefficient

Trace metals generally exist in two phases in coastal and estuarine waters, i.e., in the dissolved phase in the water column and in the particulate phase adsorbed on the sediments. The distribution between suspended particles and water column determines the relative concentrations of a chemical in each phase, hence its reactivity, bioavailability, transport, and fate. In estuaries, the partitioning of chemicals is of particular interest since the reaction-controlling variables are subject to rapid and significant change. The dissolved fraction of the trace metals may be transported through the water column via the processes of advection and dispersion, while the adsorbed particulate fraction may be transported with the sediments, which are governed by sediment dynamics. A key parameter for modelling trace metal transport is the partitioning coefficient (K_D), which is defined as the ratio of the particulate concentration to the dissolved concentration.

Comber et al. (1995) studied the partitioning of trace metals in the Humber and Mersey Estuaries. They found for the Humber, the majority of metals show positive deviations of conservative mixing behaviour. In the Mersey, however, the removal of cadmium and zinc occurs at the freshwater/saline interface and at low salinity regions. The effect is most pronounced for copper and cadmium, and is reflected in very much higher partitioning coefficients for these elements on Mersey suspended solids compared to Humber suspended sediments.

Turner et al. (1993) applied the concept of partitioning coefficient (K_D) to study the trace metal removal and de-sorption during estuarine mixing in the Humber Estuary, UK. Turner and Millward (1994) and Turner et al (2001) studied the partitioning of trace metal in a macro-tidal estuary and pointed out that K_D depends on the physical and chemical characteristics of the suspended particles, together with various ambient conditions, such as: salinity, pH, type and concentration of dissolved

organic matter.

Martino et al. (2002) studied the behaviour of trace metals in the Mersey Estuary, UK, and found that the concentrations of trace metals, with the exception of Cu and Zn, are substantially greater on bed particles than on Suspended Particulate Matter (SPM) and there exists the possibility of de-sorption of metals from bed particles re-suspending in fresh or brackish water.

The behaviour of trace metals in the aquatic environment is strongly influenced by their adsorption to organic and inorganic particles. Turner et al. (2002) studied the partitioning coefficients for trace metals (Cd, Cr, Cu, Hg, Ni, Pb, Zn) from a number of independent studies conducted in the Mersey Estuary which is an organic-rich estuary. It was found that K_D increases with salinity for all metals except Cd. This behaviour is not consistent with inorganic speciation calculations or empirical modelling studies in other estuaries, which predict an inverse relationship between K_D and salinity due to competitive adsorption and complexation with seawater ions. The most possible reason is that trace metals are complexed by and, subsequently, neutralize organic ligands, and that the resulting neutral assemblages are salted out.

Hatje et al. (2003) studied the kinetics of trace element uptake and release by particles in Sydney Harbour. They point out that although the K_D has been reported to be independent of SPM loadings in many studies, this should only occur when the ratio of adsorbing metal to SPM levels is low. Under these conditions, the adsorbed concentration will be proportional to the dissolved concentration. They found that Cd in seawater presented an inverse dependency between K_D and the SPM concentration.

2.5.2 Development of Numerical Models

Numerical models provide a valuable tool for predicting the fate and transport of trace metals in estuarine and coastal environments and are increasingly used for such hydro-environmental management studies of estuarine and coastal waters. However, computer-based tools for predicting the trace metal concentration distributions, although they can support decision-making by the regulatory authorities, marine environment agencies and industry, are still used relatively infrequently (Ng, et al, 1996). Coupled numerical models involving hydrodynamic and contaminant geochemistry processes are very few in number, and they are largely research

oriented, rather than being applied tools for managing estuarine and coastal waters.

Ng et al. (1996) developed a two-dimensional depth integrated numerical model for predicting the transport and fate of contaminants in estuaries. In this study K_D is varied as a function of salinity in either of the following two ways: 1) using the relationship suggested by Turner and Millward (1994); 2) using explicit tabulations of measured values of K_D as a function of salinity. This model was applied to simulate the dissolved Cd and Zn in the Humber Estuary, and reasonably accurate results have been obtained. Ng et al. (1996) emphasized that because the chemical driving variables are empirically derived, the simulation of other metals and trace organic contaminants would rely on further experimental studies.

The transformation processes between the dissolved and adsorbed particulate phase are very complex. Thus it is difficult to calculate the dissolved phase and particulate phase separately due to the difficulty of determining the source/sink term. Noting that $S_i^d = -S_i^p$ (S_i^d = transformation term defining adsorbed or desorbed particulate fluxes to or from the sediments; S_i^p = transformation term defining metal flux from, or to, dissolved phase in the water column), Wu et al (2005) introduced a new method to avoid calculating the transformation rate between the dissolved and adsorbed particulate phases by first calculating the total trace metal concentration distributions, and then dividing the dissolved and adsorbed particulate phases using a partition relationship.

2.6 RESIDENCE TIME

The ecosystem in an estuary is governed by the physical, chemical and biological processes occurring in the water column. The rate of water exchange between an estuary and the open sea plays a critical role in controlling the chemical and biological processes within the basin. Thus it can affect significantly the fate of contaminated substances. In recent years the water exchange has been increasingly investigated in estuarine and coastal water quality studies (e.g., Fukumoto and Kobayashi, 2005; Delhez et al, 2004; Liu et al, 2004; Dong and Su, 1999a and 1999b; Kithaka, 1997; Luff and Pohlman, 1996). As a related concept to water exchange, the residence time is often used as a parameter for representing the time scale of the physical transport processes (Bolin and Rodhe, 1973; Zimmerman, 1976; Takeoka,

1984). It is also often used as an indicator for studying the time scales of the bio-chemical fluxes and processes. A pollutant exerts most of its effects within an estuary if its bio-chemical time scales are comparable to, or shorter than, the residence time. The concept of residence time has also been widely used in many recent studies on water exchange in estuarine waters.

Several concepts of time scales, such as age, residence time, transit time and turn-over time, have been developed for studying water exchange between inner and outer water bodies. The definitions of these concepts have often been confusing: sometimes different concepts are called by the same name, whereas at other times the same concept is called by different names. Bolin and Rodhe (1973) introduced the concept of 'age' of a water particle remaining in a water body and summarised several, then existing, concepts on the basis of 'age' and gave a rigorous definition to each. Zimmerman (1976) introduced a new 'residence time', which was different from that defined by Bolin and Rodhe (1973). Following the definition given by Zimmerman (1976), Takeoka (1984) established relationships between the residence time and other time scales, and thus complemented the concept of residence time.

Residence time is a measure of the average amount of time that a dissolved constituent (biological or chemical) spends in a volume within the estuary. Residence time is an important indicator for global understanding of an estuary. Estuaries with a short residence time will export nutrients from upstream sources more rapidly than estuaries with long residence time.

2.7 SUMMARY

In this chapter previous studies on hydrodynamic and solute and mass transport modelling are summarised at first. Detailed review of the methods for treating the moving boundary problem is then undertaken. Following this, the sediment and trace metal transport modelling are reviewed with particular attentions being paid to the partitioning coefficient and numerical methods for solving the governing equations of trace metal transport model. Finally, the concept of residence time is introduced.

CHAPTER 3

GOVERNING EQUATIONS OF HYDRODYNAMIC AND SOLUTE TRANSPORT PROCESSES

3.1 INTRODUCTION

It is widely accepted that the solute, suspended sediment and trace metal transport processes can be modelled by using the advective-diffusion equation with well defined initial and boundary conditions, plus suitable source and sink terms. Thus it is necessary to understand the solute and mass transport processes before developing the mathematic model to predict solute, sediment and trace metal processes. On the other hand, before any attempt can be made to model the solute, sediment or trace metal transport processes in estuarine and coastal waters, it is first necessary to predict the hydrodynamic features of the flow, including the water surface elevation and velocity field. The fluctuations of groundwater level in coastal aquifers have also been found to affect the solute, sediment and trace metal processes in estuarine and coastal waters (Li, et al, 2000). Thus it is helpful to take the effect of the groundwater flow into account to some extent, although it is not the main goal of this thesis.

This chapter is devoted to the establishment of the governing equations of hydrodynamic and solute transport processes in estuarine and coastal waters, as well as the hydrodynamic governing equations for unconfined groundwater flow in coastal aquifers. The corresponding equations are based on the conservation laws of mass (continuity equation and solute transport equation) and momentum (Newton's second law of motion).

3.2 BASIC THREE DIMENSIONAL GOVERNING EQUATIONS

In a real world the hydrodynamic and solute transport processes are always in three dimension, thus it is necessary to establish the three dimensional governing equations at first. Depending upon the nature of the flow and transport process, sometimes the governing equations may be integrated into two dimensional or one dimensional form

to predict the flow field and transport processes.

3.2.1 Solute and Mass Transport Processes

In modelling numerically the fluxes of sediments or water quality constituents within estuarine and coastal waters, the conservation of mass equation can be written in general terms for any substance introduced into a fluid medium.

Considering the infinitesimal control volume as shown in Figure 3-1, at anytime the total substance flux pass through the surface of this volume is:-

$$\text{Substance Flux} = \iint_{\Delta S} (\varphi \vec{n} \cdot \vec{V}_s - \vec{n} \cdot \mathbf{D} \nabla \varphi) dS \quad (3-1)$$

where, $\vec{V}_s = \vec{V} + \vec{V}_r$ is the velocity of the substance on the surface of the control volume, with \vec{V} and \vec{V}_r are the flow velocity and the velocity of the substance relative to the flow, respectively, \vec{n} is the outward normal direction of the surface, φ is the concentration of the substance, \mathbf{D} is a second order tensor of the molecular diffusion coefficient, and ΔS is the total surface of the control volume. The change rate of the substance in the control volume is:-

$$\text{Substance Change Rate} = \frac{\partial}{\partial t} \iiint_{\Delta V} \varphi dV \quad (3-2)$$

where, ΔV is the total volume of the control volume.

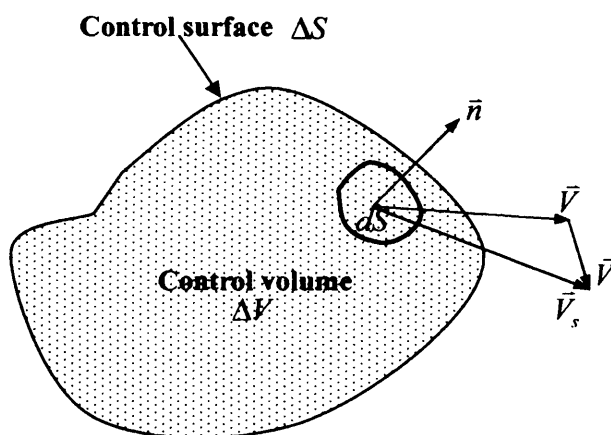


Figure 3-1 Schematic illustration of control volume for solute and mass transport

If there is not any source or sink in the control volume, and assuming that the

molecular diffusion coefficient is isotropic (i.e. the tensor \mathbf{D} can be replaced with a scalar D), applying mass balance of the substance entering/leaving the infinitesimal control volume and the substance change rate in the control volume gives:-

$$\frac{\partial}{\partial t} \iiint_{\Delta V} \phi dV + \iint_{\Delta S} (\phi \bar{n} \cdot \bar{V}_s - \bar{n} \cdot D \nabla \phi) dS = 0 \quad (3-3)$$

Using the Green's theorem, Equation (3-3) can be re-written as:-

$$\iiint_{\Delta V} \left[\frac{\partial \phi}{\partial t} + \nabla \cdot (\phi \bar{V}_s) - \nabla \cdot (D \nabla \phi) \right] dV = 0 \quad (3-4)$$

As the control volume is arbitrary, the kernel of the integration must equal to zero, giving:-

$$\frac{\partial \phi}{\partial t} + \nabla \cdot (\phi \bar{V}_s) = \nabla \cdot (D \nabla \phi) \quad (3-5)$$

In some cases, the substance can be considered as Passive Dissolved Conservative Matter (PDCM), i.e. the substance moves with the same velocity as fluid particles, resulting in $\bar{V}_r = 0$, and $\bar{V}_s = \bar{V}$. Thus Equation (3-5) can be changed to:-

$$\frac{\partial \phi}{\partial t} + \nabla \cdot (\phi \bar{V}) = \nabla \cdot (D \nabla \phi) \quad (3-6)$$

Re-writing Equation (3-6) in Cartesian coordinate system gives:-

$$\frac{\partial \phi}{\partial t} + \frac{\partial(u\phi)}{\partial x} + \frac{\partial(v\phi)}{\partial y} + \frac{\partial(w\phi)}{\partial z} = \frac{\partial}{\partial x} \left(D \frac{\partial \phi}{\partial x} \right) + \frac{\partial}{\partial y} \left(D \frac{\partial \phi}{\partial y} \right) + \frac{\partial}{\partial z} \left(D \frac{\partial \phi}{\partial z} \right) \quad (3-7)$$

where, u , v , w = instantaneous fluid velocity components in the x -, y -, z -directions respectively.

If there is any source or sink of the substance in the studying area, a source or sink item ϕ_o can be added to the right hand side of Equation (3-7) to give the well known three dimensional advective-diffusion equation:-

$$\frac{\partial \phi}{\partial t} + \frac{\partial(u\phi)}{\partial x} + \frac{\partial(v\phi)}{\partial y} + \frac{\partial(w\phi)}{\partial z} = \frac{\partial}{\partial x} \left(D \frac{\partial \phi}{\partial x} \right) + \frac{\partial}{\partial y} \left(D \frac{\partial \phi}{\partial y} \right) + \frac{\partial}{\partial z} \left(D \frac{\partial \phi}{\partial z} \right) + \phi_o \quad (3-8)$$

3.2.2 Governing Equations for Hydrodynamic Processes

Fluid motion can be described by two sets of partial differential equations, namely the continuity equation and the momentum equation. The continuity equation (or the

conservation equation of fluid mass) describes that the mass inflow per unit time equals the mass outflow per unit time plus the change in mass within the control volume per unit time. While the momentum equation describes that the rate of change of momentum is proportional to the resultant applied force and is along the line of action of the force. For an incompressible flow, the governing three dimensional equations for fluid flow in a Cartesian coordinate system are derived below. Details of the derivation of these equations can be found elsewhere in a variety of text book such as Liggett (1994) and Falconer (1994).

3.2.2.1 Continuity Equation

Continuity equation can be considered as a special case of the governing equation of solute and mass transport equation with the diffusion term equalling to zero, as both of them express the mass balance in a control volume. Let the substance be the fluid itself, i.e.,

$$\vec{V}_r = 0, \text{ and } \vec{V}_s = \vec{V} \quad (3-9a)$$

The concentration of the substance (φ) can be replaced with the product of the density of the fluid (ρ) and the porosity of the media (n_e), which gives:-

$$\varphi = \rho n_e \quad (3-9b)$$

Substituting (3-9) into (3-6) and considering that the diffusion term equals to zero gives the following continuity equation:-

$$\frac{\partial(\rho n_e)}{\partial t} + \nabla \cdot (\rho n_e \vec{V}) = 0 \quad (3-10)$$

For incompressible flow involving only a single phase of fluid in the domain, ρ remains invariant with time. Furthermore assuming that the porosity does not vary with time, thus Equation (3-10) can be written as:-

$$\nabla \cdot (n_e \vec{V}) = 0 \quad (3-11a)$$

This is the continuity equation for the incompressible three-dimensional flow in porous media. Assuming the porosity, $n_e = 1$, gives:-

$$\nabla \cdot \vec{V} = 0 \quad (3-11b)$$

This is the continuity equation for the incompressible three-dimensional surface water flow. It means that the divergence of the velocity is zero. Re-writing Equation (3-11a)

in Cartesian coordinate system gives:-

$$\frac{\partial(n_e u)}{\partial x} + \frac{\partial(n_e v)}{\partial y} + \frac{\partial(n_e w)}{\partial z} = 0 \quad (3-12)$$

3.2.2.2 Momentum Equation

According to Newton's second law of motion, the sum of the external forces acting on a unit mass element must equal to the rate of linear momentum giving:-

$$\sum \vec{F} = \frac{d\vec{M}}{dt} \quad (3-13)$$

where \vec{F} is the resultant force, and \vec{M} is the momentum.

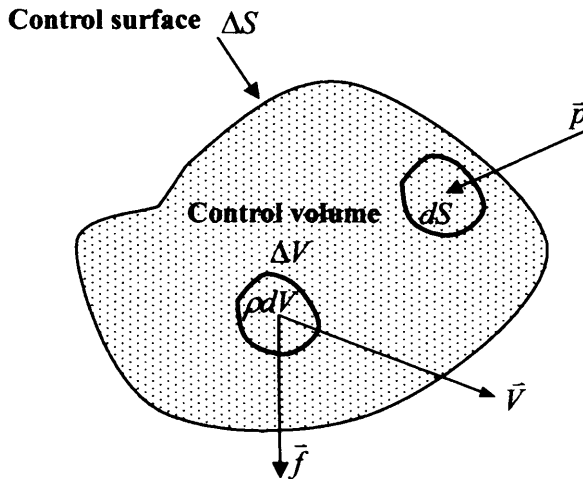


Figure 3-2 Schematic illustration of control volume for momentum equation

Considering the infinitesimal control volume as shown in Figure 3-2, the resultant force acting on the control volume can be expressed as follows:-

$$\sum \vec{F} = \iiint_{\Delta V} \rho \vec{f} dV + \iint_{\Delta S} \bar{p} dS \quad (3-14)$$

where \vec{f} is the body force acting on the fluid, and \bar{p} is the surface force acting on the control volume. The momentum, \vec{M} , can be evaluated with the following integration:-

$$\vec{M} = \iiint_{\Delta V} \rho \vec{V} dV \quad (3-15)$$

The surface force can be expressed as:-

$$\bar{p} = \bar{n} \cdot \nabla \mathbf{P} \quad (3-16)$$

where \mathbf{P} is the stress tensor. Using the notation that the first subscript defines the plane normal to the subscript and the second subscript defines the stress direction on the plane (see Figure 3-3), then the stress tensor (\mathbf{P}) can be expressed as:-

$$\mathbf{P} = \begin{bmatrix} \sigma'_{xx} & \tau_{xy} & \tau_{xz} \\ \tau_{yx} & \sigma'_{yy} & \tau_{yz} \\ \tau_{zx} & \tau_{zy} & \sigma'_{zz} \end{bmatrix} \quad (3-17)$$

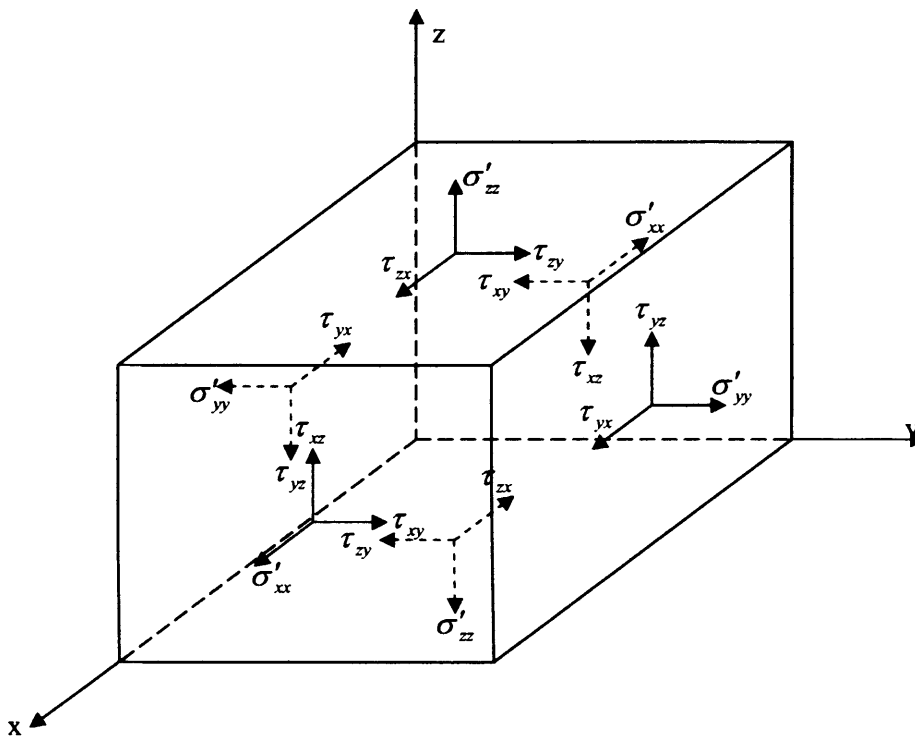


Figure 3-3 Schematic illustration of definition of stress components

Substituting Equation (3-14) and (3-15) into Equation (3-13), and by using the Green's theorem gives:-

$$\iiint_{\Delta V} \left[\frac{d(\rho \bar{V})}{dt} - \rho \bar{f} - \nabla \cdot \mathbf{P} \right] dV = 0 \quad (3-18)$$

Since the control volume is arbitrary, the kernel of the integration must equal to zero, giving:-

$$\frac{d(\rho\bar{V})}{dt} - \rho\bar{f} - \nabla \cdot \mathbf{P} = 0 \quad (3-19)$$

Equation (3-19) is the general momentum equation. For incompressible flow involving only a single species of fluid in the domain, ρ remains invariant with time, thus Equation (3-19) can be re-written as:-

$$\frac{d\bar{V}}{dt} - \bar{f} - \frac{1}{\rho} \nabla \cdot \mathbf{P} = 0 \quad (3-20)$$

The normal tensile fluid stress σ'_{xx} (or σ'_{yy} or σ'_{zz}) is composed of two components: firstly, the hydrostatic pressure P , which is a negative stress, and secondly the component σ_{xx} (or σ_{yy} or σ_{zz}), which is proportional to the time rate of change of strain. The normal stresses can be defined as (Schlichting, 1979):-

$$\begin{cases} \sigma'_{xx} = \bar{\sigma} + \sigma_{xx} \\ \sigma'_{yy} = \bar{\sigma} + \sigma_{yy} \\ \sigma'_{zz} = \bar{\sigma} + \sigma_{zz} \end{cases} \quad (3-21)$$

$$\text{where } \bar{\sigma} = \frac{1}{2}(\sigma'_{xx} + \sigma'_{yy} + \sigma'_{zz}) = -P.$$

Substituting Equation (3-21) into (3-20) gives the momentum equation for laminar or turbulent flow in the x-, y- and z-directions as follows:-

$$\frac{du}{dt} = X - \frac{1}{\rho} \frac{\partial P}{\partial x} + \frac{1}{\rho} \left(\frac{\partial \sigma_{xx}}{\partial x} + \frac{\partial \tau_{yx}}{\partial y} + \frac{\partial \tau_{zx}}{\partial z} \right) \quad (3-22a)$$

$$\frac{dv}{dt} = Y - \frac{1}{\rho} \frac{\partial P}{\partial y} + \frac{1}{\rho} \left(\frac{\partial \tau_{xy}}{\partial x} + \frac{\partial \sigma_{yy}}{\partial y} + \frac{\partial \tau_{zy}}{\partial z} \right) \quad (3-22b)$$

$$\frac{dw}{dt} = Z - \frac{1}{\rho} \frac{\partial P}{\partial z} + \frac{1}{\rho} \left(\frac{\partial \tau_{xz}}{\partial x} + \frac{\partial \tau_{yz}}{\partial y} + \frac{\partial \sigma_{zz}}{\partial z} \right) \quad (3-22c)$$

where X , Y and Z are the x-, y- and z-direction components of the body force (\bar{f}).

However, for three-dimensional unsteady flows, $\bar{V} = \bar{V}(x, y, z, t)$, and the total acceleration can be decomposed into its local and advective components, giving:-

$$\frac{d\bar{V}}{dt} = \frac{\partial \bar{V}}{\partial t} + \bar{V} \cdot \nabla \bar{V} \quad (3-23)$$

Substituting the x-direction component of Equation (3-23) into (3-22a) gives another form of the x-direction momentum equation as follows:-

$$\frac{\partial u}{\partial t} + u \frac{\partial u}{\partial x} + v \frac{\partial u}{\partial y} + w \frac{\partial u}{\partial z} = X - \frac{1}{\rho} \frac{\partial P}{\partial x} + \frac{1}{\rho} \left(\frac{\partial \sigma_{xx}}{\partial x} + \frac{\partial \tau_{yx}}{\partial y} + \frac{\partial \tau_{zx}}{\partial z} \right) \quad (3-24)$$

The y- and z-direction momentum equations can be re-written in similar forms.

Multiplying the continuity equation (Equation (3-12)) by u with $n_z = 1$, giving:-

$$u \frac{\partial u}{\partial x} + u \frac{\partial v}{\partial y} + u \frac{\partial w}{\partial z} = 0 \quad (3-25)$$

Substituting Equation (3-25) into Equation (3-24) gives the conservative form of the momentum equation for incompressible flow in the x-direction:-

$$\begin{aligned} \frac{\partial u}{\partial t} + \frac{\partial(uu)}{\partial x} + \frac{\partial(uv)}{\partial y} + \frac{\partial(uw)}{\partial z} = X - \frac{1}{\rho} \frac{\partial P}{\partial x} \\ + \frac{1}{\rho} \left\{ \frac{\partial}{\partial x} \left[\mu \left(\frac{\partial u}{\partial x} + \frac{\partial u}{\partial x} \right) \right] + \frac{\partial}{\partial y} \left[\mu \left(\frac{\partial v}{\partial x} + \frac{\partial u}{\partial y} \right) \right] + \frac{\partial}{\partial z} \left[\mu \left(\frac{\partial w}{\partial x} + \frac{\partial u}{\partial z} \right) \right] \right\} \end{aligned} \quad (3-26)$$

where μ is the kinetic viscosity coefficient, and the relationship between μ and the normal and shear stresses for incompressible flow can be defined as (Schlichting, 1979):-

$$\begin{cases} \sigma_{xx} = \mu \left(\frac{\partial u}{\partial x} + \frac{\partial u}{\partial x} \right) \\ \tau_{yx} = \mu \left(\frac{\partial v}{\partial x} + \frac{\partial u}{\partial y} \right) \\ \tau_{zx} = \mu \left(\frac{\partial w}{\partial x} + \frac{\partial u}{\partial z} \right) \end{cases} \quad (3-27)$$

The y- and z-direction momentum equations can be re-written in similar forms with similar definitions of normal and shear stresses in the y- and z-directions.

3.3 THREE DIMENSIONAL GOVERNING EQUATIONS FOR TURBULENT FLOW

Fluid flow can be classified into two broad categories, laminar and turbulent flows. An index relating the flow conditions to the flow category is the Reynolds number (R_c)

defined as:-

$$R_e = \rho \frac{LU}{\mu} \text{ or } \frac{LU}{\nu} \quad (3-28)$$

where U is a characteristic velocity, L is a characteristic length scale (taken to be the hydraulic radius, or in wide channels the depth of flow), and ν is the kinematic viscosity with $\nu = \mu/\rho$. For free-surface flows, the critical Reynolds number dividing the flow categories is generally assumed to be 500, with turbulent free-surface flow occurring at values of R_e greater than 500 and laminar flow at Reynolds numbers less than 500. In practical model studies of estuarine and coastal flows, the flow is almost always highly turbulent and is defined by the Reynolds equations, which describe the three-dimensional turbulent motion of the incompressible fluid.

3.3.1 Continuity Equation

For turbulent flow, the instantaneous velocity component u can be expressed as

$$u = \bar{u} + u' \quad (3-29a)$$

where

$$\bar{u} = \text{temporal average velocity component} = \frac{1}{\Delta t} \int_t^{t+\Delta t} u dt \quad (3-29b)$$

and

$$u' = \text{fluctuating velocity component where } \bar{u'} = \frac{1}{\Delta t} \int_t^{t+\Delta t} u' dt = 0. \quad (3-29c)$$

Substituting the time average fluctuating components into Equation (3-12) gives the following continuity equation based on the temporal average velocity:-

$$\frac{\partial(n_e \bar{u})}{\partial x} + \frac{\partial(n_e \bar{v})}{\partial y} + \frac{\partial(n_e \bar{w})}{\partial z} = 0 \quad (3-30)$$

3.3.2 Momentum Equation

Substituting the time average fluctuating components into Equation (3-26) gives the following well known form of the Reynolds average Navier-Stokes equation in the x -direction (Falconer, 1994):-

$$\begin{aligned}
\underbrace{\frac{\partial \bar{u}}{\partial t}}_{\text{term1}} + \underbrace{\bar{u} \frac{\partial \bar{u}}{\partial x} + \bar{v} \frac{\partial \bar{u}}{\partial y} + \bar{w} \frac{\partial \bar{u}}{\partial z}}_{\text{term2}} &= \underbrace{X}_{\text{term3}} - \underbrace{\frac{1}{\rho} \frac{\partial P}{\partial x}}_{\text{term4}} \\
&+ \underbrace{\frac{1}{\rho} \left[\frac{\partial}{\partial x} \left[\mu \left(\frac{\partial \bar{u}}{\partial x} + \frac{\partial \bar{u}}{\partial x} \right) - \rho \overline{u'u'} \right] + \frac{\partial}{\partial y} \left[\mu \left(\frac{\partial \bar{v}}{\partial x} + \frac{\partial \bar{u}}{\partial y} \right) - \rho \overline{v'u'} \right] + \frac{\partial}{\partial z} \left[\mu \left(\frac{\partial \bar{w}}{\partial x} + \frac{\partial \bar{u}}{\partial z} \right) - \rho \overline{w'u'} \right] \right]}_{\text{term5}}
\end{aligned} \quad (3-31a)$$

In Equation (3-31a) the terms 1 to 5 refer to: (1) local acceleration, (2) advective or convective acceleration, (3) body force, (4) pressure gradient, and (5) laminar and turbulent shear stresses.

In the y- and z-directions similar equations for the conservation of momentum are given respectively as follows:-

$$\begin{aligned}
\frac{\partial \bar{v}}{\partial t} + \bar{u} \frac{\partial \bar{v}}{\partial x} + \bar{v} \frac{\partial \bar{v}}{\partial y} + \bar{w} \frac{\partial \bar{v}}{\partial z} &= Y - \frac{1}{\rho} \frac{\partial P}{\partial y} \\
&+ \frac{1}{\rho} \left[\frac{\partial}{\partial x} \left[\mu \left(\frac{\partial \bar{u}}{\partial y} + \frac{\partial \bar{v}}{\partial x} \right) - \rho \overline{v'u'} \right] + \frac{\partial}{\partial y} \left[\mu \left(\frac{\partial \bar{v}}{\partial y} + \frac{\partial \bar{v}}{\partial y} \right) - \rho \overline{v'v'} \right] + \frac{\partial}{\partial z} \left[\mu \left(\frac{\partial \bar{w}}{\partial y} + \frac{\partial \bar{v}}{\partial z} \right) - \rho \overline{v'w'} \right] \right]
\end{aligned} \quad (3-31b)$$

$$\begin{aligned}
\frac{\partial \bar{w}}{\partial t} + \bar{u} \frac{\partial \bar{w}}{\partial x} + \bar{v} \frac{\partial \bar{w}}{\partial y} + \bar{w} \frac{\partial \bar{w}}{\partial z} &= Z - \frac{1}{\rho} \frac{\partial P}{\partial z} \\
&+ \frac{1}{\rho} \left[\frac{\partial}{\partial x} \left[\mu \left(\frac{\partial \bar{u}}{\partial z} + \frac{\partial \bar{w}}{\partial x} \right) - \rho \overline{w'u'} \right] + \frac{\partial}{\partial y} \left[\mu \left(\frac{\partial \bar{v}}{\partial z} + \frac{\partial \bar{w}}{\partial y} \right) - \rho \overline{w'v'} \right] + \frac{\partial}{\partial z} \left[\mu \left(\frac{\partial \bar{w}}{\partial z} + \frac{\partial \bar{w}}{\partial z} \right) - \rho \overline{w'w'} \right] \right]
\end{aligned} \quad (3-31c)$$

3.3.2.1 Reynolds Stresses

The terms $-\rho \overline{u'u'}$, $-\rho \overline{v'u'}$ and $-\rho \overline{w'u'}$ in Equation (3-31) are known as the

Reynolds (or apparent) stresses, with their form being similar to the viscous shear stresses. These additional terms arise from the time averaging of the turbulence and are zero for laminar flow. In solving for these Reynolds stresses, Boussinesq (see Rodi, 2000) proposed that they could be represented in a diffusive manner whereby:-

$$\begin{cases} -\overline{\rho u'u'} = \eta \left(\frac{\partial \bar{u}}{\partial x} + \frac{\partial \bar{u}}{\partial x} \right) \\ -\overline{\rho u'v'} = \eta \left(\frac{\partial \bar{u}}{\partial y} + \frac{\partial \bar{v}}{\partial x} \right) \\ -\overline{\rho u'w'} = \eta \left(\frac{\partial \bar{u}}{\partial z} + \frac{\partial \bar{w}}{\partial x} \right) \end{cases} \quad (3-32)$$

where η is the absolute eddy viscosity, or, as for laminar viscosity, ε is the kinematic eddy viscosity which equals η/ρ . In general, for turbulent flow, $\eta \gg \mu$ or $\varepsilon \gg \nu$.

To determine the Reynolds stresses given in Equation (3-32), many different and varyingly complicated expressions exist for ε (or η), which can be summarized as follows (Falconer, 1994):-

- The simplest method of closing the equation for evaluating ε is to assume a constant value based on field data. Typically $\varepsilon = 10\text{m}^2\text{s}^{-1}$ (see Falconer, 1993).
- The representation most widely used in estuarine and coastal flows is to apply a zero-equation turbulence model similar to that prescribed by Prandtl's mixing length hypothesis (see Rodi, 2000) where, for the x-direction:-

$$\varepsilon = l^2 J$$

where l is the characteristic mixing length and

$$J = \left[\begin{aligned} &2 \left(\frac{\partial \bar{u}}{\partial x} \right)^2 + 2 \left(\frac{\partial \bar{v}}{\partial y} \right)^2 + 2 \left(\frac{\partial \bar{w}}{\partial z} \right)^2 \\ &+ \left(\frac{\partial \bar{w}}{\partial y} + \frac{\partial \bar{v}}{\partial z} \right)^2 + \left(\frac{\partial \bar{u}}{\partial z} + \frac{\partial \bar{w}}{\partial x} \right)^2 + \left(\frac{\partial \bar{v}}{\partial x} + \frac{\partial \bar{u}}{\partial y} \right)^2 \end{aligned} \right]^{1/2} \quad (3-33)$$

with this expression J generally being simplified due to the dominance of one or more velocity gradients. In determining the mixing length l , Prandtl suggested that $l = \kappa z$ near the bed or a wall, where κ = von Karman's constant and z =

distance perpendicular to the bed or wall, with $z = 0$ at the bed. Other expressions can be used for l , including, for example, von Karman's representation, given for the x -direction as:-

$$l = \kappa \left(\frac{\partial u}{\partial z} / \frac{\partial^2 u}{\partial z^2} \right) \quad (3-34)$$

- c) For more refined turbulence models, transport equations exist for the turbulent kinetic energy and the energy dissipation, i.e. the $k - \varepsilon$ model, or for the Reynolds stresses directly, i.e. algebraic stress models. Further details of these refined models are given by Rodi (2000).

In this study the Prandtl's mixing length hypothesis is used in view of its simplicity and requirement of minimal computational effort.

3.3.2.2 Body Forces and Coriolis Acceleration

In modelling estuarine and coastal flows, the studying areas are usually in large sizes, thus the effect of the earth's rotation cannot be ignored and an additional component of acceleration arises due to relative motion. This additional acceleration component is known as the Coriolis acceleration and can be included in the body force as:-

$$\begin{cases} X = +2\bar{v}\omega \sin \theta \\ Y = -2\bar{u}\omega \sin \theta \\ Z = -g \end{cases} \quad (3-35)$$

where g is the gravitational acceleration, ω is the speed of earth's rotation $\approx 7.3 \times 10^{-5} \text{ rad s}^{-1}$, i.e. $2\pi/(24 \times 3600)$, and θ is the earth's latitude at the site of interest.

3.3.3 Solute and Mass Transport Processes

Similar to the turbulence flow (see Equation (3-29)), the instantaneous concentration of a substance φ can be expressed as:-

$$\varphi = \bar{\varphi} + \varphi' \quad (3-36a)$$

where

$$\bar{\varphi} = \text{temporal average concentration} = \frac{1}{\Delta t} \int_t^{t+\Delta t} \varphi dt \quad (3-36b)$$

and

$$\phi' = \text{fluctuating concentration with } \overline{\phi'} = \frac{1}{\Delta t} \int_t^{t+\Delta t} \phi' dt = 0 \quad (3-36c)$$

Substituting the time average fluctuating components (Equation (3-29) and (3-36)) into Equation (3-8) gives:-

$$\begin{aligned} & \underbrace{\frac{\partial \overline{\phi}}{\partial t}}_{\text{term1}} + \underbrace{\frac{\partial(\overline{u\phi})}{\partial x} + \frac{\partial(\overline{v\phi})}{\partial y} + \frac{\partial(\overline{w\phi})}{\partial z}}_{\text{term2}} + \underbrace{\frac{\partial(\overline{u'\phi'})}{\partial x} + \frac{\partial(\overline{v'\phi'})}{\partial y} + \frac{\partial(\overline{w'\phi'})}{\partial z}}_{\text{term3}} \\ & = \underbrace{\frac{\partial}{\partial x} \left(D \frac{\partial \overline{\phi}}{\partial x} \right) + \frac{\partial}{\partial y} \left(D \frac{\partial \overline{\phi}}{\partial y} \right) + \frac{\partial}{\partial z} \left(D \frac{\partial \overline{\phi}}{\partial z} \right)}_{\text{term4}} + \underbrace{\phi_o}_{\text{term5}} \end{aligned} \quad (3-37)$$

The individual terms in the advective-diffusion equation (3-37) refer to: local effects (term 1), transport by advection (term 2), turbulent effects (term 3), molecular diffusion (term 4), and source/sink (term 5).

The cross-product terms $\overline{u'\phi'}$, etc., represent the mass flux of solute due to the turbulent fluctuations and, by analogy with Fick's law of diffusion, it can be assumed that this flux is proportional to the gradient of the mean concentration and is in the direction of decreasing concentration (Harleman, 1966). Hence, the terms can be written as:-

$$\begin{cases} \overline{u'\phi'} = -D_x \frac{\partial \overline{\phi}}{\partial x} \\ \overline{v'\phi'} = -D_y \frac{\partial \overline{\phi}}{\partial y} \\ \overline{w'\phi'} = -D_z \frac{\partial \overline{\phi}}{\partial z} \end{cases} \quad (3-38)$$

where D_x , D_y , D_z = turbulent diffusion coefficients in the x-, y- and z-directions, respectively. For estuarine and coastal flows it is common to assume isotropic turbulence and to set the horizontal turbulent diffusion terms according to the depth mean diffusion coefficient given by Fischer (1973) wherein:-

$$D_x = D_y = 0.15u_*H \quad (3-39)$$

Likewise, for the vertical diffusion coefficient, in the absence of stratification it is common to assume a linear shear stress distribution and a logarithmic velocity distribution giving:-

$$D_z = u_* \kappa z \left(1 - \frac{z}{H} \right) \quad (3-40)$$

where z = elevation above the bed.

In general, for turbulent flow, D_x , D_y , and D_z are much greater than the molecular diffusion coefficient D , thus it is reasonable to drop term 4 in Equation (3-37), which gives:-

$$\frac{\partial \bar{\varphi}}{\partial t} + \frac{\partial(\bar{u}\bar{\varphi})}{\partial x} + \frac{\partial(\bar{v}\bar{\varphi})}{\partial y} + \frac{\partial(\bar{w}\bar{\varphi})}{\partial z} = \frac{\partial}{\partial x} \left(D_x \frac{\partial \bar{\varphi}}{\partial x} \right) + \frac{\partial}{\partial y} \left(D_y \frac{\partial \bar{\varphi}}{\partial y} \right) + \frac{\partial}{\partial z} \left(D_z \frac{\partial \bar{\varphi}}{\partial z} \right) + \varphi_o \quad (3-41)$$

3.4 DEPTH INTEGRATED GOVERNING EQUATIONS

For many estuarine, coastal and groundwater flow problems the vertical velocity component is relatively small in comparison with the horizontal velocity components. Hence it is appropriate to integrate these equations over the depth of water, resulting in simplified depth integrated two dimensional equations. Hereafter, the over bars of the temporal average velocity components and concentration are discarded because the flows in estuarine and coastal waters are always assumed to be turbulent in this study.

3.4.1 Hydrodynamic Governing Equations for Surface Water Flow

3.4.1.1 Continuity Equation

Using the notations shown in Figure 3-4, the depth integration of the continuity equation (3-30) with the porosity $n_e = 1$, gives:-

$$\int_{-h}^{\zeta} \left(\frac{\partial u}{\partial x} + \frac{\partial v}{\partial y} + \frac{\partial w}{\partial z} \right) dz = \int_{-h}^{\zeta} \left(\frac{\partial u}{\partial x} + \frac{\partial v}{\partial y} \right) dz + w_{\zeta} - w_{-h} \quad (3-42)$$

where, h is the water depth below datum, ζ is the water surface elevation above datum (see Figure 3-4).

Using the Leibnitz rule, given as:-

$$\int_a^b \frac{\partial}{\partial y} f(x, y) dz = \frac{\partial}{\partial y} \int_a^b f(x, y) dz - f(b, y) \frac{\partial b}{\partial y} + f(a, y) \frac{\partial a}{\partial y} \quad (3-43)$$

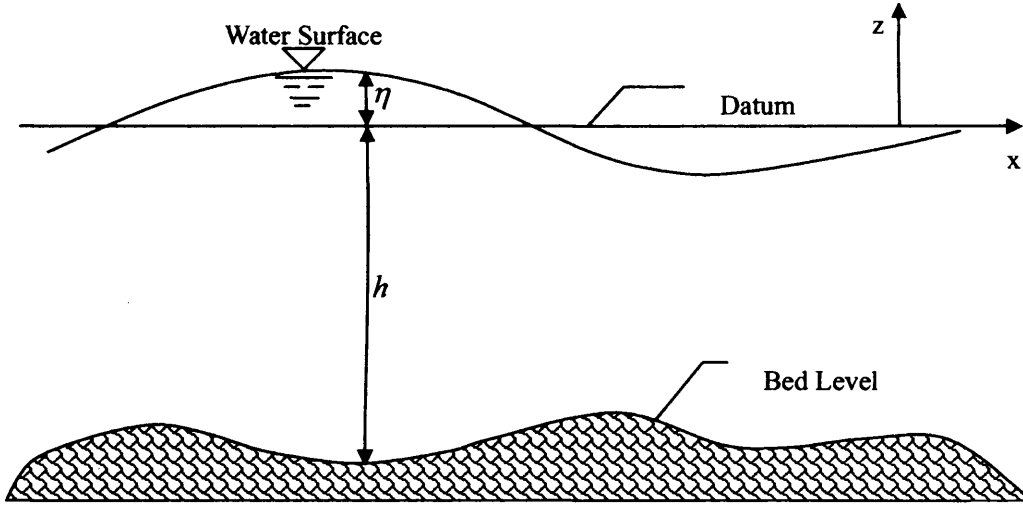


Figure 3-4 Coordinate system for depth integrated equations

Equation (3-42) can be expanded to give:-

$$\begin{aligned} \frac{\partial}{\partial x} \int_{-h}^{\zeta} u dz + \frac{\partial}{\partial y} \int_{-h}^{\zeta} v dz - u_{\zeta} \frac{\partial \zeta}{\partial x} \Big|_{\zeta} + u_{-h} \frac{\partial(-h)}{\partial x} \Big|_{-h} \\ - v_{\zeta} \frac{\partial \zeta}{\partial y} \Big|_{\zeta} + v_{-h} \frac{\partial(-h)}{\partial y} \Big|_{-h} + w_{\zeta} - w_{-h} = 0 \end{aligned} \quad (3-44)$$

At the bed, the no-slip boundary condition gives $u_{-h} = v_{-h} = w_{-h} = 0$, and at the surface the kinematic free surface condition, which assumes that a fluid particle remains on the surface (Mei, 2003), gives:-

$$\frac{d\zeta}{dt} \Big|_{\zeta} = \left(\frac{\partial \zeta}{\partial t} + \frac{\partial \zeta}{\partial x} \frac{dx}{dt} + \frac{\partial \zeta}{\partial y} \frac{dy}{dt} \right) \Big|_{\zeta} = \left(\frac{\partial \zeta}{\partial t} + u \frac{\partial \zeta}{\partial x} + v \frac{\partial \zeta}{\partial y} \right) \Big|_{\zeta} = w_{\zeta} \quad (3-45)$$

Substituting Equation (3-45) into Equation (3-44) gives, for the depth integrated continuity equation:-

$$\frac{\partial \zeta}{\partial t} + \frac{\partial(UH)}{\partial x} + \frac{\partial(VH)}{\partial y} = 0 \quad (3-46)$$

where U , V = depth average velocity components, defined as:-

$$U = \frac{1}{H} \int_{-h}^{\zeta} u dz, \quad V = \frac{1}{H} \int_{-h}^{\zeta} v dz \quad (3-47)$$

$$\left\{ \begin{array}{l} D_{xx} = \frac{(D_l U^2 + D_t V^2) H \sqrt{g}}{C \sqrt{U^2 + V^2}} + D_w \\ D_{yy} = \frac{(D_l V^2 + D_t U^2) H \sqrt{g}}{C \sqrt{U^2 + V^2}} + D_w \\ D_{xy} = D_{yx} = \frac{(D_l - D_t) UVH \sqrt{g}}{C \sqrt{U^2 + V^2}} + D_w \end{array} \right. \quad (3-86)$$

where D_l = dispersion constant, D_t = depth averaged turbulent diffusion constant and D_w = wind-induced dispersion-diffusion coefficient. For values of D_l and D_t , these can be set to minimum values assuming a logarithmic velocity distribution, wherein $D_l = 5.93$ (Elder, 1959) and $D_t = 0.15$ (Fischer, 1976). However, in practical studies these values tend to be rather low (Fischer et al., 1979), with measured values of D_l and D_t ranging from 8.6 to 7500 and 0.42 to 1.61 respectively. In the absence of extensive dye dispersion field data, these values can be determined by calibration when limited spatial solute concentration distribution data are available. In this study, the effect of wind is not taken into account, thus the coefficient D_w is set to be zero.

3.5 SUMMARY

In this chapter the governing hydrodynamic equations of fluid motion and the general form of solute transport equations in three- and two-dimensional frameworks for estuarine and coastal waters and groundwater are reviewed. Different terms of the conservative forms of the mass and momentum partial differential equations for three-dimensional framework are discussed. The depth integrated forms of the governing hydrodynamic equations for both surface water and groundwater flows are presented for the two-dimensional model studies. The terms in the two-dimensional momentum equations i.e. the surface wind shear stress, the bed shear stress, the momentum correction factor, the body forces, the depth averaged eddy viscosity, and the atmospheric pressure are also discussed. The turbulent diffusion coefficients in the three-dimensional solute and mass transport equation are discussed, and the dispersion-diffusion terms in the depth-integrated solute transport equation are formulised.

of Equation (3-80) gives:-

$$\bar{Q} = -KH\nabla\zeta \quad (3-82)$$

where \bar{Q} is the discharge per unit width, H is the thickness of the aquifer, and ζ is the elevation of the free surface (Figure 3-5).

In Cartesian coordinates, Equation (3-82) can be written as follows:-

$$p = -KH \frac{\partial\zeta}{\partial x} \quad (3-83)$$

$$q = -KH \frac{\partial\zeta}{\partial y} \quad (3-84)$$

Equations (3-83) and (3-84) are used as the equivalent of Equations (3-72) and (3-73) for groundwater flow in this study.

3.4.3 Depth Integrated Governing Equations for Solute Transport

Although it is an important objective to develop a dynamically linked surface water and groundwater flow model of this thesis, the main purpose of this thesis focus on the solute transport processes in estuarine and coastal waters, thus only the solute transport processes occurs in surface water will be studied.

For a horizontal or quasi-horizontal flow, the three-dimensional solute transport equation (Equation (3-41)) can be integrated over the water depth in the similar way as that in section 3.4.1 to give the two-dimensional depth integrated advective-diffusion equation (Falconer, 1991):-

$$\begin{aligned} \frac{\partial(\phi H)}{\partial t} + \frac{\partial(p\phi)}{\partial x} + \frac{\partial(q\phi)}{\partial y} - \frac{\partial}{\partial x} \left(HD_{xx} \frac{\partial\phi}{\partial x} + HD_{xy} \frac{\partial\phi}{\partial y} \right) \\ - \frac{\partial}{\partial y} \left(HD_{yx} \frac{\partial\phi}{\partial x} + HD_{yy} \frac{\partial\phi}{\partial y} \right) - H\phi_o = 0 \end{aligned} \quad (3-85)$$

where ϕ = depth-averaged solute concentration, ϕ_o = corresponding depth-averaged concentration for ϕ_o , and D_{xx} , D_{xy} , D_{yx} , D_{yy} = dispersion and turbulent diffusion coefficients in the x - and y -directions, respectively.

For the dispersion-diffusion terms, these coefficients can be shown to be of the following form in two-dimensions (Preston, 1985):-

$$\frac{Q}{A} = K \frac{\Delta h}{\Delta l} \quad (3-78)$$

where K is a constant of proportionality termed hydraulic conductivity. The value of K is usually determined via experiment.

Equation (3-78) can be written in a differential form, given as follows:-

$$u_d = -K \frac{dh}{dl} \quad (3-79)$$

where $u_d = Q/A$ is the Darcy velocity. The negative sign indicates that the flow is in the direction of decreasing head.

Generally, Darcy's law in three dimensional anisotropic materials is expressed as follows (Schwartz and Zhang, 2003):-

$$\vec{V}_d = -\mathbf{K}\nabla h \quad (3-80)$$

where \vec{V}_d is the Darcy velocity vector, and \mathbf{K} is the hydraulic conductivity tensor, and ∇h is the gradient of hydraulic head. In Cartesian coordinates, \mathbf{K} is written as follows:-

$$\mathbf{K} = \begin{bmatrix} K_{xx} & K_{xy} & K_{xz} \\ K_{yx} & K_{yy} & K_{yz} \\ K_{zx} & K_{zy} & K_{zz} \end{bmatrix} \quad (3-81)$$

where the first subscript defines the plane normal to the subscript and the second subscript defines the stress direction on the plane (similar to the stress tensor shown in Figure 3-3)

In this thesis, only isotropic and homogeneous material is considered, thus hereafter the tensor \mathbf{K} is replaced with a constant scalar K .

➤ Dupuit's theory

Groundwater flow problems in which the upper boundary is a free surface can be depth integrated on the basis of Dupuit's theory of unconfined flow. This theory is founded on three assumptions made by Dupuit in 1863 (see Bedient and Huber, 1988): 1) The water table of the free surface is only slightly inclined, 2) streamlines may be considered horizontal and equipotential lines vertical, and 3) slopes of the free surface and hydraulic gradient are equal. With the assumptions, the depth integration

(3-22)) still holds, it is more practical to use Darcy's law and Dupuit's theory.

➤ **Darcy's law**

The movement of groundwater is well established by hydraulic principles reported in 1856 by Henri, Darcy. He discovered one of the most important laws in hydrology, i.e. the flow rate through porous media is proportional to the head loss and inversely proportional to the length of the flow path. Darcy's law serves as the basis for present-day knowledge of groundwater flow and well hydraulics (Bedient and Huber, 1988).

In his search for this law, Darcy conducted experiments using an apparatus similar to that shown in Figure 3-6. This testing system consisted of a cylinder having a known cross-sectional area A , which was filled with various filter sands. Appropriate plumbing was provided to flow water through the column. The cylinder contained two manometers whose intakes were separated by a distance Δl . Water was flowed into (or out of) the cylinder at a known rate Q , and the elevation of water levels in the manometers, h_1 and h_2 , was measured relative to a local datum.

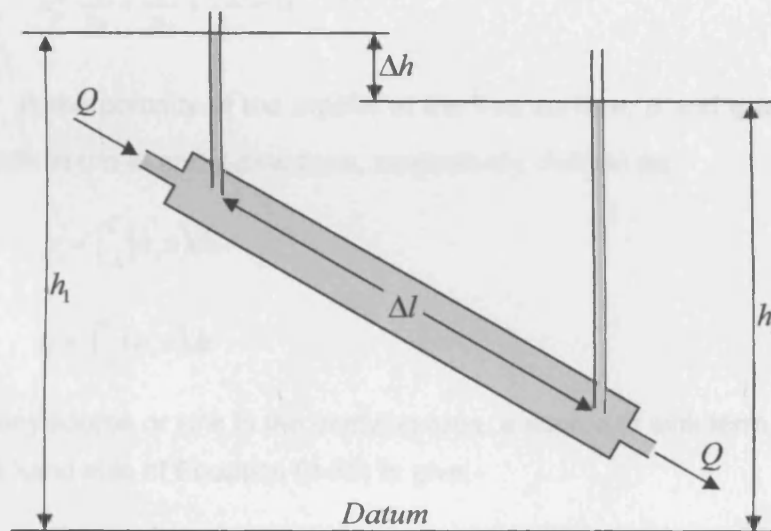


Figure 3-6 Experimental apparatus to demonstrate Darcy's law

Darcy conducted a variety of experiments in which the flow rate Q , or the types of filter medium were changed. He derived the following relationship, now known as Darcy's equation:-

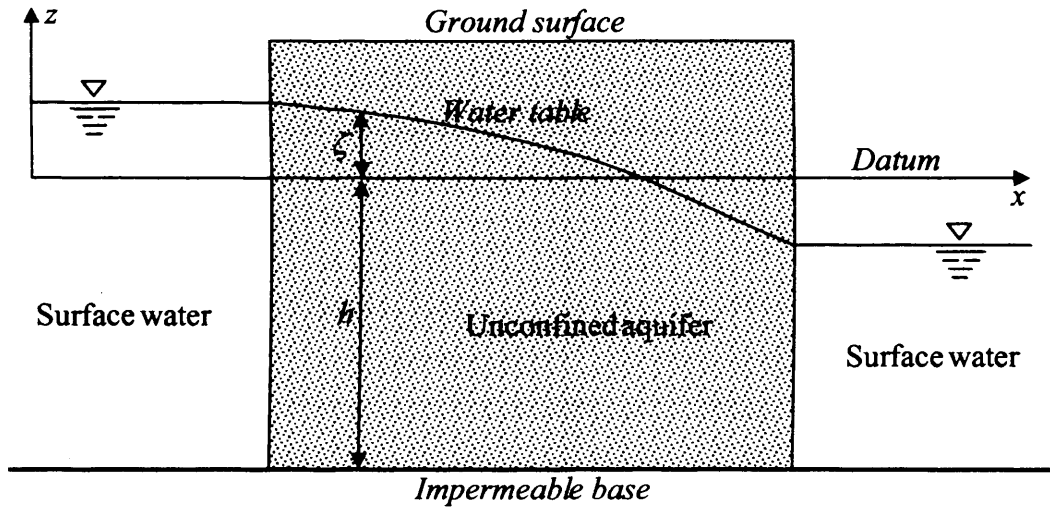


Figure 3-5 Schematic illustration of unconfined aquifer

Following the same procedure as in Section 3.4.1.1, the depth-integrated continuity equation for groundwater flow can be given as follows:-

$$n_e^\zeta \frac{\partial \xi}{\partial t} + \frac{\partial p}{\partial x} + \frac{\partial q}{\partial y} = 0 \quad (3-75)$$

where n_e^ζ is the porosity of the aquifer at the free surface, p and q are discharges per unit width in the x - and y -directions, respectively, defined as:-

$$p = \int_{-h}^{\zeta} (n_e u) dz \quad (3-76a)$$

$$q = \int_{-h}^{\zeta} (n_e v) dz \quad (3-76b)$$

If there is any source or sink in the studying area, a source or sink term can be added to the right hand side of Equation (3-75) to give:-

$$n_e^\zeta \frac{\partial \xi}{\partial t} + \frac{\partial p}{\partial x} + \frac{\partial q}{\partial y} = q_m \quad (3-77)$$

where q_m is source or sink discharge per unit horizontal area.

It is obvious that Equation (3-50) is a special case of Equation (3-77) with the porosity equalling to unit.

3.4.2.2 Momentum Equation

For groundwater flow, although the three dimensional momentum equation (Equation

$$P(z) = \rho g(\zeta - z) + P_a \quad (3-70)$$

The derivatives of the pressure in any horizontal direction can be expressed in terms of the water elevation giving for the x-direction:-

$$\frac{\partial P}{\partial x} = \rho g \frac{\partial \zeta}{\partial x} + \frac{\partial P_a}{\partial x} \quad (3-71)$$

Differences in atmospheric pressure at the water surface can give rise to water level variations which may be of significance if the area being modelled is relatively large. However, in most estuarine and coastal engineering studies the barometric pressure gradient is insignificant and is not included in the governing equations.

Hence, in modelling estuarine and coastal flows where the vertical accelerations are small and the flow is well mixed vertically, the governing momentum equations can be obtained by substituting Equations (3-57), (3-63), (3-67), and (3-71) into Equation (3-53), giving for the x-direction:-

$$\begin{aligned} \frac{\partial p}{\partial t} + \frac{\partial}{\partial x}(\beta U p) + \frac{\partial}{\partial y}(\beta p V) = f q - g H \frac{\partial \zeta}{\partial x} + \frac{\gamma \rho_a W_x W_s}{\rho} \\ - \frac{g p \sqrt{p^2 + q^2}}{H^2 C^2} + E \left(\frac{\partial^2 p}{\partial x^2} + \frac{\partial^2 p}{\partial y^2} \right) \end{aligned} \quad (3-72)$$

and similarly for the y-direction:-

$$\begin{aligned} \frac{\partial q}{\partial t} + \frac{\partial}{\partial x}(\beta U q) + \frac{\partial}{\partial y}(\beta V q) = f p - g H \frac{\partial \zeta}{\partial y} + \frac{\gamma \rho_a W_y W_s}{\rho} \\ - \frac{g q \sqrt{p^2 + q^2}}{H^2 C^2} + E \left(\frac{\partial^2 q}{\partial x^2} + \frac{\partial^2 q}{\partial y^2} \right) \end{aligned} \quad (3-73)$$

3.4.2 Hydrodynamic Governing Equations for Groundwater Flow

3.4.2.1 Continuity Equation

Let ζ be the free surface elevation for the unconfined groundwater flow (Figure 3-5), depth integration of Equation (3-30) gives:-

$$\int_{-h}^{\zeta} \left[\frac{\partial(n_e u)}{\partial x} + \frac{\partial(n_e v)}{\partial y} + \frac{\partial(n_e w)}{\partial z} \right] dz = 0 \quad (3-74)$$

$$u_* = \sqrt{\frac{\tau_b}{\rho}} = \frac{\sqrt{g(U^2 + V^2)}}{C} \quad (3-65)$$

herein, τ_b is the bed shear stress.

However, field data by Fischer (1979) for turbulent diffusion in rivers has shown that the value for E is generally greater than that given by Equation (3-64), and is more accurately given by

$$E = C_e u_* H \quad (3-66)$$

Substituting Equation (3-65) into Equation (3-66) gives the eddy viscosity as:-

$$E = C_e \frac{H}{C} \sqrt{g(U^2 + V^2)} \quad (3-67)$$

where C_e = eddy viscosity coefficient and Fisher's (1979) suggestion of the eddy viscosity coefficient, $C_e \approx 0.15$ is based upon laboratory data. Values of C_e are frequently found to be much larger for actual tidal flows in estuaries and coastal waters.

In the cases where free-shear-layer turbulence and turbulent advection are important (e.g. as in tidal jets), then the two-equation depth-integrated $k - \varepsilon$ turbulence model can be used to evaluate E (Rodi, 2000).

➤ Pressure Gradient

For nearly horizontal flows, the vertical acceleration due to hydrodynamic processes is generally small in comparison with gravity effects. Consequently, in the z-direction momentum equation (Equation (3-31c)), the vertical acceleration and shear stresses are neglected, such that a hydrostatic pressure variation results (Falconer, 1977), giving:-

$$\frac{\partial P}{\partial z} + \rho g = 0 \quad (3-68)$$

Integrating Equation (3-68) gives a linear pressure distribution with depth, that is:

$$P(z) = \int -\rho g dz = -\rho g z + \text{constant} \quad (3-69)$$

Using the boundary condition that the pressure at the free surface, i.e. $z = \zeta$ is at atmospheric pressure, P_a , then Equation (3-69) becomes:-

flood plains, where the Reynolds number effects may be significant (Falconer and Owens, 1987).

In this study, the values $a_1 = 4, a_2 = 12, a_3 = 2.5$ are adopted. Substituting these values and equation (3-60) into Equation (3-59) gives the expression:-

$$C = -\sqrt{32g} \log_{10} \left(\frac{k_s}{12R} + \frac{5C}{Re\sqrt{32g}} \right) \quad (3-61)$$

For fully rough flow this can be reduced to

$$C = -\sqrt{32g} \log_{10} \left(\frac{k_s}{12R} \right) \quad (3-62)$$

➤ The effect of wind

Wind exerts a drag force as it blows over the water surface. The shear stress at the air-water interface is calculated by assuming that it is proportional to the square of the wind speed at a particular height above the water surface. For the surface shear stress due to wind action, resolving forces horizontally for a steady uniform flow gives for the x-direction:-

$$\tau_{xw} = \gamma \rho_a W_x W_s \quad (3-63)$$

where γ is the air-water resistance coefficient, ρ_a is the air density, W_x is the wind velocity component in the x-direction, $W_s = \sqrt{W_x^2 + W_y^2}$ is the wind speed and W_y is the wind velocity component in the y-direction. Various constant value and formulae have been proposed for the air-water resistance coefficient, with the most widely used representation being that attributed to Munk (Dronkers, 1964) whereby $\gamma = 0.0026$.

➤ Turbulence

Values of the depth averaged turbulent eddy viscosity, E , can either be estimated from field data or, assuming that bed generated turbulence dominates over free shear layer, by a logarithmic velocity profile, such as (Elder, 1959):-

$$E = \kappa/6u_*H \quad (3-64)$$

where u_* is the bed shear velocity defined as:-

$$\tau_{xb} = \frac{\rho g U \sqrt{U^2 + V^2}}{C^2} \quad (3-57)$$

To determine the Chezy value either a constant value can be included directly for C (typically $30m^{1/2}s^{-1} < C < 100m^{1/2}s^{-1}$ for such flows) or C can be evaluated from the Manning equation, that is:-

$$C = \frac{H^{1/6}}{n} \quad (3-58)$$

where n is the Manning roughness coefficient (typically $0.015 < n < 0.04$). Alternatively, the Colebrook-White equation can be used, giving (Henderson, 1966):-

$$C = \sqrt{\frac{8g}{f}} \quad (3-59)$$

where f is the Darcy-Weisbach friction coefficient and is calculated using a formula of the Colebrook type, that is:

$$\sqrt{\frac{1}{f}} = -a_1 \log_{10} \left(\frac{k_s}{a_2 R} + \frac{a_3}{\text{Re} \sqrt{f}} \right) \quad (3-60)$$

where

R = hydraulic radius

k_s = Nikuradse equivalent sand roughness size (sand grains)

$\text{Re} = \frac{4H|U|}{\nu}$ = Reynolds number

$|U|$ = magnitude of velocity

ν = kinematic viscosity

a_1, a_2, a_3 = constants

The advantage of using the Colebrook-White equation to calculate C is that the value of the roughness coefficient k_s can be more closely related to bed features such as ripples or dunes and the representation of the Chezy's value can include transitional turbulent flow (or turbulent rough flow that is not fully developed). This refinement can be particular important when modelling the flooding and drying of tidal

$$\begin{aligned} \frac{\partial(UH)}{\partial t} + \frac{\partial(\beta U^2 H)}{\partial x} + \frac{\partial(\beta UVH)}{\partial y} = fVH - \frac{1}{\rho} \int_{-h}^{\zeta} \frac{\partial P}{\partial x} dz + \frac{\tau_{xw}}{\rho} + \frac{\tau_{xb}}{\rho} \\ + 2 \frac{\partial}{\partial x} \left(EH \frac{\partial U}{\partial x} \right) + \frac{\partial}{\partial y} \left[EH \left(\frac{\partial U}{\partial y} + \frac{\partial V}{\partial x} \right) \right] \end{aligned} \quad (3-53)$$

where β is the momentum correction factor, τ_{xw} is the surface wind shear stress component, τ_{xb} is the bed shear stress component.

➤ The momentum correction factor

In practical model studies, and in the absence of extensive field data, the momentum correction factor β is either set to unity or a specific vertical velocity profile is assumed.

For an assumed logarithmic vertical velocity profile of the form

$$u = \frac{u_*}{\kappa} \log_e(h+z) + U.C_1 \quad (3-54)$$

where u_* is the shear velocity (equal to $\sqrt{\tau_b/\rho}$, with τ_b being the boundary shear stress), it can be readily shown that

$$\beta = 1 + \frac{g}{C^2 \kappa^2} \quad (3-55)$$

where C is the Chezy's bed roughness coefficient, and κ is the von Karmann's constant.

Alternatively, for a wind generated flow field, a parabolic velocity distribution can be assumed of the form (Koutitas and Cousidou-Koutita, 1986):-

$$u = \left(\frac{3a_x}{4} - \frac{3U}{2} \right) \left(\frac{z^2}{h} - 1 \right) + a_x \left(\frac{z}{h} + 1 \right) \quad (3-56)$$

where $a_x = H\tau_{xw}/\rho\varepsilon_\zeta$ and ε_ζ is the eddy viscosity at the free surface, giving, $\beta = 1.2$. For a velocity profile defined by the seventh power law, the value of β is 1.016.

➤ Bottom friction

In most coastal and estuarine flow studies the bed shear stress is presented in a manner similar to that for steady, uniform open-channel flow (Henderson, 1966). Thus, in the x-direction the bed shear stress is given as:-

and $H =$ total depth of water column $= h + \zeta$.

Equation (3-46) can also be expressed as follows:-

$$\frac{\partial \zeta}{\partial t} + \frac{\partial p}{\partial x} + \frac{\partial q}{\partial y} = 0 \quad (3-48)$$

where p , q are discharges per unit width in the x - and y -directions, respectively, defined as:-

$$p = \int_{-h}^{\zeta} u dz = UH, \quad q = \int_{-h}^{\zeta} v dz = VH \quad (3-49)$$

If there is any source or sink in the studying area, a source or sink term can be added to the right hand side of Equation (3-49) to give:-

$$\frac{\partial \zeta}{\partial t} + \frac{\partial p}{\partial x} + \frac{\partial q}{\partial y} = q_m \quad (3-50)$$

where q_m is source or sink discharge per unit horizontal area.

3.4.1.2 Momentum Equation

Similarly, for incompressible turbulent flow, substitution of Equations (3-32) and (3-35) into Equation (3-31a) and integration over the depth gives:-

$$\int_{-h}^{\zeta} \left[\frac{\partial u}{\partial t} + \frac{\partial(uu)}{\partial x} + \frac{\partial(uv)}{\partial y} + \frac{\partial(uw)}{\partial z} \right] dz = \int_{-h}^{\zeta} f v dz - \frac{1}{\rho} \int_{-h}^{\zeta} \frac{\partial P}{\partial x} dz \quad (3-51)$$

$$+ \int_{-h}^{\zeta} \left\{ \frac{\partial}{\partial x} \left[(\varepsilon + \nu) \left(2 \frac{\partial u}{\partial x} \right) \right] + \frac{\partial}{\partial y} \left[(\varepsilon + \nu) \left(\frac{\partial u}{\partial y} + \frac{\partial v}{\partial x} \right) \right] + \frac{\partial}{\partial z} \left[(\varepsilon + \nu) \left(\frac{\partial u}{\partial z} + \frac{\partial w}{\partial x} \right) \right] \right\} dz$$

where $f = 2\omega \sin \varphi$ is the Coriolis parameter.

Applying the kinematic free surface condition, assuming $\varepsilon \gg \nu$ and making the approximation that:-

$$\frac{\partial}{\partial x} \int_{-h}^{\zeta} \varepsilon \frac{\partial u}{\partial x} dz = \frac{\partial}{\partial x} \left(EH \frac{\partial U}{\partial x} \right) \quad (3-52)$$

where E is the depth mean eddy viscosity (Falconer, 1977), this gives, for the x -direction momentum equation (3-31a):-

CHAPTER 4

DISCRETIZATION OF GOVERNING EQUATIONS AND NUMERICAL SOLUTION PROCEDURE

4.1 INTRODUCTION

The governing partial differential equations (PDE) given in Chapter 3 generally do not have analytical solutions and approximate solutions of the equations can only be obtained using numerical methods with proper initial and boundary conditions. In this chapter, numerical methods used for solving the governing differential equations given in Chapter 3 are presented, as well as the numerical techniques used to treat the different boundary conditions. Details are also given of the link of surface water and groundwater models.

In this study, the particular finite difference method based upon the Alternating Direction Implicit (ADI) technique is used for solving both hydrodynamic and solute transport governing equations (or the advective-diffusion equation). According to the ADI technique, each time step is split up into two half-time steps. Thus a two-dimensional problem can be solved considering only one dimension implicitly for each half-time step, without the solution for a full two-dimensional matrix. On the first half-time step the water elevation (ζ) and the flux/velocity component in the x -direction (p/U) are solved implicitly in the x -direction, while the other variables are represented explicitly. Similarly, for the second half-time, the water elevation (ζ) and the flux/velocity component in the y -direction (q/V) are solved implicitly in the y -direction, with the other variables being represented explicitly.

A space staggered grid system is used for discretizing the governing equations, with the variables ζ (water elevation) and ϕ (solute concentration) being located at the grid centre and with U/p (velocity/flux component in x -direction) and V/q (velocity/flux component in y -direction) at the centre of the grid sides as shown in

Figure 4-1. The use of a staggered grid system prevents the appearance of oscillatory solutions which tend to occur in a non-staggered grid for space centred differences (Fletcher, 1991). The depths are specified at the corners of grids.

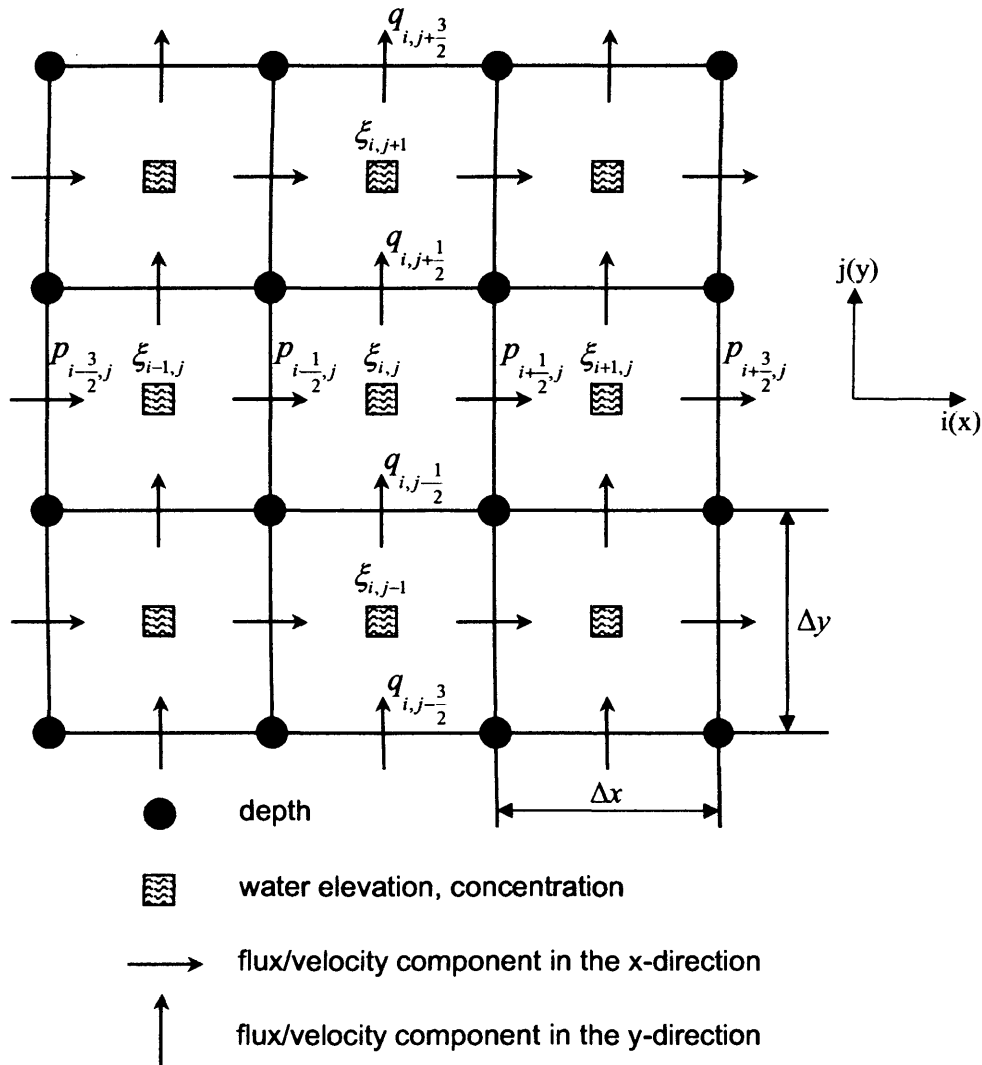


Figure 4-1 Schematic illustration of space staggered grid system

4.2 DISCRETIZATION OF HYDRODYNAMIC EQUATIONS

An alternating direction implicit finite difference scheme (ADI scheme) is used to solve the governing equations. With the boundary conditions included, the resulting finite difference equations for each half time step are arranged into a tri-diagonal system and solved by using the method of Gauss elimination and back substitution.

4.2.1 Discretization of Continuity Equation

In this section Equation (3-77) is selected to show the finite different scheme of the continuity equation, as the continuity equation of the surface water flow (Equation (3-50)) is a special case of that of the groundwater flow (Equation (3-77)) with the porosity of the aquifer equalling to unity.

For the first half-time step the terms in the x-direction are treated implicitly and the terms in the y-direction are treated explicitly. The continuity equation (3-77) can therefore be discretized as:-

$$n_e^\xi \frac{\xi^{n+1/2} - \xi^n}{\Delta t / 2} + \frac{p_{i+1/2,j}^{n+1/2} - p_{i-1/2,j}^{n+1/2}}{\Delta x} + \frac{q_{i,j+1/2}^n - q_{i,j-1/2}^n}{\Delta y} = q_m \quad (4-1a)$$

where i, j = grid point location in the x- and y-directions respectively, superscripts n , $n+1/2$, and $n+1$ represent variables evaluated at time $t = n\Delta t$, $t = (n+1/2)\Delta t$, and $t = (n+1)\Delta t$ time levels, respectively, Δt represents the time-step for computations and n is the time-step number.

Rearranging Equation (4-1a) gives the following form:-

$$a_{2i-1} \cdot p_{i-1/2,j}^{n+1/2} + b_{2i-1} \cdot \xi_{i,j}^{n+1/2} + c_{2i-1} \cdot p_{i+1/2,j}^{n+1/2} = d_{2i-1} \quad (4-1b)$$

where

$$a_{2i-1} = -\frac{\Delta t}{\Delta x} \quad (4-2a)$$

$$b_{2i-1} = 2n_e \quad (4-2b)$$

$$c_{2i-1} = \frac{\Delta t}{\Delta x} \quad (4-2c)$$

$$d_{2i-1} = 2n_e^\xi \xi_{i,j}^n - \frac{\Delta t}{\Delta y} \cdot (q_{i,j+1/2}^n - q_{i,j-1/2}^n) + \Delta t \cdot q_m \quad (4-2d)$$

For the second half-time step, the terms in the y-direction are treated implicitly and the terms in the x-direction are treated explicitly. In this case, the continuity equation is discretized as:-

$$n_e^\xi \frac{\xi^{n+1} - \xi^{n+1/2}}{\Delta t / 2} + \frac{p_{i+1/2,j}^{n+1/2} - p_{i-1/2,j}^{n+1/2}}{\Delta x} + \frac{q_{i,j+1/2}^{n+1} - q_{i,j-1/2}^{n+1}}{\Delta y} = q_m \quad (4-3a)$$

Rearranging Equation (4-3a) gives the following form:-

$$a_{2j-1} \cdot q_{i,j-1/2}^{n+1} + b_{2j-1} \cdot \xi_{i,j}^{n+1} + c_{2j-1} \cdot q_{i,j+1/2}^{n+1} = d_{2j-1} \quad (4-3b)$$

where

$$a_{2j-1} = -\frac{\Delta t}{\Delta y} \quad (4-4a)$$

$$b_{2j-1} = 2n_e^\xi \quad (4-4b)$$

$$c_{2j-1} = \frac{\Delta t}{\Delta y} \quad (4-4c)$$

$$d_{2j-1} = 2n_e^\xi \xi_{i,j}^{n+1/2} - \frac{\Delta t}{\Delta x} \cdot (p_{i+1/2,j}^{n+1/2} - p_{i-1/2,j}^{n+1/2}) + \Delta t \cdot q_m \quad (4-4d)$$

Equations (4-1) and (4-3) are fully centred in both time and space over the whole time step, giving a second order accuracy. For surface water flow, the porosity n_e^ξ in Equations (4-1) and (4-3) equals to unity.

4.2.2 Discretization of Momentum Equations for Surface Water Flow

The momentum equation for surface water flow in the x-direction, Equation (3-72) can be discretized in the same manner as the continuity equation. Therefore, for the first-half time step:-

$$\begin{aligned} & \frac{p_{i+1/2,j}^{n+1/2} - p_{i+1/2,j}^{n-1/2}}{\Delta t} \\ & + \beta \frac{(\hat{p}\hat{U})_{i+3/2,j}^n - (\hat{p}\hat{U})_{i-1/2,j}^n}{2\Delta x} + \beta \frac{(\bar{p}\bar{V})_{i+1/2,j+1/2}^n - (\bar{p}\bar{V})_{i+1/2,j-1/2}^n}{\Delta y} \\ & = f \cdot \bar{q}_{i+1/2,j}^n - gH \frac{\left(\frac{\xi_{i+1,j}^{n+1/2} + \xi_{i+1,j}^{n-1/2}}{2} \right) - \left(\frac{\xi_{i,j}^{n+1/2} + \xi_{i,j}^{n-1/2}}{2} \right)}{\Delta x} \\ & + \varepsilon \left(\frac{\hat{p}_{i+3/2,j}^n - 2 \cdot \hat{p}_{i+1/2,j}^n + \hat{p}_{i-1/2,j}^n}{\Delta x^2} + \frac{\hat{p}_{i+1/2,j+1}^n - 2 \cdot \hat{p}_{i+1/2,j}^n + \hat{p}_{i+1/2,j-1}^n}{\Delta y^2} \right) \\ & + \frac{\rho_a}{\rho} C_w W_x W_s \sin \phi - \frac{g \cdot \frac{p_{i+1/2,j}^{n+1/2} + p_{i+1/2,j}^{n-1/2}}{2} \cdot \sqrt{(\hat{p}_{i+1/2,j}^n)^2 + (\bar{q}_{i+1/2,j}^n)^2}}{[(HC)_{i+1/2,j}^n]^2} \end{aligned} \quad (4-5a)$$

where \hat{p} denotes a term that is updated by iteration as:-

$$\hat{p}^n = \begin{cases} p^{n-1/2} & \text{for the first iteration} \\ \frac{1}{2}(p^{n-1/2} + p^{n+1/2}) & \text{for the second and remaining iteration} \end{cases} \quad (4-6a)$$

\bar{q} / \bar{V} denotes a flux/velocity value obtained by averaging corresponding values at surrounding grid points:-

$$\bar{q}_{i+\frac{1}{2},j+\frac{1}{2}} = \frac{1}{2} \left(q_{i,j+\frac{1}{2}}^n + q_{i+1,j+\frac{1}{2}}^n \right) \quad (4-6b)$$

$$\bar{V}_{i+\frac{1}{2},j+\frac{1}{2}} = \frac{1}{2} \left(V_{i,j+\frac{1}{2}}^n + V_{i+1,j+\frac{1}{2}}^n \right) \quad (4-6c)$$

and \bar{p} denotes a value obtained from the upwind algorithm where

$$\bar{p}_{i+\frac{1}{2},j}^n = \begin{cases} p_{i+\frac{1}{2},j-1}^n & \text{if } V_{i+\frac{1}{2},j}^n > 0 \\ p_{i+\frac{1}{2},j+1}^n & \text{if } V_{i+\frac{1}{2},j}^n < 0 \end{cases} \quad (4-6d)$$

Rearranging Equation (4-5a) gives the following form:-

$$a_{2i} \cdot \zeta_{i,j}^{n+1/2} + b_{2i} \cdot p_{i+1/2,j}^{n+1/2} + c_{2i} \cdot \zeta_{i+1,j}^{n+1/2} = d_{2i} \quad (4-5b)$$

where

$$a_{2i} = -gH \frac{\Delta t}{\Delta x} \quad (4-7a)$$

$$b_{2i} = \left(2 + \Delta t \cdot \frac{g \cdot \sqrt{(\hat{p}_{i+1/2,j}^n)^2 + (\bar{q}_{i+1/2,j}^n)^2}}{[(HC)_{i+1/2,j}^n]^2} \right) \quad (4-7b)$$

$$c_{2i} = gH \frac{\Delta t}{\Delta x} \quad (4-7c)$$

$$\begin{aligned}
d_{2i} = & \left(2 - \Delta t \cdot \frac{g \cdot \sqrt{(\hat{p}_{i+1/2,j}^n)^2 + (\bar{q}_{i+1/2,j}^n)^2}}{[(HC)_{i+1/2,j}^n]^2} \right) \cdot p_{i+1/2,j}^{n-1/2} \\
& - gH \frac{\Delta t}{\Delta x} (\xi_{i+1,j}^{n-1/2} - \xi_{i,j}^{n-1/2}) \\
& - \beta \left[\frac{\Delta t}{\Delta x} ((\hat{p}\hat{U})_{i+3/2,j}^n - (\hat{p}\hat{U})_{i-1/2,j}^n) \right. \\
& \quad \left. + \frac{2\Delta t}{\Delta y} ((\bar{p}\bar{V})_{i+1/2,j+1/2}^n - (\bar{p}\bar{V})_{i+1/2,j-1/2}^n) \right] \\
& + 2E \left[\frac{\Delta t}{\Delta x^2} (\hat{p}_{i+3/2,j}^n - 2 \cdot \hat{p}_{i+1/2,j}^n + \hat{p}_{i-1/2,j}^n) \right. \\
& \quad \left. + \frac{\Delta t}{\Delta y^2} (\hat{p}_{i+1/2,j+1}^n - 2 \cdot \hat{p}_{i+1/2,j}^n + \hat{p}_{i+1/2,j-1}^n) \right] \\
& + 2\Delta t \cdot \frac{\rho_a}{\rho} C_w W_x W_s + 2\Delta t \cdot f \cdot \bar{q}_{i+1/2,j}^n
\end{aligned} \tag{4-7d}$$

Likewise, the momentum equation in the y-direction, Equation (3-73) can be written for the second-half time step as:-

$$a_{2j} \cdot \xi_{i,j}^{n+1} + b_{2j} \cdot q_{i,j+1/2}^{n+1} + c_{2j} \cdot \zeta_{i,j+1}^{n+1} = d_{2j} \tag{4-8}$$

where

$$a_{2j} = -gH \frac{\Delta t}{\Delta y} \tag{4-9a}$$

$$b_{2j} = \left(2 + \Delta t \frac{g \cdot \sqrt{(\bar{p}_{i,j+1/2}^{n+1/2})^2 + (\hat{q}_{i,j+1/2}^{n+1/2})^2}}{[(HC)_{i,j+1/2}^{n+1/2}]^2} \right) \tag{4-9b}$$

$$c_{2j} = gH \frac{\Delta t}{\Delta y} \tag{4-9c}$$

$$\begin{aligned}
d_{2j} = & \left(2 - \Delta t \frac{g \cdot \sqrt{(\bar{p}_{i,j+1/2}^{n+1/2})^2 + (\hat{q}_{i,j+1/2}^{n+1/2})^2}}{[(HC)_{i,j+1/2}^{n+1/2}]^2} \right) \cdot q_{i,j+1/2}^n \\
& - gH \frac{\Delta t}{\Delta y} (\xi_{i,j+1}^n - \xi_{i,j}^n) \\
& - \beta \left[\frac{2\Delta t}{\Delta x} ((\bar{q}\bar{U})_{i+1/2,j+1/2}^{n+1/2} - (\bar{q}\bar{U})_{i-1/2,j+1/2}^{n+1/2}) \right. \\
& \quad \left. + \frac{\Delta t}{\Delta y} ((\hat{q}\hat{V})_{i,j+3/2}^{n+1/2} - (\hat{q}\hat{V})_{i,j-1/2}^{n+1/2}) \right] \\
& + 2E \left[\frac{\Delta t}{\Delta x^2} (\hat{q}_{i+1,j+1/2}^{n+1/2} - 2 \cdot \hat{q}_{i,j+1/2}^{n+1/2} + \hat{q}_{i-1,j+1/2}^{n+1/2}) \right. \\
& \quad \left. + \frac{\Delta t}{\Delta y^2} (\hat{q}_{i,j+3/2}^{n+1/2} - 2 \cdot \hat{q}_{i,j+1/2}^{n+1/2} + \hat{q}_{i,j-1/2}^{n+1/2}) \right] \\
& + 2\Delta t \frac{\rho_a}{\rho} C_w W_y W_s - 2\Delta t \cdot f \cdot \bar{p}_{i,j+1/2}^{n+1/2}
\end{aligned} \tag{4-9d}$$

where terms \bar{p} , \hat{q} , \bar{U} and \hat{V} have similar expressions to those given in Equations (4-6a)–(4-6d) except that the time level is $n+1/2$ instead of n .

The ADI scheme being used in this study is basically second order accurate both in time and space with no stability constraints. However, it has been recognized that the time steps needs to be restricted so that a reasonable computational accuracy can be achieved (Chen, 1992). A maximum Currant number (C_r) was suggested (Stelling et al., 1985) as:-

$$C_r = 2\Delta t \sqrt{gH \left(\frac{1}{\Delta x^2} + \frac{1}{\Delta y^2} \right)} \leq 4\sqrt{2} \tag{4-10}$$

with an average depth being adopted for H . When the two-dimensional solute transport equation is also solved for each half time step, the choice of time step should also consider the stability requirements for the solute transport equation.

4.2.3 Discretization of Momentum Equations for Groundwater Flow

Although the form of the momentum equations for groundwater flow (Equations (3-83) and (3-84)) are different from the corresponding equations for surface water flow (Equations (3-72) and (3-73)), they have same physical base. One of the objectives of this thesis is to develop a dynamically linked surface water and groundwater flow model, thus it is better to write the discretized momentum equations for the groundwater flow in the same form as that for the surface water flow.

The momentum equation for groundwater flow in the x-direction, Equation (3-83)

can be discretized for the first-half time step as follows:-

$$p_{i+1/2,j}^{n+1/2} = -KH_{i+1/2,j}^{n+1/2} \frac{\xi_{i+1,j}^{n+1/2} - \xi_{i,j}^{n+1/2}}{\Delta x} \quad (4-11a)$$

Rearranging Equation (4-11a) gives the following normalized form:-

$$a_{2i} \cdot \xi_{i,j}^{n+1/2} + b_{2i} \cdot p_{i+1/2,j}^{n+1/2} + c_{2i} \cdot \xi_{i+1,j}^{n+1/2} = d_{2i} \quad (4-11b)$$

where

$$a_{2i} = -\frac{KH_{i+1/2,j}^{n+1/2}}{\Delta x} \quad (4-12a)$$

$$b_{2i} = 1 \quad (4-12b)$$

$$c_{2i} = \frac{KH_{i+1/2,j}^{n+1/2}}{\Delta x} \quad (4-12c)$$

$$d_{2i} = 0 \quad (4-12d)$$

Likewise, the momentum equation for groundwater flow in the y-direction, Equation (3-84) can be written for the second-half time step as:-

$$a_{2j} \cdot \xi_{i,j}^{n+1} + b_{2j} \cdot q_{i,j+1/2}^{n+1} + c_{2j} \cdot \xi_{i,j+1}^{n+1} = d_{2j} \quad (4-13)$$

where

$$a_{2j} = -\frac{KH_{i,j+1/2}^{n+1}}{\Delta x} \quad (4-14a)$$

$$b_{2j} = 1 \quad (4-14b)$$

$$c_{2j} = \frac{KH_{i,j+1/2}^{n+1}}{\Delta x} \quad (4-14c)$$

$$d_{2j} = 0 \quad (4-14d)$$

4.2.4 Linked Discretized Momentum Equations

It is obvious that Equations (4-5b) and (4-11b), and Equations (4-8) and (4-13) have the same format with different coefficients, thus they can be dynamically linked and solved together. Now consider a computational cell on a sloping beach. During a tidal cycle, this cell could be submerged (wet) or emerged (dry) due to the wetting and drying processes. If a cell is dry, then only groundwater flow needed to be calculated,

i.e. Equations (4-11b) and (4-13) should be used in the computation. If a cell is wet and the beach is permeable, then both surface water and groundwater flow should be taken into account. In this case, Equations (4-5b) and (4-11b) should be solved simultaneously in the x-direction, and Equations (4-8) and (4-13) should be solved simultaneously in the y-direction.

In order to show the procedures to link the discretized momentum equations for surface water and groundwater flows, Equations (4-5b) and (4-11b) are rewritten as follows:-

$$a^s \cdot \xi_{i,i}^{n+1/2} + b^s \cdot (p_{i+1/2,i}^{n+1/2})^s + c^s \cdot \xi_{i+1,i}^{n+1/2} = d^s \quad (4-15a)$$

$$a_{2i}^s \cdot \xi_{i,j}^{n+1/2} + b_{2i}^s \cdot (p_{i+1/2,j}^{n+1/2})^s + c_{2i}^s \cdot \xi_{i+1,j}^{n+1/2} = d_{2i}^s \quad (4-15b)$$

$$a_{2i}^g \cdot \xi_{i,j}^{n+1/2} + b_{2i}^g \cdot (p_{i+1/2,j}^{n+1/2})^g + c_{2i}^g \cdot \xi_{i+1,j}^{n+1/2} = d_{2i}^g$$

where the superscripts s and g represent surface water flow and groundwater flow, respectively. For any wet cell, the total flux consists of two parts: one part from surface water flow, and the other part from groundwater flow. Thus, we have:-

$$p_{i+1/2,j}^{n+1/2} = (p_{i+1/2,j}^{n+1/2})^s + (p_{i+1/2,j}^{n+1/2})^g \quad (4-16)$$

Combination of Equations (4-15a) and (4-15b) gives:-

$$a_{2i} \cdot \xi_{i,j}^{n+1/2} + b_{2i} \cdot p_{i+1/2,j}^{n+1/2} + c_{2i} \cdot \xi_{i+1,j}^{n+1/2} = d_{2i} \quad (4-17a)$$

where

$$a_{2i} = a_{2i}^s b_{2i}^g + a_{2i}^g b_{2i}^s \quad (4-17b)$$

$$b_{2i} = b_{2i}^s b_{2i}^g \quad (4-17c)$$

$$c_{2i} = c_{2i}^s b_{2i}^g + c_{2i}^g b_{2i}^s \quad (4-17d)$$

$$d_{2i} = d_{2i}^s b_{2i}^g + d_{2i}^g b_{2i}^s \quad (4-17e)$$

Equation (4-17) is the linked discretized momentum equation in the x-direction for both surface water and groundwater flow. Similar equations can be obtained for the linked discretized momentum equation in the y-direction, given as follows:-

$$a_{2j} \cdot \xi_{i,j}^{n+1} + b_{2j} \cdot q_{i,j+1/2}^{n+1} + c_{2j} \cdot \xi_{i,j+1}^{n+1} = d_{2j} \quad (4-18a)$$

where

Equation (4-18a), to solve for q^{n+1} and ξ^{n+1} . The system of Equations (4-19a) is solved by the method of Gauss elimination and back substitution.

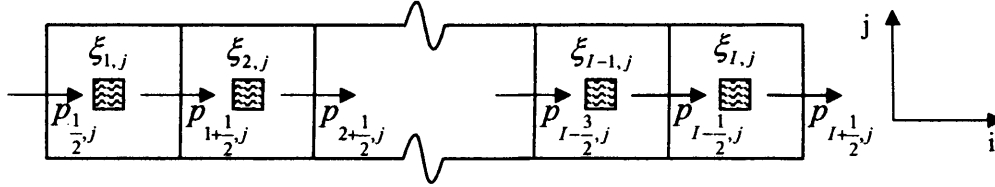


Figure 4-2 Demonstration of variables at j^n row

4.3 DISCRETIZATION OF SOLUTE TRANSPORT EQUATION

The depth integrated two dimensional solute transport equation (Equation (3-85)) can be written for the first half time step as:-

$$\begin{aligned}
 & (H\phi)_{i,j}^{n+1/2} + \frac{\Delta t}{4\Delta x} \left[p_{i+1/2,j}^{n+1/2} (\phi_{i+1,j}^{n+1/2} + \phi_{i,j}^{n+1/2}) - p_{i-1/2,j}^{n+1/2} (\phi_{i-1,j}^{n+1/2} + \phi_{i,j}^{n+1/2}) \right] \\
 & - \frac{\Delta t}{2\Delta x^2} \left[(HD_{xx})_{i+1/2,j}^{n+1/2} (\phi_{i+1,j}^{n+1/2} - \phi_{i,j}^{n+1/2}) - (HD_{xx})_{i-1/2,j}^{n+1/2} (\phi_{i,j}^{n+1/2} - \phi_{i-1,j}^{n+1/2}) \right] \\
 & = (H\phi)_{i,j}^n - \frac{\Delta t}{4\Delta y} \left[q_{i,j+1/2}^n (\phi_{i,j+1}^n + \phi_{i,j}^n) - q_{i,j-1/2}^n (\phi_{i,j-1}^n + \phi_{i,j}^n) \right] \\
 & + \frac{\Delta t}{2\Delta y^2} \left[(HD_{yy})_{i,j+1/2}^n (\phi_{i,j+1}^n - \phi_{i,j}^n) - (HD_{yy})_{i,j-1/2}^n (\phi_{i,j}^n - \phi_{i,j-1}^n) \right] \\
 & + \frac{\Delta t}{2\Delta x\Delta y} \left[(HD_{xy})_{i+1/2,j}^n (\phi_{i+1/2,j+1/2}^n - \phi_{i+1/2,j-1/2}^n) - (HD_{xy})_{i-1/2,j}^n (\phi_{i-1/2,j+1/2}^n - \phi_{i-1/2,j-1/2}^n) \right] \\
 & + \frac{\Delta t}{2\Delta x\Delta y} \left[(HD_{yx})_{i,j+1/2}^n (\phi_{i+1/2,j+1/2}^n - \phi_{i-1/2,j+1/2}^n) - (HD_{yx})_{i,j-1/2}^n (\phi_{i+1/2,j-1/2}^n - \phi_{i-1/2,j-1/2}^n) \right] \\
 & + \frac{\beta^s \Delta t}{2\Delta x} \left[p_{i+1/2,j}^{n+1/2} \nabla_{xx}^2 \phi_{i+1/2,j}^n - p_{i-1/2,j}^{n+1/2} \nabla_{xx}^2 \phi_{i-1/2,j}^n \right] \\
 & + \frac{\beta^s \Delta t}{2\Delta y} \left[q_{i,j+1/2}^n \nabla_{yy}^2 \phi_{i,j+1/2}^n - q_{i,j-1/2}^n \nabla_{yy}^2 \phi_{i,j-1/2}^n \right] + \frac{\Delta t}{2} \phi_s \delta(x_s, y_s)
 \end{aligned} \tag{4-20}$$

where

$$\nabla_{xx}^2 \phi_{i+1/2,j}^n = \begin{cases} \phi_{i+1,j}^n - 2\phi_{i,j}^n + \phi_{i-1,j}^n & \text{if } U_{i+1/2,j}^n \geq 0 \\ \phi_{i+2,j}^n - 2\phi_{i+1,j}^n + \phi_{i,j}^n & \text{if } U_{i+1/2,j}^n < 0 \end{cases} \tag{4-21a}$$

$$\nabla_{yy}^2 \phi_{i,j+1/2}^n = \begin{cases} \phi_{i,j+1}^n - 2\phi_{i,j}^n + \phi_{i,j-1}^n & \text{if } V_{i,j+1/2}^n \geq 0 \\ \phi_{i,j+2}^n - 2\phi_{i,j+1}^n + \phi_{i,j}^n & \text{if } V_{i,j+1/2}^n < 0 \end{cases} \quad (4-21b)$$

$$\phi_{i+1/2,j+1/2}^n = \frac{1}{4} (\phi_{i+1,j+1}^n + \phi_{i+1,j}^n + \phi_{i,j+1}^n + \phi_{i,j}^n) \quad (4-21c)$$

where $\delta(x_s, y_s)$ is a point unit pulse function used to introduce source or sink at the given point (x_s, y_s) . The function takes the value:-

$$\delta(x_s, y_s) = \begin{cases} 1 & \text{if } x = x_s \text{ and } y = y_s \\ 0 & \text{otherwise} \end{cases} \quad (4-21d)$$

The value for β^s of 1/6, 1/8 and 0 corresponds to ADI-TOASOD, ADI-QUICK and second order central difference schemes respectively, where TOASOD stands for Third Order Advection and Second Order Diffusion, and QUICK stands for Quadratic Upwind Interpolation for Convective Kinematics.

Similar scheme can be written for the second half time step as:-

$$\begin{aligned} & (H\phi)_{i,j}^{n+1} + \frac{\Delta t}{4\Delta y} \left[q_{i,j+1/2}^{n+1} (\phi_{i,j+1}^{n+1} + \phi_{i,j}^{n+1}) - q_{i,j-1/2}^{n+1} (\phi_{i,j-1}^{n+1} + \phi_{i,j}^{n+1}) \right] \\ & - \frac{\Delta t}{2\Delta y^2} \left[(HD_{yy})_{i,j+1/2}^{n+1} (\phi_{i,j+1}^{n+1} - \phi_{i,j}^{n+1}) - (HD_{xx})_{i,j-1/2}^{n+1} (\phi_{i,j}^{n+1} - \phi_{i,j-1}^{n+1}) \right] \\ & = (H\phi)_{i,j}^{n+1/2} - \frac{\Delta t}{4\Delta x} \left[p_{i+1/2,j}^{n+1/2} (\phi_{i+1,j}^{n+1/2} + \phi_{i,j}^{n+1/2}) - p_{i-1/2,j}^{n+1/2} (\phi_{i-1,j}^{n+1/2} + \phi_{i,j}^{n+1/2}) \right] \\ & + \frac{\Delta t}{2\Delta x^2} \left[(HD_{xx})_{i+1/2,j}^{n+1/2} (\phi_{i+1,j}^{n+1/2} - \phi_{i,j}^{n+1/2}) - (HD_{yy})_{i-1/2,j}^{n+1/2} (\phi_{i,j}^{n+1/2} - \phi_{i-1,j}^{n+1/2}) \right] \\ & + \frac{\Delta t}{2\Delta x\Delta y} \left[(HD_{xy})_{i+1/2,j}^{n+1/2} (\phi_{i+1/2,j+1/2}^{n+1/2} - \phi_{i+1/2,j-1/2}^{n+1/2}) - (HD_{xy})_{i-1/2,j}^{n+1/2} (\phi_{i-1/2,j+1/2}^{n+1/2} - \phi_{i-1/2,j-1/2}^{n+1/2}) \right] \\ & + \frac{\Delta t}{2\Delta x\Delta y} \left[(HD_{yx})_{i,j+1/2}^{n+1/2} (\phi_{i+1/2,j+1/2}^{n+1/2} - \phi_{i-1/2,j+1/2}^{n+1/2}) - (HD_{yx})_{i,j-1/2}^{n+1/2} (\phi_{i+1/2,j-1/2}^{n+1/2} - \phi_{i-1/2,j-1/2}^{n+1/2}) \right] \\ & + \frac{\beta^s \Delta t}{2\Delta x} (p_{i+1/2,j}^{n+1/2} \nabla_{xx}^2 \phi_{i+1/2,j}^{n+1/2} - p_{i-1/2,j}^{n+1/2} \nabla_{xx}^2 \phi_{i-1/2,j}^{n+1/2}) \\ & + \frac{\beta^s \Delta t}{2\Delta y} (q_{i,j+1/2}^{n+1/2} \nabla_{yy}^2 \phi_{i,j+1/2}^{n+1/2} - q_{i,j-1/2}^{n+1/2} \nabla_{yy}^2 \phi_{i,j-1/2}^{n+1/2}) + \frac{\Delta t}{2} \phi_s \delta(x_s, y_s) \end{aligned} \quad (4-22)$$

The expressions for $\nabla_{xx}^2 \phi_{i+1/2,j}^{n+1/2}$, $\nabla_{yy}^2 \phi_{i,j+1/2}^{n+1/2}$ and $\phi_{i+1/2,j+1/2}^{n+1/2}$ are similar to those given in Equations (4-21), with time level index n being replaced by $n+1/2$. For both the first-half and the second-half time step, the resulting discretized equations are arranged into a tri-diagonal system and solved by using the method of Gauss

elimination and back substitution.

According to the linear analysis of stability the second order central difference scheme (where $\beta^s = 0$) is unconditionally stable, the scheme gives rise to severe oscillations especially when the transport processes are advection dominated. The ADI-TOASOD and ADI-QUICK schemes have the same stability constraint as for the case of pure advection, given as follows:-

$$\frac{U\Delta t}{\Delta x} + \frac{V\Delta t}{\Delta y} \leq 2 \quad (4-23)$$

Although the ADI-TOASOD and ADI-QUICK schemes are similar in formulation, the former has a third order accuracy in space whereas the latter only has a second order accuracy. Therefore in this study the ADI-TOASOD scheme is selected in view of its higher order accuracy.

4.4 BOUNDARY CONDITIONS

Boundary conditions of water elevation or fluxes/velocities for the hydrodynamic processes and solute values for the solute transport processes need to be specified throughout the simulation time at every boundary for each computational row and column within the model domain, when solving the hydrodynamic and solute transport governing equations. There are generally two types of boundary conditions, the first being the closed boundary and the second the open boundary. For the identification of boundary values it is important to note that the velocity components in the x- and y-directions are specified at different points for the staggered grid, and solving equations parallel to a boundary requires values of variables just outside the boundary to be used.

4.4.1 Closed Boundary

A closed boundary can be regarded as a "wall" boundary so that no flow or solute fluxes are permitted to cross the closed boundary. This type of boundary occurs along coastlines or adjacent to structures. Values outside the modeling domain are obtained by assuming a "no slip" condition (or zero flow velocity at the wall) parallel to the boundary and zero flow perpendicular to the boundary. Hence all velocities on the wall are set as zero, whereas the velocities outside that boundary are assigned the same value as the corresponding velocity inside the domain, but with a negative sign. This

is done to satisfy the condition of zero flow across the boundary.

For the case described in Figure 4-3, the closed hydrodynamic boundary conditions are described as follows:-

$$\begin{cases} U_j = 0 & (j = 0,1,2) \\ V_{bj} = -V_j & (j = 0,1,2,3) \end{cases} \quad (4-24)$$

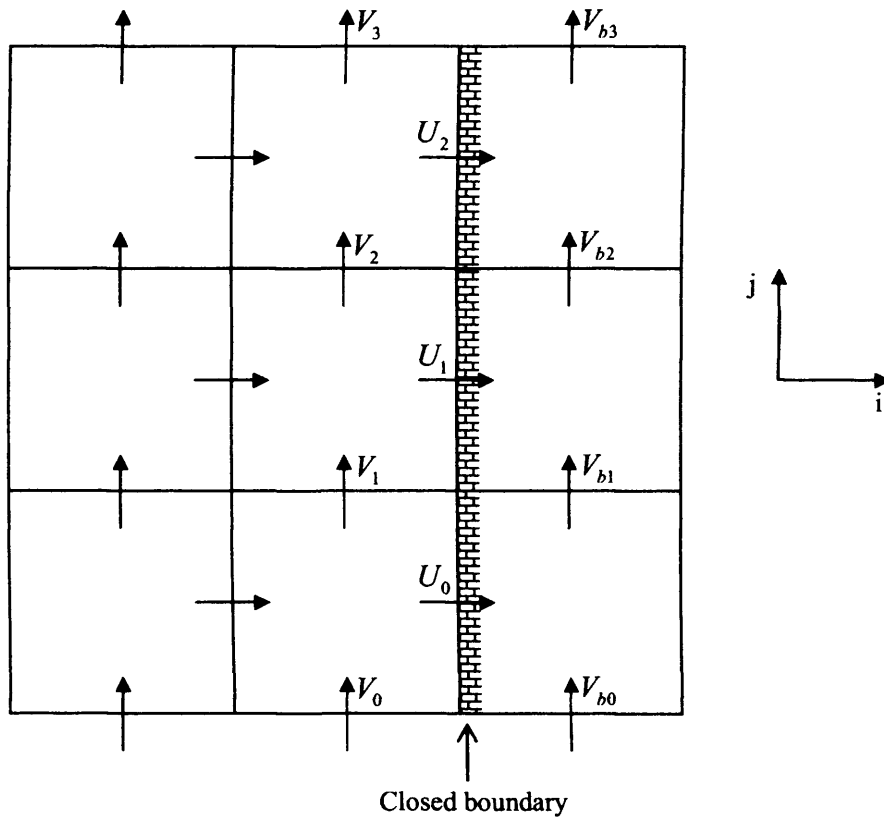


Figure 4-3 Description of closed boundary condition

The closed boundary condition for the solute transport equation is:-

$$\left. \frac{\partial \phi}{\partial n} \right|_w = 0 \quad \text{and} \quad \left. \frac{\partial^2 \phi}{\partial n^2} \right|_w = 0 \quad (4-25)$$

which means that there is no solute flux across the solid boundary. Where n represents the normal direction of the closed boundary, and the subscript w indicates that the value is taken at the closed (wall) boundary.

4.4.2 Open Boundary

Generally, open boundaries are artificial boundaries, since the models have to be run in a limited domain. At the open boundary, appropriate hydrodynamic and solute conditions need to be specified, such as by measured water surface elevation, velocities/fluxes and solute concentration.

If an open boundary is a flow boundary and the velocities at the boundary can be defined as shown in Figure 4-4, the following boundary conditions can be obtained for the hydrodynamics:-

$$\begin{cases} U_j = U_{bj} & (j = 0,1,2) \\ V_j = V_{bj} & (j = 0,1,2,3) \end{cases} \quad (4-26)$$

where U_{bj} and V_{bj} are known velocity values in the x- and y-directions at the open boundary.

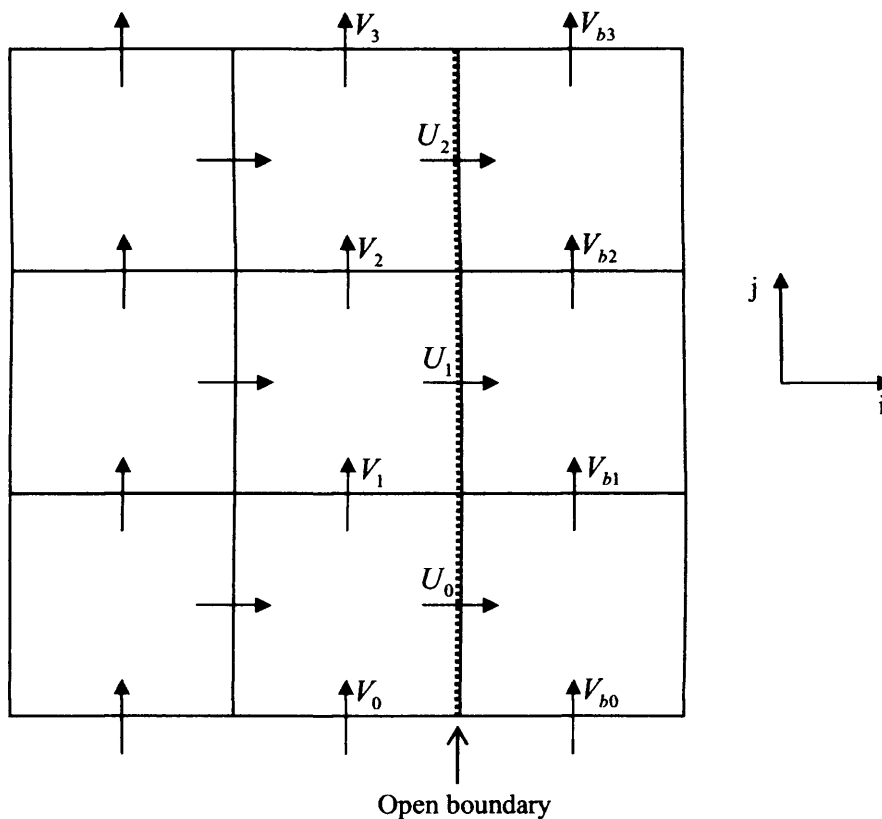


Figure 4-4 Description of flow boundary

If an open boundary condition is of water elevation type, as shown in Figure 4-5,

then the following conditions can be obtained for the hydrodynamics:-

$$\begin{cases} U_j = U_{aj} & (j = 0,1,2) \\ V_j = V_{aj} & (j = 0,1,2,3) \\ \xi_j = \xi_{bj} & (j = 0,1,2,3) \end{cases} \quad (4-27)$$

where ξ_{bj} is the known water elevation values at the open boundary.

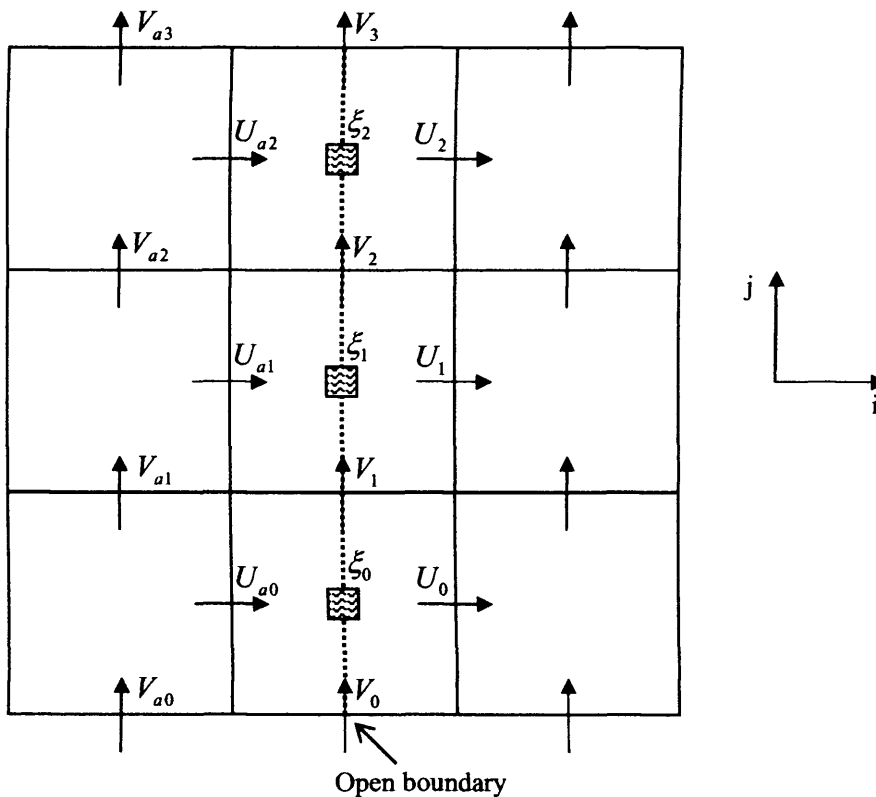


Figure 4-5 Description of water elevation boundary

If the flow at the open boundary is leaving the domain, specification of solute concentration values outside the boundary is not needed. However, if the flow at the open boundary is entering the domain, then the solute values immediately outside the boundary are required, i.e.:-

$$\phi_j = \phi_{bj} \quad (j = 0,1,2) \quad (4-28)$$

4.4.3 Moving Boundary

The moving boundary on the beach is due to the wetting and drying processes during a tidal cycle (Figure 4-6). Since the surface water flow and the groundwater flow

models are dynamically linked in this study, the moving boundary is treated implicitly and naturally, i.e. no additional numerical effort is needed for treating the moving boundary explicitly at every time step.

In this model, the status of a cell is defined as follows:-

$$\begin{aligned} \zeta > z_b & \text{ if the cell is wet} \\ \zeta \leq z_b & \text{ if the cell is dry} \end{aligned} \quad (4-29a)$$

where ζ and z_b are the elevations of the free water surface and the ground surface, respectively. Equation (4-29a) can also be expressed as:-

$$\begin{aligned} H^s > 0 & \text{ if the cell is wet} \\ H^s \leq 0 & \text{ if the cell is dry} \end{aligned} \quad (4-29b)$$

where $H^s = \zeta - z_b$ is the total surface water depth.

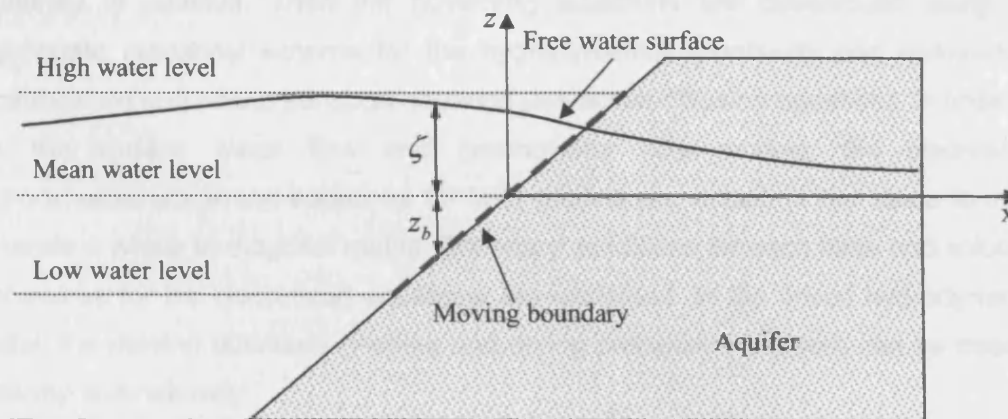


Figure 4-6 Schematic illustration of moving boundary on a beach slope

If a cell is dry, then only the groundwater flow is calculated. If a cell is wet and the beach is permeable, then the surface water and groundwater flow are solved together. Since the surface water and groundwater flow models are dynamically linked in this study, a proper model can be chosen automatically according to the status of a cell (dry or wet) during the simulation. Thus, the moving boundary can be treated implicitly, as the moving boundary can be considered as an interface between surface water and groundwater.

If the bed is impermeable, both the porosity and the hydraulic conductivity are set to zero, thus only the surface water flow model is used. This poses an additional

challenge to the integrated modelling approach. However, it will be shown in Chapter 5 that in this situation the flow field in the surface water will be affected only very slightly if small porosity and hydraulic conductivity coefficients are assumed in the bed. Thus, if the bed is impermeable, the moving boundary can still be treated implicitly with the linked model by assuming the bed is porous with small porosity and hydraulic conductivity values being assumed.

It should be mentioned that in this study the development of the seepage face is ignored since it generally has little effect on the water level landward of the intertidal region (Raubenheimer and Guza, 1999).

4.5 SUMMARY

Numerical solution methods are briefly reviewed in this chapter. The alternating direction implicit scheme technique which is based on the finite difference method is explained in detailed. Then the governing equations are discretized using an appropriate numerical scheme for the hydrodynamics (continuity and momentum conservation) and solute transport equation (advective-diffusion equation). In order to link the surface water flow and groundwater flow models, the discretized hydrodynamic governing equations for both models are written in the same form to generate a whole tri-diagonal matrix. Boundary conditions for each case and solution procedures for the discretized equations are explained. In the linked hydrodynamic model, the moving boundary (wetting and drying processes) problem can be treated implicitly and naturally.

CHAPTER 5

VERIFICATION AND CALIBRATION OF HYDRODYNAMIC AND SOLUTE TRANSPORT MODEL

5.1 INTRODUCTION

Numerical model can be applied to practice only after systematic and careful verification and calibration. In this study the hydrodynamic and the solute transport models have been verified against a number of analytical solutions and experimental data, and several typical test cases are selected to show the verification of the models in this chapter.

The dynamically-linked hydrodynamic model is verified against analytical solutions and experimental data for both surface water and groundwater flows, and the solute transport model is verified for surface water flows. Particular attention is paid on checking the capability of the linked hydrodynamic model for treating moving boundary (wetting and drying processes), because the practical studying area in this thesis (the Mersey Estuary) is an estuary with large area of tidal flat.

5.2 FLOW AND SOLUTE TRANSPORT IN SURFACE WATER

5.2.1 Tidal Flow in a Semi-Closed Open Channel

This is a widely used test, with known exact solution, for evaluating the effectiveness of the hydrodynamic models. In this test, the stability, precision, repeatability and symmetry of the hydrodynamic model is investigated.

Assuming that the flow is invicid and it moves along a semi-enclosed channel with uniform slope bed (Figure 5-1), then Equations (3-50), (3-72) and (3-73) can be simplified to give the following equations to describe the flow:-

$$\frac{\partial \zeta}{\partial t} + \frac{\partial(UH)}{\partial x} = 0 \quad (5-1)$$

$$\frac{\partial(UH)}{\partial t} + gH \frac{\partial \zeta}{\partial x} = 0 \quad (5-2)$$

where ζ is the water elevation, U is the depth-averaged velocity in the x-direction, and H is the water depth.

With well-defined initial and boundary conditions, analytical solution can be obtained for Equations (5-1) and (5-2).

5.2.1.1 The Exact Solution

For this linear system, the following general solution can be obtained (Lynch, 1978):-

$$\zeta(x) = \zeta_0(x) e^{-i\omega x} \quad (5-3)$$

$$U(x) = U_0(x) \cdot e^{-i\omega x} \quad (5-4)$$

where $\omega = 2\pi/T$ is the angular frequency of the tide, T is the tidal period, $\zeta_0(x)$ and $U_0(x)$ are the amplitudes of the tidal elevation and velocity respectively, and

$$\zeta_0(x) = a \cdot J_0(2k\sqrt{x}) + b \cdot Y_0(2k\sqrt{x}) \quad (5-5)$$

$$U_0(x) = -\frac{ig}{\omega} \frac{d[\zeta_0(x)]}{dx} \quad (5-6)$$

herein a and b are two constants which can be determined with well-posed boundary conditions, $J_0()$ is the zero order first kind Bessel function, and $Y_0()$ is the zero order second kind Bessel function, and

$$k^2 = \frac{\omega^2}{g} \frac{L_2}{H_2} \quad (5-7)$$

where g is the acceleration due to gravity, H_2 is the water depth at the right boundary, and L_2 is the distance from the original point (o) to the right boundary (Figure 5-1).

The following boundary conditions are introduced:-

$$\zeta_0(x) \Big|_{x=L_2} = A \quad (5-8a)$$

$$\frac{\partial[\zeta_0(x)]}{\partial x} \Big|_{x=L_1} = 0 \quad (5-8b)$$

where L_1 is the distance from the original point (o) to the left boundary (Figure 5-1).

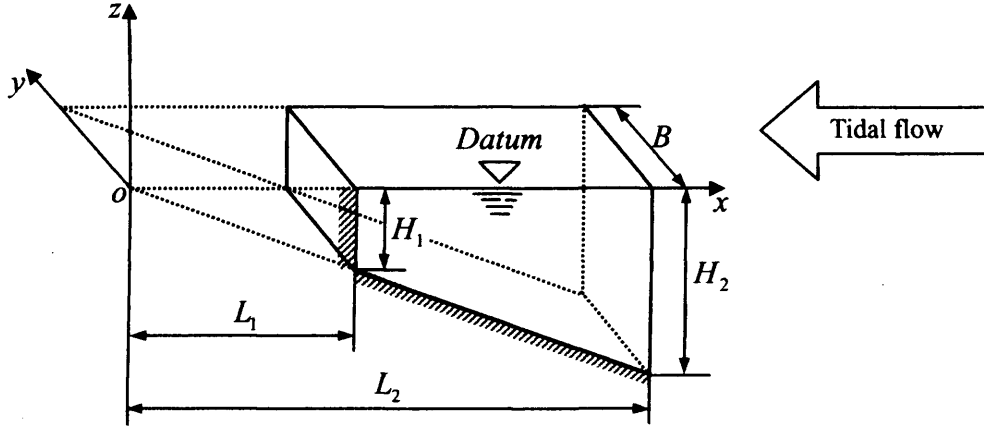


Figure 5-1 Schematic illustration of semi-closed open channel

The two constants (a and b) in Equation (5-5) can be determined and the following special solution can be obtained:-

$$\zeta_0(x) = A \cdot \frac{J_0(2k\sqrt{x}) \cdot Y_1(2k\sqrt{L_1}) - J_1(2k\sqrt{L_1}) \cdot Y_0(2k\sqrt{x})}{J_0(2k\sqrt{L_2}) \cdot Y_1(2k\sqrt{L_1}) - J_1(2k\sqrt{L_1}) \cdot Y_0(2k\sqrt{L_2})} \quad (5-9)$$

$$U_0(x) = i \cdot A \frac{L_2}{H_2} \frac{\omega}{\sqrt{x}} \cdot \frac{J_1(2k\sqrt{x}) \cdot Y_1(2k\sqrt{L_1}) - J_1(2k\sqrt{L_1}) \cdot Y_1(2k\sqrt{x})}{J_0(2k\sqrt{L_2}) \cdot Y_1(2k\sqrt{L_1}) - J_1(2k\sqrt{L_1}) \cdot Y_0(2k\sqrt{L_2})} \quad (5-10)$$

where $J_1()$ is the first order first kind Bessel function, $Y_1()$ is the first order second kind Bessel function, H_1 is the water depth at the left boundary. It is obvious that the above exact solution represents a flow which is symmetrical in the y -direction.

5.2.1.2 Computational Parameters, Initial and Boundary Conditions

In the numerical simulation, the geometric parameters of the channel are as follows:-

$$H_1 = 10m, \quad H_2 = 20m, \quad B = 20Km, \quad L_1 = 200Km, \quad L_2 = 400Km$$

where B is the width of the channel. The parameters of the tide is set as

$$A = 1m, \quad T = 12.4206 \text{ hours}$$

The computational time step is set as, $dt = 22.35708s$, and the whole domain is divided into 200 and 20 segments in the x - and y -direction, respectively, i.e. spatial

steps in both x - and y -directions are $dx = dy = 1000m$.

The initial and open boundary conditions are determined with the aforementioned exact solution. The slip boundary condition is applied at both lateral boundaries since the flow is symmetrical in the y -direction.

5.2.1.3 Repeatability and Symmetry

Figure 5-2 illustrates the temporal distribution of the water elevation at three different points during 5 tidal cycles (see Table 5-1 for the coordinates of the three points). It can be seen that after three tidal cycles, the numerical results become stable, and the numerical results show good repeatability. Figure 5-3 demonstrates the temporal distribution of velocity component in the x -direction at the three points during 5 tidal cycles. From figure 5-3 it can be seen that the x -components of the velocity at the three points vary periodically. The results are also stable. Considering the run-off error, the y -component of the velocity is zero at any time step (in the order of $1.e^{-18}$ m/s). In Figure 5-4 the spatial distribution of water elevation at three cross sections which are perpendicular to the x -axes are demonstrated (see Table 5-1 for the location of the cross sections). It can be seen from this figure that the same as the exact solution, the numerical result is also symmetrical and keeps as constant along the y -direction. This means that the numerical predicted flow in the channel is parallel to the x -axes, i.e. the flow is two-dimensional and symmetrical in the y -direction. Thus all the numerical results mentioned in the following context are collected at the central longitudinal axes after the computation becomes stable.

Table 5-1 Coordinates of three sampling points and sections

Title	x (Km)	y (Km)
Point A	390	15
Point B	300	10
Point C	210	5
Cross section A	390	-
Cross section B	300	-
Cross section C	210	-

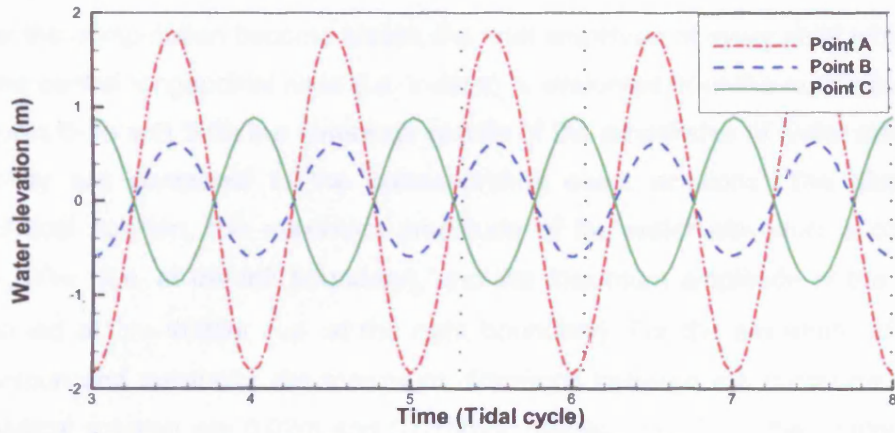


Figure 5-2 Temporal distribution of water elevation at three points

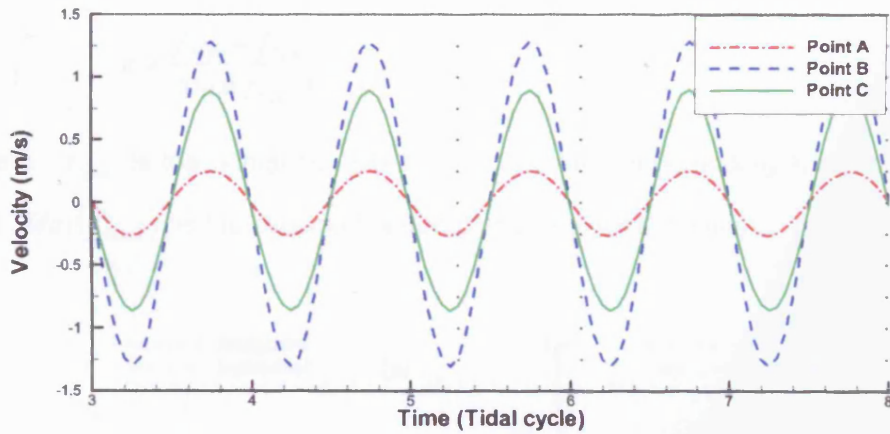


Figure 5-3 Temporal distribution of x-component of velocity at three points

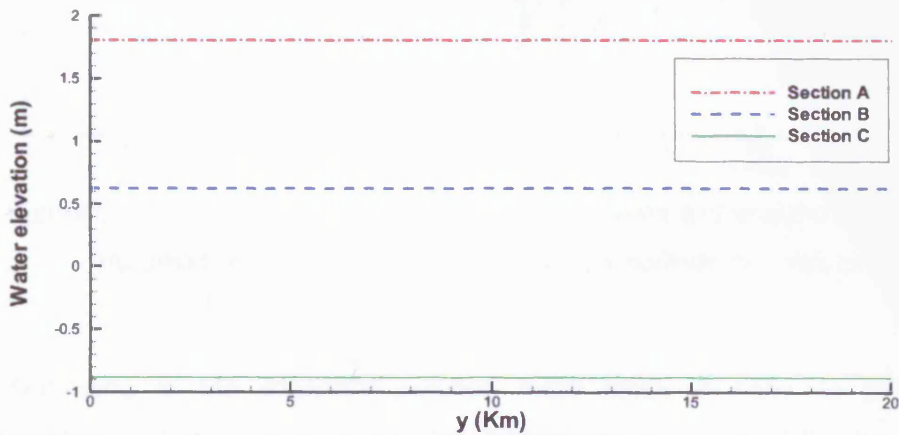


Figure 5-4 Spatial distribution of water elevation at three cross sections

5.2.1.4 Comparison between Numerical Results and Exact Solutions

After the computation become stable, the tidal amplitude at every point which located at the central longitudinal axes (i.e. x -axes) is evaluated from the numerical result. In Figures 5-5a and 5-5b the numerical results of the amplitudes of water elevation and velocity are compared to the corresponding exact solutions. The same as the analytical solution, the maximum amplitude of the water elevation is observed at $x = 200m$ (i.e. at the left boundary), and the maximum amplitude of the velocity is obtained at $x = 400km$ (i.e. at the right boundary). For the amplitude of the water elevation and x -velocity, the maximum difference between the numerical result and analytical solution are $0.02m$ and $0.015m/s$, respectively. Thus the relative error for both water elevation and velocity are within 1.2%, with the relative error ε being defined as follows:-

$$\varepsilon = \frac{f_{Num} - f_{Exact}}{Max(f_{Exact})} \quad (5-11)$$

herein, f_{Num} is the numerical result, f_{Exact} is the corresponding analytical solution, and $Max(f_{Exact})$ is the maximum value of the analytical solution.

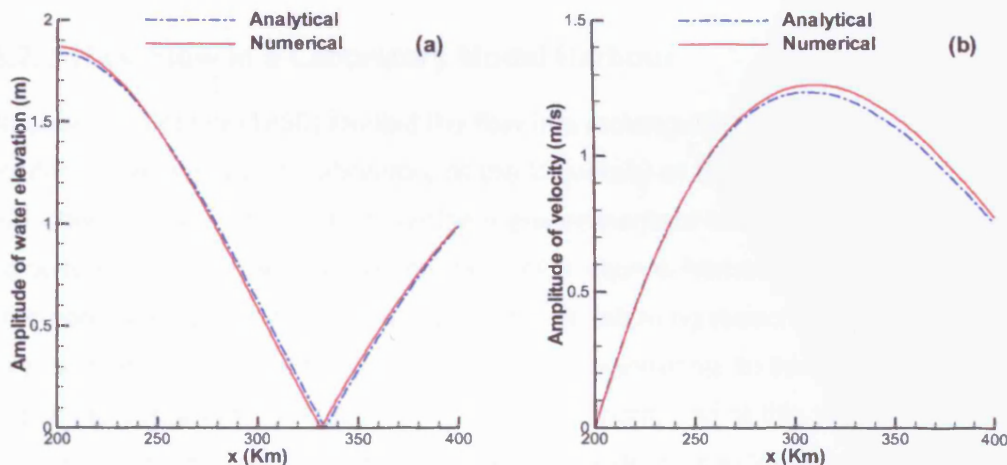


Figure 5-5 Comparison between numerical results and analytical solutions
(a) amplitude of water elevation and (b) amplitude of x -velocity

According to the analytical solution there exists a node (a point of no displacement) at $x = 333km$ due to the bathymetry. In Figure 5-6a the numerical predicted temporal distribution of water elevation is compared with the corresponding

analytical solution during a half tidal cycle. It can be seen that the numerical result agree well with the analytical solution, and the node from the numerical result locates at around $x = 332\text{km}$. Figure 5-6b compares the numerical predicted temporal distribution of x -velocity with the corresponding analytical solution. For velocity the numerical result is also in good agreement with the analytical solution.

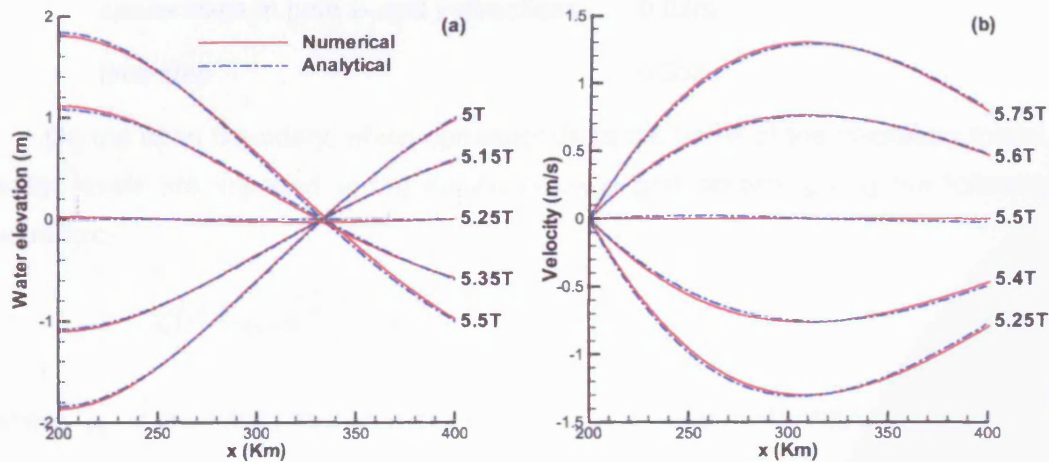


Figure 5-6 Comparison between numerical results and analytical solutions
(a) evolution of water elevation and (b) evolution of x -velocity (T: tidal cycle)

5.2.2 Tidal Flow in a Laboratory Model Harbour

Nece and Falconer (1989) studied the flow in a rectangular harbour with experimental model in the Hydraulics Laboratory at the University of Bradford. One of the aims of the laboratory work is to obtain precise measurements of the ebb tide depth-averaged velocity profiles across the central axes of a square harbour. This experimental is selected as a test case in this study due to the following reasons: a) the prototype of this experimental model is common in coastal engineering, b) this test can be used to check the bottom friction based on roughness length, and c) this test is very rigorous for the stability and precision of the numerical model due to the quickly varying of the flow field around the gate.

The laboratory harbour is illustrated schematically in Figure 5-7 with the following parameters:-

square planform area	1.08m • 4.08m
asymmetric entrance of width	0.12m

mean water level	0.15m
tidal amplitude	0.05m
tidal period	708s

Computational parameters of the numerical model for the laboratory harbour are as follows:-

space steps in both x - and y -directions	0.02m
time step	0.354s

On the open boundary, which corresponds to the baffle of the laboratory model, water levels are imposed at the centre of each grid square, giving the following equation:-

$$\zeta(t) = a \cos\left(\frac{2\pi t}{T} + \phi_0\right) \quad (5-12)$$

where ϕ_0 is the initial phase in radians, and $\phi_0 = \pi$ for a model starts at low tide.

The size of the diameter of roughness particles, k_s affects the Chezy coefficient through Equation (3-61) and hence the bed friction in Equation (3-57). For the rectangular harbour study, the value of k_s is taken as 0.0005m.

The predicted x -component velocity at the mean water level across the central axis BOD of the harbour is compared against the laboratory measured data in Figure 5-8, as well as the numerical result obtained by Nece and Falconer (1989). It can be seen that the present numerical result agrees well with the experimental data and is better than the result obtained by Nece and Falconer (1989) with their result underestimating the peak value around the centre of the entrance. The main reasons for the better results being obtained by using the present model may be: a) less numerical dissipation in the current simulation due to a finer spatial grid system being used (in Nece's simulation a nested grid system was used with the space step around the gate is 0.02m and the space step in other area is 0.04m), and b) different treatment of the closed boundary condition (in Nece and Falconer's model a partially slip boundary condition is used at boundary ABC, while in the present model a non-slip boundary condition is used).

Figure 5-9 demonstrates the evolution of the velocity distribution in the laboratory model harbour. A main circulation exists around the centre of the harbour during the

whole tidal cycle. The main circulation becomes stronger as the tide flooding in and becomes weaker as the tide ebbing out. During ebb tide (Time = 0 and Time = 0.75T), three small circulations occur around the three corners of the harbour. Due to the limitation of the experimental data, these results have not been verified quantitatively, but they are reasonable and similar to those observed by Nece and Faloner (1989).

This test shows that the numerical model responses correctly to the bottom friction based on roughness length and can be used to simulate the flow field with a considerable gradient.

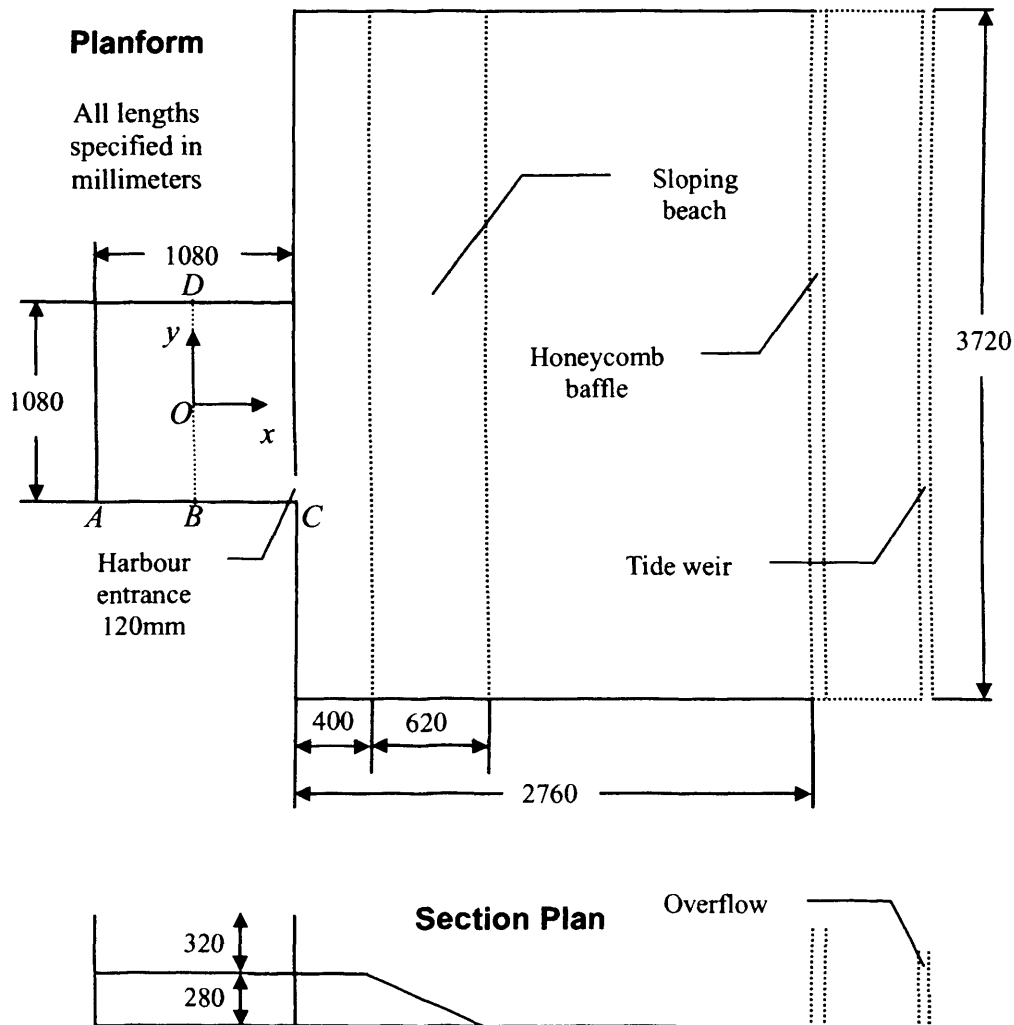


Figure 5-7 Schematic illustration of tidal basin

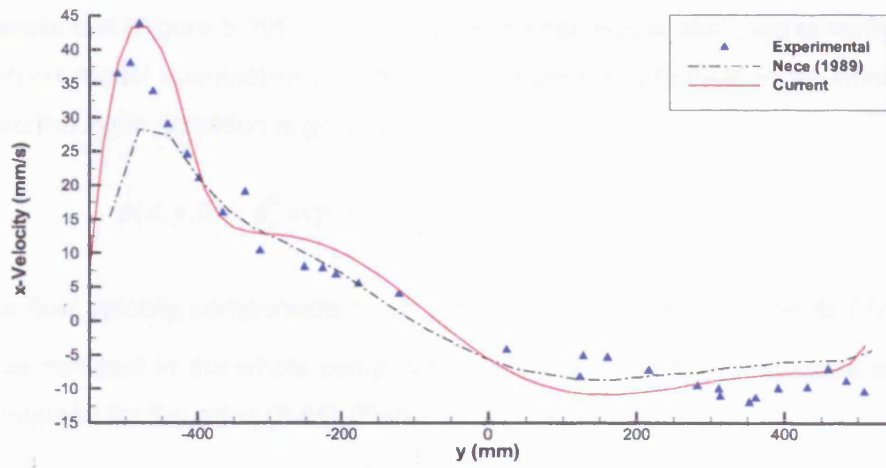


Figure 5-8 Velocity profile across axis BOD at Time=1.25T (T: tidal cycle)

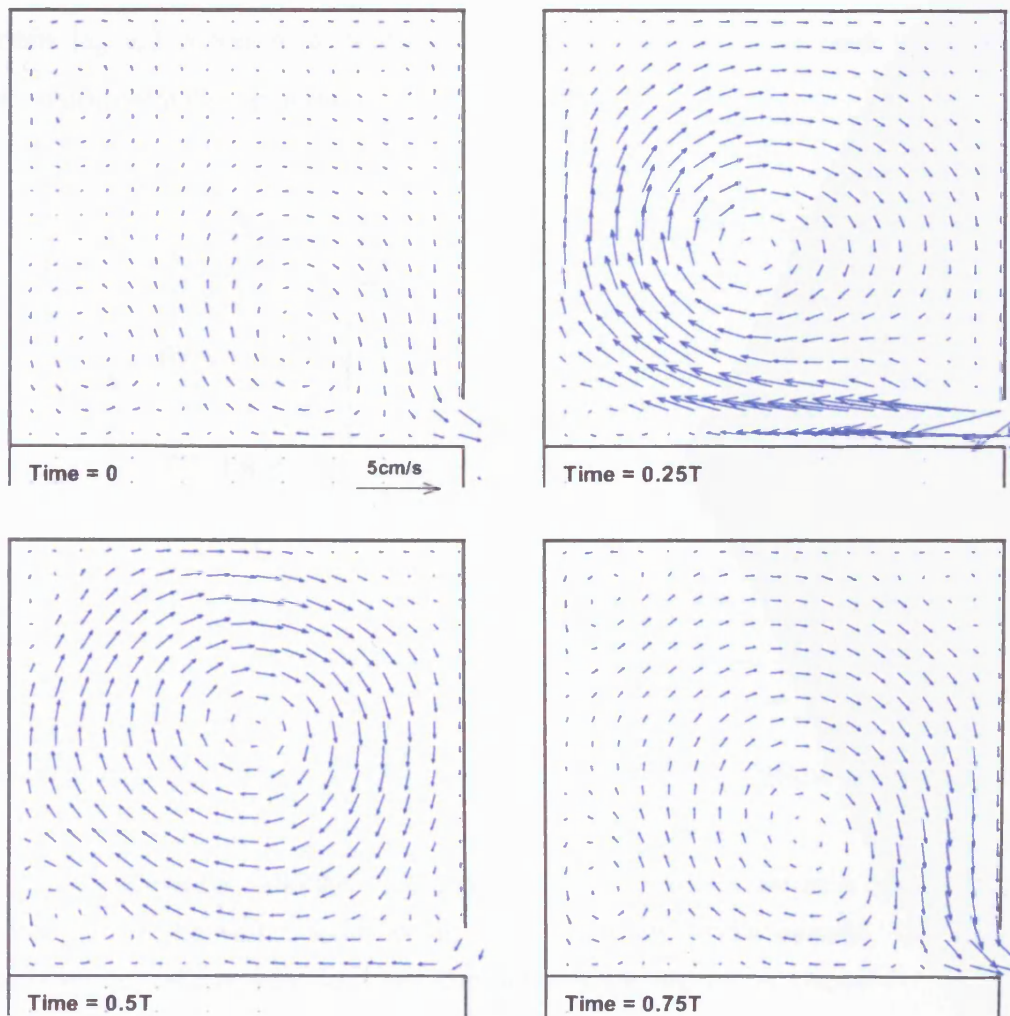


Figure 5-9 Evolution of velocity distribution in model harbour (T: tidal cycle)

5.2.3 Solute Transport in a Uniform Flow Field

A special test (Figure 5-10) with a known exact solution is designed to verify the solute transport model quantitatively. Consider the transport of solute in an infinite domain, where the initial condition is given as:-

$$\phi(x, y, 0) = \phi_p^0 \exp \left[-\frac{(x-x_0)^2}{D_{xx}} - \frac{(y-y_0)^2}{D_{yy}} \right] \quad (5-13a)$$

If the flow velocity components (U, V) and the dispersion coefficients (D_{xx}, D_{yy}) are set as constant in the whole computational domain, the following exact solution can be obtained for Equation (3-85) (Fisher et al., 1979):-

$$\phi(x, y, t) = \frac{\phi_p^0}{4t+1} \exp \left[-\frac{(x-x_0-Ut)^2}{D_{xx}(4t+1)} - \frac{(y-y_0-Vt)^2}{D_{yy}(4t+1)} \right] \quad (5-13b)$$

where (x_0, y_0) is the initial centre of the solute, and ϕ_p^0 is the peak value of the concentration at the initial time.

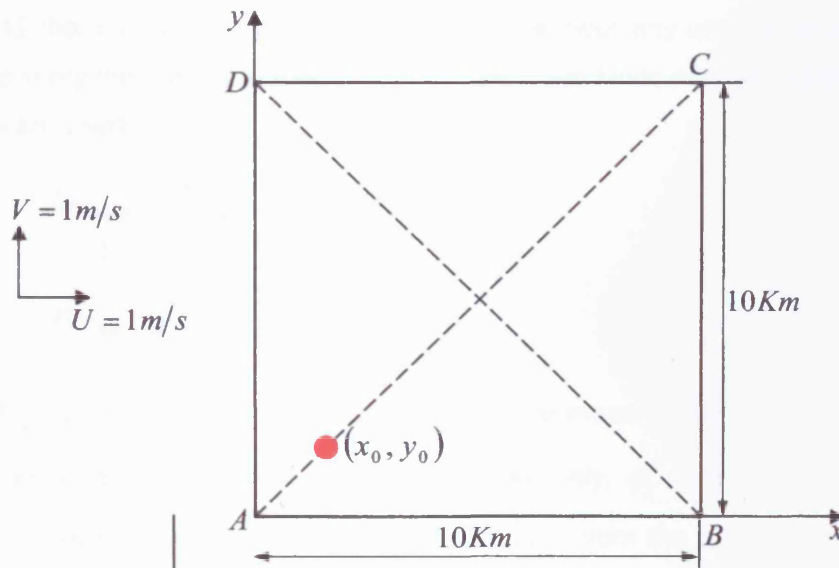


Figure 5-10 Schematic illustration of test case for verifying solute transport model

In the numerical simulation the computational domain is set as a square of side length 10km. The water depth is set as 10m for the whole domain. The velocity components and the initial concentration of the solute are set as follows:-

$$U = 1m/s, V = 1m/s \text{ and } \phi_p^0 = 1$$

The Manning's roughness coefficient is set as 0.02, and the coefficients in Equation (3-85) are set as follows:-

$$D_l = 100, D_k = 1.2 \text{ and } D_w = 0$$

According to Equation (3-86), the corresponding dispersion coefficients in Equation (5-13) are:-

$$D_{xx} = 30.5396 \text{ m}^2/\text{s} \text{ and } D_{yy} = 30.5396 \text{ m}^2/\text{s}$$

The initial centre of the solute is set as:-

$$x_0 = 2000\text{m} \text{ and } y_0 = 2000\text{m}$$

The space steps in both the x- and y-directions are 100m with 100 cells in both directions, and the time step is 10s.

In Figure 5-11, the numerical results of the concentration along Section A-C and Section B-D are compared against the corresponding exact solutions at $t = 2500\text{s}$, 3000s and 3500s . The numerical results agree very well with the exact solutions. Figure 5-12 illustrates a 3D plot of the concentration distribution. It can be seen from Figure 5-12 that the numerical results are smooth without any unphysical oscillation. In order to verify the numerical model quantitatively, two kinds of relative error defined as follows are used:-

$$Err_{Mass} = \frac{M_{Num} - M_{Ana}}{M_{Ana}} \quad (5-14a)$$

$$Err_{Peak} = \frac{\phi_p^N - \phi_p^A}{\phi_p^A} \quad (5-14b)$$

where M_{Num} and M_{Ana} are the total values of the mass in the domain evaluated with numerical data and analytical solution, respectively, ϕ_p^N and ϕ_p^A are the peak (maximum) value of the concentration in the domain from the numerical simulation and analytical solution, respectively. Thus, Err_{Mass} and Err_{Peak} represent the relative errors of the total mass and the peak value in the domain, respectively. Table 5-2 lists the values of Err_{Mass} and Err_{Peak} at the selected times ($t = 2500\text{s}$, 3000s and 3500s). It can be seen from Table 5-2 that the relative errors are very small, i.e. the numerical results agree very well with the analytical solutions. Table 5-2 also shows that the numerical dissipation of the numerical model is very small and the mass conservative property of the model is satisfied. Due to the numerical dissipation, all of the values of relative errors in Table 5-2 are negative.

Table 5-2 Relative errors of the total mass and the peak value

Time (s)	2500	3000	3500
$Err_{Mass} \times 10^{-7}$	-7.186	-3.482	-5.535
$Err_{Peak} \times 10^{-3}$	-2.899	-4.411	-5.044

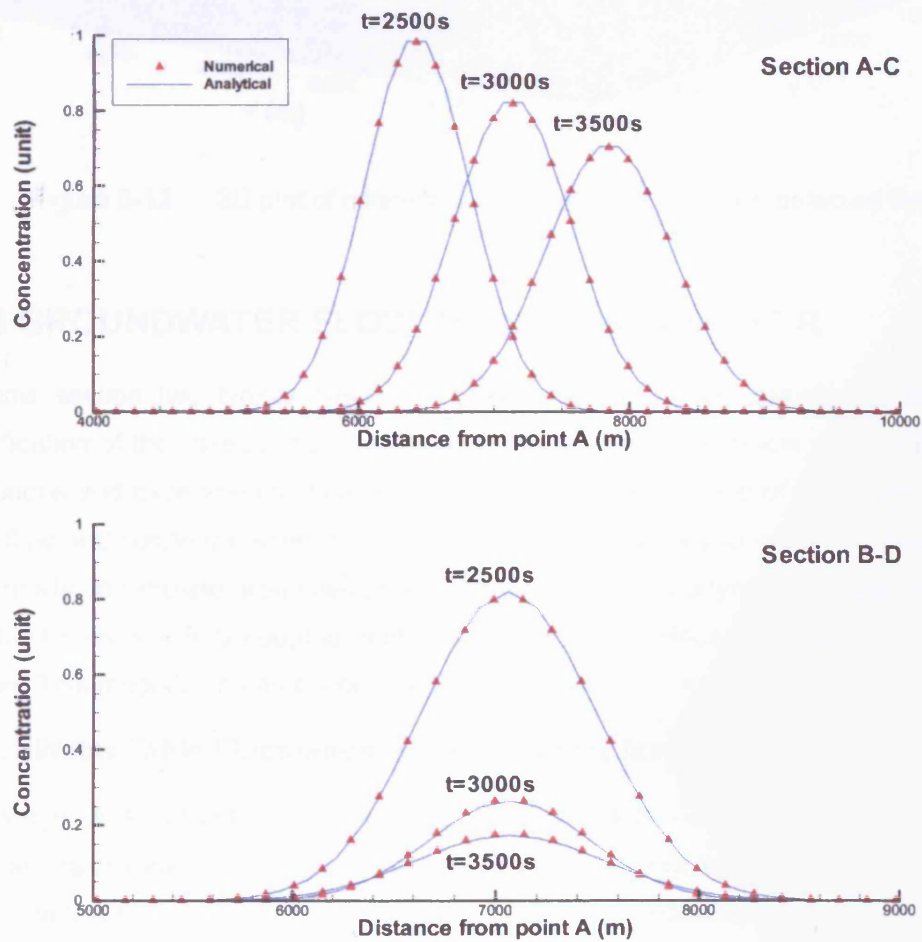


Figure 5-11 Comparison of numerical results and exact solutions along Section A-C and Section B-D (Figure 5-12) at selected times

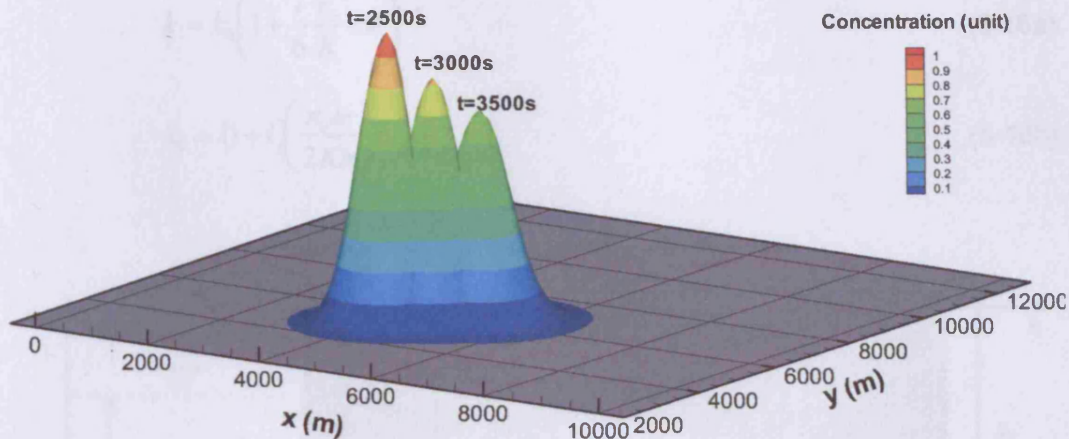


Figure 5-12 3D plot of concentration distribution at three selected times

5.3 GROUNDWATER FLOW IN COASTAL AQUIFER

In this section two typical cases for groundwater flow are selected to show the verification of the linked surface water and groundwater flow model against analytical solutions and experimental data. Although it is out of the scope of this thesis to study the flow and solute transport in groundwater, it is necessary to verify the capability of the model to simulate groundwater flow, because the hydrodynamic model developed in this thesis is a fully coupled model including both surface water and groundwater flows. This model also can become a good foundation for future research.

5.3.1 Water Table Fluctuation in a Laboratory Model Aquifer

Parlange et al. (1984) performed a set of laboratory experiments measuring the elevations of water table in porous media driven by an oscillating piston in a reservoir in contact with the porous media (Figure 5-13). They observed that steady periodic motions could be reached and presented their measurements of the steady oscillating water levels at four locations in the porous media. Liu and Wen (1997) obtained a periodic perturbation solution for this type of problem, given as:-

$$\zeta = Ae^{i(kx-\omega t)} + \frac{a^2}{4h} \left\{ 2 \left[e^{i(\sqrt{2k_0}x-2\omega t)} - e^{2i(k_0x-\omega t)} \right] + \left[1 - e^{i(k_0-k_0^*)x} \right] \right\} \quad (5-15)$$

where A is the wave amplitude in the reservoir, h is the still water depth, $i = \sqrt{-1}$ is the imaginary unit number, ω is the angular frequency of the oscillation, k_0^* is the complex conjugate of k_0 , and k is the wave number defined as follows:-

$$k = k_0 \left(1 + \frac{i n_e \omega}{6 K} \omega h \right) \quad (5-16a)$$

$$k_0 = (1 + i) \left(\frac{n_e \omega}{2 K h} \right)^{1/2} \quad (5-16b)$$

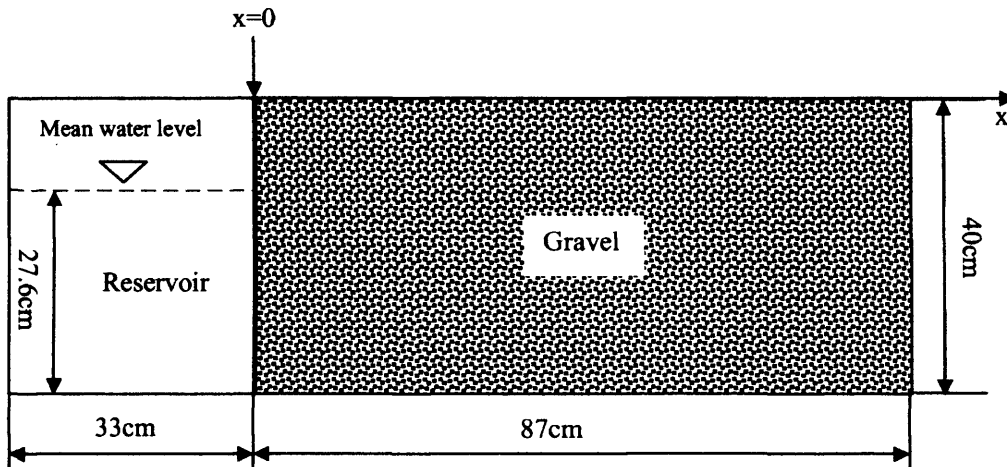


Figure 5-13 Schematic illustration of experiment layout

In the experiment, the water level in the reservoir oscillates with a period of 35s. The mean water level in the flume is 27.6cm and the wave amplitude is 9cm. The ratio of the porosity to hydraulic conductivity is $n_e/K \approx 34.5m^{-1}s$.

In the numerical simulation the space steps in both the x - and y -directions are 1cm, with 120 cells in the x -direction and 40 cells in the y -direction. The time step is 10s. Tidal wave is generated at the left boundary and the other three boundaries are set as solid vertical walls.

Figure (5-14a) demonstrates the water elevation distribution along the x -direction for a wave period. It can be seen that the wave passes through the interface of the surface water and groundwater smoothly, and the amplitude of the wave decreases rapidly in the porous media. Due to the partial reflection of the interface, some small oscillations appear near the interface. Figure (5-14b) shows that steady periodic motions can be reached in the numerical simulation and even the small oscillations appeared periodically. Figure (5-15) compares the numerical results against both the experimental data and the analytical solutions. The numerical model results, the experimental data and the analytical solutions agree closely.

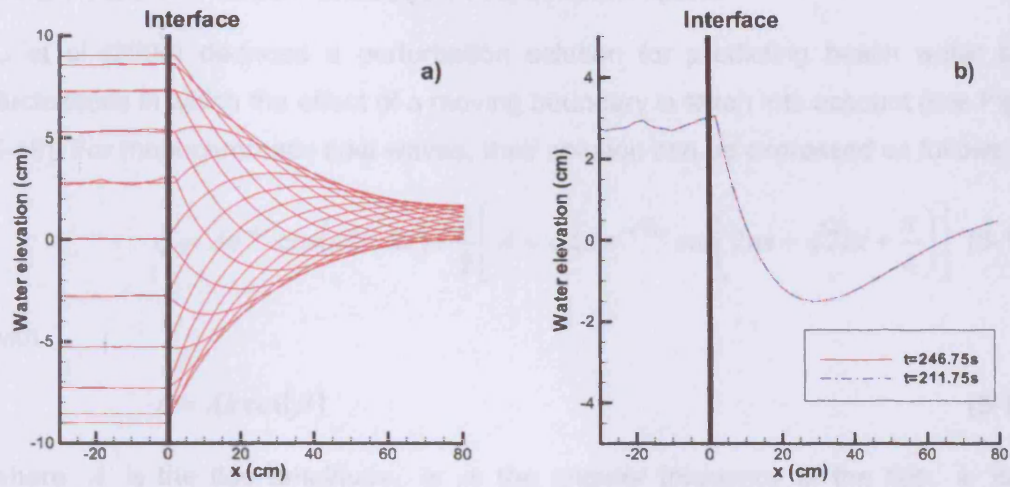


Figure 5-14 Water elevation along x-direction: a) for a wave period with time interval being 1.75s; b) for two selected time

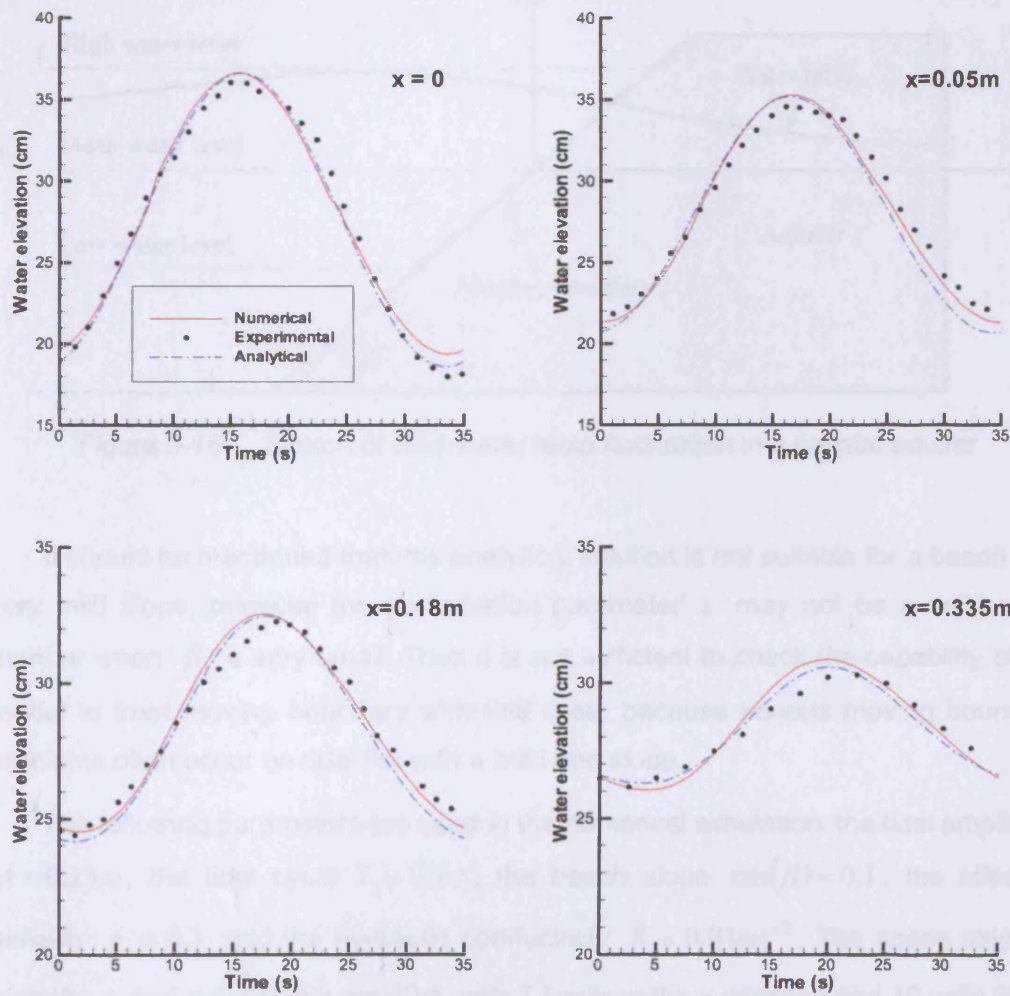


Figure 5-15 Water elevations in porous media at $x=0m$, $0.05m$, $0.18m$ and $0.335m$

5.3.2 Tidal Water Table Fluctuation in a Coastal Aquifer

Li et al (2000) deduced a perturbation solution for predicting beach water table fluctuations in which the effect of a moving boundary is taken into account (see Figure 5-16). For monochromatic tidal waves, their solution can be expressed as follows:-

$$\zeta = Ae^{-kx} \cos(\omega t - kx) + \frac{\varepsilon}{2} \left[A + \sqrt{2} Ae^{-\sqrt{2}kx} \cos\left(2\omega t - \sqrt{2}kx + \frac{\pi}{4}\right) \right] \quad (5-17a)$$

with

$$\varepsilon = Ak \cot(\beta) \quad (5-17b)$$

where A is the tide amplitude, ω is the angular frequency of the tide, k is the wave number, and β is the beach angle (see Figure 5-16).

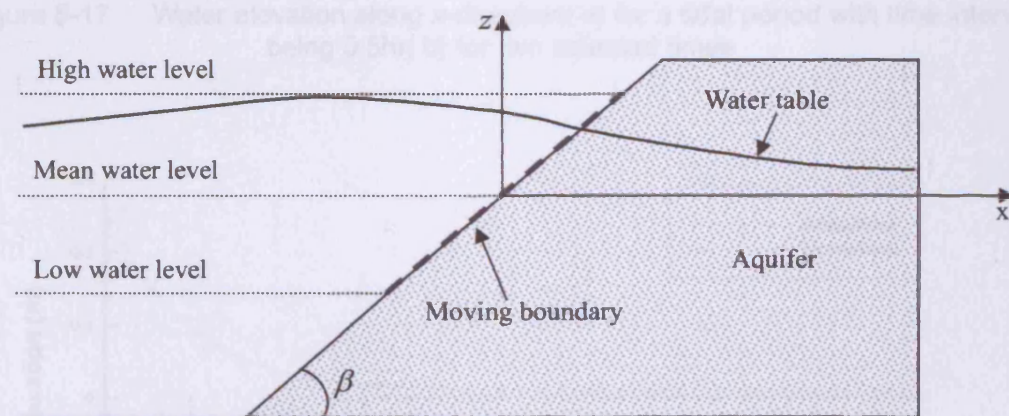


Figure 5-16 Sketch of tidal water table fluctuation in a coastal aquifer

It should be mentioned that this analytical solution is not suitable for a beach with very mild slope, because the perturbation parameter ε may not be a valid small number when β is very small. Thus it is not sufficient to check the capability of the model to treat moving boundary with this case, because serious moving boundary problems often occur on tidal flat with a mild bed slope.

The following parameters are used in the numerical simulation: the tidal amplitude $A = 0.25m$, the tidal cycle $T = 12hr$, the beach slope $\tan(\beta) = 0.1$, the effective porosity $n_e = 0.3$ and the hydraulic conductivity $K = 0.01ms^{-1}$. The space steps in both the x - and y -directions are 10m, with 72 cells in the x -direction and 10 cells in the y -direction. The time step is 5s. Tidal waves are generated on the left boundary and

the simulation starts at mean water level with zero velocity.

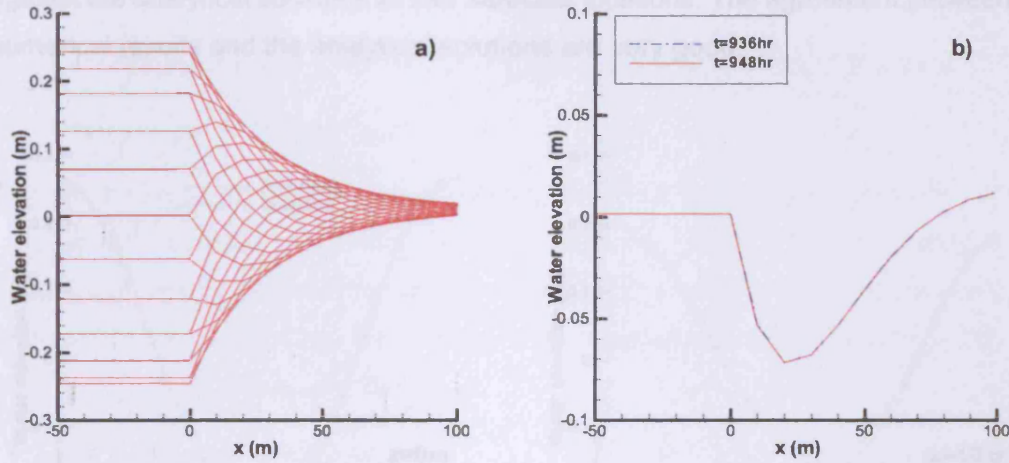


Figure 5-17 Water elevation along x-direction: a) for a tidal period with time interval being 0.5hr; b) for two selected times

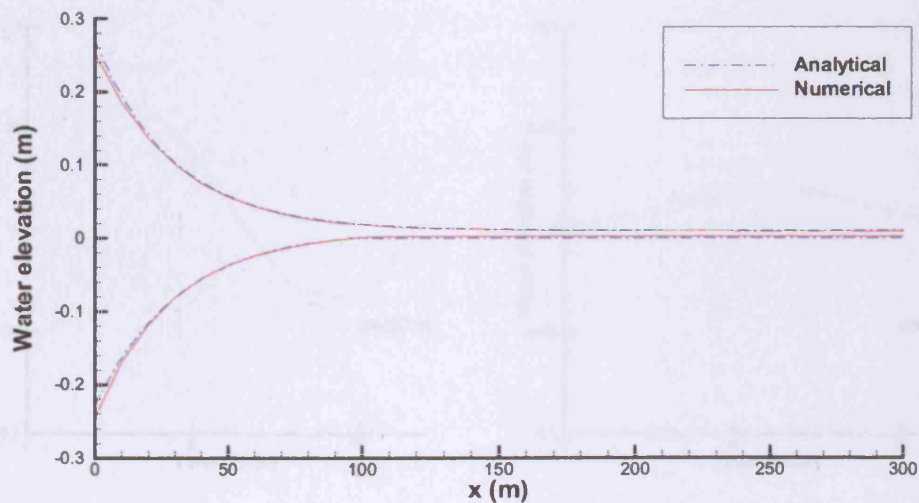


Figure 5-18 Upper and lower limits of water elevation along x-axis

5.4 MOVING BOUNDARIES

Figure (5-17a) demonstrates the water elevation distributions along the x-direction for a tidal period. It can be seen that the tidal wave passes through the interface of the surface water and the groundwater smoothly without any obvious oscillations. Figure (5-17b) shows that steady periodic motions can be reached in the numerical simulation, which is consistent with the analytical solution. In Figure (5-18) the numerical results of the upper and lower limits of the water elevation are

compared against the analytical solutions along the x -axis. The numerical results agree well with the analytical solutions. Figure (5-19) compares the numerical results against the analytical solutions at four selected locations. The agreement between the numerical results and the analytical solutions are very good.

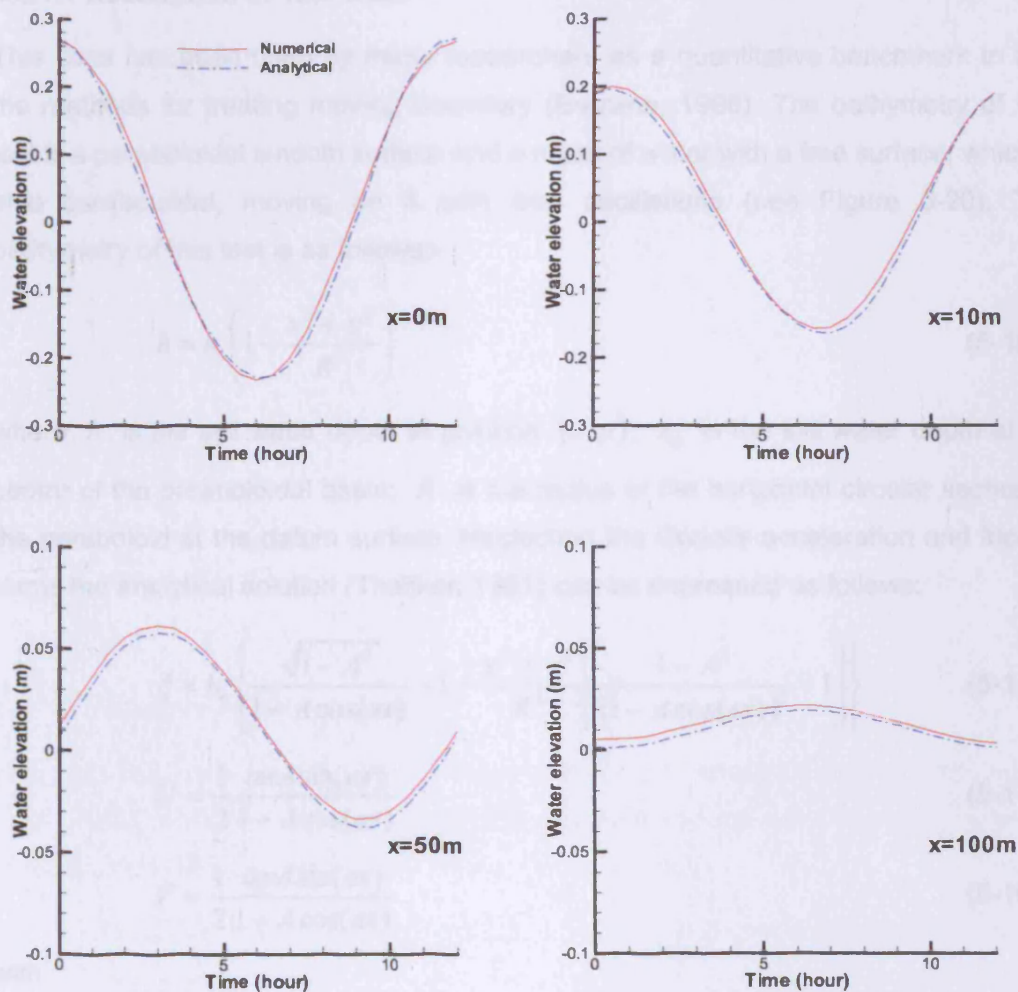


Figure 5-19 Water table in coastal aquifer at $x=0m$, $10m$, $50m$ and $100m$

5.4 MOVING BOUNDARIES

Three test cases are selected to show the capability of the linked surface water and groundwater flow model for modelling moving boundary problems, where the bed is impermeable. In order to treat the moving boundary problems by using the linked surface water and groundwater model, small values of artificial porosity and hydraulic conductivity coefficients are assumed in the bed. The effect of using the artificial

porosity and hydraulic conductivity is investigated in detail. The numerical results from the present model are compared with those obtained from other existed surface water model and analytical solutions.

5.4.1 Oscillating Flow in a Circular Lake with Paraboloidal Bottom

5.4.1.1 Description of Test Case

This case has been used by many researchers as a quantitative benchmark to test the methods for treating moving boundary (Balzano, 1998). The bathymetry of this test is a paraboloidal smooth surface and a mass of water with a free surface, which is also paraboloidal, moving on it with free oscillations (see Figure 5-20). The bathymetry of this test is as follows:-

$$h = h_o \left(1 - \frac{x^2 + y^2}{R^2} \right) \quad (5-18)$$

where h is the still water depth at position (x, y) , h_o is the still water depth at the centre of the paraboloidal basin; R is the radius of the horizontal circular section of the paraboloid at the datum surface. Neglecting the Coriolis acceleration and friction terms the analytical solution (Thacker, 1981) can be expressed as follows:

$$\xi = h_o \left\{ \frac{\sqrt{1-A^2}}{1-A\cos(\omega t)} - 1 - \frac{x^2 + y^2}{R^2} \left[\frac{1-A^2}{(1-A\cos(\omega t))^2} - 1 \right] \right\} \quad (5-19a)$$

$$U = \frac{1}{2} \frac{\omega x A \sin(\omega t)}{1-A\cos(\omega t)} \quad (5-19b)$$

$$V = \frac{1}{2} \frac{\omega y A \sin(\omega t)}{1-A\cos(\omega t)} \quad (5-19c)$$

with

$$\omega = \frac{2\pi}{T} = \frac{\sqrt{8gh_o}}{R} \quad (5-20a)$$

$$A = \frac{(h_o + z_o)^2 - h_o^2}{(h_o + z_o)^2 + h_o^2} \quad (5-20b)$$

where z_o is the water elevation at the initial time at the centre of the paraboloidal basin, and T is the period of the free oscillation.

In this study, the computational domain is set as a square with sides length of 20

km, $R = 8000\text{m}$ and $T = 1800\text{s}$, so that $h_o = 9.94\text{m}$ was obtained using Equation (5-20a). The domain is discretized by a space step of 100m , and the time step is set to 10s . Bottom friction and eddy viscosity are set as zero. The initial condition is obtained using Equation (5-19) with $t = 0$.

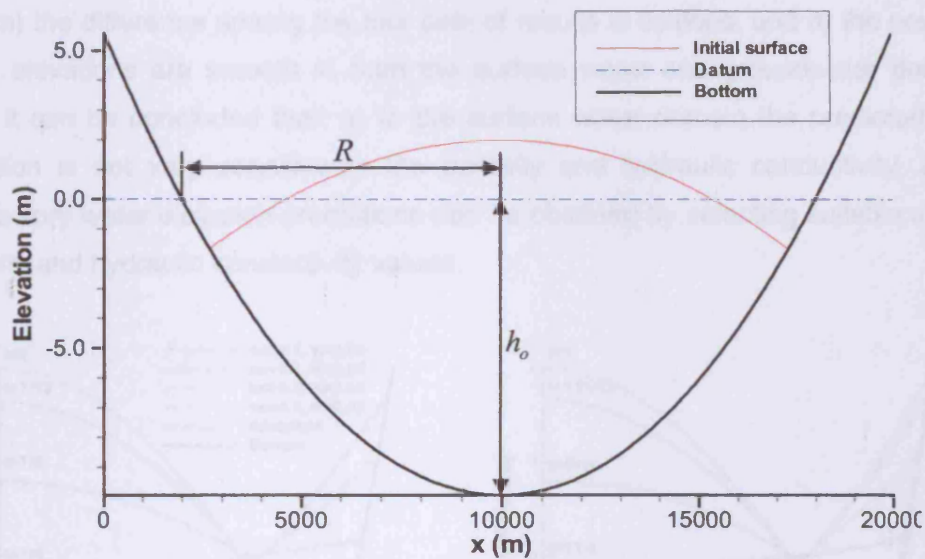


Figure 5-20 Sketch of paraboloidal basin and initial free water surface

5.4.1.2 Results and Discussions

Four numerical simulations, with different porosity and hydraulic conductivity values being listed in Table 5-3, are selected to demonstrate the effect of using artificial porosity and hydraulic conductivity on the model solutions.

Table 5-3 Porosity and hydraulic conductivity in model simulations

Case number	Porosity	Hydraulic conductivity (m/s)
1	0.1	0.01
2	0.1	0.05
3	0.5	0.01
4	0.5	0.05

The predicted water elevations along the x-axis are shown together with the analytical solutions, see Figure 5-21. Since the water elevation is symmetric at any time, only the right half section plans (along x-axis) of the water elevations are

illustrated. Figure 5-22 demonstrates the predicted water elevations near the bottom at $t=5/6T$ and $t=11/12T$. From the two figures it can be seen that: a) the groundwater flow model is used automatically for the four cases listed in Table 5-3, b) the predicted surface water elevations of the four cases are largely the same and all of them agree well with the analytical solutions, c) in the imaginary groundwater domain (i.e. under bottom) the difference among the four sets of results is obvious, and d) the predicted water elevations are smooth in both the surface water and groundwater domains. Thus it can be concluded that: a) in the surface water domain the predicted water elevation is not very sensitive to the porosity and hydraulic conductivity, and b) satisfactory water elevation predictions can be obtained by selecting suitable artificial porosity and hydraulic conductivity values.

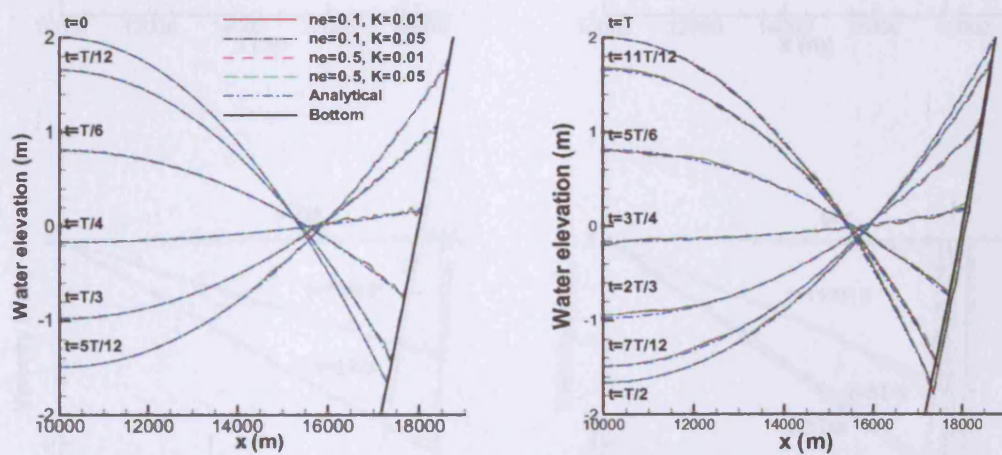


Figure 5-21 Comparison of spatial distribution of water elevations along x-axis for a period with time interval being $T/12$ (T : period)

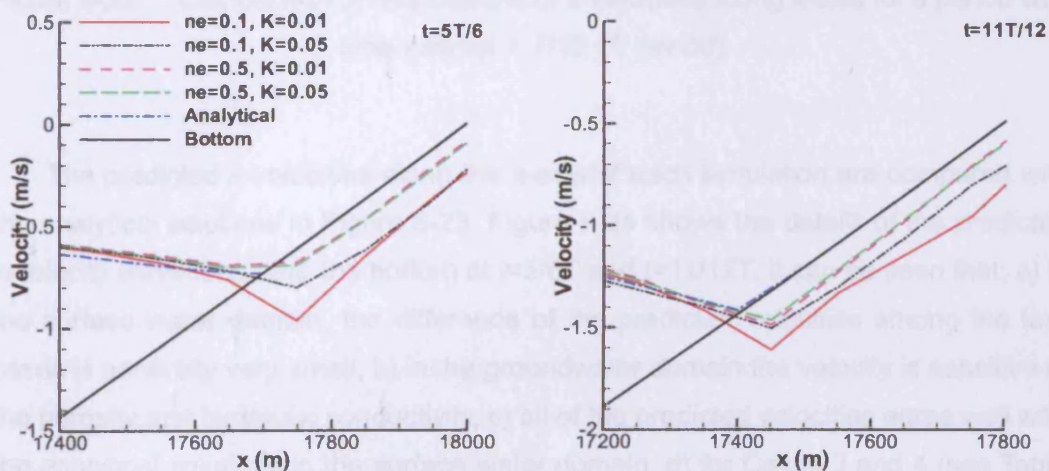


Figure 5-22 Comparison of spatial distributions of water elevations along x-axis for two selected times

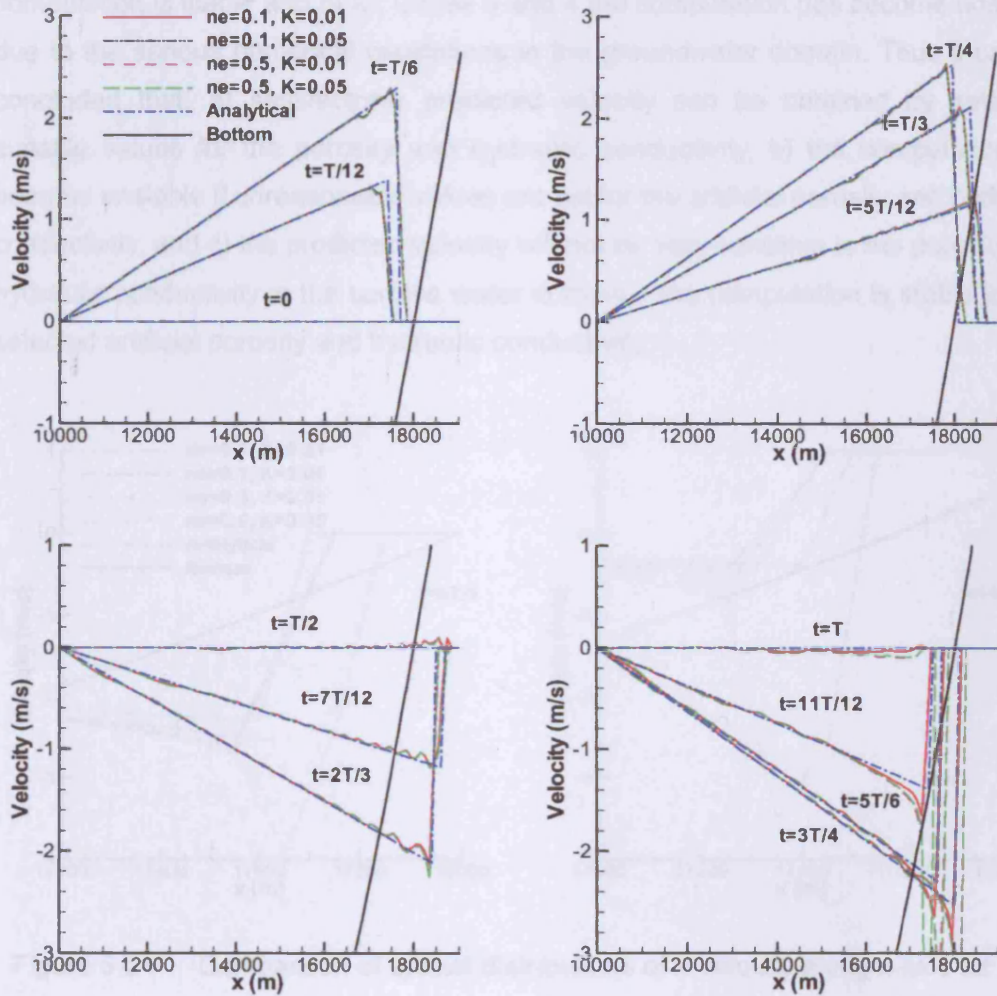


Figure 5-23 Comparison of distributions of x-velocities along x-axis for a period with time interval = $T/12$ (T : period)

The predicted x-velocities along the x-axis of each simulation are compared with the analytical solutions in Figure 5-23. Figure 5-24 shows the details of the predicted x-velocity elevations near the bottom at $t=5/6T$ and $t=11/12T$. It can be seen that: a) in the surface water domain, the difference of the predicted velocities among the four cases is generally very small, b) in the groundwater domain the velocity is sensitive to the porosity and hydraulic conductivity, c) all of the predicted velocities agree well with the analytical solutions in the surface water domain, d) for Cases 3 and 4 (see Table 5-3), serious numerical oscillations occur in the groundwater domain, and e) the

difference between the predicted velocities for Cases 1 and 2 is very small. In addition to the above observations, numerical tests also show that: a) although some small wiggles appear in the results for Cases 1 and 2, they will not be amplified and the computation is stable and b) for Cases 3 and 4 the computation has become unstable due to the serious numerical oscillations in the groundwater domain. Thus it can be concluded that: a) satisfactorily predicted velocity can be obtained by selecting suitable values for the porosity and hydraulic conductivity, b) the computation will become unstable if unreasonable values are set for the artificial porosity and hydraulic conductivity, and c) the predicted velocity will not be very sensitive to the porosity and hydraulic conductivity in the surface water domain if the computation is stable for the selected artificial porosity and hydraulic conductivity.

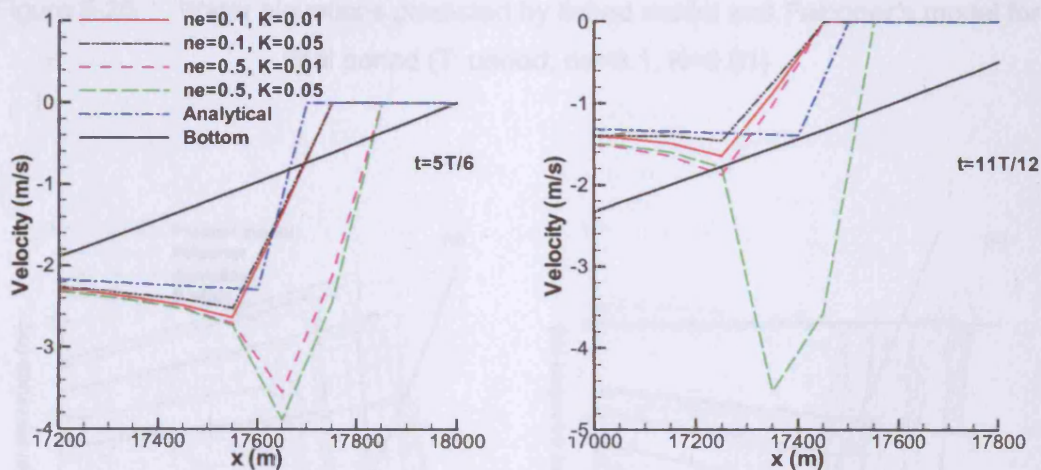


Figure 5-24 Comparison of spatial distributions of x-velocity along x-axis for two selected times

From Figures 5-21, 5-22, 5-23 and 5-24 it can be seen that for this test case, when the artificial porosity and hydraulic conductivity are small enough (Cases 1 and 2 in Table 5-3), both the predicted water elevation and velocity are consistent with the analytical solutions. Thus no substantial problem in the conservation of mass and momentum will be caused.

Figures 5-25 and 5-26 show the spatial distributions of predicted water elevations and x-velocities along the x-axis (Case 1 in Table 5-2) with the corresponding results by using Falconer's (1991) method. It can be seen that the results obtained from the present model are smoother than that obtained from using Falconer's method with

less numerical oscillations being observed.

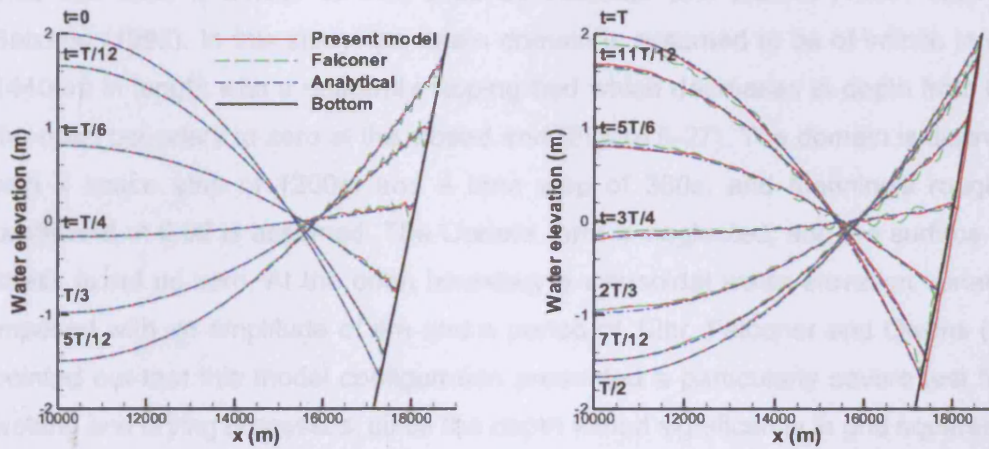


Figure 5-25 Water elevations predicted by linked model and Falconer's model for a tidal period (T : period, $ne=0.1$, $K=0.01$)

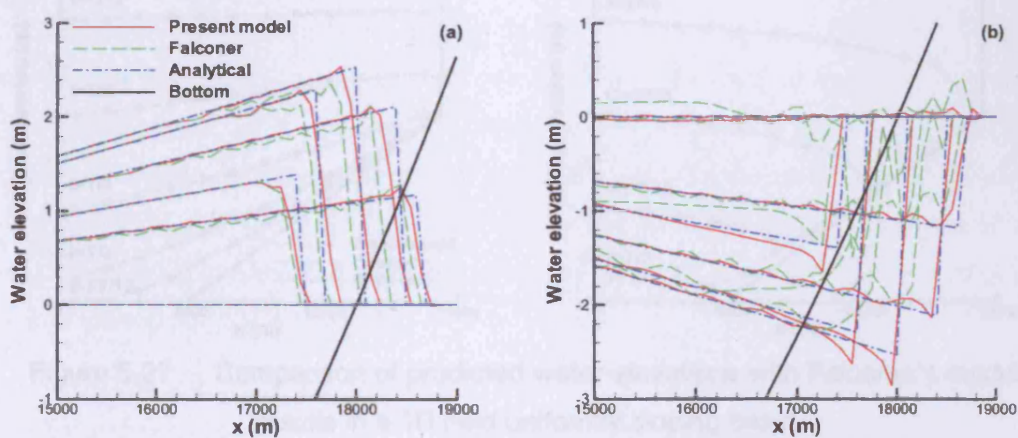


Figure 5-26 x -velocity components predicted by linked model and Falconer's model for (a) $t=0$ to $t=5/12T$ and (b) $t=T/2$ to $t=T$ (T : period)

In this study the threshold used to determine whether a cell dry or wet is 20cm. Numerical tests show that amplitude of numerical oscillations increases when the value of δ decreases. In addition, it should be mentioned that the finite difference scheme and solution procedures used in the present model are the same as those in Falconer's model. Thus, it can be concluded that the difference between the model results is only due to the different methods used for treating moving boundary.

5.4.2 One Dimensional Uniformly Sloping Basin

This test case is similar to that used by Falconer and Owens (1987, 1991) and Balzano (1998). In this study, the basin domain is assumed to be of infinite in width, 14400m in length with a uniformly sloping bed which decreases in depth from 6m at the open boundary to zero at the closed end (Figure 5-27). The domain is discretized with a space step of 1200m and a time step of 360s, and Manning's roughness coefficient of 0.02 is assumed. The Coriolis term is neglected, and the surface shear stress is set as zero. At the open boundary a sinusoidal water elevation variation is imposed with an amplitude of 4m and a period of 12hr. Falconer and Owens (1987) pointed out that this model configuration presented a particularly severe test for the wetting and drying processes, since the depth varied significantly in grid squares, with the bottom elevation step being 0.5m. The porosity and hydraulic conductivity are set as 0.1 and 0.01m/s for the present model. The threshold δ is set as 0.01m.

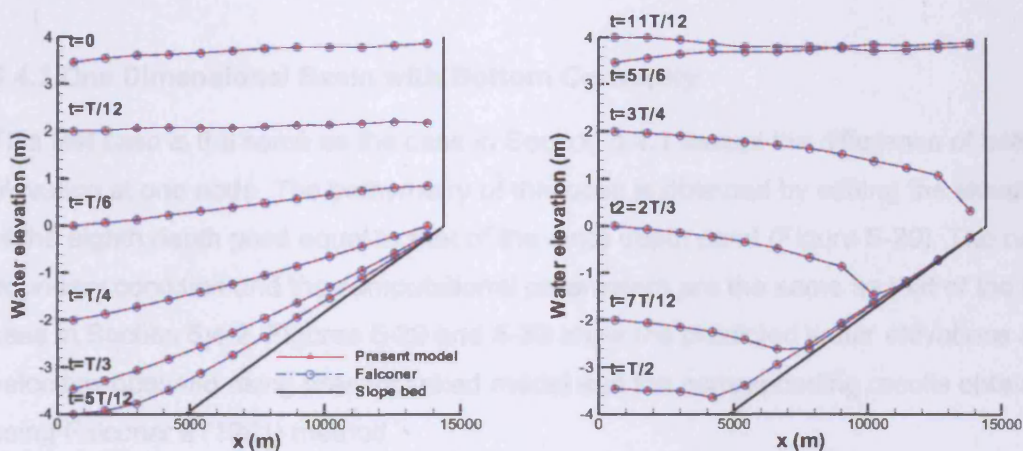


Figure 5-27 Comparison of predicted water elevations with Falconer's model results in a 1D mild uniformly sloping basin

Figures 5-27 and 5-28 compare the predicted water elevations and velocities obtained using the present linked model with those obtained using Falconer's (1991) wetting and drying method. It can be seen from the figures that the model predicted water elevations and velocities are smooth without excessive wiggles being produced by the present wetting and drying model, and the results of the present model are almost the same as that obtained by using Falconer's (1991) wetting and drying method.

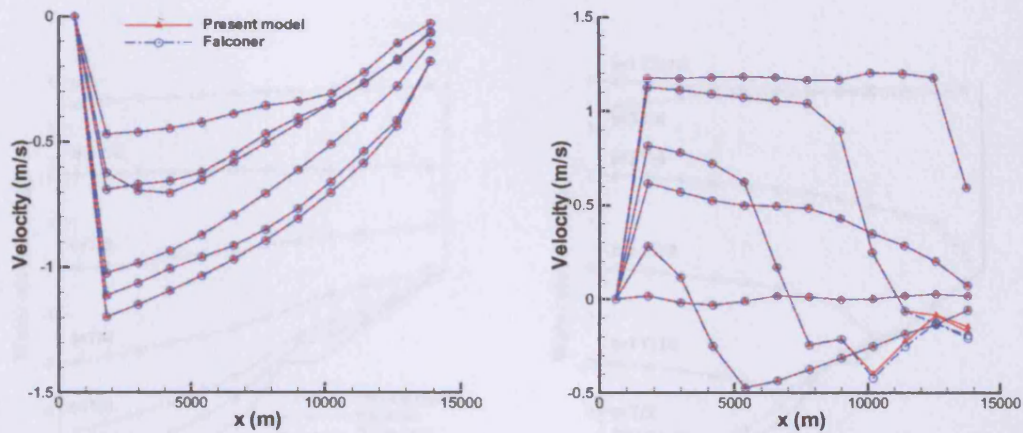


Figure 5-28 Comparison of x-velocities with Falconer's model results in a 1D mild uniformly sloping basin for (a) $t=0$ to $t=5/12T$ and (b) $t=T/2$ to $t=T$ with time interval being $T/12$ (T : period)

5.4.3 One Dimensional Basin with Bottom Convexity

This test case is the same as the case in Section 5.4.1 except the difference of bottom elevation at one node. The bathymetry of this case is obtained by setting the elevation of the eighth depth point equal to that of the ninth depth point (Figure 5-29). The open boundary condition and the computational parameters are the same as that of the test case in Section 5.4.2. Figures 5-29 and 5-30 show the predicted water elevations and velocities obtained using present linked model and the corresponding results obtained using Falconer's (1991) method.

It can be seen that in this test the predicted water elevations and velocities are smooth and without any non-physical oscillation. The predicted water elevations of the present model are almost the same as those by Falconer's (1991). The predicted velocities of the present model are slightly different from that of Falconer's, especially at the time when the free water surface crosses the convexity. Figure 5-31 provides a detailed comparison of the temporal distributions of velocity between the present model and Falconer's model at $x=8400\text{m}$, 9600m , 10800m and 12000m . The predicted velocities of the two models are consistent for most time during a tidal cycle. When the free water surface crosses the convexity (about $t=7T/12$), oscillations appear in the predicted velocities of both model. The results of the present model are slightly smoother than those from Falconer's models.

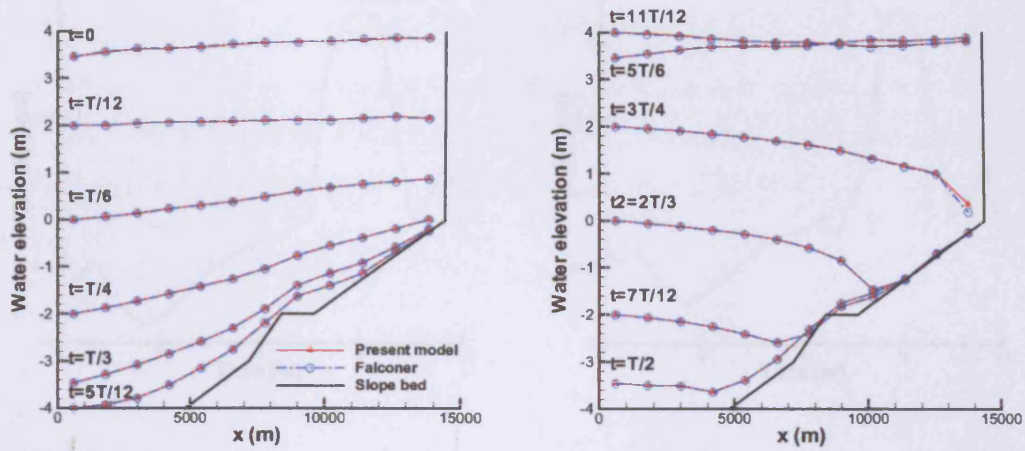


Figure 5-29 Comparison of predicted water elevations with Falconer's model results in a 1D mild uniformly sloping basin with convexity

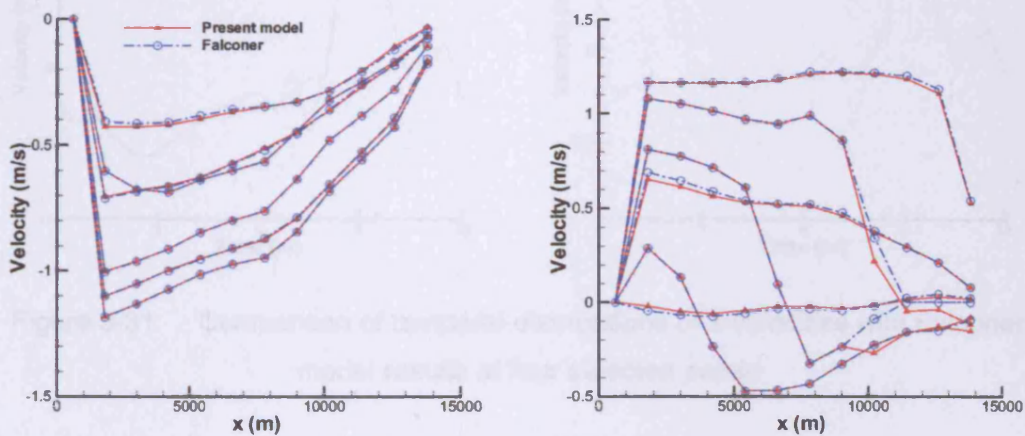


Figure 5-30 Comparison of x-velocities with Falconer's model results in a 1D mild uniformly sloping basin with convexity for (a) $t=0$ to $t=5/12T$ and (b) $t=T/2$ to $t=T$ with time interval being $T/12$ (T : period)

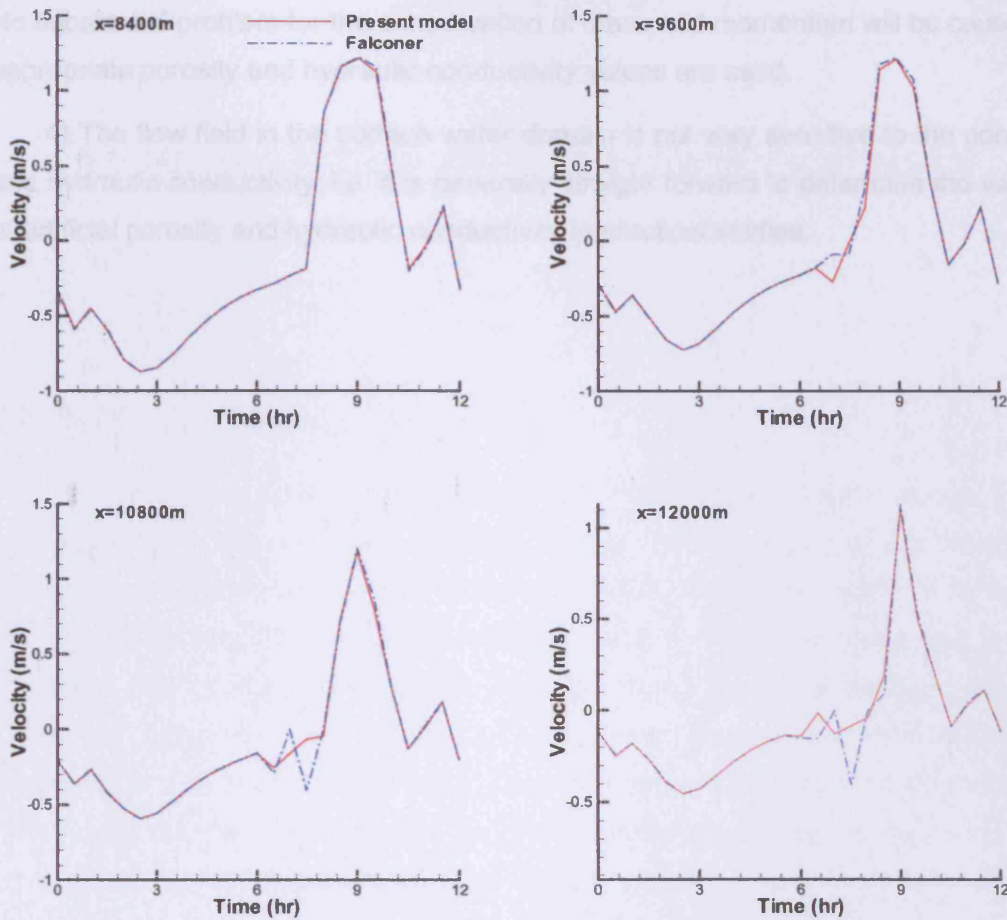


Figure 5-31 Comparison of temporal distributions of x-velocities with Falconer's model results at four selected points

5.5 SUMMARY

In this chapter the numerical model described in Chapters 3 and 4 is systematically verified against analytical solutions and experimental data, with particular attention being paid to checking the capability of this model for treating the moving boundary. The three test cases show that:-

- 1) The linked hydrodynamic model is able to give reliable and accurate results for both surface water and groundwater flows, and the numerical results are stable.
- 2) The solute transport model is capable of predicting accurately the transport and dispersion of solute in surface water flows.
- 3) The dynamically linked surface water and groundwater flow model is able to

treat the moving boundary problem (wetting and drying processes) more effectively. No substantial problem for the conservation of mass and momentum will be caused if appropriate porosity and hydraulic conductivity values are used.

4) The flow field in the surface water domain is not very sensitive to the porosity and hydraulic conductivity, i.e. it is generally straight forward to determine the values of artificial porosity and hydraulic conductivity in practical studies.

CHAPTER 6

RESIDENCE TIME OF THE MERSEY ESTUARY

6.1 INTRODUCTION

The residence time is an important index for evaluating the environmental impact assessment for estuarine and coastal waters. In this chapter the integrated hydrodynamic and solute transport model is applied to study the water exchange of the Mersey Estuary. The numerical model is firstly verified against six sets of field measured data of water elevation and salinity. Then a numerical method based on Takeoka's (1984) concept is established to evaluate the residence time. Finally the residence time of the Mersey Estuary is studied for various scenarios with different tidal ranges and freshwater discharges. The mechanism of how the residence time being affected by the hydrodynamic factors is discussed in detail.

6.2 MODEL CALIBRATION AND VERIFICATION

6.2.1 Description of Study area, Field Survey Data and Computational Parameters

The Mersey Estuary (Figure 6-1) is a macro tidal estuary, with typical spring-neap cycle tidal ranges varying between about 3.5 m (extreme neap) to 10.5 m (extreme spring). Freshwater inflow from the River Mersey into the Mersey Estuary varies from about $5\text{m}^3\text{s}^{-1}$ to $300\text{m}^3\text{s}^{-1}$ (412 ML/d to 29520 ML/d) at the extremes, with typical flows being in the range of 20-40 m^3s^{-1} . The Upper Estuary (upstream of Runcorn) is a narrow meandering channel of about 15 km in length. Below Runcorn, the estuary opens up into a large shallow basin to form the Inner Estuary, of about 20 km in length, with extensive inter-tidal banks and salt marshes on its southern margins. Further downstream of the Inner Estuary, the estuary converges to form the Narrows, a straight narrow channel of up to 30m depth, at low water. Seaward of the Narrows, the

Estuary, is represented horizontally using a mesh of 218×216 uniform grid squares, each with a length of 100m, and with extensive bathymetric data being collected during the most recent bathymetric surveys, conducted by HR Wallingford Ltd and APB in 1997. The locations of the sampling sites are illustrated in Figure 6-1. The data collected at Gladstone are used to specify the seaward open boundary condition, and the freshwater inputs from the River Mersey are used as the upstream open boundary condition. All the model runs start at high water, with the initial velocities being set to zero. The initial salinity across the computational domain is set to the initial salinity at the seaward boundary. A time step of 10s is used in the model runs. The model is run for three tidal cycles before predictions are considered, with the aim being to reduce the effects of the initial conditions.

Table 6-1 Six sets of field data for model calibration

Date	Tide type	Tide range (m)	High water (m)	Flow rate (ML/d)	Case number
18-9-89	Spring	9.36	10.07	1,050	1
21-3-90	Neap	3.27	7.15	2,000	2
28-3-90	Spring	9.79	9.94	1,900	3
13-9-90	Neap	4.29	7.29	570	4
18-3-91	Spring	8.99	9.59	2,760	5
15-7-91	Spring	8.45	9.36	1,070	6

6.2.2 Water Elevations

The main parameter used for calibrating the hydrodynamic model is the Manning's roughness coefficient n . The roughness coefficient is calibrated by trial and error, based on the above six sets of data. Due to the lack of measured velocity data, only water elevation data could be used for model calibration. Different roughness coefficients are assumed in the model domain, with smaller roughness coefficients being used along the upper part of the estuary and with larger roughness coefficients used in the downstream part. This is due to the fact that fine sediments are found in the upper region of the estuary and coarser sediments are measured downstream (Wu et al., 2005). The calibrated roughness coefficients are 0.03 downstream of Eastham, 0.02 between Eastham and Runcorn, and 0.012 upstream of Runcorn. It



should be mentioned that the calibrated roughness coefficient is not only related to the bed form size, but also related to the mesh resolution and its ability to capture the actual bathymetry. The eddy viscosity coefficient C_e in Equation (3-67) is set as 1 according to Falconer et al. (1999).

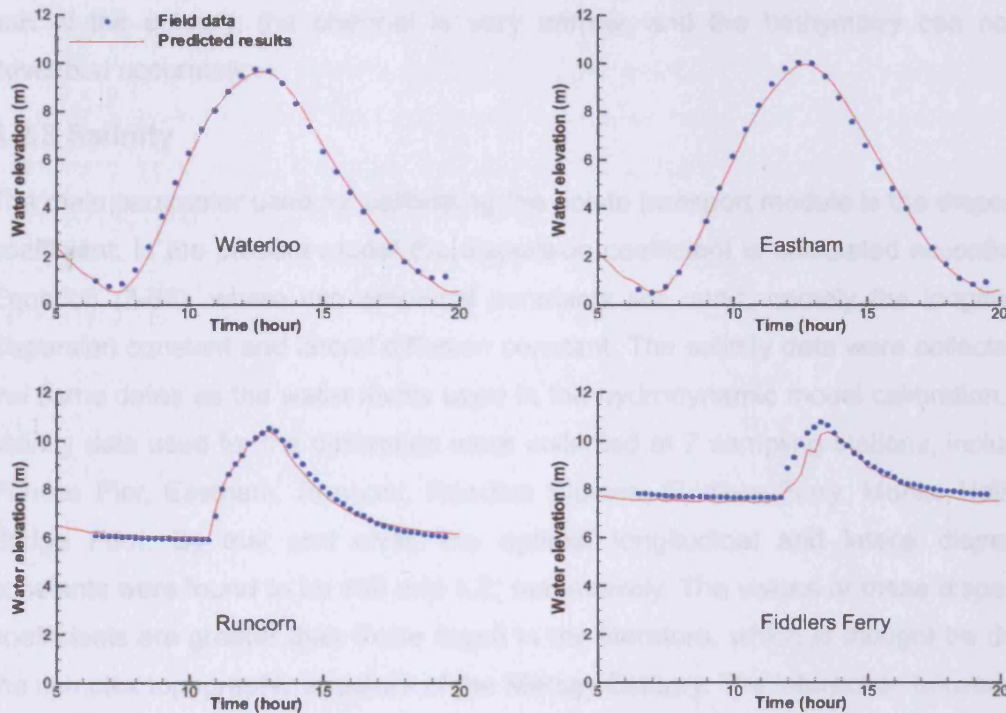


Figure 6-2 Comparison of predicted and measured water elevations on 18 March, 1991

The predicted water elevations are compared for all of the six sets of field data, as listed in Table 6-1. Good agreement is obtained between the model-predicted water levels and the field data at Waterloo and Eastham, with the difference in tidal range generally being less than 20cm (giving a relative error of than 3%). The model predicted water levels agree reasonably well with the observed water levels at Runcorn and Fiddlers Ferry. As an example, Figure 6-2 shows a detailed comparison between the predicted and surveyed water levels at Waterloo, Eastham, Runcorn and Fiddlers Ferry for the sampling event on 18 March, 1991. It can be seen that the predicted results are in good agreement with the field data for all four stations studied, with the level of agreement reduced at the most upstream station, i.e. Fiddlers Ferry. The peak water elevation predicted by the numerical model is about 20cm lower than the field measured value, and there is also a 15 to 20 minute phase difference between the predicted and measured peaks. This discrepancy is possibly caused by:

(a) the cumulative errors associated with increasing sensitivity to the bed roughness coefficients, (b) errors in the bathymetric data. As mentioned previously, the bathymetric data obtained in 1997 are used for the calibration of the sampling event in 1991, with the bathymetry of the Mersey Estuary known to change frequently and especially around Runcorn Gap, and (c) low grid resolution of the bathymetry. As mentioned previously, the grid size used in this study is 100m. While in the upstream part of the estuary, the channel is very narrow, and the bathymetry can not be described accurately.

6.2.3 Salinity

The main parameter used for calibrating the solute transport module is the dispersion coefficient. In the present model the dispersion coefficient is calculated according to Equation (3-86), where two empirical constants are used, namely the longitudinal dispersion constant and lateral diffusion constant. The salinity data were collected on the same dates as the water levels used in the hydrodynamic model calibration. The salinity data used for the calibration were collected at 7 sampling stations, including: Princes Pier, Eastham, Runcorn, Randles Sluices, Fiddlers Ferry, Monks Hall and Bridge Foot. By trial and error, the optimal longitudinal and lateral dispersion constants were found to be 180 and 1.2, respectively. The values of these dispersion coefficients are greater than those found in the literature, which is thought to be due to the complex topographic structure of the Mersey Estuary. The interaction between the flows in the deep channels and those in the shallow areas may lead to strong turbulent mixing.

The predicted salinity levels are also compared with the six sets of field data listed in Table 6-1. The predicted results generally agree well with the field data, with the differences generally being less than 3ppt. Figure 6-3 shows a detailed comparison between the predicted and surveyed salinity at Princes Pier, Eastham, Runcorn and Randles Sluices on 18 March, 1991. It can be seen that the predicted results agree closely with the field data, even to the extent that a small dip in the salinity level at Runcorn at 13.5hr is accurately predicted. According to the numerical model results this drop is not some occasional phenomenon, but the cause of this reduction is due to the strong circulation occurring around Runcorn. Figure 6-4 demonstrates the evolution of the flow current circulation and the salinity distributions at Runcorn. For convenience in highlighting this phenomenon, the starting time is shifted to the time when the flood tide reaches Runcorn (see Figure 6-4(a), at $t = 0$). The sea water from the downstream part flows through Runcorn along the right side of the channel, where

the salinity levels start to increase. As the flow velocity and the concentration of salinity continued to increase, a circulation forms on the left side of the channel (see Figure 6-4(b)). The strength of the circulation reaches a maximum at about $t = 90$ min (see Figure 6-4(c)). After this time the main flow direction starts to change towards the downstream direction, and the circulation area begins to reduce. Before the formation of the circulation cell, most of the sea water flows along the right hand side of the channel, thus causing the salinity levels to be higher along the right, compared with the left channel. When the strength of the circulation cell reaches a certain level it starts to entrain the lower salinity water from the left hand side of the channel to the right hand side. Thus, the concentration of the salinity is reduced when it almost reaches the peak value. As the volume of the water on the left hand side is limited, the reduction in the salinity level only occurred for a short period of time, after which the level starts to increase again until the main flow again changes direction.

Figure 6-3c shows a positive phase difference and Figures 6-3c and 6-3d show an under-prediction of the peak concentration which suggesting longitudinal mixing is marginally over-predicted, hence insufficient transverse mixing or turbulent diffusion.

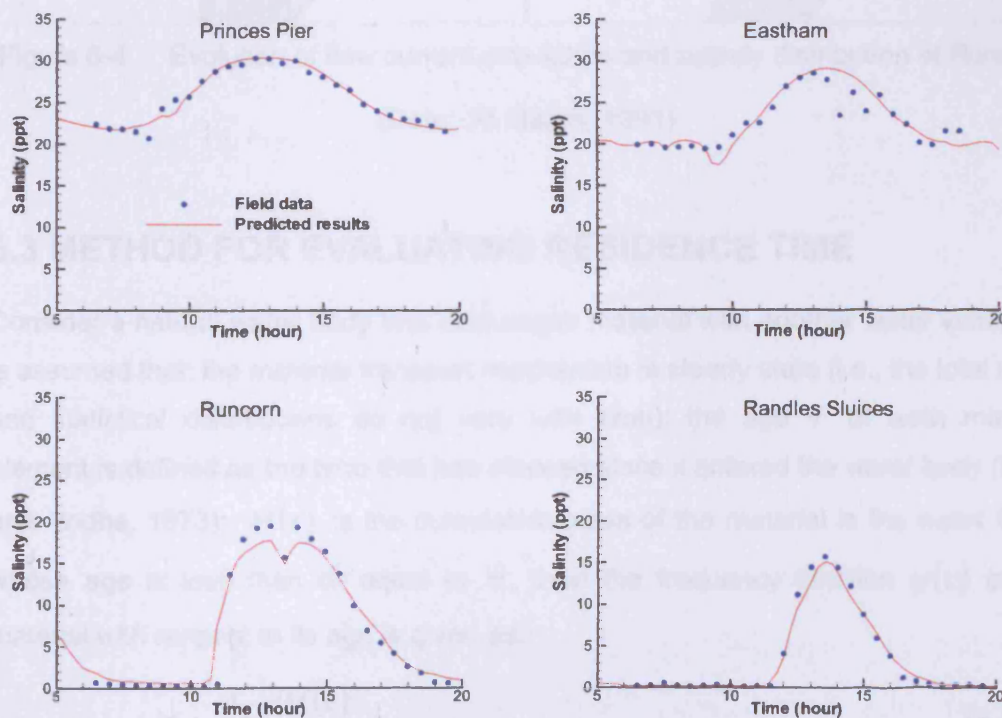


Figure 6-3 Comparison of predicted and measured salinity on 18 March, 1991

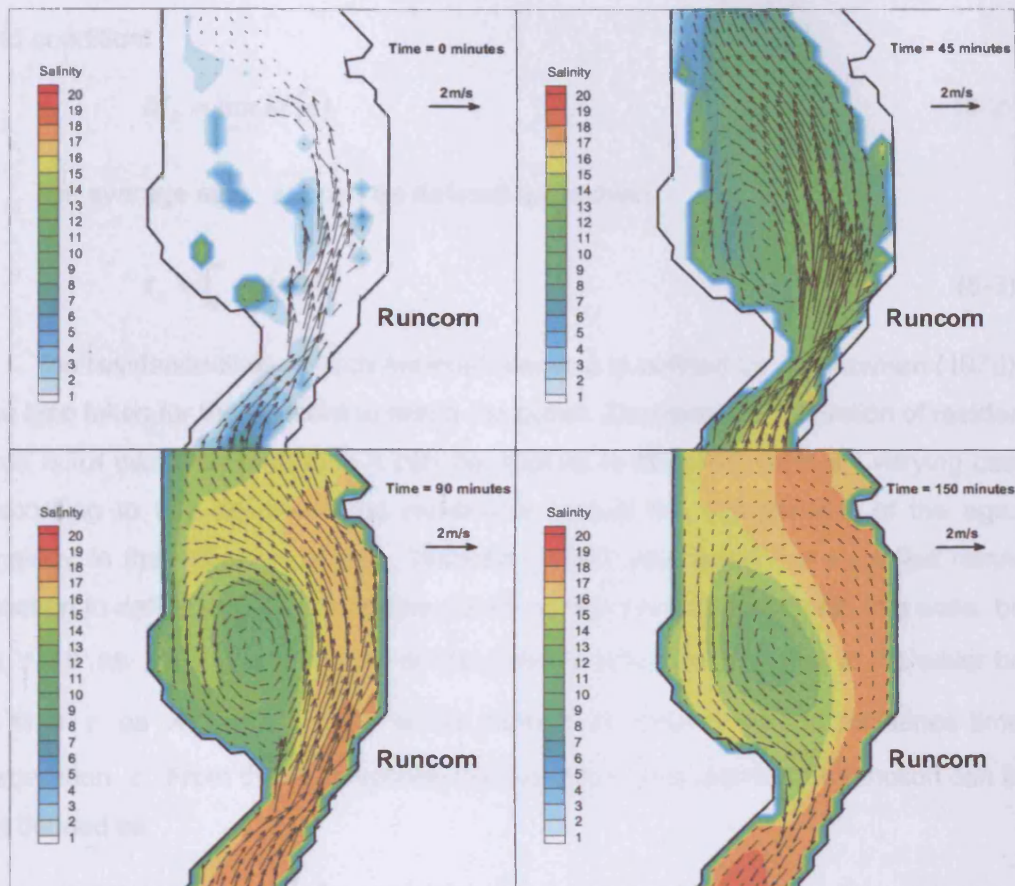


Figure 6-4 Evolution of flow current circulation and salinity distribution at Runcom
(Date: 18 March, 1991)

6.3 METHOD FOR EVALUATING RESIDENCE TIME

Consider a natural water body that exchanges material with another water volume. It is assumed that: the material transport mechanism is steady state (i.e., the total mass and statistical distributions do not vary with time); the age τ of each material element is defined as the time that has elapsed since it entered the water body (Bolin and Rodhe, 1973); $M(\tau)$ is the cumulative mass of the material in the water body, whose age is less than or equal to τ , then the frequency function $\psi(\tau)$ of the material with respect to its age is given as:

$$\psi = \frac{1}{M_0} \frac{dM(\tau)}{d\tau} \quad (6-1)$$

where M_0 is the final amount of the material in the water body, which satisfies the end condition:

$$M_0 = \lim_{\tau \rightarrow \infty} M(\tau) \quad (6-2)$$

The average age, τ_a , can be defined as follows:

$$\tau_a = \int_0^{\infty} \tau \psi(\tau) d\tau \quad (6-3)$$

The residence time of each material element is defined by Zimmerman (1976) as the time taken for the element to reach the outlet. Zimmerman's definition of residence time is for each element, thus it can be applied to deal with spatially varying cases. According to this definition, the residence time is the complement of the age. In analogy to the definition of age, Takeoka (1984) introduced the so called remnant function to define the residence time. Defining the amount of material in a water body at $\tau = 0$ as R_0 and the amount of the material which still remains in the water body at time τ as $R(\tau)$, then $R(\tau)$ is the amount of material whose residence time is larger than τ . From these definitions the residence time distribution function can then be defined as:

$$\phi = -\frac{1}{R_0} \frac{dR(\tau)}{d\tau} \quad (6-4)$$

It can further be assumed that:

$$\lim_{\tau \rightarrow \infty} R(\tau) = 0 \quad (6-5)$$

with the average residence time, τ_r , being defined as:

$$\tau_r = \int_0^{\infty} \tau \phi(\tau) d\tau \quad (6-6)$$

Integrating the above equation by parts gives:

$$\tau_r = \int_0^{\infty} \frac{R(\tau)}{R_0} d\tau = \int_0^{\infty} r(\tau) d\tau \quad (6-7)$$

where $r(\tau) = R(\tau)/R_0$ is called the remnant function (Takeoka, 1984). Since the remnant function is defined for an individual parcel of the material considered, it can be directly applied to calculate the residence time for a pollutant that is discharged into a water body at a particular location and time. The remnant function can be

obtained by integrating temporal model-predicted pollutant concentration distributions over the model domain. The numerical model developed in this study is used to predict the concentration distribution of a passive conservative material in the Mersey estuary. The local residence time is determined according to Equation (6-7) and by initially distributing the tracer over a particular area. If the tracer is distributed over the whole water body in an estuary, then the overall residence time is obtained.

6.4 RESULTS AND DISCUSSIONS

In order to understand the influence of the tidal range and freshwater discharges on the average residence time, 16 model scenario runs are undertaken, based on the 6 sampling data sets listed in Table 6-1. For each data set the model is first run for 2 freshwater discharge conditions: one using the average flow rates measured on the sampling day and the other assuming a zero freshwater discharge at the upstream boundary. For the two cases with the smallest and largest tidal ranges (i.e. on 21-3-90 and 28-3-90 in Table 6-1), further model runs are undertaken with increased freshwater discharges. More details of the cases simulated are listed in Table 6-2. In order to minimise the effect of unknown solute concentrations at the open boundary, the seaward boundary is set at a large distance away from the mouth of the estuary (see Figure 6-1). As the water depth of the expanded area is deeper than the average water depth inside the estuary, the total volume of water in this area is much bigger than that of the estuary. Hence, the tracer concentration of water leaving the estuary is found to be generally small. Therefore the tracer concentration for the in-coming water is assumed to be zero along the open boundary.

The Mersey Estuary is a macro-tidal estuary with the ratio of the tidal prism (i.e. the volume of water that flows into and out of the estuary during a tidal cycle) to the mean volume of water in the whole estuary ranged from 0.35 to 1.06 for the cases considered in this study. It was therefore necessary to check the sensitivity of the model results to the release time of Passive Dissolved Conservative Matter (PDCM). The PDCM is initialised at either high tide or low tide, when the average velocity is a minimum. A constant mass concentration of the tracer material is set over the whole study domain.

In order to evaluate numerically the average residence time using Equation (6-7), the upper limit of infinity in the integration needed to be replaced with an applicable finite value. Thus a criterion is needed to be established to enable the model

simulation to stop after sufficient time elapses.

Table 6-2 Additional cases studied for evaluating average residence time

Date	Tide type	Tide range (m)	High water (m)	Flow rate (ML/d)	Case number
18-9-89	Spring	9.36	10.07	0	1
				1,050	2
21-3-90	Neap	3.27	7.15	0	3
				2,000	4
				4,000	5
				8,000	6
28-3-90	Spring	9.79	9.94	0	7
				1,900	8
				4,000	9
				8,000	10
13-9-90	Neap	4.29	7.29	0	11
				570	12
18-3-91	Spring	8.99	9.59	0	13
				2,760	14
15-7-91	Spring	8.45	9.36	0	15
				1,070	16

6.4.1 Convergence of Calculation

An accumulative average residence time (τ_r^t) is used in the study to determine the convergence criterion, as given by:-

$$\tau_r^t = \int_0^t r(\tau) d\tau \quad (6-8)$$

It is clear that when $t \rightarrow \infty$, Equation (6-8) reduces to Equation (6-7).

For each simulation the model is run until the relative error of the accumulative average residence time (τ_{Err}^n) for the whole estuary is less than τ_{CR} , where τ_{Err}^n is defined as follows:

$$\tau_{Err}^n = \frac{\tau_r^{(n+1)T} - \tau_r^{nT}}{\tau_r^{(n+1)T}} \quad (6-9)$$

where T = period of a tidal cycle. In this study τ_{cr} was set to 0.001.

Thus the Average Residence Time (ARTME) for the whole Mersey Estuary (with the plan area of the whole estuary being defined as the area from Gladstone to Fiddlers Ferry) is evaluated using Equation (6-8) and for all of the cases listed in Table 6-2. The upper limit of infinity is also replaced with the upper limit of $(n + 1)T$.

Figure 6-5 illustrates the temporal distribution of the relative residual PDCM (M_r), the accumulative average residence time (τ_r^t), and the relative change of the accumulative average residence time (τ_{Err}^n) of the Mersey Estuary for Case 8 of Table 6-2, with PDCM being initialised at high water. M_r is defined as follows:

$$M_r = \frac{\int_V S(t) dV}{M_0} \quad (6-10)$$

herein, $S(t)$ is the concentration of the PDCM at time t , V is the volume of the whole estuary, and M_0 is the total mass of the PDCM in the estuary at the release time.

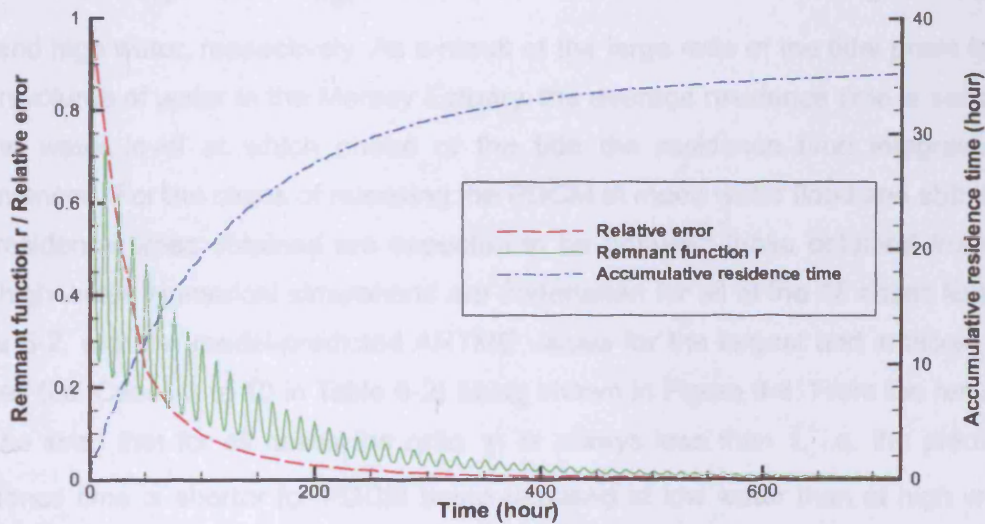


Figure 6-5 Relative residual PDCM, cumulative average residence time and relative error of accumulative average residence time for the Mersey Estuary (Case 8 in Table 6-2, with PDCM initialised at high water)

The result from spatial integration defined by Equation (6-10) is used in the time

integration defined by Equation (6-8) to give the average residence. From Figure 6-5 it can be seen that although the relative residual PDCM (M_r) oscillates during every tidal cycle, the amplitude of M_r decreases rapidly with time. The relative change of the residence time (τ_{Err}^n) decreases monotonously to zero, and the cumulative residence time converges monotonously to the average residence time, as defined by Equation (6-7). Similar convergence patterns are also observed for all of the other test cases, irrespective of whether PDCM is released at high water or low water.

6.4.2 Sensitivity to Initial Condition

In order to analyse the sensitivity of the predicted average residence time to the initial condition, a test is undertaken to compare the ARTME values, obtained for PDCM released at high water, to those released at low water. A new parameter is introduced, gamma, defined as the ratio of the residence time predicted for PDCM being released at low water to that released at high water, i.e.

$$\gamma = \frac{ARTME_{Low}}{ARTME_{High}} \quad (6-11)$$

where $ARTME_{Low}$, $ARTME_{High}$ = ARTME obtained with PDCM being released at low and high water, respectively. As a result of the large ratio of the tidal prism to the mean volume of water in the Mersey Estuary, the average residence time is sensitive to the water level at which phase of the tide the residence time integration is commenced. For the cases of releasing the PDCM at mean water flood and ebb tides, the residence times obtained are expected to be between those obtained from low and high water. Numerical simulations are undertaken for all of the 16 cases listed in Table 6-2, with the model-predicted ARTME values for the largest and smallest tidal ranges (i.e. Cases 3 to 10 in Table 6-2) being shown in Figure 6-6. From the results it can be seen that for all cases the ratio γ is always less than 1, i.e. the predicted residence time is shorter for PDCM being released at low water than at high water. The ratio γ decreases slightly when the freshwater discharge increases, but it decreases significantly when the tidal range was increases. Thus when estimating the residence time the initial water level at which PDCM is released is important, which is particularly true for macro tidal estuaries.

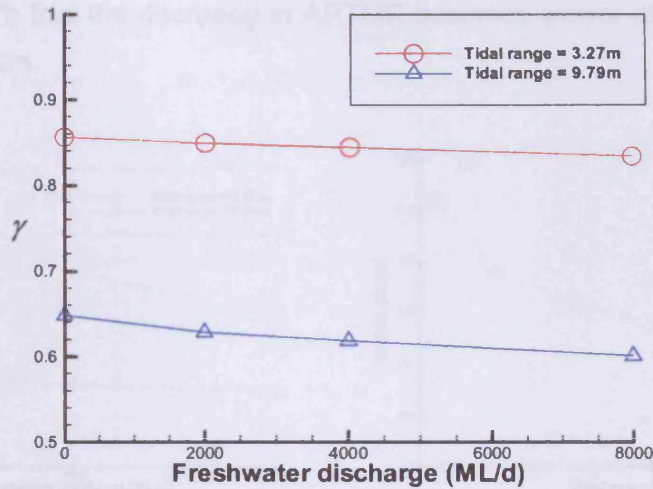


Figure 6-6 Sensitivity of ARTME to release time of PDCM

6.4.3 Effect of Tidal Range and Freshwater Discharge

For all of the cases listed in Table 6-2 (including those with PDCM being released at both high and low water) the model-predicted overall residence time ARTME varies from 17hr to 104hr (i.e. from less than 1 day to about 4 days) and its value varies with both the tidal range and freshwater discharge. In the following discussion results will be shown only for the cases when PDCM is released at high water, with similar observations being found for the cases when PDCM is released at low water.

Figure 6-7a demonstrates the influence of the freshwater discharge on the residence time. It can be seen that for smaller tidal ranges then ARTME decreases significantly as the freshwater discharge increases. Whilst for larger tidal ranges ARTME varies only slightly with the freshwater discharge. Figure 6-7b shows the influence of the tidal range on the residence time. The freshwater discharge is assumed to be zero for the results shown in this figure. It can be seen that ARTME is significantly affected by the tidal range, and it decreases from 104hr to 34hr as the tidal range increases from 3.27m to 9.79m. It is understandable that the residence time decreases as the tidal range increases, as tides are the main forcing function to drive the water flow, with the tidal currents representing the intensity of the water movement. When the tidal range increases from 3.27m to 4.29m, ARTME decreases by 30hr, while it decreases only by 3 hr when the tidal range increases from 8.45m to 9.79m. For the cases where the tidal range is between 9.36m and 9.79m (i.e. Cases 1

and 7 in Table 6-2) the predicted ARTME values are almost the same. It can be seen from Figure 6-7b that the decrease in ARTME becomes slower after the tidal range reaches about 9m.

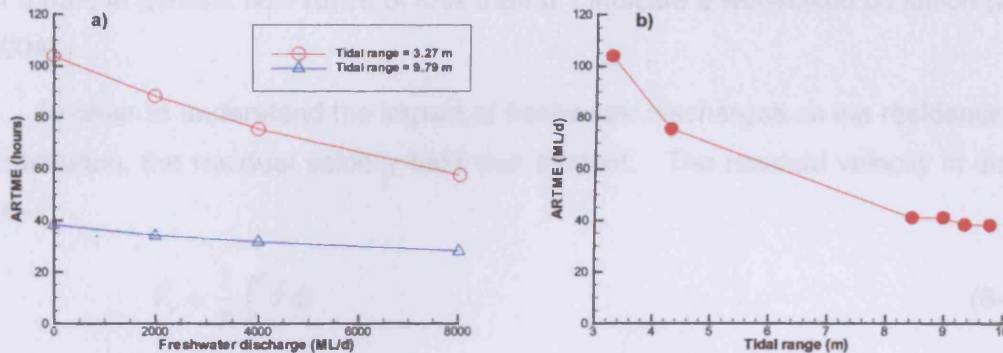


Figure 6-7 a) Relationship between ARTME and freshwater discharge; b) Relationship between ARTME and tidal range for freshwater discharge $Q = 0$

Numerical model experiments are undertaken to estimate the local residence time in the areas around Runcorn and Stanlow (see Figure 6-1) for various tidal and fresh water discharge conditions (i.e. Cases 3, 6, 7 and 13 listed in Table 6-2). For each run the PDCM is distributed only over a small area of the model domain. It is found that if both the tidal range and the freshwater discharge were small (i.e. Case 3), then the PDCM initially released at the upper part of the estuary will remain in the estuary for a considerably longer time period than that released at the lower part of the estuary. For example, if the tracer is released at Runcorn the average residence time could reach up to 450 hours. Whilst if the tracer is released at a location near Stanlow (see Figure 6-1), then the maximum residence time predicted is about 170 hours. If the volume of freshwater discharge is relatively large (i.e. Case 6), then the average residence time decreases significantly in the upper reaches of the estuary. The lower residence time is 150 hours for Case 6. When the tidal range is large (i.e. Cases 7 and 13) and the tidal current reaches the upper part of the estuary. If there is no freshwater discharge, then the average residence times for Runcorn and Stanlow are found to be 240 and 115 hours, respectively.

A mean flow ratio R_f is defined herein to measure the contribution from both tides and fresh water flows, and given as:-

$$R_f = \frac{Q_f}{\Delta V} \quad (6-12)$$

where Q_f = accumulative freshwater discharge over a tidal cycle, and ΔV = total water volume between high and low water levels. For all of the cases investigated in this study the values of R_f are found to be between 0 and 0.055, with a mean value of 0.009. In general flow ratios of less than 0.1 indicate a well-mixed condition (Lane, 2004).

In order to understand the impact of freshwater discharges on the residence time distribution, the residual velocity field was studied. The residual velocity is defined as:-

$$\bar{V}_r = \frac{1}{T} \int_0^T \bar{v} dt \quad (6-13)$$

where T = tidal period, $\bar{V} = (U, V)$, is the depth averaged velocity.

Figure 6-8 illustrates the distribution of the intensity of the residual velocity, given by $|\bar{V}_r|$, for test Cases 3 and 6. It is clear that although the mean flow ratio is small, even for the largest discharge and smallest tidal range (i.e. Case 3 in Table 6-2, $R_f = 0.055$), the residual velocity distribution varies significantly with the discharge in the Upper Estuary. As a large proportion of the upper and inner reaches of the estuary dry out during low tide, the deep channels play an important role in the transport of the tracer material. An increase in the freshwater discharge causes a considerable increase in the intensity of the residual velocity along the deep channels; this in turn results in a reduction in the average residence time. As seen from Figure 6-7a, as the freshwater discharge increases from 0 to 8000 ML/D, the value of ARTME reduces by about 40% for the smaller tidal range. Although it is still hard for the tidal current to reach the upstream limit, the PDCM in the upstream estuary can be washed downstream by the freshwater and then moved out of the estuary. From Figures 6-8a and 6-8b it can be seen that the freshwater flows primarily along the deep channels, with this phenomenon being observed for all other test cases.

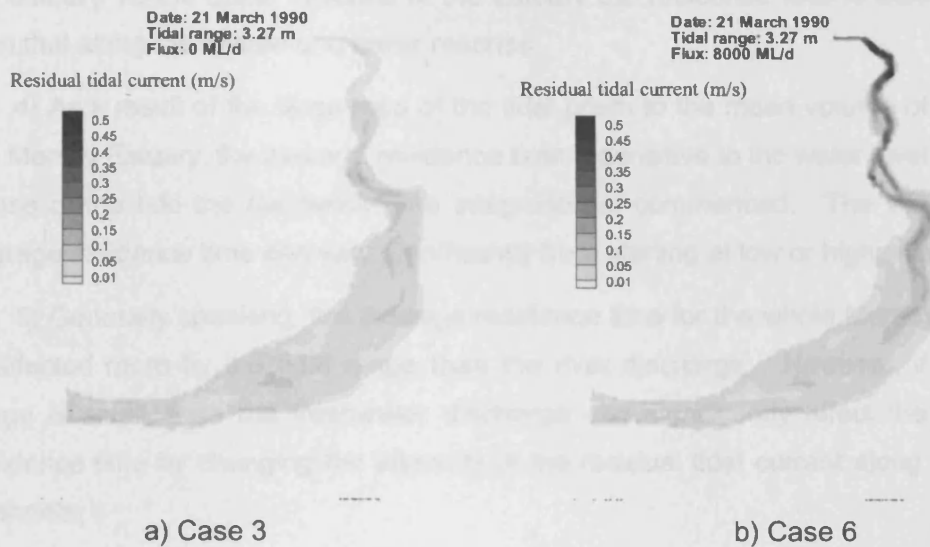


Figure 6-8 Distribution of intensity of residual tidal current

6.5 SUMMARY

In this chapter, details are given of a modelling study to estimate the residence time of a conservative tracer in a macro-tidal estuary, namely the Mersey Estuary, UK. A series of numerical model simulations was undertaken to predict the residence time for various tidal and fresh water flow conditions. Details are given of the setting-up and the calibration of the integrated hydrodynamic-dispersion model. Details are also given of the methodology developed in this study through numerical integration to obtain both the local and overall residence times. The main conclusions drawn from the model predictions can be summarised as follows:

1) Comparison of the predicted water elevations and salinity against the field survey data shows that the integrated hydrodynamic and solute transport model developed in this thesis is able to simulate the hydrodynamic and solute transport processes accurately even for a estuary with complex bathymetry.

2) The average residence time for the whole of the Mersey Estuary is relatively short for a large estuary, ranging from 17hr to 104 hours (i.e. from less than 1 day to about 4 days).

3) Due to the complex bathymetric features of the estuary, the deep channel plays an important role in transporting a conservative tracer material through the estuary. As a result of this impact, the local residence time varies significantly for different parts of

the estuary. At the upper reaches of the estuary the residence time is much longer than that along the middle and lower reaches.

4) As a result of the large ratio of the tidal prism to the mean volume of water in the Mersey Estuary, the average residence time is sensitive to the water level at which phase of the tide the residence time integration is commenced. The value of the average residence time can vary significantly from starting at low or high water.

5) Generally speaking, the average residence time for the whole Mersey Estuary is affected more by the tidal range than the river discharge. However, if the tidal range is small, then the freshwater discharge can significantly affect the average residence time by changing the intensity of the residual tidal current along the main channels.

CHAPTER 7

DEVELOPMENT AND VERIFICATION OF SEDIMENT TRANSPORT MODEL

7.1 INTRODUCTION

Sediment characteristics are morphological and biological important for estuaries and coasts. The movement of sediments can cause deposition to occur in waterways and harbour docks, or erosion of estuarine and coastal banks etc. To deal with these problems, expensive dredging or bank protection operations are generally needed. Contaminated sediments, resulting from industrial and municipal effluents, accidental oil spill etc, could release heavy metals, mineral oils and other toxic contaminants into the water column, which may be adsorbed onto suspended sediments later and then be deposited to the bed. The contaminated bed sediments will be available for re-suspension by strong tidal current, short wave action and dredging operation etc. This adsorption/de-sorption of contaminants to/from their particulate phase can impact significantly on the ecological balance of estuarine and coastal waters. Therefore, the understanding of sediment dynamics in estuarine and coastal waters is of vital importance for the environmental management of estuarine and coastal waters.

In this chapter details are first given of the sediment transport model. Then the model is verified against published experimental data. Finally, the model is verified and calibrated against the measured data from the Mersey Estuary.

7.2 SEDIMENT PROPERTIES

It is necessary to understand the physical properties of the sediments before developing any numerical model for simulating the sediment transport processes. In this section, some basic sediment properties that are closely related to the numerical model used in this study will be introduced, such as density, porosity, angle of repose,

settling velocity, and so on.

7.2.1 Density and Porosity

Density is a basic quantity that is used in modelling porous media, which can be represented in terms of more fundamental parameters as:-

$$\rho_s = \frac{M_s}{V_p} \quad (7-1)$$

where ρ_s = sediment density, M_s = mass of the solid phase in the sediments and V_p = volume of the solid or particulate phase of the sediment. The density of quartz and clay materials approximately equal to 2650 kg/m^3 . The density of carbonate material may be slightly smaller ($\rho_s = 2500$ to 2650 kg/m^3) (van Rijn, 1993). Another parameter related to density is the specific density defined as:-

$$s = \frac{\rho_s}{\rho} \quad (7-2)$$

where ρ = density of water. The density of freshwater and seawater are 1000 kg/m^3 in 4°C and 1025 kg/m^3 , respectively. The specific density of sand is usually set to 2.65 in the literature.

The porosity of sediment (n_e) describes how densely the sediment is packed. It is the proportion of the void (non-solid) volume to the total volume of sediment, and is defined by the ratio:

$$n_e = \frac{V_v}{V} = \frac{1 - V_p}{V} \quad (7-3)$$

where V_v is the non-solid volume (pores and liquid) and V is the total volume of material, including the solid and non-solid parts.

The porosity of sediment material is often related to the deposition history of the sediment bed. Loose packing occurs when sediments settle from suspension in still water. Basically, four packing arrangements are possible for spherical particles. The most unstable arrangement is the cubic arrangement with the sphere centres forming a cube yielding a porosity of 48%. The Rhombohedral arrangement with the spheres in the hollows of each other yields the most stable packing and the smallest porosity of 26%. Random packing of spheres yields porosity ranges from 36% to 40%. Natural

sediments with particles of various sizes have relatively small porosity values because the smaller particles can occupy the large void spaces. A poorly sorted (many sizes) coarse sand has a porosity of about 40%. A well sorted (almost uniform) fine sand has a porosity of about 45%.

7.2.2 Shape

Most of the sand particles on the face of the earth are more or less rounded because their edges and corners are smoothed by abrasion as running water or wind moves the sand particles from their origin to their final resting place. Roundness is a function of abrasion induced by transport and it increases slowly with distance. Thousands of kilometres of transport in a river are required to achieve even moderate rounding. Beaches are ideal places for rounding of sand particles if they stay there for any length of time where sand moves in and out with each wave.

The shape of particles is generally represented by the Corey shape factor, defined as:-

$$S_F = \frac{c}{\sqrt{ab}} \quad (7-4)$$

in which:

a = length along longest axis perpendicular to other two axes

b = length along intermediate axis perpendicular to other two axes

c = length along short axis perpendicular to other two axes

The S_F factor for natural sand is approximately 0.7.

The shape factor is essentially a flatness ratio which does not take into account the distribution of the surface area and the volume of the particle. To overcome this, another shape factor S_F^* is also applied, defined as:-

$$S_F^* = S_F \frac{D_s}{D_n} \quad (7-5)$$

in which D_s is the diameter of a sphere having the same surface area as that of the particle, and D_n is the diameter of a sphere having the same volume as that of the particle. S_F^* approaching unity implies particles close to spherical.

7.2.3 Size

The flux of sediment particles in water can be either in the form of suspended or bed load transport. In any case sediment is fragmental material, primarily formed by the physical and chemical disintegration of rocks from the Earth's crust. Such particles range in size from large boulders to colloidal size fragments and vary in shape from rounded to angular. In engineering sediment is usually referred to as gravel, sand, silt or clay. These terms refer to the size of the sediment particle as being listed in Table 7-1 (van Rijn, 1993).

Table 7-1 Grain size scale defined by American Geophysical Union

Class name	Scale (millimetres)	Class name	Scale (millimetres)
Boulders	>256	Coarse silt	0.062-0.031
Cobbles	256-64	Medium silt	0.031-0.016
Gravel	64-2	Fine silt	0.016-0.008
Very coarse sand	2.0-1.0	Very fine silt	0.008-0.004
Coarse sand	1.0-0.5	Coarse clay	0.004-0.002
Medium sand	0.50-0.25	Medium clay	0.002-0.001
Fine sand	0.250-0.125	Fine clay	0.0010-0.0005
Very fine sand	0.125-0.062	Very fine clay	0.00050-0.00024
		Colloids	<0.00024

Most of the early work was concentrated on steady flow over uniform spherical particles and a number of empirical relationships have been developed, relating sediment flux to fluid flow and sediment particle properties.

With uniform spherical particles it is easy to define sediment size as the diameter. However, when considering natural particles with different shapes this becomes more difficult. The size of a sediment particle is closely related to the analysis method. Typical diameters are:-

Sieve diameter diameter of a sphere equal to the length of the size of a square sieve opening through which the given particle will just pass

Nominal diameter diameter of a sphere that has the same volume of the

particle

Standard fall diameter diameter of a sphere that has a specific gravity of 2.65 and the same fall velocity as the particle in still, distilled water of 24°C (van Rijn, 1993)

When dealing with real sediment consisting of particles with a range of sizes, a representative diameter must be chosen. Often the median diameter (D_{50}) is used (where the subscript denotes the percentage by weight of sediment finer than that diameter).

7.2.4 Angle of Repose

The angle of repose (ϕ) is an engineering property of granular materials. When bulk granular materials are poured onto a horizontal surface, a conical pile will form. The angle between the edge of the pile and the horizontal surface is known as the angle of natural repose (ϕ_n). This parameter appears to be a function of size, shape and porosity. The angle increases with decreasing roundness. Values of the angle of natural repose from the literature are in the range of 30° to 40°. The angle of repose (ϕ) also referred to as the angle of internal friction is a characteristic angle related to the stability of a particle on a horizontal or sloping bed. The angle of ϕ may differ from the angle of natural repose (ϕ_n).

Usually the angle of repose is determined from initiation of motion experiments for horizontal and sloping beds. The critical bed-shear stress for a particle on a sloping bed can be expressed as follows:-

$$\tau_{b,cr} = \tau_{b,cr}^0 \frac{\sin(\phi - \beta)}{\sin \phi} \quad (7-6)$$

where $\tau_{b,cr}$ is the critical bed-shear stress on a sloping bottom, $\tau_{b,cr}^0$ is the critical bed-shear stress on a horizontal bottom, and β is the angle of the bottom slope. For a given β value, the values of $\tau_{b,cr}$ and $\tau_{b,cr}^0$ can be determined from the measurement. Thus Equation (7-6) can be used to calculate the value of the angle of repose (ϕ).

7.2.5 Flocculation

Sediment mixtures with a fraction of clay particles larger than about 10% have cohesive properties because electro-static forces comparable to or higher than the gravity forces are acting between the particles. Consequently, the sediment particles do not behave as individual particles but tend to stick together forming aggregates known as flocs whose size and settling velocity are much larger than those of the individual particles.

7.2.6 Settling Velocity

The settling velocity (or fall velocity, or terminal velocity) of sand grains in water is determined by their diameter and density, and the viscosity of the water. At the finest end of the sand range of diameters ($D = 62\mu m$), grains settle according to Stokes' law of viscous drag; at the coarsest end ($D = 2mm$) they obey a quadratic bluff-body drag law; and intermediate sizes experience a mixture of viscous and bluff-body drag. Terminal settling velocity (w_s) can be obtained when the hydrodynamic forces are counterbalanced by the gravitational forces giving as:-

$$\underbrace{\frac{1}{2}(C_D \rho w_s^2) \cdot \frac{1}{4} \pi D^2}_{\text{Hydrodynamic force}} = \underbrace{\frac{\pi}{6} (\rho_s - \rho) g D^3}_{\text{Gravitational force}} \quad (7-7)$$

Hence,

$$w_s = \sqrt{\frac{4(s-1)gD}{3C_D}} \quad (7-8)$$

where C_D = a drag coefficient, D = sphere diameter.

The drag on natural sand grains is difficult to calculate with analytical formula due to their irregular shape. Thus C_D is usually determined by experiment. There are a number of formulae for calculating the settling velocity w_s of isolated sand grains in still water, in which the formula of van Rijn (1984a) for natural sand is now widely accepted, given as follows:-

$$\begin{cases} w_s = \frac{vD_*^3}{18D} & D_* \leq 16.187 \\ w_s = \frac{10v}{D} \left[(1 + 0.01D_*^3)^{0.5} - 1 \right] & 16.187 < D_* \leq 16187 \\ w_s = \frac{1.1vD_*^{1.5}}{D} & D_* > 16187 \end{cases} \quad (7-9)$$

herein D_* is the dimensionless grain size defined as:-

$$D_* = \left[\frac{(s-1)g}{\nu^2} \right]^{1/3} D \quad (7-10)$$

where, D = sieve diameter of grains, s = specific density, ν = kinematic viscosity of water, and g = acceleration due to gravity.

Soulsby (1997) derived the following formula for natural sands, based on optimizing two coefficients in a combined viscous plus bluff-body drag law against data from irregular grains:-

$$w_s = \frac{\nu}{D} \left[\left(10.36^2 + 1.049 D_*^3 \right)^{1/2} - 10.36 \right] \quad \text{for all } D_* \quad (7-11)$$

A comparison of the prediction of settling velocity as given by the above two formulae (Equation (7-9) and (7-11)) and other two formulae (Gibbs et al., 1971 and Hallermeier, 1981) has been carried out by Soulsby (1997) against a large data set comprising 115 measurements of settling velocities of natural sands and irregular shaped light-weight grains. The data were collated and tabulated by Hallermeier (1981). Table 7-2 shows the percentage of predictions lying within 10% or 20% of the observations.

Table 7-2 Comparison of prediction of settling velocity

Formula	10%	20%
Gibbs et al., 1971	35	50
Hallermeier, 1981	60	89
Van Rijn, 1984	59	90
Soulsby, 1997	66	90

According to Soulsby (1997) Equation (7-11) gives the best result, and is also the simplest. This good agreement may partly because the coefficients were optimised for the test data set. The Hallermeier and van Rijn formulae are also as good, but are more complicated. The poor performance of the Gibbs formula is because it is intended for spheres, not natural grains.

At high concentrations the flows around adjacent settling grains interact to give a larger drag than for the same grain in isolation (hindered settling). This causes the hindered settling velocity w_{sm} at high concentration to be smaller than that at low concentration. According to Richardson and Zaki (1954), the settling velocity in a

fluid-sediment suspension can be evaluated as:-

$$w_{sm} = (1 - c)^\gamma w_s \quad (7-12)$$

where, w_{sm} is the particle settling velocity in a suspension, w_s is the particle settling velocity in a clear fluid, c is volumetric sediment concentration, and γ is a coefficient.

For particles in the range of $50\mu m$ to $500\mu m$ under normal flow conditions the value of the γ -coefficient is about 4 to 5 (van Rijn, 1993).

Oliver (1961) gives another formula which reads as:-

$$w_{sm} = (1 - 2.15c)(1 - 0.75c^{0.33})w_s \quad (7-13)$$

This formula yields good results over the full range of concentration.

Soulsby (1997) yields the following formula for the settling velocity w_{sm} of grains in a dense suspension having volumetric concentration c :-

$$w_{sm} = \frac{v}{d} \left\{ \left[10.36^2 + 1.049(1 - c)^{4.7} D_*^3 \right]^{1/2} - 10.36 \right\} \quad \text{for all } D_* \text{ and } c \quad (7-14)$$

For small values of D_* , Equation (7-14) shows that the ratio $w_{sm}/w_s = (1 - c)^{4.7}$, whereas for large values of D_* , Equation (7-14) gives $w_{sm}/w_s = (1 - c)^{2.35}$. In practice, the effect of hindered settling need only be taken into account for volumetric concentrations larger than 0.05, which usually occur only within a few millimetres of the bed, since the difference between w_s and w_{sm} is less than 20% for smaller concentrations.

7.3 INITIATION OF MOTION AND SUSPENSION

7.3.1 Initiation of Motion

Particle movement starts when the instantaneous fluid force on a particle is just larger than the instantaneous resisting force related to the submerged particle weight and the friction coefficient. Early work on the initiation of motion was done by Brahms (1753), who proposed a sixth power relationship between the flow velocity and the required weight of a stone to be stable. Dubuat (1786) introduced the concept of

critical bed-shear stress (see van Rijn, 1993).

Shields (1936) proposed a relationship for the initiation of motion, which is now widely accepted, between two dimensionless parameters, namely the shear Reynold's number R_e^* , and the mobility parameter (θ), defined as follows:-

$$R_e^* = \frac{u_* D}{\nu} \quad (7-15)$$

$$\theta = \frac{u_*^2}{(s-1)gd} = \frac{\tau_b}{(\rho_s - \rho)gd} \quad (7-16)$$

where D = characteristic particle diameter. Usually, the median particle diameter (D_{50}) is used as the characteristic particle diameter.

Although Shields' curve is widely used in the sediment transport formulae it suffers from the disadvantage that the bed-shear velocity (u_*) is included in both dimensionless parameters. Bonnefille (1963, see van Rijn, 1993) and Yalin (1972) showed that the Shields' curve can be expressed in terms of a dimensionless mobility parameter (θ) and a dimensionless particle parameter (D_*). Thus the critical Shields' parameter can be represented as:-

$$\begin{cases} \theta_{cr} = 0.24(D_*)^{-1} & D_* \leq 4 \\ \theta_{cr} = 0.14(D_*)^{-0.64} & 4 < D_* \leq 10 \\ \theta_{cr} = 0.04(D_*)^{-0.10} & 10 < D_* \leq 20 \\ \theta_{cr} = 0.013(D_*)^{0.29} & 20 < D_* \leq 150 \\ \theta_{cr} = 0.055 & D_* > 150 \end{cases} \quad (7-17)$$

where the dimensionless particle parameter D_* is calculated with Equation (7-10) with $D = D_{50}$.

7.3.2 Initiation of Suspension

Bagnold (1966) stated that a particle only remained in suspension when the turbulent eddies had dominant vertical velocity components which exceed the settling velocity (w_s). Assuming that the vertical velocity component of the eddy (w') is represented by the vertical turbulence intensity ($|w'|$), the critical value for initiation of suspension can be expressed as:-

$$|w'| = \sqrt{(w')^2} \geq w_s \quad (7-18)$$

Detailed studies on turbulence phenomena in boundary layer flow (Hinze, 1975) suggest that the maximum value of the vertical turbulence intensity is of the same order as the bed-shear velocity (u_*). Using these values, the critical bed-shear velocity ($u_{*,cr}$) for initiation of suspension becomes:-

$$\frac{u_{*,cr}}{w_s} = 1 \quad (7-19)$$

which can be expressed as (van Rijn, 1984b):-

$$\theta_{cr} = \frac{u_{*,cr}^2}{(s-1)gD_{50}} = \frac{w_s^2}{(s-1)gD_{50}} \quad (7-20)$$

Van Rijn (1984b) reviewed some results of experimental research at the Delft Hydraulics Laboratory and determined the critical flow conditions at which instantaneous upward turbulent motions of the sediment particles (bursts) with jump lengths of the order of 100 particle diameters were observed. According to the experimental results, the initiation condition of suspension is given as (van Rijn, 1984b):-

$$\left\{ \begin{array}{l} \frac{u_{*,cr}}{w_s} = \frac{4}{D_*}, \quad \text{for } 1 < D_* \leq 10 \\ \frac{u_{*,cr}}{w_s} = 0.4, \quad \text{for } D_* > 10 \end{array} \right. \quad (7-21)$$

7.4 GOVERNING EQUATIONS FOR SEDIMENT TRANSPORT PROCESSES

7.4.1 Bed Load Transport

Although the main purpose of this thesis is to develop a suspended sediment transport model, it is necessary to introduce the concept and formulations for bed load transport first, as the suspended sediment model is closely related to the bed load model.

Basically, the bed load transport rate can be defined as the product of particle

concentration, particle velocity and bed layer thickness, i.e.:-

$$q_b = c_b u_b \delta_b \quad (7-22)$$

where q_b = volumetric bed-load transport rate, c_b = volumetric concentration, u_b = particle velocity, and δ_b = thickness of bed load layer.

The thickness of bed load layer (δ_b) is defined as the saltation height of the bed particles. Van Rijn (1993) found that the saltation height was related to a dimensionless bed-shear stress parameter (or the transport stage parameter) T and a dimensionless particle parameter D_* (Equation (7-10)), given as follows:-

$$\frac{\delta_b}{D} = 0.3 D_*^{0.7} T^{0.5} \quad (7-23)$$

in which D = sieve diameter of grains.

The dimensionless bed-shear stress parameter T represents the strength of the flow and is expressed as:-

$$T = \frac{(u'_*)^2 - u_{*cr}^2}{u_{*cr}^2} \quad (7-24)$$

where the critical bed shear velocity u_{*cr} can be calculated from Shields' diagram:-

$$u_{*cr} = \sqrt{\theta_{cr}(s-1)gD_{50}} \quad (7-25)$$

with θ_{cr} being calculated with Equation (7-20), and the effective bed-shear velocity u'_* is calculated as follows:-

$$u'_* = \frac{\sqrt{g|V|}}{C'} \quad (7-26)$$

where $|V| = \sqrt{U^2 + V^2}$, and C' is the Chezy coefficient related to the grain size, given as:-

$$C' = 18 \log_{10} \left(\frac{4h}{D_{90}} \right) \quad (7-27)$$

where h = water depth and D_{90} = sediment diameter for which 90% of the bed material is finer.

Through analysing the force balance consisting of the drag force, the gravitational force and the friction force, the particle velocity can be expressed as follows:-

$$u_b = u_* \left[\alpha_1 - \alpha_2 \left(\frac{\theta_{cr} \sin(\phi - \beta)}{\theta \sin \phi} \right)^{0.5} \right] \quad (7-28)$$

in which, α_1 and α_2 are coefficients, ϕ is the angle of repose, and β is the angle of local bottom slope. The term $\sin(\phi - \beta)/\sin \phi$ represents the bottom slope effect on the particle velocity. The bed shear velocity u_* should be replaced with the effective bed-shear velocity u'_* in case of bed forms.

Based on Equation (7-28) and data fitting, van Rijn (1984a) summarised the following formula for calculating particle velocity:-

$$u_b = u_* \left[9 + 2.6 \log D_* - 8 \left(\frac{\theta_{cr}}{\theta} \right)^{0.5} \right] \quad (7-29)$$

The computed particle velocities by using Equation (7-29) appear too high for large particles ($D_* > 15$). Through analyzing the computed results, van Rijn (1984a) induced the following expression:-

$$u_b = 1.5T^{0.6} [(s-1)gD]^{0.5} \quad (7-30)$$

Compared to Equation (7-29), Equation (7-30) yields smaller values for large particles.

Using Equations (7-22), (7-23) and (7-29) (or (7-30)), the bed load concentration (c_b) can be calculated from the measured bed-load transport rate. Analyzing the computed results based on the 130 series of flume experimental data, van Rijn (1984a) expressed the bed-load concentration as follows:-

$$c_b = 0.18c_o \frac{T}{D_*} \quad (7-31)$$

where $c_o = 0.65$ is the maximum volumetric concentration.

Substituting Equations (7-23), (7-30) and (7-31) into Equation (7-22) gives the formulation for calculating bed load transport as follows (van Rijn's, 1984a):-

$$q_b = \frac{0.053T^{2.1}[g(s-1)]^{0.5}D_{50}^{1.5}}{D_*^{0.3}} \quad 0 < T < 3 \quad (7-32)$$

Equation (7-33) was found to over-predict (factor 2) the transport rate for $T \geq 3$. Therefore, a modified expression is proposed for this range as follows (van Rijn, 1993):-

$$q_b = \frac{0.1T^{1.5}[g(s-1)]^{0.5}D_{50}^{1.5}}{D_*^{0.3}} \quad T \geq 3 \quad (7-33)$$

7.4.2 Suspended Load Transport

Most sediment transport formulae for prescribing suspended sediment flux predictions in a two-dimensional numerical model are based on the numerical solution of the depth-integrated advective-diffusion equation (3-85), rewritten in the following form:-

$$\begin{aligned} \frac{\partial(SH)}{\partial t} + \frac{\partial(pS)}{\partial x} + \frac{\partial(qS)}{\partial y} - \frac{\partial}{\partial x} \left(HD_{xx} \frac{\partial S}{\partial x} + HD_{xy} \frac{\partial S}{\partial y} \right) \\ - \frac{\partial}{\partial y} \left(HD_{yx} \frac{\partial S}{\partial x} + HD_{yy} \frac{\partial S}{\partial y} \right) = E \end{aligned} \quad (7-34)$$

where S = depth-averaged suspended sediment concentration in mass, and the source/sink term E = net erosion or deposition per unit area of the bed.

The source/sink term E represents the exchange of sediment between the water column and the bed. The mass exchange due to the motion of suspended sediment consists of two parts: a) sediment settling, and b) diffusion. Therefore the source/sink term E can be expressed as follows:-

$$E = \varepsilon_s \frac{\partial s_b}{\partial z} - w_s s_b \quad (7-35)$$

where s_b is the concentration near the bed, and ε_s is the mixing coefficient of sediment which will be discussed later.

The boundary condition at the bed is assumed to follow Equation (7-36):-

$$\varepsilon_s \frac{\partial s_b}{\partial z} = w_s s_{eb} \quad (7-36)$$

Substituting Equation (7-36) into Equation (7-35) yields:-

$$E = w_s (s_{eb} - s_b) \quad (7-37)$$

It is clear that $s_{eb} = s_b$ represents the equilibrium status. Thus s_{eb} is the equilibrium sediment concentration near the bed.

In order to relate the concentration near the bed to the depth-averaged concentration, the following assumption can be adopted (see Li et al, 2001):-

$$s_{eb} = \gamma_1 S_e \quad \text{and} \quad s_b = \gamma_2 S \quad (7-38)$$

where S_e is the depth-averaged equilibrium concentration. Then Equation (7-37) can be modified as follows:-

$$E = w_s (\gamma_1 S_e - \gamma_2 S) \quad (7-39)$$

where γ_1 and γ_2 are termed profile parameters.

It can be seen from Equation (7-39) that there are two key points for complementing the suspended sediment transport model: a) how to determine the depth-averaged equilibrium sediment concentration, and b) how to determine the profile parameters. Both will be discussed in details in the following text.

It is widely accepted that turbulence is the main reason for the suspension of sediment. Assuming the time-averaged upward and downward transport rates are equal (i.e. in the equilibrium case), the following relationship between the time averaged variables and instantaneous variables can be derived:-

$$c w_s - c' w' = 0 \quad (7-40)$$

where c is the time averaged concentration of sediment, w_s is the sediment settling velocity, c' and w' are the fluctuated sediment concentration and vertical velocity respectively.

Adopting the diffusion model (i.e. the law of Fick), the vertical transport of sediment by turbulence ($c'w'$) is proportional to the vertical concentration gradient (dc/dz), given as follows:-

$$c'w' = -\varepsilon_s \frac{dc}{dz} \quad (7-41)$$

where the proportional coefficient (ε_s) is called the diffusion or mixing coefficient of sediment, which is mainly due to turbulence.

Usually, the diffusion or mixing coefficient of sediment (ε_s) is related to the mixing

coefficient in a clear fluid (ε) as follows:-

$$\varepsilon_s = \beta\phi\varepsilon \quad (7-42)$$

where β and ϕ are two factors.

Various distributions of the fluid mixing coefficient (ε) can be found in the literature, among which the most widely used are constant distribution, linear distribution, parabolic distribution and parabolic-constant distribution. The parabolic distribution is most satisfactory in a physical sense because it is based on linear shear stress distribution and a logarithmic velocity profile, which can be expressed as follows:-

$$\varepsilon = \kappa u_* H \frac{z}{H} \left(1 - \frac{z}{H}\right) \quad (7-43)$$

where κ is Von Karmann constant, z is vertical coordinate, H is the water depth, and u_* is the bed-shear velocity. The corresponding logarithmic velocity distribution is:-

$$u = \frac{u_*}{\kappa} \ln \left(\frac{z}{z_o} \right) \quad (7-44)$$

where $z_o = 0.033k_s$ is the zero-velocity level, and k_s is the equivalent or effective roughness height of Nikuradse.

However, the parabolic distribution yields a zero concentration at the water surface, which is not consistent with the experimental and field measured data. Based on the measured concentration profiles, Coleman (1970) suggested a parabolic-constant distribution, given as follows:-

$$\begin{cases} \varepsilon = \kappa u_* H \frac{z}{H} \left(1 - \frac{z}{H}\right) & \text{for } \frac{z}{H} < 0.5 \\ \varepsilon = 0.25 \kappa u_* H & \text{for } \frac{z}{H} \geq 0.5 \end{cases} \quad (7-45)$$

The β factor describes the difference between the diffusion of a fluid "particle" (or small coherent fluid structure) and a discrete sediment particle. Carsten (1952) concluded that $\beta < 1$ as the sediment particles cannot fully respond to the turbulent velocity fluctuations, which were assumed to be one-dimensional. Singamsetti (1966) found $\beta > 1$ for two-dimensional eddy motion because the presence of centrifugal

forces acting on the particles causes the particles to be thrown to the outside of the eddies which resulting in an increase of the effective mixing length. Through analyzing Coleman's (1970) experimental results, Van Rijn (1984b) induced the following formula:-

$$\beta = 1 + 2 \left(\frac{w_s}{u_*} \right)^2 \quad \text{for } 0.1 < \frac{w_s}{u_*} < 1 \quad (7-46)$$

Van Rijn (1993) suggested that it is better to keep the value of β being smaller than 2 as the mechanics of the physical processes involved is not very clear.

The ϕ factor represents the influence of the sediment particles on the turbulence structure of the fluid. This effect is extremely important in the flows with high sediment concentrations ($S > 10 \text{ kg/m}^3$) because this results in stratification and hence damping of turbulence. While in the flow with low sediment concentration, it is reasonable to set ϕ as one.

Substituting Equation (7-40) into (7-41) gives:-

$$c w_s = -\varepsilon_s \frac{dc}{dz} \quad (7-47)$$

Expressions for the sediment concentration profiles can be obtained by integration of Equation (7-47) with relevant expressions for the mixing coefficient. Assuming the concentration is low (i.e. $\phi = 1$), integration of Equation (7-47) with the parabolic distribution of mixing coefficient (Equation (7-43)) yields:-

$$\frac{c}{c_a} = \left(\frac{H-z}{z} \frac{a}{H-a} \right)^Z \quad (7-48)$$

where c_a is the reference sediment concentration at a small distance (a) above the bed, and the parameter $Z = w_s / \beta \kappa u_*$ is termed the suspension number. Adopting parabolic-constant distribution of mixing coefficient (Equation (7-45)) in the integration gives:-

$$\begin{cases} \frac{c}{c_a} = \left(\frac{H-z}{z} \frac{a}{H-a} \right)^Z & \text{for } \frac{z}{H} < 0.5 \\ \frac{c}{c_a} = \left(\frac{a}{H-a} \right)^Z e^{-4Z \left(\frac{z}{H} - 0.5 \right)} & \text{for } \frac{z}{H} \geq 0.5 \end{cases} \quad (7-49)$$

The most logical assumption for the reference level ($z = a$) of the sediment profile is the upper edge of the bed load layer ($z = \delta_b$). Thus the reference concentration is defined to equal to the bed load concentration, given as follows:-

$$c_a = c_b \quad \text{at } z = a = \delta_b \quad (7-50)$$

where c_b can be calculated using Equation (7-31). In case of bed forms Van Rijn (1984b) proposed the following effective reference concentration:-

$$c_a = 0.015 \frac{D_{50}}{a} \frac{T^{1.5}}{D_*^{0.3}} \quad (7-51)$$

The depth-integrated suspended load transport rate is defined as follows:-

$$q_s = \int_a^H ucdz \quad (7-52)$$

In order to relate q_s to the depth-averaged variables, Equation (7-52) can be rearranged as follows:-

$$q_s = c_a UHF \quad (7-53)$$

where U is the depth-averaged velocity, and

$$F = \frac{1}{H} \int_a^H \frac{u}{U} \frac{c}{c_a} dz \quad (7-54)$$

Assuming the velocity distribution is logarithmic (Equation (7-44)) and the distribution of the mixing coefficient is parabolic-constant (Equation (7-45)), integration of Equation (7-54) can give the expression of the F factor. However, the analytical solution of this integration cannot be obtained, thus an approximate solution is given as follows (van Rijn, 1984b):-

$$F = \frac{\left(\frac{a}{H}\right)^Z - \left(\frac{a}{H}\right)^{1.2}}{\left(1 - \frac{a}{H}\right)^Z (1.2 - Z)} \quad (7-55)$$

In order to take the stratification effects in high concentration suspensions into account, van Rijn (1984b) suggested that the suspension number Z should be modified as follows:-

$$Z' = Z + \psi \quad (7-56)$$

where

$$\psi = 2.5 \left(\frac{w_s}{u_*} \right)^{0.8} \left(\frac{c_a}{c_o} \right)^{0.4} \quad \text{for} \quad 0.01 \leq \frac{w_s}{u_*} \leq 1 \quad (7-57)$$

The ψ parameter represents the turbulence damping effect and the hindered settling effect.

The mean volumetric concentration \bar{c} is defined as follows:-

$$\bar{c} = \frac{q_s}{q} \quad (7-58)$$

For fine sediment the mean concentration (\bar{c}) approximately equal to the depth averaged concentration (C). Therefore the depth-averaged equilibrium sediment concentration (S_e) in Equation (7-39) can be expressed as follows:-

$$S_e = \rho_s \frac{q_s}{q} = \rho_s \frac{c_a UHF}{q} \quad (7-59)$$

Considering $q = UH$, Equation (7-59) can be rewritten as follows:-

$$S_e = \rho_s c_a F \quad (7-60)$$

The profile parameter γ_1 in Equation (7-39) can be determined by the ratio of the bed concentration s_{eb} to depth-averaged concentration S_e by integrating the vertical distribution of the concentration (Equation (7-48) or (7-49)). The profile parameter γ_2 in Equation (7-39) is basically calibrated using the measured data since there is not a common analytical expression for the vertical distribution of the sediment concentration under non-equilibrium condition. In practice it is better to keep both γ_1 and γ_2 as adjustable parameters because there is not a theory which is very accurate for practice due to the complexity of sediment transport. Furthermore, according to Equations (7-38) and (7-60), if c_a is considered as the equilibrium volumetric concentration near the bed, then the first estimation of the value of γ_1 can be expressed as follows:-

$$\gamma_1 = 1/F \quad (7-61)$$

Some authors (e.g. Owen (1987)) assumed that $\gamma_1 \approx \gamma_2 = \gamma$, then Equation (7-39)

can be simplified as follows:-

$$E = \gamma w_s (S_e - S) \quad (7-62)$$

The profile parameter γ_1 is basically greater than one because the concentration near the bed (s_{eb}) is usually greater than the depth-averaged concentration S_e under equilibrium (saturated) condition. Assuming the hydrodynamic condition is fixed, the near-bed concentration does not vary significantly as the depth-averaged sediment concentration varies. Therefore γ_2 may be greater than, equal to or less than unity. Thus it is only reasonable to assume $\gamma_1 \approx \gamma_2$ when the suspended sediment concentration is close to the saturated value.

Equation (7-39) can be rewritten as follows:-

$$E = \gamma w_s (S_e - \alpha S) \quad (7-63)$$

where $\gamma = \gamma_1$, and $\alpha = \gamma_2 / \gamma_1$. It is obvious that α may be greater than, equal to or less than unity when the suspension is under-saturated, saturated or over-saturated, respectively.

According to Equations (7-37) and (7-38), the source/sink item can also be expressed as follows:-

$$E = w_s (s_{eb} - \gamma_2 S) \quad (7-64)$$

in which:

$$s_{eb} = \rho_s c_a \quad (7-65)$$

where the volumetric concentration (c_a) can be calculated using Equation (7-51).

Compared to Equation (7-63), the source/sink term expressed with Equation (7-64) looks simpler and more accurate in theory. While Equation (7-63) is used more widely in the depth-averaged models for the following reasons: a) the depth-averaged concentrations are consistent with the model; b) The using of the two adjustable parameters in Equation (7-63) is better for practice due to the mechanics of the sediment transport has not been known clearly. In this thesis, Equation (7-63) is adopted in the model for its flexibility.

Summing up the depth-integrated suspended load flux (i.e. obtained from the product of S – calculated from Equation (7-34) – and Q from the depth-integrated

velocity field) and the depth-integrated bed load flux (i.e. obtained from Equation (7-32) or (7-33)), gives the total sediment flux across the computational domain.

7.4.3 Cohesive Sediment Transport

During the past decades considerable effort has been made to study the mechanisms of the cohesive sediment transport, and many experimental and field studies have been carried out to investigate the deposition and erosion rates for the cohesive sediments (e.g. Krone, 1962, Parchure and Metha, 1985, Lick et al., 1995).

In modelling cohesive sediment transport the governing depth-integrated advective-diffusion equation (7-34) is used, but with the net erosion term E (on the right hand side of equation (7-34)) being rewritten in the following form:

$$E = \begin{cases} q_{dep} & \text{when } \tau_b \leq \tau_d \\ 0 & \text{when } \tau_d < \tau_b < \tau_e \\ q_{ero} & \text{when } \tau_b \geq \tau_e \end{cases} \quad (7-66)$$

where q_{dep} , q_{ero} = the deposition and erosion rates respectively, τ_b = bed shear stress, τ_d = critical shear stress for deposition, and τ_e = critical shear stress for erosion.

The widely used deposition rate proposed by Krone (1962) is adopted in this study, giving:-

$$\text{Deposition: } q_{dep} = w_s S \left(\frac{\tau_b}{\tau_d} - 1 \right) \quad (7-67)$$

Likewise, the erosion rate from bed given by Partheniades (1965) is used:-

$$\text{Erosion: } q_{ero} = M \left(\frac{\tau_b}{\tau_e} - 1 \right) \quad (7-68)$$

where, M = empirical erosion constant.

Most of the parameters included in the above formulations are much depend upon the sediment characteristics locally and the values must be chosen with extreme care. Typical values of the critical shear stress for erosion and deposition are given in van Rijn (1993) for a range of different mud types. For the empirical coefficient (M),

reported values are typically in the range of $(10^{-5}$ to $5 \times 10^{-4})$ for soft natural mud.

7.5 BED EVOLUTION

7.5.1 Depth Integrated Mass Balance Equation

Depth integrated mass balance equation due to sediment transport can be derived using a control volume in the water body from the bed to the water surface and applying the general form of the mass conservation law:-

$$\frac{\partial z_b}{\partial t} + \frac{1}{1-n_e} \left(\frac{\partial HS}{\partial t} + \frac{\partial q_x}{\partial x} + \frac{\partial q_y}{\partial y} \right) = 0 \quad (7-69)$$

where z_b = bed level (see Figure 7-1), n_e = porosity of the sediment material, q_x and q_y = total sediment load transport rates per unit width in the x and y -directions respectively. The storage term (the first term in the parenthesis) in this equation can be neglected if a quasi-steady flow condition is assumed (van Rijn, 1987). Therefore Equation (7-69) becomes:-

$$\frac{\partial z_b}{\partial t} + \frac{1}{1-n_e} \left(\frac{\partial q_x}{\partial x} + \frac{\partial q_y}{\partial y} \right) = 0 \quad (7-70)$$

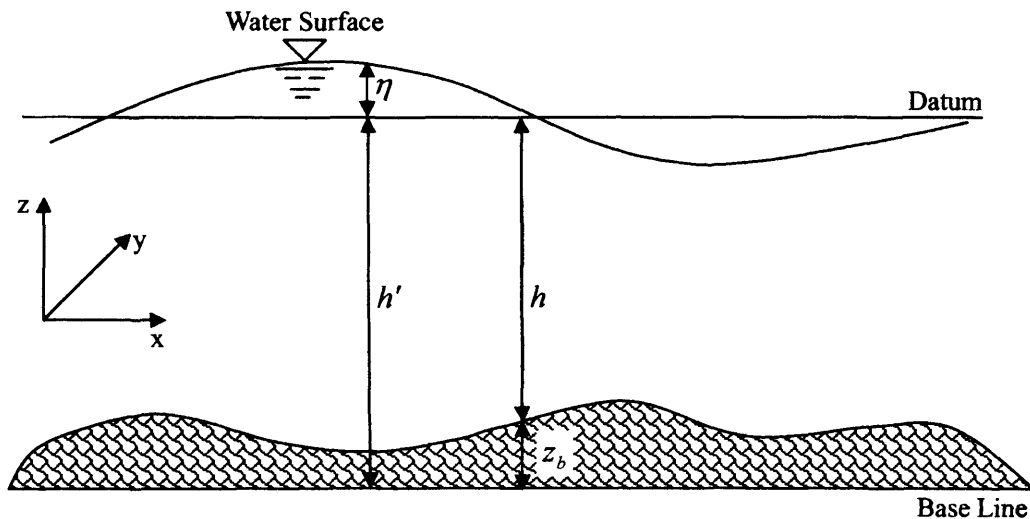


Figure 7-1 Schematic illustration of variables referred in depth integrated mass balance equation

Bed level changes can be defined in terms of mean water depth (h = the distance between the bed and the datum) using the following geometrical relationship (see Figure 7-1):-

$$\frac{\partial z_b}{\partial t} = \frac{\partial(h' - h)}{\partial t} = \frac{\partial h'}{\partial t} - \frac{\partial h}{\partial t} \quad (7-71)$$

and

$$\frac{\partial h'}{\partial t} = 0 \quad (7-72)$$

Substitution of Equations (7-71) and (7-72) into (7-70) gives:-

$$-\frac{\partial h}{\partial t} + \frac{1}{1 - n_e} \left(\frac{\partial q_x}{\partial x} + \frac{\partial q_y}{\partial y} \right) = 0 \quad (7-73)$$

7.5.2 Numerical Algorithm

The depth integrated bed evolution equation (Equation (7-73)) can be discretized using a control volume shown in Figure 7-2, in which the bed level is specified in the centre of a grid. The equation is discretized in a fully centred manner for both space and time terms resulting for the first part in the following form:-

$$-\frac{\partial h}{\partial t} = -\frac{h_{i,j}^{n+1} - h_{i,j}^n}{\Delta t} \quad (7-74a)$$

The second part of Equation (7-73) indicates the variation of the total transport rate per unit width by time along the x - and y -directions in the control volume, as shown in Figure 7-2. This term can be discretized in the x -direction as follows:-

$$\frac{\partial q_x}{\partial x} = \frac{q_{x(i+1/2,j)}^n - q_{x(i-1/2,j)}^n}{\Delta x} \quad (7-74b)$$

and in the y -direction:-

$$\frac{\partial q_y}{\partial y} = \frac{q_{y(i,j+1/2)}^n - q_{y(i,j-1/2)}^n}{\Delta y} \quad (7-741c)$$

The final form of the bed level changes can be written in an explicit form as follows:-

$$h_{i,j}^{n+1} = h_{i,j}^n + \frac{1}{1 - n_e} \left(\frac{q_{x(i+1/2,j)}^n - q_{x(i-1/2,j)}^n}{\Delta x} + \frac{q_{y(i,j+1/2)}^n - q_{y(i,j-1/2)}^n}{\Delta y} \right) \Delta t \quad (7-75)$$

where $q_{x(i+1/2,j)}^n$, $q_{x(i-1/2,j)}^n$, $q_{y(i,j+1/2)}^n$ and $q_{y(i,j-1/2)}^n$ are calculated by averaging their neighbour cells' values:-

$$q_{x(i+1/2,j)}^n = \frac{q_{x(i,j)}^n + q_{x(i+1,j)}^n}{2} \quad (7-76a)$$

$$q_{x(i-1/2,j)}^n = \frac{q_{x(i,j)}^n + q_{x(i-1,j)}^n}{2} \quad (7-76b)$$

$$q_{y(i,j+1/2)}^n = \frac{q_{y(i,j)}^n + q_{y(i,j+1)}^n}{2} \quad (7-76c)$$

$$q_{y(i,j-1/2)}^n = \frac{q_{y(i,j)}^n + q_{y(i,j-1)}^n}{2} \quad (7-76d)$$

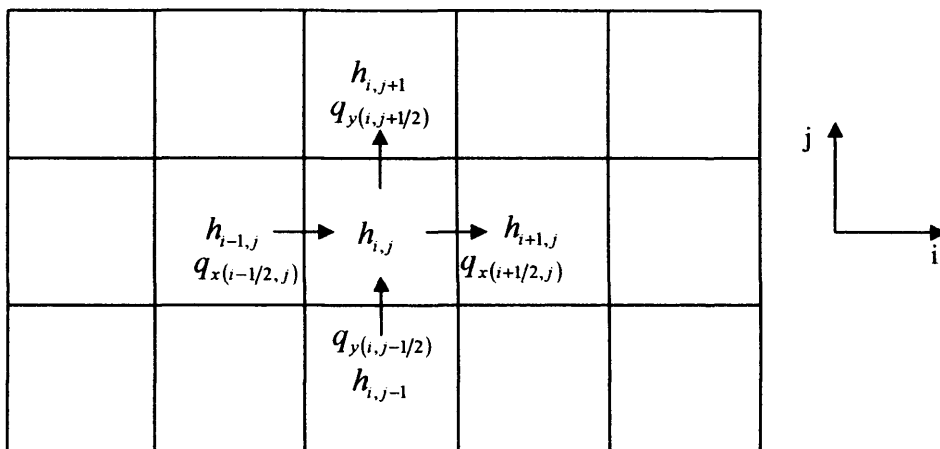


Figure 7-2 A control volume for discretization of sediment mass balance

7.6 MODEL VERIFICATION AGAINST EXPERIMENTAL DATA

In this section three typical test cases with published experimental data are selected to show the verification of the sediment transport model. It is not sufficient to verify the model only against the experimental data from these experiments, because: a) the distribution of the sediment size used in the experiments is limit. b) The hydrodynamic conditions being set in the experiments are limit, and c) the scales of the experimental domains are small compared to real estuaries and coastal waters. However, it should be mentioned that the sediment transport model used in this study has developed by van Rijn (1984a, b) and verified by using various experimental and measured data.

The verification carried out in this section is not used to check the sediment model itself, and the purpose of the verification is to check whether the sediment sub-model is complemented correctly in the integrated model developed in this study.

7.6.1 Sediment Transport over a Porous Bed

This case study is reported by Wang and Ribberink (1986). A steady sediment laden flow is allowed to pass over a porous bed consisting of perforated plates. Deposition can occur, as sediment falls through the perforation, but no re-suspension is possible. The experiment is carried out in a straight flume, with a length of 30m, and width and depth of 0.5 m (Figure 7-3). The flow is uniform, with a water depth of 0.216 m, a longitudinal slope of 9.7×10^{-4} and a discharge of $0.0601 \text{ m}^3/\text{s}$. Sediment is supplied at a rate of 70.8 kg/hr dry weight, above the water surface at the upstream end of the inflow section, and the transport rate is kept below the transport capacity of the flow. The median sediment diameter D_{50} is $100 \mu\text{m}$, with a ratio D_{84}/D_{16} of 1.46.

Wang and Ribberink (1986) pointed out that in this case the sediment flux near the bottom equalled $-w_s s_b$ because re-suspension hardly occurred. Therefore the source/sink item is less than zero and Equation (7-63) or (7-64) can be simplified as follows:-

$$E = -\gamma w_s \alpha S = -\gamma_2 w_s S \quad (7-77)$$

The bed evolution is not taken into account in this case study because the bottom is perforated and rigid and the transport rate is kept below the transport capacity of the flow.

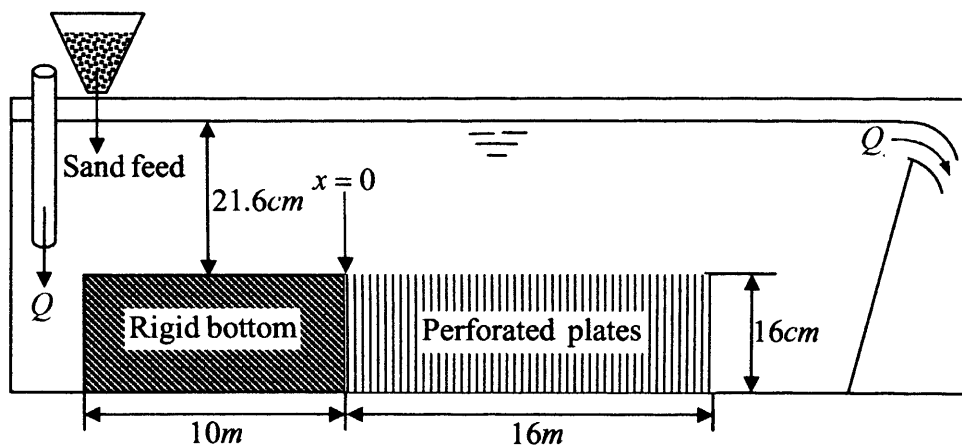


Figure 7-3 Schematic illustration of Wang and Ribberink's (1986) experiment

The value of the profile factor γ_2 is determined as 3.6 in this study by trial and error. The predicted suspended sediment concentrations are compared to the measured data and the second order asymptotic solution (Wang and Ribberink, 1986) in Figure 7-4. It can be seen that the numerical solution agrees almost perfectly with the asymptotic solution and agrees well with the measured data. Wang and Ribberink (1986) pointed out that the experimental errors were possibly the main reason for the measured data being systematically lower than the asymptotic solutions.

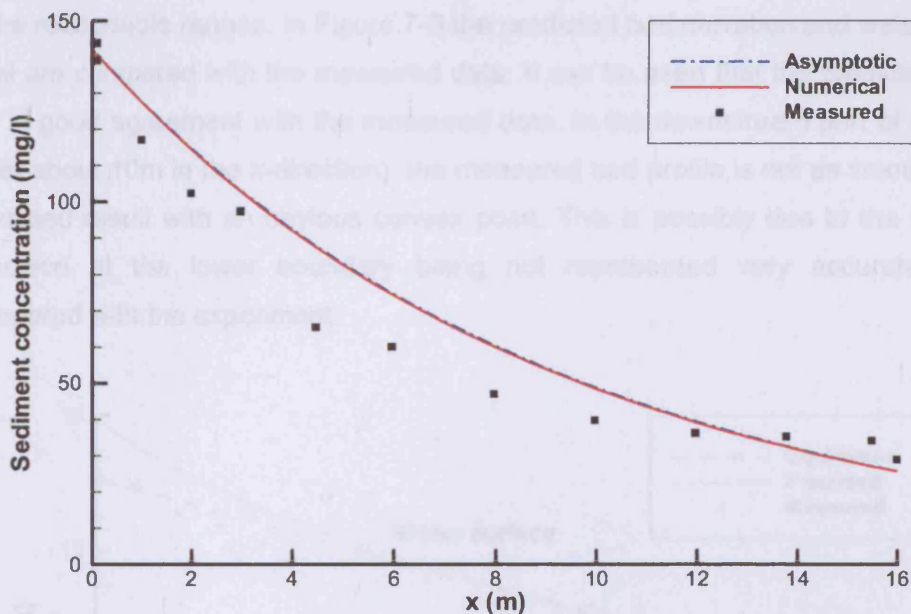


Figure 7-4 Depth-averaged concentration over a porous bed

7.6.2 Bed Evolution in a Sloping Flume

Soni et al. (1980) conducted experiments in a mobile bed flume, with a length of 30m, width of 0.2m and depth of 0.5m. After establishing steady state conditions with a given flow and sediment discharge, the sediment supply rate is increased by continuously feeding in excess sediments at the upstream end of the flume. The transient bed profile is then monitored along the flume at various times following the sediment injection. The initial bed slope, flow depth and discharge are 2.25×10^{-3} , 86 mm and $0.007 \text{ m}^3/\text{s}$, respectively. The mean diameter of the bed and the injected

sediments are both $320\mu\text{m}$, with a geometric deviation of 1.3. The bed porosity is taken as 0.4 and the sediment flux at the left boundary is computed using the established equation by Soni et al. (1980) as $q_s = 3.5 \times 1.45 \times 10^{-3} \rho_s U^5 (\text{m}^2/\text{s})$, where U is the flow velocity at the boundary.

By using Equation (7-63), the first estimation of the profile factor γ is about 3.6. The other profile parameter (α) is estimated as being less than unity since the flow is over-saturated with sediments in this case. As being mentioned before, γ is also an adjustable parameter in the model. The values of the two profile parameters are determined as $\gamma = 3.5$ and $\alpha = 0.32$ by trial and error. Both of the parameters are in the reasonable ranges. In Figure 7-5 the predicted bed elevation and water surface level are compared with the measured data. It can be seen that the predicted results are in good agreement with the measured data. In the downstream part of the flume (after about 10m in the x-direction), the measured bed profile is not as smooth as the predicted result with an obvious convex point. This is possibly due to the boundary condition at the lower boundary being not represented very accurately when compared with the experiment.

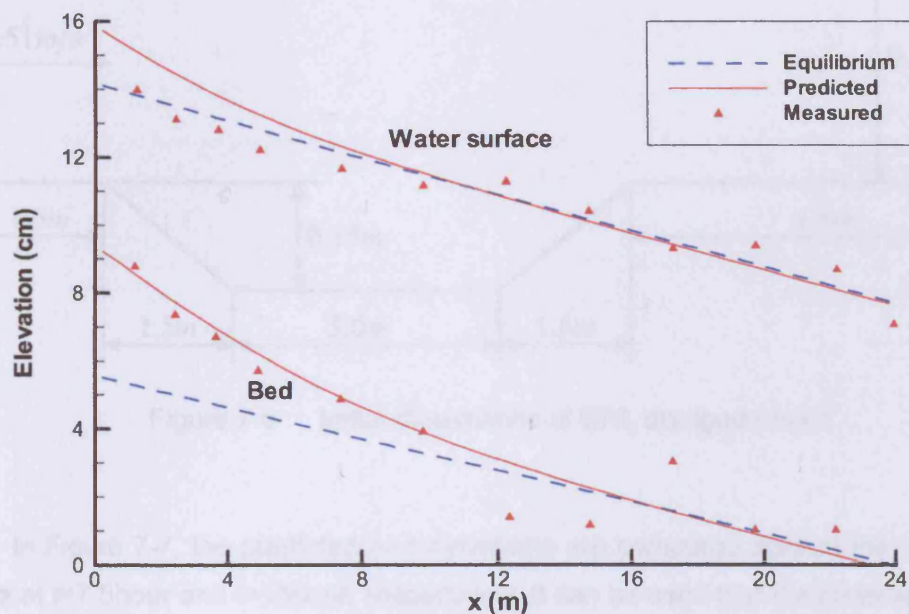


Figure 7-5 Comparison of predicted water surface and bed elevation against measured data ($t = 30$ mins)

7.6.3 Bed Evolution over a Dredged Trench

This study involves the saltation of a dredged trench and the experiment was originally undertaken at the Delft Hydraulics Laboratory (1980). A trench, initially 0.15 m deep with 1:10 side slope (Figure 7-6), is allowed to fill by passing a sediment laden flow over it. The relevant parameters which are measured during the experiment are given in Table 7-3, together with their corresponding values. The transient bed profiles were measured after 7.5 hours and 15 hours. An equilibrium concentration calculated using Van Rijn's (1984a) formula is set at the inlet boundary. By using Equation (7-61), the first estimation of the profile factor γ is 36.23. The value of α should be less than unity in the upstream for deposition dominates in this area and be greater than unity in the downstream for erosion dominates in this area. In this study, a uniform average value of α is used in the model. Optimized values of $\gamma = 30$ and $\alpha = 1$ are obtained by trail and error for this case.

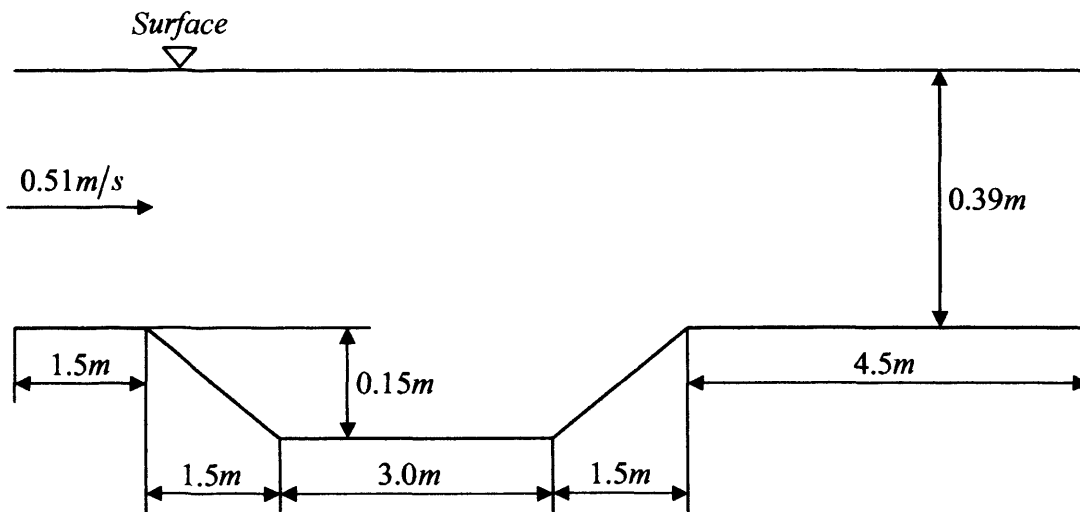


Figure 7-6 Initial dimensions of DHL dredged trench

In Figure 7-7, the predicted bed elevations are compared against the measured data at $t=7.5$ hour and $t=15$ hour, respectively. It can be seen that the predicted results agree well with the measured data.

Table 7-3 Parameters used in the DHL dredged trench experiment

Parameter	Value
Incoming sediment load q_s	0.04 kg/sm
Upstream flow velocity U	0.51 m/s
Settling velocity w_s	0.013 m/s
Sand roughness k_s	0.025 m
Bed porosity n_e	0.4
Sediment density ρ_s	2650 kg/m ³

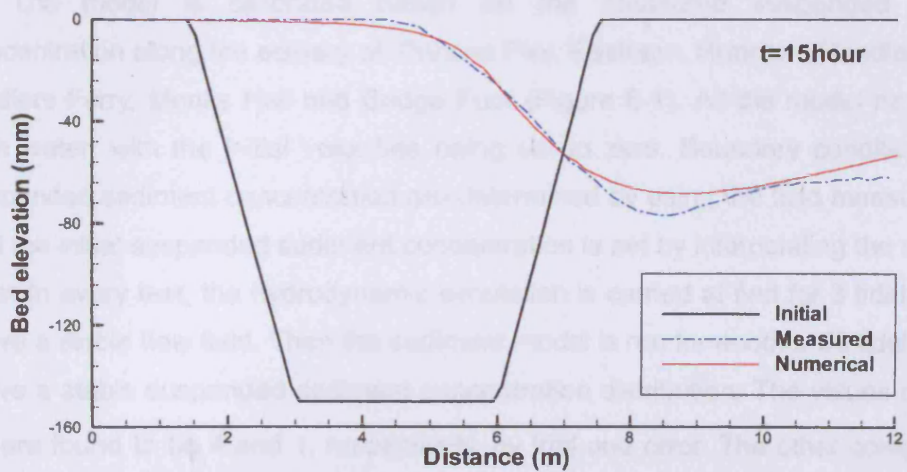
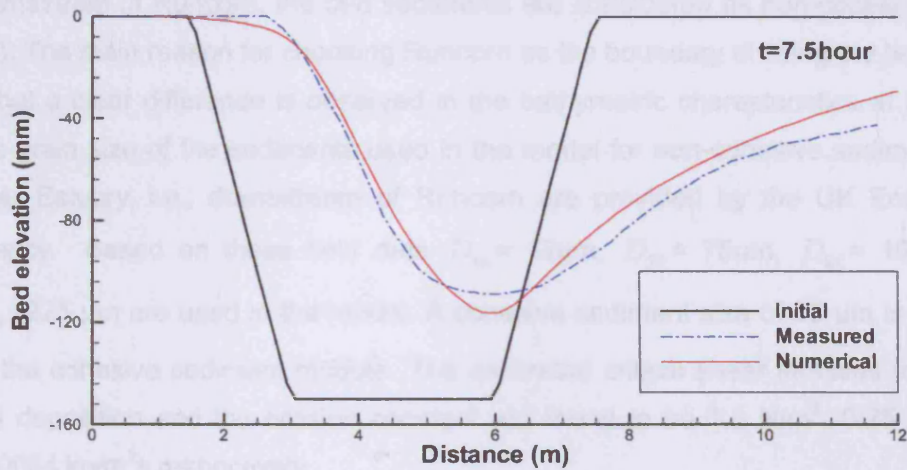


Figure 7-7 Comparison of the predicted bed elevation against the measured data

7.7 VERIFICATION AND CALIBRATION OF MODEL FOR THE MERSEY ESTUARY

7.7.1 Description of Field Data and Computational Parameters

In order to ensure the accuracy of the numerical modelling results, the model is calibrated and verified against three sets of data (see Table 7-4), provided by the UK Environment Agency, and for the period from September 1989 to March 1991. From these data and the two sets of axial measurements to be described in the next Chapter, it is found that finer sediments exist primarily towards the upstream end of the estuary and coarser sediments downstream of the estuary. Therefore, two sediment size regimes are assumed in the model simulations. In the Upper Estuary (upstream of Runcorn) the bed sediments are considered as cohesive, while downstream of Runcorn, the bed sediments are considered as non-cohesive (Figure 6-1). The main reason for choosing Runcorn as the boundary dividing the two regions is that a clear difference is observed in the bathymetric characteristics at this point. The grain size of the sediments used in the model for non-cohesive sediment in the Inner Estuary, i.e., downstream of Runcorn are provided by the UK Environment Agency. Based on these field data $D_{16} = 12\mu\text{m}$, $D_{50} = 75\mu\text{m}$, $D_{84} = 195\mu\text{m}$ and $D_{90} = 225\mu\text{m}$ are used in the model. A cohesive sediment size of $20\mu\text{m}$ is assumed for the cohesive sediment module. The calibrated critical shear stresses for erosion and deposition and the erosion constant are found to be 1.0 N/m^2 , 0.25 N/m^2 and $0.00004\text{ kg/m}^2\text{s}$ respectively.

The model is calibrated based on the measured suspended sediment concentration along the estuary at: Princes Pier, Eastham, Runcorn, Randles Sluices, Fiddlers Ferry, Monks Hall and Bridge Foot (Figure 6-1). All the model runs start at high water, with the initial velocities being set to zero. Boundary conditions of the suspended sediment concentration are determined by using the field measured data, and the initial suspended sediment concentration is set by interpolating the measured data. In every test, the hydrodynamic simulation is carried at first for 3 tidal cycles to arrive a stable flow field. Then the sediment model is run for another 50 tidal cycles to arrive a stable suspended sediment concentration distribution. The values of γ and α are found to be 4 and 1, respectively, by trial and error. The other computational parameters are the same as that used in Section 6.2.

Table 7-4 Three sets of field data for model calibration

Date	Tide type	Tide range (m)	High water (m)	Flow rate (ML/d)	Case number
18-9-89	Spring	9.36	10.07	1,050	1
28-3-90	Spring	9.79	9.94	1,900	2
18-3-91	Spring	8.99	9.59	2,760	3

7.7.2 Results and Discussions

The predicted suspended sediment concentrations are compared against the measured data at six sampling points shown in Figure 6-1 for the three cases listed in Table 7-4. In all cases when the comparison are made directly between the model predictions and measured data it is shown that the model represents the major sediment transport process during the ebb and flood tides quite well, with model predictions increasing at similar times to the increasing measured data. Here, only the results obtained for Case 1 in Table 7-4 are illustrated in Figure 7-8.

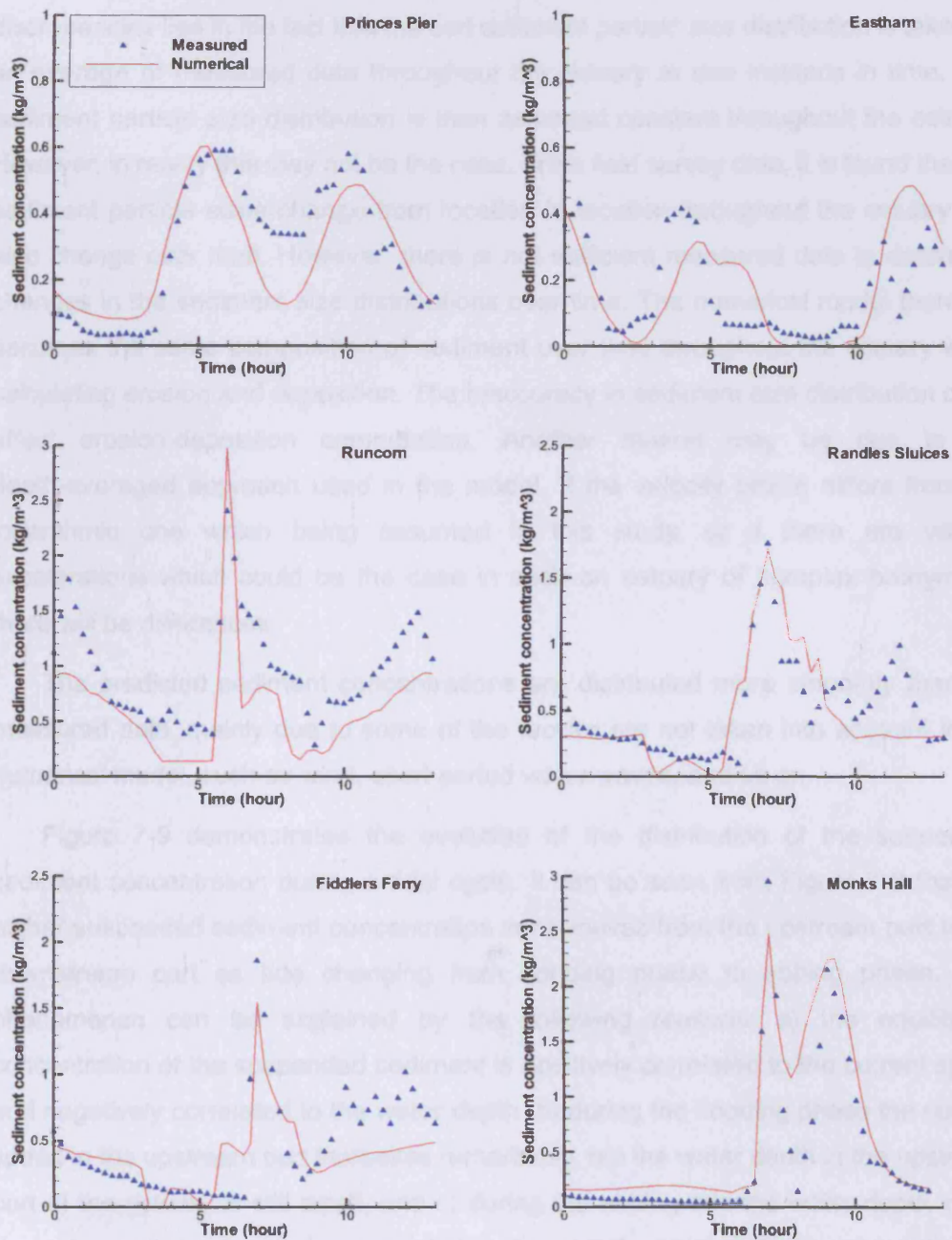


Figure 7-8 Comparison of predicted and measured sediment concentrations at sampling points (see Figure 6-1) for Case 1 in Table 7-4

Although effort has been made to get the model predicted suspended sediment concentration distributions as close as possible to the available data, there are still obvious discrepancies between the model predictions and the measured data. There

are a number of reasons for the discrepancies. One of the reasons for the discrepancies lies in the fact that the bed sediment particle size distribution is taken as an average of measured data throughout the estuary at one instance in time. The sediment particle size distribution is then assumed constant throughout the estuary. However, in reality this may not be the case. From field survey data, it is found that the sediment particle sizes change from location to location throughout the estuary and also change over time. However, there is not sufficient measured data to determine changes in the sediment size distributions over time. The numerical model therefore assumes the same composition of sediment over time throughout the estuary when calculating erosion and deposition. The inaccuracy in sediment size distribution could affect erosion-deposition computation. Another reason may be due to the depth-averaged approach used in the model. If the velocity profile differs from the logarithmic one which being assumed in this study, or if there are vertical accelerations which could be the case in such an estuary of complex bathymetry, there will be differences.

The predicted sediment concentrations are distributed more smoothly than the measured data, mainly due to some of the factors are not taken into account in the numerical model, such as wind, short period water waves, and so on.

Figure 7-9 demonstrates the evolution of the distribution of the suspended sediment concentration during a tidal cycle. It can be seen from Figure 7-9 that the higher suspended sediment concentration zone moves from the upstream part to the downstream part as tide changing from flooding phase to ebbing phase. This phenomenon can be explained by the following reasons: a) the equilibrium concentration of the suspended sediment is positively correlated to the current speed and negatively correlated to the water depth, b) during the flooding phase the current speed in the upstream part increases remarkably, but the water depth in the upstream part of the estuary is still small, and c) during the ebbing tide the water depth in the downstream part decreases remarkably (especially around Eastham), while the current speed is still relatively high. It can be seen that during the ebbing phase high suspended sediment concentration appears around Eastham, while high concentration is not observed around the Narrow, for water depth at the Narrow is always large, while around Eastham water depth could become very small due to the characteristics of the bathymetry.

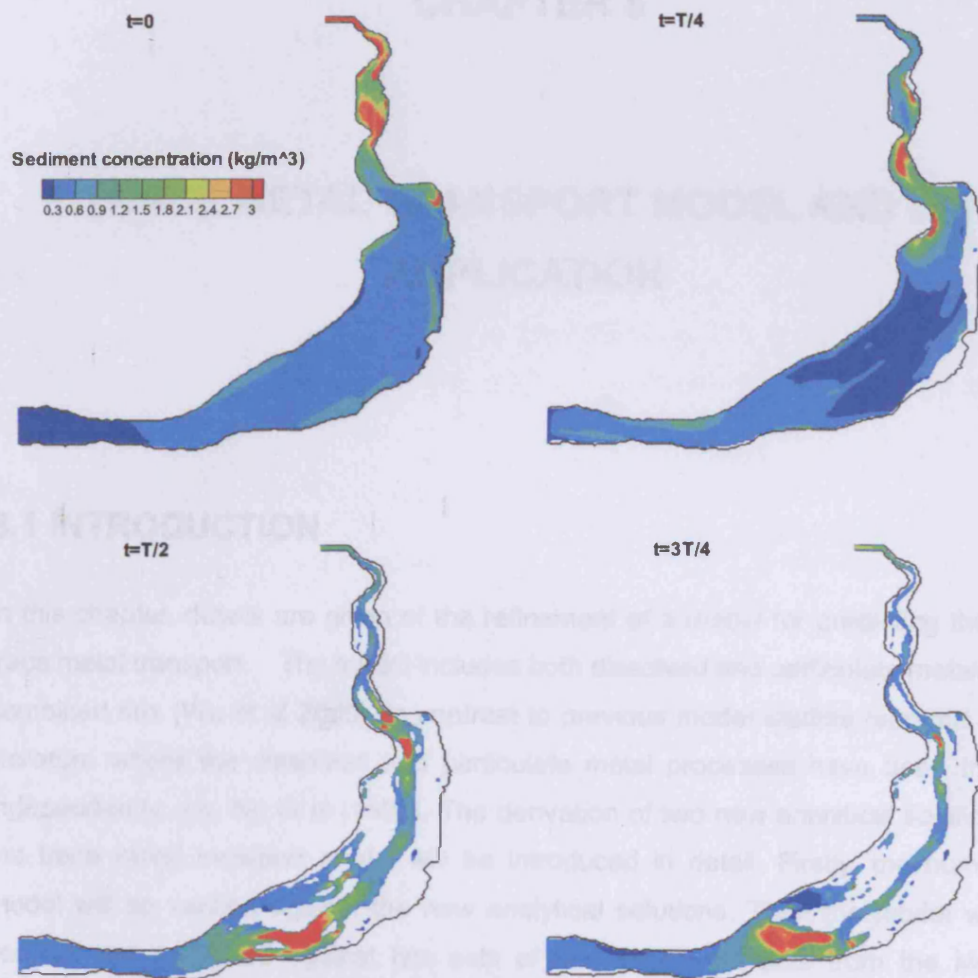


Figure 7-9 Distribution of the predicted suspended sediment concentrations for a tidal cycle (Case1 in Table 7-4)

7.8 SUMMARY

In this chapter the theoretic basis of the sediment transport model is introduced, and the key coefficients used in the model are discussed in detail. Comparisons of the predicted suspended sediment concentrations and bed evolutions against the published experimental data show that satisfied results can be obtained by using this model. Furthermore, the model is calibrated and verified against the measured data of suspended sediment concentration in the Mersey Estuary, and reasonably good results are obtained.

CHAPTER 8

TRACE METAL TRANSPORT MODEL AND ITS APPLICATION

8.1 INTRODUCTION

In this chapter, details are given of the refinement of a model for predicting the total trace metal transport. The model includes both dissolved and particulate metals as a combined flux (Wu et al 2005), in contrast to previous model studies reported in the literature where the dissolved and particulate metal processes have been treated independently, e.g. Ng et al (1996). The derivation of two new analytical solutions of the trace metal transport model will be introduced in detail. Firstly, the numerical model will be verified against the new analytical solutions. Then the model will be verified and calibrated against two sets of field measured data from the Mersey Estuary. Finally, the calibrated model will be used to investigate trace metal behaviour in the Mersey Estuary for three different scenarios.

8.2 TRANSPORT AND FATE OF TRACE METAL IN ESTUARINE AND COASTAL WATERS

8.2.1 Basic Concepts and General Processes

With regard to environmental pollution, metals may be classified according to three criteria: 1) non-critical, 2) toxic but very insoluble or very rare, and 3) very toxic and relatively accessible (Forstner and Wittmann, 1979). For example, Na, K, Mg and Ca are non-critical since they are widely present and not considered as trace metals but as macro-elements, while Ni, Cu, Zn, Cd, Hg and Pb can be considered as very toxic

and relatively accessible metals.

Essential trace metals will become toxic when the nutritional supply becomes excessive. A metal in trace amount is essential if an organism fails to grow in the absence of that metal. However, the same trace metal is toxic when concentration levels exceed required level (Forstner and Wittmann, 1979). Compared to conventional pollutants, toxic substances have three distinctive features: 1) the tendency to adsorb to particulates in the water body, 2) the tendency to be concentrated by aquatic organisms and transferred up the food chain, and 3) the tendency to be toxic at relatively low concentrations of $\mu\text{g/l}$ or ng/l level (Thomann and Mueller, 1987).

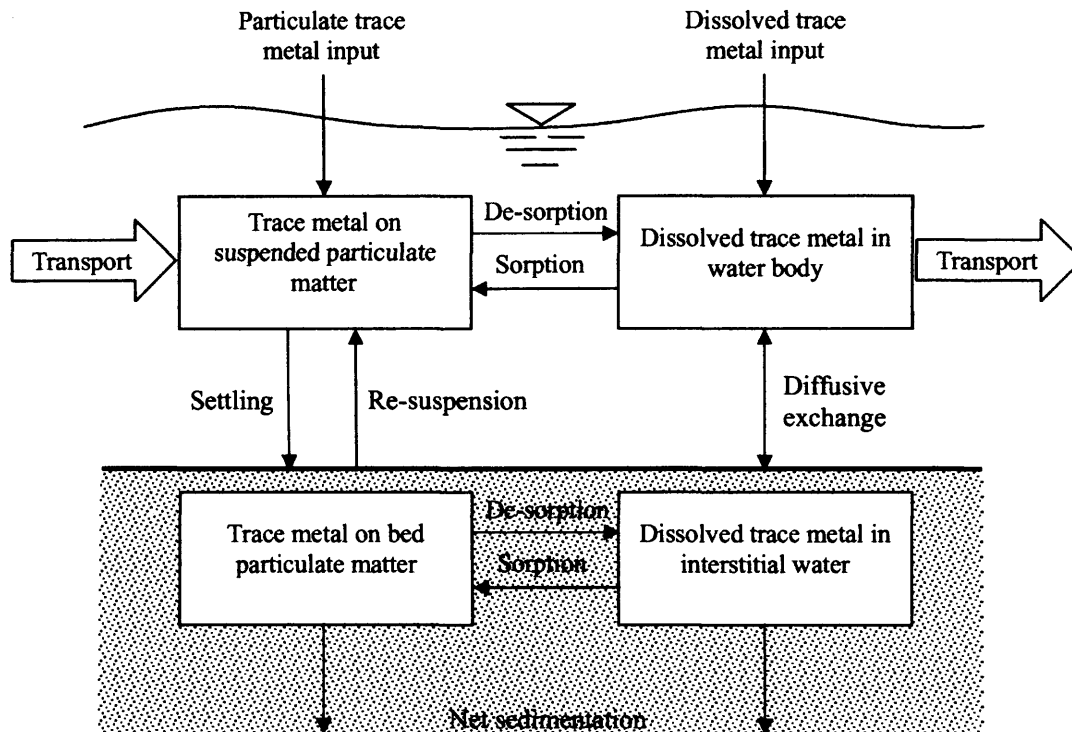


Figure 8-1 Schematic diagram of transport and fate of trace metal

Figure 8-1 shows the general processes of the transport and fate of a trace metal in estuarine and coastal waters. As with all water quality problems, specification of the inputs of the trace metal is essential. The inputs include all sources such as municipal and industrial discharges, urban and agricultural runoff, and atmospheric inputs. The principal processes included in Figure 8-1 are: 1) sorption and de-sorption between dissolved and particulate forms in the water column and sediment, 2) settling and

re-suspension of particulates between the bed sediment and the water column, 3) diffusive exchange between the sediment (interstitial water) and the water column, 4) transport of the trace metal due to advection and dispersion of the flow, and 5) net deposition and loss of trace metal to deep bed sediments.

Since some trace metals adsorb to solids, the sediments become particularly significant as a potential long-term storage reservoir for these trace metals. Therefore, it is necessary to simulate the fate and transport processes of trace metals and the sediment transport processes simultaneously.

8.2.2 Basic Definitions

As shown in Figure 8-1, trace metals can exist in two phases, namely particulate phase and dissolved phase. Special care must be taken in defining the concentration of the dissolved and particulate trace metal, as well as some other related variables.

The concentration of a dissolved trace metal (C'_d) is defined as follows:-

$$C'_d = \frac{M_d}{V_w} \quad (8-1)$$

where V_w is the volume of water considered, and M_d is the mass of trace metal in V_w .

The concentration of a particulate trace metal (C_p) is defined as follows:-

$$C_p = \frac{M_p}{V_{w+s}} \quad (8-2)$$

where V_{w+s} is the volume of the water plus solids, the bulk volume, and M_p is the mass of the particulate trace metal. Thus term C_p represents the mass of trace metal adsorbed on and in the particulates relative to the total volume of water and solids.

The porosity (n_e) is defined as the ratio of the volume of water to the bulk volume, given as:-

$$n_e = \frac{V_w}{V_{w+s}} \quad (8-3)$$

The total trace metal concentration anywhere in the water body or sediment is then

$$C_T = C_p + n_e C'_d \quad (8-4)$$

or

$$C_T = C_p + C_d \quad (8-5)$$

where C_d is the porosity corrected dissolved trace metal concentration, given as:-

$$C_d = n_e C'_d \quad (8-6)$$

For the water column, $n_e \approx 1$ since the volume of water is essentially equal to the bulk volume and then $C_d \approx C'_d$. For the upper strata of the bed sediment, n_e is generally from about 0.7 to 0.8 (Thomann and Mueller, 1987). In all subsequent work in this study it is assumed that the dissolved form is porosity corrected and all trace metal concentrations are calculated based on a bulk volume.

For a given concentration of suspended solids, the particulate form, C_p can also be expressed as:-

$$C_p = C_{SPM} P \quad (8-7)$$

where C_{SPM} is the solid concentration, and P is the trace metal concentration expressed on a dry weight solid basis, being defined as follows:-

$$C_{SPM} = \frac{M_s}{V_{w+s}} \quad (8-8)$$

$$P = \frac{M_p}{M_s} \quad (8-9)$$

where M_s is the solid mass.

8.2.3 Sorption and De-sorption

Figure 8-2 illustrates the mechanism of sorption of the trace metal to the particulates and de-sorption from the particulates back into the dissolved phase. Assuming that all the kinetic transformations are linear, the interaction can be represented by the following equations (Thomann and Mueller, 1987):-

$$\frac{dC_p}{dt} = k_u C_{SPM} C'_d - KC_p \quad (8-10)$$

$$n_e \frac{dC'_d}{dt} = -k_u C_{SPM} C'_d + KC_p \quad (8-11)$$

where k_u is the sorption rate and K is the desertion rate. In terms of the particulate concentration on solid particles and for a constant particle concentration, Equation (8-10) becomes:-

$$\frac{dP}{dt} = k_u C'_d - KP \quad (8-12)$$

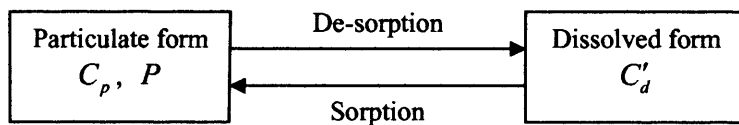


Figure 8-2 Schematic illustration of sorption and de-sorption of trace metal

8.2.4 Partitioning Coefficient

Generally, the time scales of the processes of sorption and de-sorption are largely depend on the time scale of the diffusion process and the flow process (Ahmed and Chen, 2006). Compared to the time scales of days to years, the processes of sorption and de-sorption may be 'fast' or 'slow' in different environments. For cadmium and zinc in the Mersey Estuary, the processes of sorption and de-sorption are found 'fast' (Comber et al., 1995, Turner and Millward, 1994, Turner et al., 2001 and Martino et al., 2002). Thus the dissolved and particulate trace metals are assumed to be always in a 'local equilibrium' state with each other in this study.

Under the equilibrium condition, the change rate of C_p is zero. Thus from Equation (8-10) the following relationship can be derived:-

$$\frac{k_u}{K} = \frac{C_p}{C_{SPM}C'_d} \quad (8-13)$$

Substituting Equation (8-7) into Equation (8-13) gives:-

$$K'_D = \frac{P}{C'_d} = \frac{k_u}{K} \quad (8-14)$$

where K'_D is the partitioning or distribution coefficient of the trace metal at equilibrium between the particulate and dissolved forms.

From Equation (8-6) the porosity corrected partitioning coefficient can be defined as:-

$$K_D = \frac{K'_D}{n_e} = \frac{P}{C_d} \quad (8-15)$$

Since the particulate trace metal concentration relative to the bulk volume is given by Equation (8-7) another relationship between C_p and C_d is

$$C_p = K_D C_{SPM} C_d \quad (8-16)$$

Substituting Equation (8-16) into Equation (8-5), for the total concentration gives:-

$$C_T = (1 + K_D C_{SPM}) C_d \quad (8-17)$$

or

$$C_d = f_d C_T \quad (8-18)$$

where f_d is the fraction of the total trace metal that is dissolved and is given by:-

$$f_d = \frac{1}{1 + K_D C_{SPM}} \quad (8-19)$$

Also, the particulate trace metal as a fraction of the total trace metal is given by:-

$$C_p = f_p C_T \quad (8-20)$$

for

$$f_p = \frac{K_D C_{SPM}}{1 + K_D C_{SPM}} \quad (8-21)$$

Also note that

$$f_d + f_p = 1 \quad (8-22)$$

The distribution of the trace metals between the particulate and dissolved phases therefore depends on the partitioning coefficient (K_D) and the solids concentration.

If experiments are carried out for a range of dissolved trace metal concentrations and the concentrations of both the particulate and dissolved forms are measured at equilibrium, the partitioning coefficient (K_D) can be determined with Equation (8-15). The partitioning coefficient depends on the physical and chemical characteristics of the suspended particles and the ambient conditions, such as salinity, pH, etc. Due to the complexity in determining the partition coefficient, a mean value for the partitioning coefficient has often been used in such applications.

Generally, in estuarine and coastal waters, K_D is affected by the salinity (S) level more obviously than other parameters, and either of the following two ways can be used to determine the relationship between K_D and S: (a) using an empirical function, and (b) using explicit tabulations of measured values of K_D as a function of S.

8.2.5 Mass Exchange between Water Column and Bed Sediments

As shown in Figure 8-1 particulate trace metal settles to or re-suspends from bed sediments via deposition and erosion processes. While the exchange of dissolved trace metal between the surface water and the interstitial water is via diffusive processes. Usually, K_D is much greater than 10^3 ml/g (e.g. Turner et al, 2002, Comber et al., 1995, Thomann and Mueller, 1987). Thus, in the bed sediment, the mass of the particulate trace metal is greater than that of the dissolved phase at least in the magnitude of 2 orders. This means the mass exchange between water body

and bed sediment is mainly due to the settling and re-suspension of sediments. It is reasonable to ignore the mass exchange of the dissolved trace metal between the water body and the interstitial water due to diffusive processes. Thus, hereafter only the mass exchange due to settling and re-suspension of particulates will be taken into account.

The mass exchange rate of trace metal due to settling and re-suspension can be represented with a source term (S_b^p) of the solute transport equation, given as follows:-

$$S_b^p = \begin{cases} q_{dep}P, & \text{Deposition} \\ q_{ero}P_b, & \text{Erosion} \\ 0, & \text{Rest} \end{cases} \quad (8-23)$$

where q_{dep} , q_{ero} = the sediment deposition and erosion rates respectively; P = concentration of trace metals adsorbed on suspended sediments; P_b = concentration of trace metals adsorbed on bed sediments.

In a sophisticated model, the bed sediment is divided into several layers, and the net sedimentation from the upper layer to lower layer (as shown in Figure 8-1) should be taken into account. Compared to the mass exchange between the water body and the top layer bed sediment, the net sedimentation is 'slow' (Thomann and Mueller, 1987). As a reasonable approximation, in this study the net sedimentation is ignored, and only the top bed sediment layer with a given thickness is taken into account.

The concentration of trace metals adsorbed on bed sediments (P_b) varies temporarily due to the mass exchange between the water body and the bed sediment. Assuming that the diffusive coefficient is infinite in the bed sediment (i.e. the deposit sediment and the bed sediment mix well immediately once the deposit sediment touches the bottom), the change rate of P_b can be expressed as follows:-

$$\frac{dP_b}{dt} = \frac{q_{dep}}{M_b}(P - P_b) \quad (8-24)$$

where M_b is the mass of the bed sediment per unit area. Equation (8-24) shows that if the concentration of the particulate trace metal adsorbed on the suspended sediment (P) is greater than that on the bed sediment (P_b), then P_b will increase

with time, and vice versa. It should be mentioned that the assumption of a well-mixed bed sediment layer will not be accurate if the thickness of the layer is not infinitesimal. However, reasonable predicted results still can be expected by using this assumption. The study under this assumption will be helpful for the development of a more sophisticated model.

The mass of the bed sediment per unit area (M_b) also varies temporarily and is calculated with the following formula:-

$$\frac{dM_b}{dt} = q_{dep} - q_{ero} \quad (8-25)$$

8.3 TRACE METAL TRANSPORT GOVERNING EQUATIONS

8.3.1 Governing Equations for Particulate and Dissolved Phases

The transport of the trace metal in the dissolved phase can be described by the following two-dimensional advective-diffusion equation (see Equation (3-85)):-

$$\begin{aligned} & \frac{\partial(HC_d)}{\partial t} + \frac{\partial(pC_d)}{\partial x} + \frac{\partial(qC_d)}{\partial y} - \frac{\partial}{\partial x} \left(HD_{xx} \frac{\partial C_d}{\partial x} + HD_{xy} \frac{\partial C_d}{\partial y} \right) \\ & - \frac{\partial}{\partial y} \left(HD_{yx} \frac{\partial C_d}{\partial x} + HD_{yy} \frac{\partial C_d}{\partial y} \right) = H(S_o^d + S_t^d) \end{aligned} \quad (8-26)$$

where S_o^d = source or sink of dissolved trace metal; and S_t^d = transformation term defining adsorbed or desorbed particulate fluxes to or from the sediments.

The adsorbed particulate phase is transported with the sediments, and this process may be described by the following equation:-

$$\begin{aligned} & \frac{\partial(HPC_{SPM})}{\partial t} + \frac{\partial(pPC_{SPM})}{\partial x} + \frac{\partial(qPC_{SPM})}{\partial y} \\ & - \frac{\partial}{\partial x} \left[HD_{xx} \frac{\partial(PC_{SPM})}{\partial x} + HD_{xy} \frac{\partial(PC_{SPM})}{\partial y} \right] \\ & - \frac{\partial}{\partial y} \left[HD_{yx} \frac{\partial(PC_{SPM})}{\partial x} + HD_{yy} \frac{\partial(PC_{SPM})}{\partial y} \right] = H(S_o^p + S_t^p) + S_b^p \end{aligned} \quad (8-27)$$

where S_o^p = source or sink of adsorbed particulate trace metal; S_i^p = transformation term defining metal flux from or to dissolved phase in the water column; and S_b^p = source term defining particulate flux from or to the bed, for sediment erosion or deposition respectively.

8.3.2 Governing Equation for Total Trace Metal Load

The transformation processes between the dissolved and adsorbed particulate phases are very complex. However, noting that $S_i^d = -S_i^p$, Wu et al (2005) introduced a new method to avoid calculating the transformation rate between the dissolved and adsorbed particulate phases by first calculating the total trace metal concentration distributions, and then dividing the dissolved and adsorbed particulate phases using a partitioning relationship of the form given in Equations (8-16) and (8-17). The evaluation of the total trace metal concentrations in this form is thought to be novel, with the corresponding equation derived by summing equations (8-26) and (8-27), and re-arranging the diffusion terms to give:-

$$\begin{aligned} \frac{\partial(HC_T)}{\partial t} + \frac{\partial(pC_T)}{\partial x} + \frac{\partial(qC_T)}{\partial y} - \frac{\partial}{\partial x} \left(HD_{xx} \frac{\partial C_T}{\partial x} + HD_{xy} \frac{\partial C_T}{\partial y} \right) \\ - \frac{\partial}{\partial y} \left(HD_{yx} \frac{\partial C_T}{\partial x} + HD_{yy} \frac{\partial C_T}{\partial y} \right) = H(S_o^d + S_o^p) + S_b^p \end{aligned} \quad (8-28)$$

where C_T = concentration of total trace metal, i.e.:-

$$C_T = C_d + PC_{SPM} \quad (8-29)$$

Equation (8-28) can be solved by using the numerical method introduced in Chapter 4 with suitable initial and boundary conditions. Then the values of C_d and C_p can be evaluated using Equations (8-16) and Equation (8-17).

8.4 NEW CASES AND THEIR ANALYTICAL SOLUTIONS

In this section two typical test cases are designed and analytical solutions derived for trace metal transport model. The first test focuses on the deposition process, and the

second one focuses on the erosion process.

The behaviour of trace metal in the water body is related to the hydrodynamic processes, the advection-diffusion processes, sediment properties and partitioning processes. If all of the factors are taken into account, it will be difficult to obtain an analytical solution due to the complexity of the trace metal transport processes even the initial and boundary conditions are simple. It is reasonable to set the hydrodynamic processes, the advective-diffusion processes and sediment properties as simple as possible when seeking the analytical solution for the trace metal transport model.

8.4.1 Case 1: Deposition process

Figure 8-3 is a schematic illustration of the first test case developed for representing the deposition process. P is the concentration of trace metals adsorbed on suspended sediments by dry weight, and the concentration of trace metal in the bed sediment by dry weight is P_b . The water depth is H and the thickness of the bed sediment layer is h_b .

The initial and boundary conditions are set as follows:-

- a) Initially, the concentration of the sediment C_{SPM}^0 and the total trace metal C_T^0 in the whole domain are both constant.
- b) The concentrations of sediment and trace metal, C_{SPM}^e and C_T^e are set as their equilibrium concentrations at the input (left) boundary.

In order to simplify the problem, the following assumptions are made:

- a) The problem is assumed to be one dimensional.
- b) The flow field is steady with a constant velocity U .
- c) The size of sediment particle is assumed uniform in the domain and the settling velocity (w_s) is set as a constant.
- d) C_{SPM}^0 is greater than C_{SPM}^e . Thus the sediment and particulate trace metal will settle down to the bed gradually and the concentrations of sediment and trace metal in the water body will decrease to their equilibrium values.
- e) The diffusive process is ignored in the domain. Thus the solutes (sediment and trace metal) will transport downstream with a velocity U , and after time

x/U the concentrations of sediment and trace metal at position x will change to their equilibrium values, i.e. the value at the left boundary.

- f) In order to keep a stable flow field, it is assumed that the change of bed elevation due to deposition of sediment is far less than the water depth.

With the above assumptions, the concentrations of sediment and trace metal in the water body, as well as the concentration of the trace metal in the bed sediment can be obtained analytically. Details of the solutions are given in the following context.

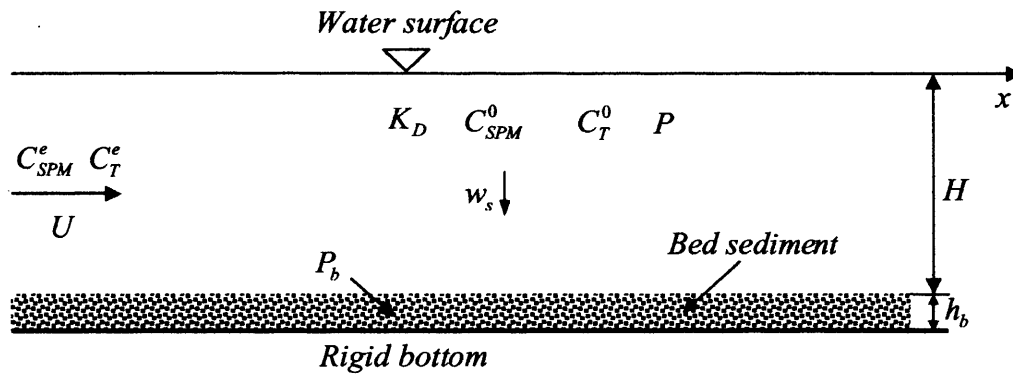


Figure 8-3 Schematic illustration of test cases

The processes in static water are considered at first, i.e. the velocity in the whole domain and on boundaries is set to zero. For this case, the governing equation for suspended sediment transport (Equation (7-34)) can be simplified as follows:-

$$\frac{dC_{SPM}}{dt} = \frac{\gamma w_s}{H} (C_{SPM}^e - \alpha C_{SPM}) \quad (8-30)$$

It is straight forward to obtain the analytical solution of Equation (8-30) for the above-mentioned case, which is:-

$$C_{SPM} = \frac{1}{\alpha} C_{SPM}^e + \left(C_{SPM}^0 - \frac{1}{\alpha} C_{SPM}^e \right) e^{-\lambda t} \quad (8-31)$$

where $\lambda = \frac{\alpha \gamma w_s}{H}$. (8-32)

The total mass of deposited sediment in a unit area during time interval t can be integrated as:-

$$m_s(t) = \gamma w_s \int_0^t (\alpha C_{SPM} - C_{SPM}^e) dt \quad (8-33)$$

Substituting Equation (8-31) into Equation (8-33) gives:-

$$m_s(t) = \frac{H}{\alpha} (\alpha C_{SPM}^0 - C_{SPM}^e) (1 - e^{-\lambda t}) \quad (8-34)$$

Similarly, the governing equation for total trace metal transport (Equation (8-28)) can be simplified for this case to give:-

$$\frac{dC_T}{dt} = \frac{1}{H} S_b^p \quad (8-35)$$

where S_b^p represents the reduction of trace metal due to the deposition of sediment, given as follows:-

$$S_b^p = q_{dep} P = \gamma w_s P (C_{SPM}^e - \alpha C_{SPM}) \quad (8-36)$$

According to Equations (8-15), (8-16) and (8-17) P can be expressed as follows:-

$$P = \frac{K_D C_T}{1 + K_D C_{SPM}} \quad (8-37)$$

Substituting Equations (8-31), (8-36) and (8-37) into Equation (8-35) gives:-

$$\frac{dC_T}{dt} = \frac{\gamma w_s}{H} \frac{K_D C_T}{1 + K_D C_{SPM}} (C_{SPM}^e - \alpha C_{SPM}) \quad (8-38)$$

Using the initial condition in this test case (Figure 8-3), Equation (8-38) can be solved analytically to give the following solution:-

$$C_T = \frac{\alpha + K_D [C_{SPM}^e + (\alpha C_{SPM}^0 - C_{SPM}^e) e^{-\lambda t}]}{\alpha (1 + K_D C_{SPM}^0)} C_T^0 \quad (8-39)$$

The total mass of deposited trace metal in a unit area (e.g. a computational cell) during time interval t can be integrated to give:-

$$m_p(t) = \gamma w_s \int_0^t P (\alpha C_{SPM} - C_{SPM}^e) dt \quad (8-40)$$

Substituting Equations (8-31), (8-37) and (8-39) into Equation (8-40) gives:-

$$m_p(t) = \frac{H}{\alpha} \frac{K_D C_T^0}{1 + K_D C_{SPM}^0} (\alpha C_{SPM}^0 - C_{SPM}^e) (1 - e^{-\lambda t}) \quad (8-41)$$

Assuming that the deposited trace metal mix well with the trace metal in the bed sediment immediately when it touches the bed and considering that the initial

concentration of trace metal in the bed sediment (P_b^0) is zero, the concentration of trace metal in the bed sediment by dry weight can be expressed as follows:-

$$P_b = \frac{m_p(t)}{h_b(1-n_e)\rho_s + m_s(t)} \quad (8-42)$$

Substituting Equations (8-34) and (8-41) into Equation (8-42) gives:-

$$P_b = \frac{HK_D(\alpha C_{SPM}^0 - C_{SPM}^e)(1 - e^{-\lambda t})C_T^0}{[\alpha h_b(1-n_e)\rho_s + H(\alpha C_{SPM}^0 - C_{SPM}^e)(1 - e^{-\lambda t})](1 + K_D C_{SPM}^0)} \quad (8-43)$$

Considering that the flow is stable in the whole domain with a constant horizontal velocity U , after time $T_x = x/U$ the concentrations of sediment and trace metal at position x in the domain will change to their equilibrium values, i.e. the value on the left boundary. Thus, Equations (8-31), (8-33), (8-39), (8-41) and (8-43) are valid only when $t < T_x$, and if $t \geq T_x$ the time t in the above equations should be replaced by T_x to represent the corresponding equilibrium status.

The concentrations of the dissolved and particulate trace metal in the water body can be evaluated by using Equations (8-18) and (8-20), respectively.

8.4.2 Case 2: Erosion process

This case is designed in the same as Case 1 except that the initial conditions are now given as :-

- a) At $t = 0$ the concentrations of sediment and trace metal in the domain are set to be lower than the equilibrium value.
- b) The initial value of P_b in the bed sediment is set to be a constant, P_b^0 .

In order to simplify the problem, it is assumed that the thickness of the bed layer is large enough. Thus the trace metal will be entrained into the water body continuously due to the suspension of sediment, and the concentration of suspended sediment will increase gradually until it reaches equilibrium.

For this case the suspended sediment concentration and the total mass of eroded sediment in a unit area can also be expressed using Equations (8-31) and (8-34). The transport of the total trace metal can also be expressed using Equation (8-35), but for this case S_b^p represents the source of trace metal due to the erosion of sediment, given as:-

$$S_b^p = q_{ero} P_b = \gamma w_s P_b (C_{SPM}^e - \alpha C_{SPM}) \quad (8-44)$$

Since the initial value of P_b is uniform in the bed sediment and no deposition occurs, P_b will be kept as a constant, i.e. P_b^0 . Substituting Equations (8-31) and (8-44) into Equation (8-35) gives:-

$$\frac{dC_T}{dt} = \frac{1}{H} \gamma w_s P_b^0 (C_{SPM}^e - \alpha C_{SPM}^0) e^{-\lambda x} \quad (8-45)$$

The solution of Equation (8-45) can be expressed as:-

$$C_T = C_T^0 + \frac{P_b^0}{\alpha} (C_{SPM}^e - \alpha C_{SPM}^0) (1 - e^{-\lambda x}) \quad (8-46a)$$

Equation (8-46) is valid only for $t < T_x$, if $t \geq T_x$ the following expression for equilibrium status should be adopted:-

$$C_T = C_T^e \quad (8-46b)$$

8.5 VERIFICATION OF MODEL AGAINST ANALYTICAL SOLUTIONS

In this section the trace metal model will be verified against the two analytical solutions obtained in the previous section.

8.5.1 Case 1: Deposition Process

This case is the same as Case 1 in Section 8.4.1. The computational parameters are set as follows:-

- In the numerical test the length of the domain, the water depth and the thickness of the bed sediment layer are set to 10km, 10m and 0.2m, respectively. The space step and the time step used in the simulation are $\Delta x = 100m$ and $\Delta t = 10s$, respectively.
- The velocity in the domain is set to $U = 1m/s$.
- The parameters in the sediment transport model are set to $\alpha = \gamma = 1$ and $w_s = 1mm/s$. The value of the partitioning coefficient is assumed to be

- 10000ml/g, which is the same order as that for zinc and cadmium in the Mersey Estuary (see Figure 8-7).
- The equilibrium concentrations of suspended sediment (C_{SPM}^e) and total trace metal (C_T^e) in the water body are set as 1 kg/m^3 and $10\text{ }\mu\text{g/l}$, respectively.
 - The initial concentration of the trace metal in bed sediment (P_b^0) is assumed to be zero. The initial concentrations of suspended sediment (C_{SPM}^0) and total trace metal (C_T^0) in the water body are set as 2 kg/m^3 and $20\text{ }\mu\text{g/l}$, respectively.
 - The concentrations of sediment and trace metal, C_{SPM}^e and C_T^e at the input (left) boundary are set as their equilibrium concentrations.
 - In order to achieve the equilibrium status in the whole domain the simulated time is set to be greater than 10000s.

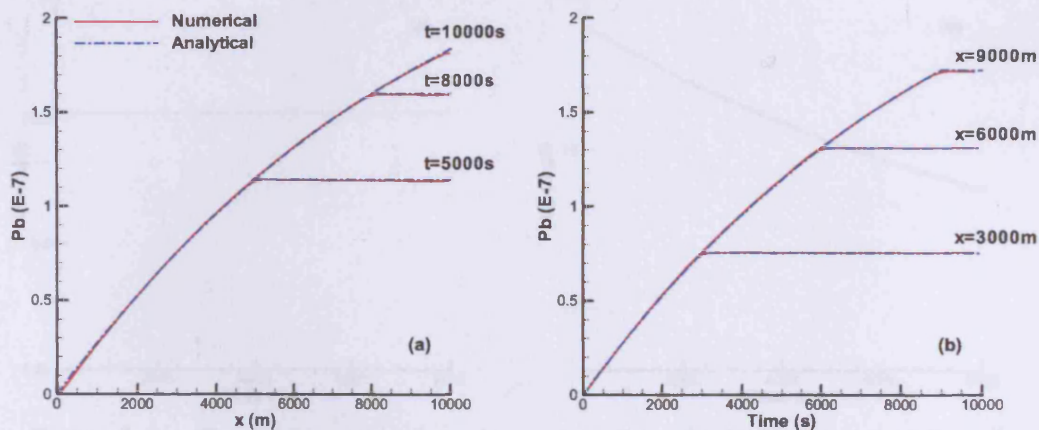


Figure 8-4 Distributions of trace metal concentration (P_b) in bed sediment

(a) Spatial distributions at three selected times and (b) Temporal distributions at three selected locations

The numerical results of the spatial (at $t=5000\text{ s}$, 8000 s and 10000 s) and temporal (at $x=3000\text{ m}$, 6000 m and 9000 m) distributions of the trace metal concentration in the bed sediment are demonstrated in Figures 8-4a and 8-4b, respectively, as well as the corresponding analytical solutions. It can be seen from both figures that the numerical results agree very well with the analytical solutions. Figure 8-4a shows that the effect of the upstream boundary condition transfer to the downstream part gradually with a

speed of 1 m/s . Figure 8-4b shows that concentration of trace metal in the bed sediment increases gradually with time and achieves the equilibrium status after $t = x/U$. These are consistent with the analytical solutions.

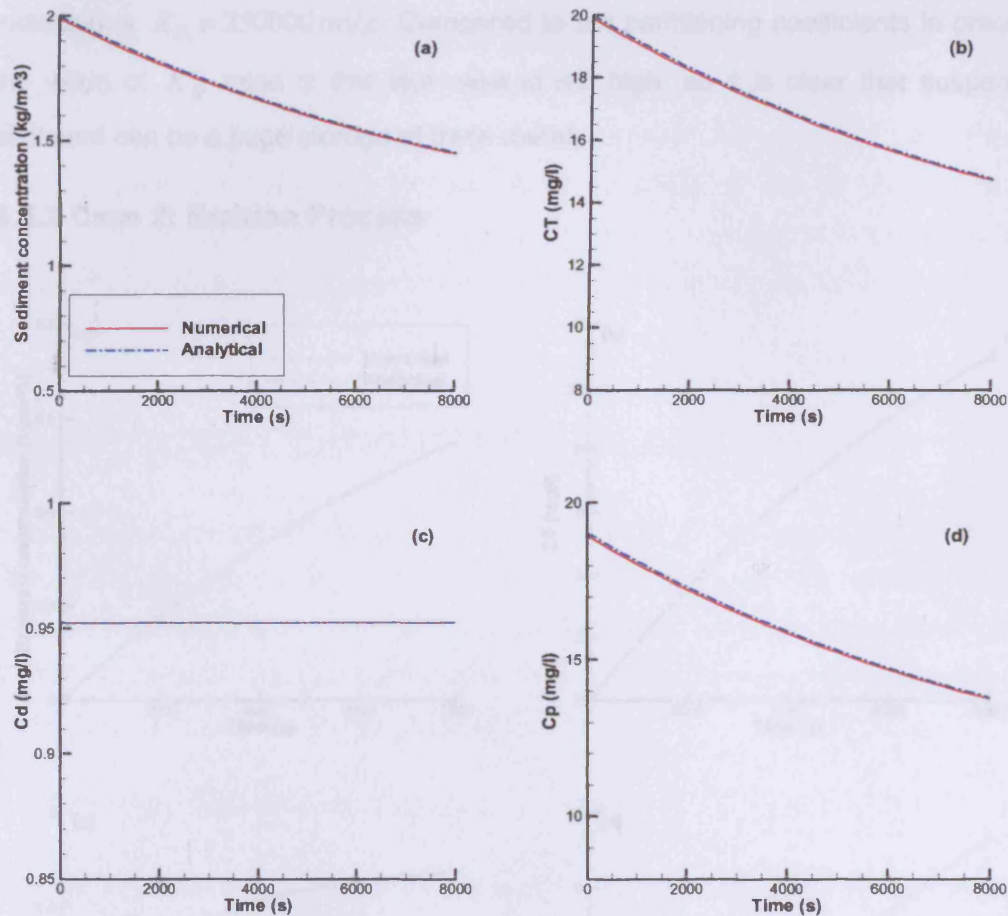


Figure 8-5 Temporal distribution of concentration of (a) suspended sediment (C_{SPM}), (b) total trace metal (C_T), (c) dissolved trace metal (C_d), and (d) particulate trace metal (C_p) in water body at $x = 9000\text{m}$ for Case 1

The temporal distributions of the concentration of suspended sediment (C_{SPM}) and the total trace metal in the water body (C_T) at $x = 9000\text{m}$ are illustrated in Figures 8-5a and 8-5b, respectively. Figures 8-5c and 8-5d compare the predicted concentrations of dissolved and particulate trace metal in the water body against the corresponding analytical solutions, respectively. The numerical results agree very well with the analytical solutions. It can be seen from the figures that the concentration of the total trace metal and the particulate trace metal vary with the concentration of the suspended sediment due to the partitioning coefficient is assumed to be a constant in

this test case. The concentration of the dissolved trace metal is much lower than the concentration of the particulate trace metal due to the high value of the partitioning coefficient. Thomann (see Thomann and Mueller, 1987) compiled water column partitioning coefficients from field data from 15 streams and rivers, and suggested an appropriate first approximation to the water column partition coefficient for the metals indicated is $K_D = 250000 \text{ ml/g}$. Compared to the partitioning coefficients in practice, the value of K_D used in this test case is not high, so it is clear that suspended sediment can be a huge storage of trace metal.

8.5.2 Case 2: Erosion Process

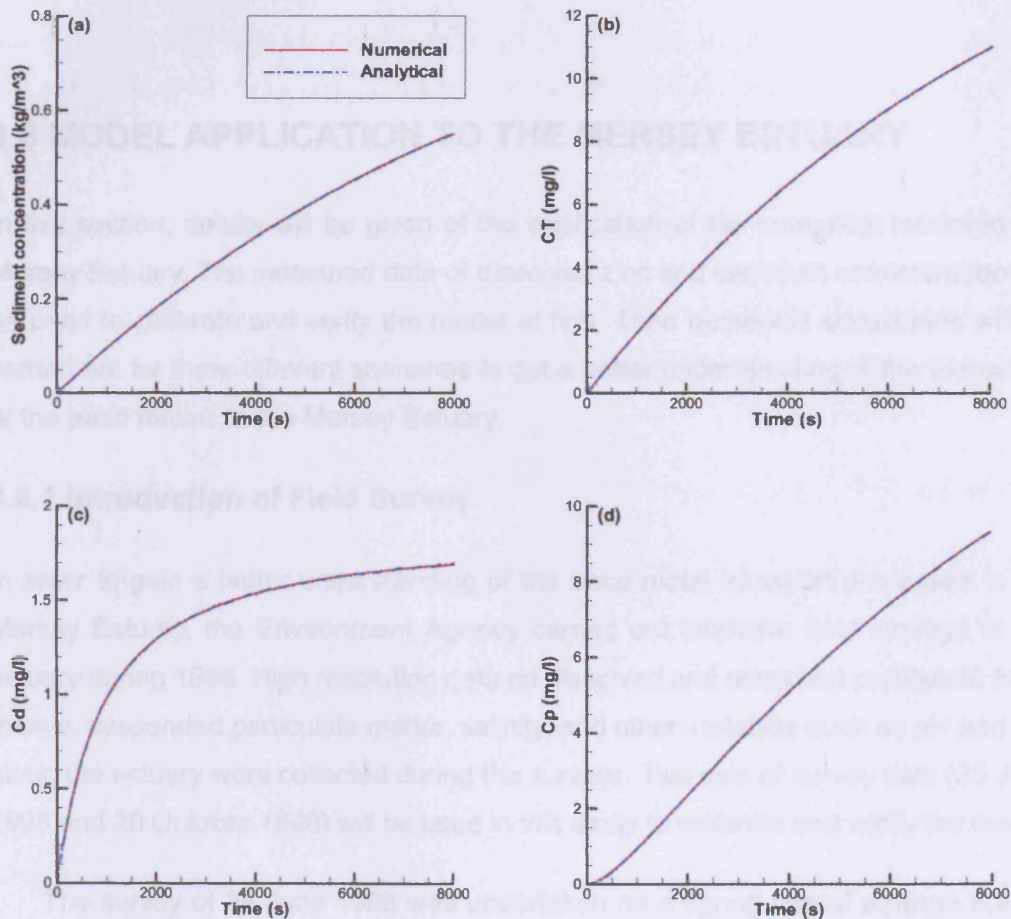


Figure 8-6 Temporal distribution of concentration of (a) suspended sediment (C_{SPM}), (b) total trace metal (C_T), (c) dissolved trace metal (C_d), and (d) particulate trace metal (C_p) in water body at $x = 9000\text{m}$ for Case 2

The set up of the numerical model for this case is the same as that for Case 1 except

the initial conditions are now given as:-

$$C_{SPM}^0 = 0 \text{ kg/m}^3 \quad C_T^0 = 0 \text{ } \mu\text{g/L} \quad P_b^0 = 2 \times 10^{-7}$$

The temporal distribution of the concentration of suspended sediment (C_{SPM}) and the total trace metal in the water body (C_T) at $x = 9000\text{m}$ are illustrated in Figure 8-6a and Figure 8-6b, respectively. Figures 8-6c and 8-6d compare the predicted concentrations of dissolved and particulate trace metal in the water body against the corresponding analytical solutions. It can be seen from the figures that the numerical results agree very well with the analytical solutions. It can be seen that the concentrations of both total trace metal and particulate trace metal in the water body are highly positively correlated to the concentration of the suspended sediment.

8.6 MODEL APPLICATION TO THE MERSEY ESTUARY

In this section, details will be given of the application of the numerical model to the Mersey Estuary. The measured data of dissolved zinc and cadmium concentration will be used to calibrate and verify the model at first. Then numerical simulations will be carried out for three different scenarios to get a better understanding of the behaviour of the trace metals in the Mersey Estuary.

8.6.1 Introduction of Field Survey

In order to gain a better understanding of the trace metal transport processes in the Mersey Estuary, the Environment Agency carried out intensive field surveys in the estuary during 1998. High resolution data on dissolved and adsorbed particulate trace metals, suspended particulate matter, salinity, and other variables such as pH and DO along the estuary were collected during the surveys. Two sets of survey data (25 June 1998 and 20 October 1998) will be used in this study to calibrate and verify the model.

The survey of 25 June 1998 was undertaken on a spring tide of a range 8.47m, with the high water reaching Liverpool at about 12:45. The fresh water input from the River Mersey was about 3600ML/d. The survey boat started from the outer estuary at 10:56 and ended at Monks Hall in the upper estuary (see Figure 6-1). Samples (including salinity, concentrations of sediment, zinc and cadmium) were collected at 20 locations along the estuary and the journey took about 3.5 hours.

The survey of 20 October 1998 was undertaken on a mid-spring tide of a range 7.69m, with the high water reaching Liverpool at about 11:50. The fresh water input from the River Mersey was about 7100ML/d. The survey boat started from the outer estuary at 9:50 and ended at Monks Hall in the upper estuary. Samples (including salinity, concentrations of sediment, zinc and cadmium) were collected at 19 locations along the estuary and the journey took about 3.25 hours.

8.6.2 Partitioning Coefficients and Computational Parameters

As aforementioned, the following two methods can be used to determine the relationship between K_D and S : (a) using an empirical function, and (b) using explicit tabulations of measured values of K_D as a function of S (Hartnett et al, 2005). In this study, the partitioning coefficients for zinc and cadmium are developed as polynomial functions of salinity by using the data provided by the Environment Agency, given as follows:-

$$K_D = a + bS + cS^2 + dS^3 \quad (8-31)$$

where S = salinity (ppt), $a - d$ are coefficients with their values being listed in Table 8-1. The initial trace metal concentrations in the bed sediments are assumed uniform in the domain and the values listed in Table 8-1 are used in the simulations.

Table 8-1 Values of coefficients for K_D and concentrations in bed sediment

Metal	Coefficients for K_D in Equation (8-31)				Concentration in bed sediment ($\mu\text{g/g}$)
	a	b	c	d	
Zinc	39726.700	-1066.360	35.783	-0.419	200
Cadmium	42074.918	-4026.180	140.853	-1.702	0.025

The measured and the predicted (with Equation (8-31)) values of K_D are compared in Figures 8-7a and 8-7b for zinc and cadmium, respectively. It can be seen that the assumed polynomial function relationship between K_D and salinity matches the measured data well for cadmium, while the predicted partitioning coefficients for zinc are less satisfied due to the measured data showing no obvious trend.

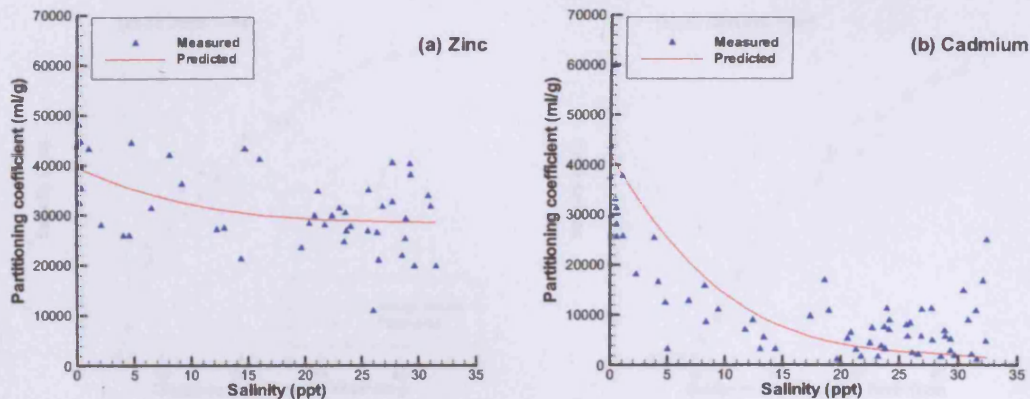


Figure 8-7 Comparison of predicted and field measured partitioning coefficients of (a) zinc and (b) cadmium in the Mersey Estuary

The coefficients and computational parameters for hydrodynamic and sediment transport modelling are the same as that in Chapters 6 and 7, except the boundary conditions being set according to the field measured data on 25 June 1998 and 20 October 1998. The trace metal concentrations in bed sediment and the partitioning coefficients are set as the values listed in Table 8-1. The thickness of the bed layer is set as 0.5m in the simulations.

8.6.3 Comparisons between Model Results and Field Data

Figure 8-8a and Figure 8-8b illustrate the comparisons between the model predicted and field measured salinity level along the estuary for the two field surveys on 25 June 1998 and 20 October 1998, respectively. The model results shown in the figures are at roughly the same time as the one when the samples were collected. It can be seen that the model predictions are in good agreement with the field data. The comparisons between the model predicted and field measured suspended sediment distributions along the estuary are demonstrated in Figure 8-9a and Figure 8-9b. For the simulation of 25 June, 1998, the model underestimates the sediment concentration to some extent, while for the simulation of 20 October, 1998, the model overestimates the sediment concentration slightly. As a whole, the model results agree reasonably well with the field data. Thus the hydrodynamic parameters, dispersion coefficients and the sediment parameters calibrated in the previous two chapters are still valid for the two field surveys for trace metal transport.

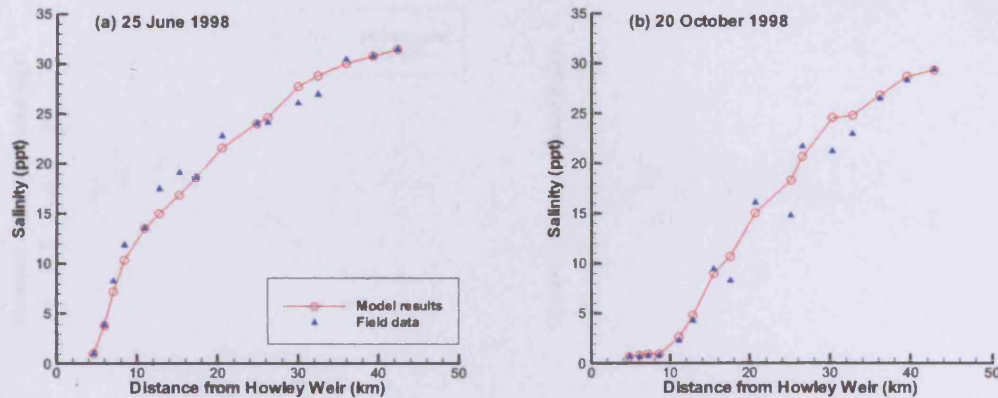


Figure 8-8 Comparison of predicted and field measured axial salinity distributions

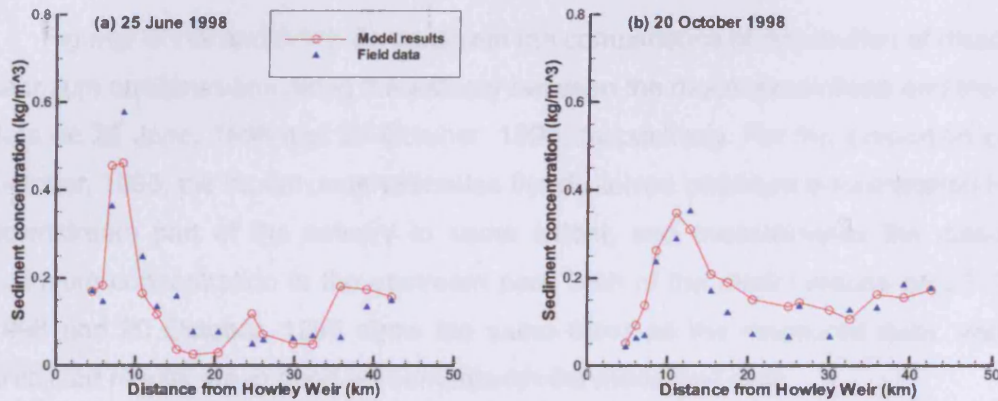


Figure 8-9 Comparison of predicted and field measured axial suspended sediment distributions

Figure 8-10a shows a comparison of distribution of dissolved zinc concentration along the estuary between the model predictions and the field data on 25 June 1998. In the lower estuary the model results are higher than the measured data, and in the upstream part the model results are lower than the measured data. Figure 8-10b illustrates the comparison of distribution of dissolved zinc concentration along the estuary between the model predictions and the field data on 20 October 1998. It can be seen that the model results also agree reasonably well with the field data. The model underestimates the concentration of dissolved zinc in the area near to the mouth of the estuary to some extent, and overestimates the concentration of dissolved zinc in the upstream part. As a whole, the model results agree reasonably well with the field data.

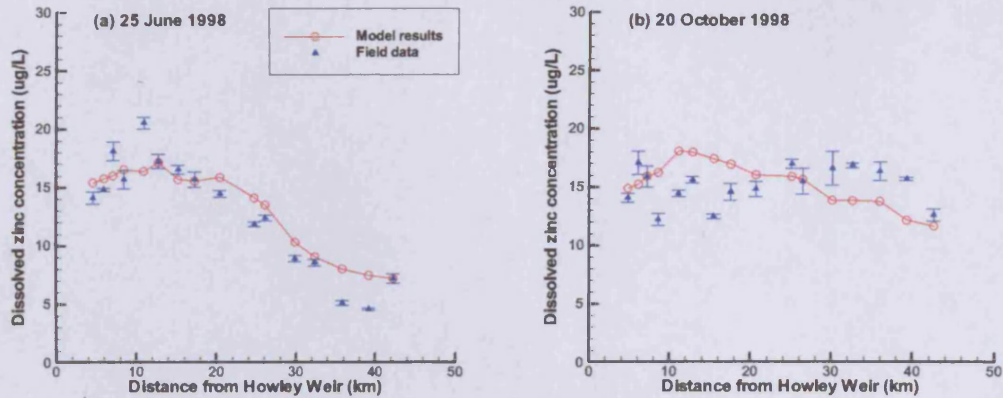


Figure 8-10 Comparison of predicted and field measured axial dissolved zinc distributions

Figures 8-11a and 8-11b demonstrate the comparisons of distribution of dissolved cadmium concentration along the estuary between the model predictions and the field data on 25 June, 1998 and 20 October, 1998, respectively. For the simulation on 20 October, 1998, the model underestimates the dissolved cadmium concentration in the downstream part of the estuary to some extent, and overestimates the dissolved cadmium concentration in the upstream part. Both of the model results on 25 June, 1998 and 20 October, 1998 show the same trend as the measured data, and the predicted results are in good agreement with the measured data.

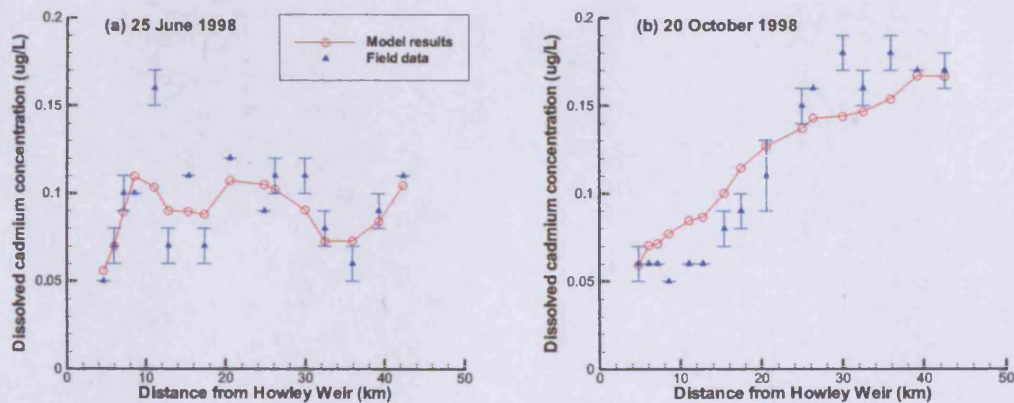


Figure 8-11 Comparison of predicted and field measured axial dissolved cadmium distributions

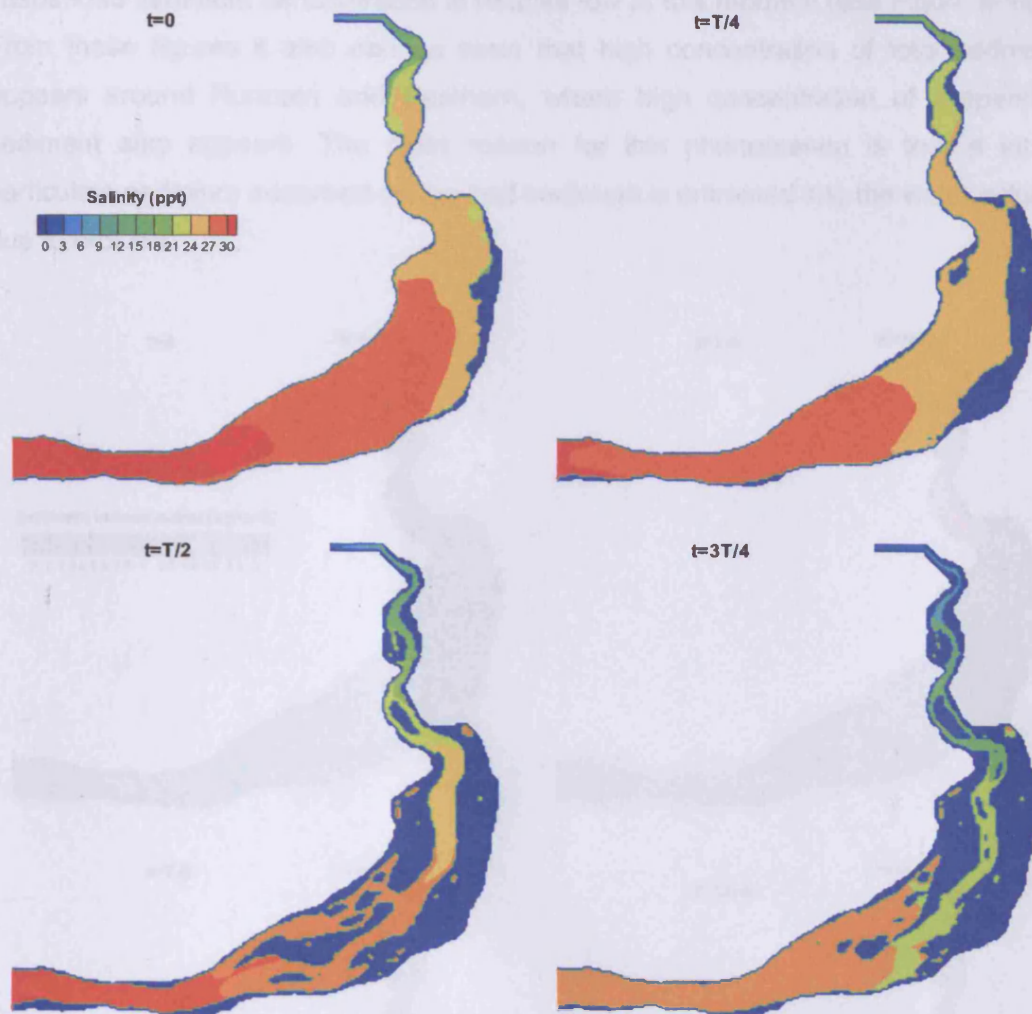


Figure 8-12a Evolution of distributions of Salinity in the Mersey Estuary during a tidal cycle (25 June, 1998)

Figures 8-12a to 8-12d illustrate the model predicted evolutions of the distributions of salinity, suspended sediment, total cadmium and dissolved cadmium during a tidal cycle. It can be seen from Figure 8-12d that during the low water level phase ($t=T/2$ and $t=3T/4$), the concentration of the dissolved cadmium in the deep channels in the upstream part of the estuary is relative high. This is because all of the water in the upstream part flows into the deep channels with dissolved and particulate cadmium during low water level phase. It can be seen from Figure 8-12d that the concentration of dissolved cadmium around the Narrow is relative high at $t=3T/4$, while from Figure 8-12c it can be seen that the concentration of the total cadmium is low around the Narrow at this moment. The main reason for this phenomenon is that a lot of cadmium released into the water body due to de-sorption, because the

suspended sediment concentration is relative low at this moment (see Figure 8-12b). From these figures it also can be seen that high concentration of total cadmium appears around Runcorn and Eastham, where high concentration of suspended sediment also appears. The main reason for this phenomenon is that a lot of particulate cadmium adsorbed on the bed sediment is entrained into the water column due to erosion.

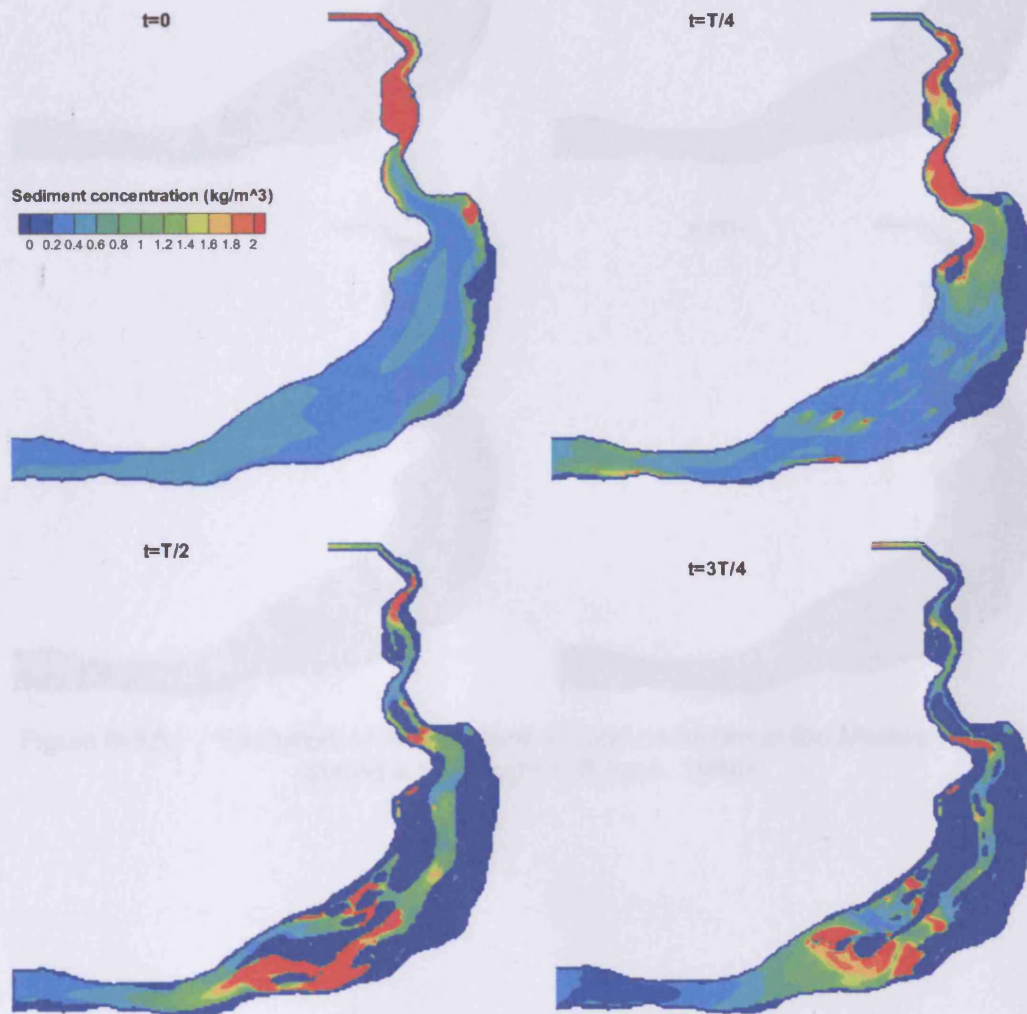


Figure 8-12b Evolution of distributions of suspended sediment in the Mersey Estuary during a tidal cycle (25 June, 1998)

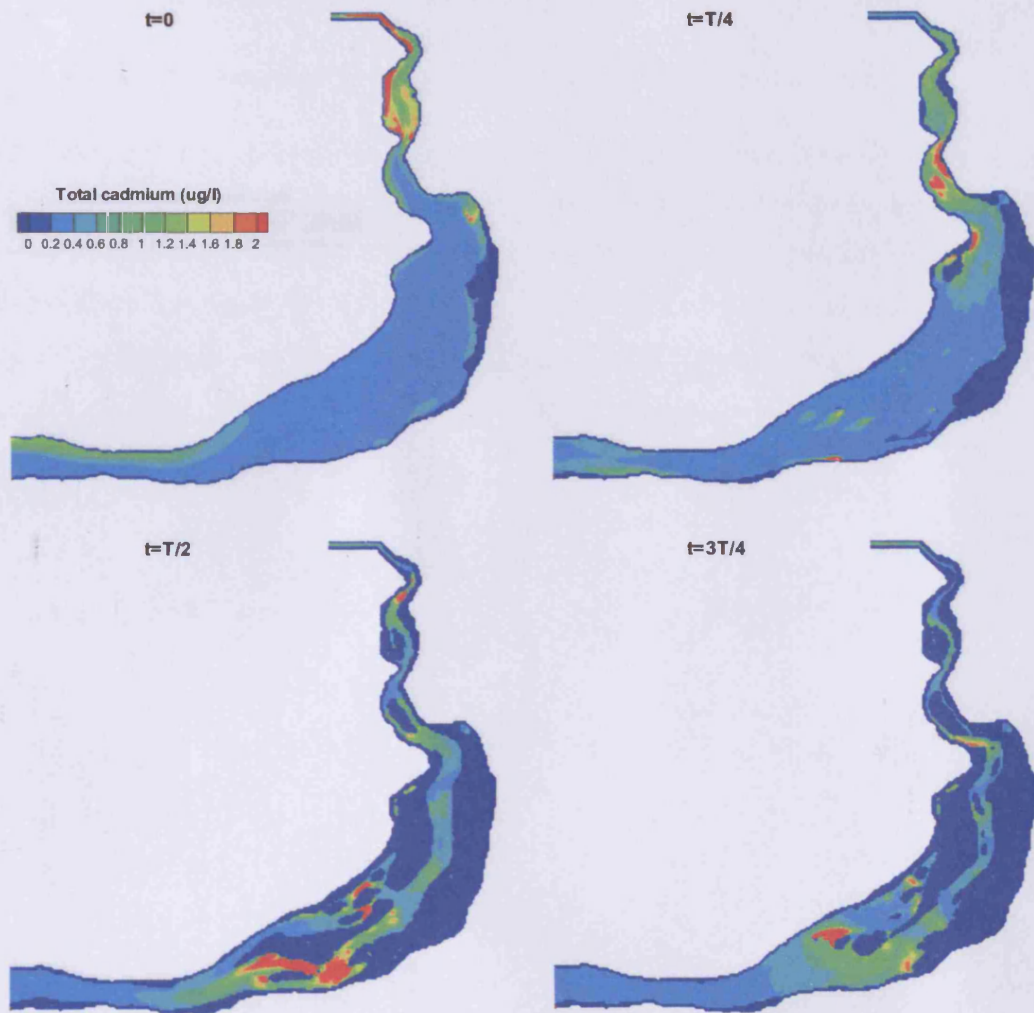


Figure 8-12c Evolution of distributions of total cadmium in the Mersey Estuary during a tidal cycle (25 June, 1998)

3.5.4 Trace Metal Behaviour in the Mersey Estuary

Input scenarios from different scenarios will be carried out to study the behaviour of the trace metal in the Mersey Estuary. In the case studies, cadmium is studied as the trace metal to be simulated. For the convenience to analyse the model results, the following scenarios are also carried out, in which cadmium is replaced by PCBs (Polychlorinated Biphenyls).

The hydrodynamic, salinity and sediment boundary conditions are determined with the input data on 25 June, 1998. The coefficients and computational parameters are the same as those used in Section 3.5.2. The model is run for 100

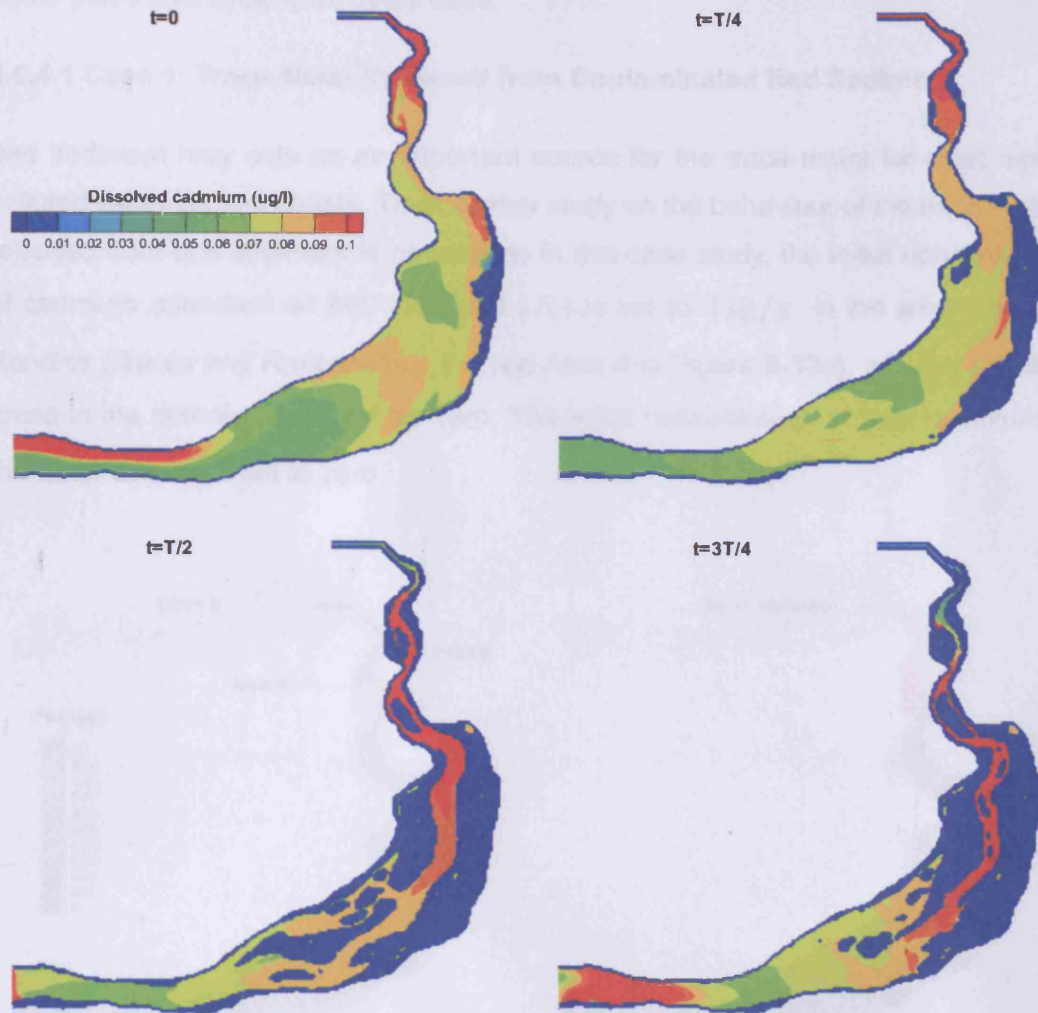


Figure 8-12d Evolution of distributions of dissolved cadmium in the Mersey Estuary during a tidal cycle (25 June, 1998)

8.6.4 Trace Metal Behaviour in the Mersey Estuary

In this section three different scenarios will be carried out to study the behaviour of the trace metal in the Mersey Estuary. In the case studies, cadmium is selected as the trace metal to be simulated. For the convenience to analyze the model results, two additional simulations are also carried out, in which cadmium is replaced by PDCM (Passive Dissolved Conservative Mass).

The hydrodynamic, salinity and sediment boundary conditions are determined with the measured data on 25 June, 1998. The coefficients and computational parameters are set the same as those used in Section 8.6.2. The model is run for 100

hours (i.e. 8 tidal cycles) for every case.

8.6.4.1 Case 1: Trace Metal Released from Contaminated Bed Sediment

Bed sediment may act as an important source for the trace metal for most highly polluted estuaries and coasts. Thus, further study on the behaviour of the trace metals released from bed sediment is necessary. In this case study, the initial concentration of cadmium adsorbed on bed sediment (P_b) is set to $1 \mu\text{g/g}$ in the area between Randles Sluices and Runcorn (i.e. the red Area A in Figure 8-13a), while in all other areas in the domain P_b is set as zero. The initial concentration of total cadmium in the water column is set to zero.

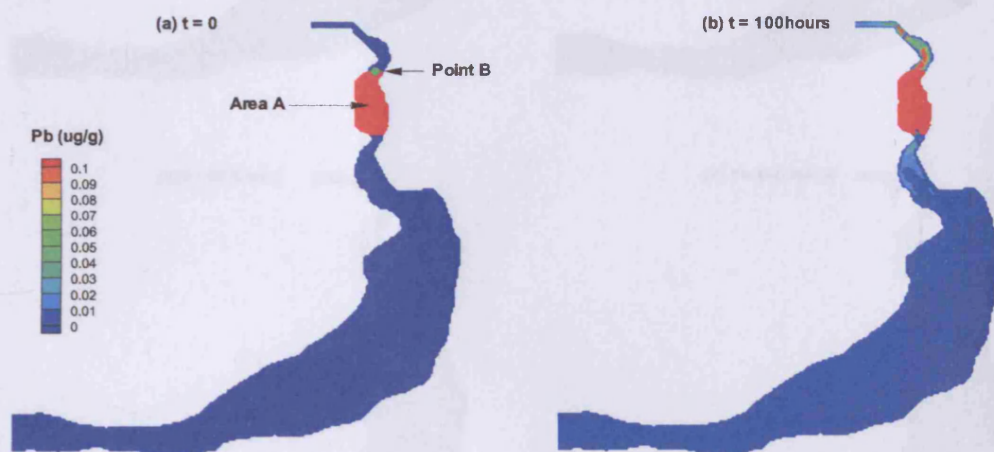


Figure 8-13 Spatial distributions of concentration of trace metal in bed sediment at (a) $t=0$ and (b) $t=100$ hour for Case 1

Figure 8-13 demonstrates the spatial distributions of the trace metal concentration in the bed sediment (P_b) at $t=0$ and $t=100$ hours for Case 1. Figures 8-14 and 8-15 show the spatial distributions of the concentration of dissolved (C_d) and particulate (C_p) trace metal in the water body during the 8th tidal cycle for Case 1, respectively. From the three figures it can be seen that after 100 hours, most of the trace metal is still in the domain very near to Area A, i.e. the transport and dispersion processes of trace metal are very slow. It also can be seen that due to the tidal effect,

trace metal moves both upstream and downstream, and the distributions of dissolved and particulate trace metal concentration in the water column are affected significantly obviously by the tidal current during a tidal cycle.

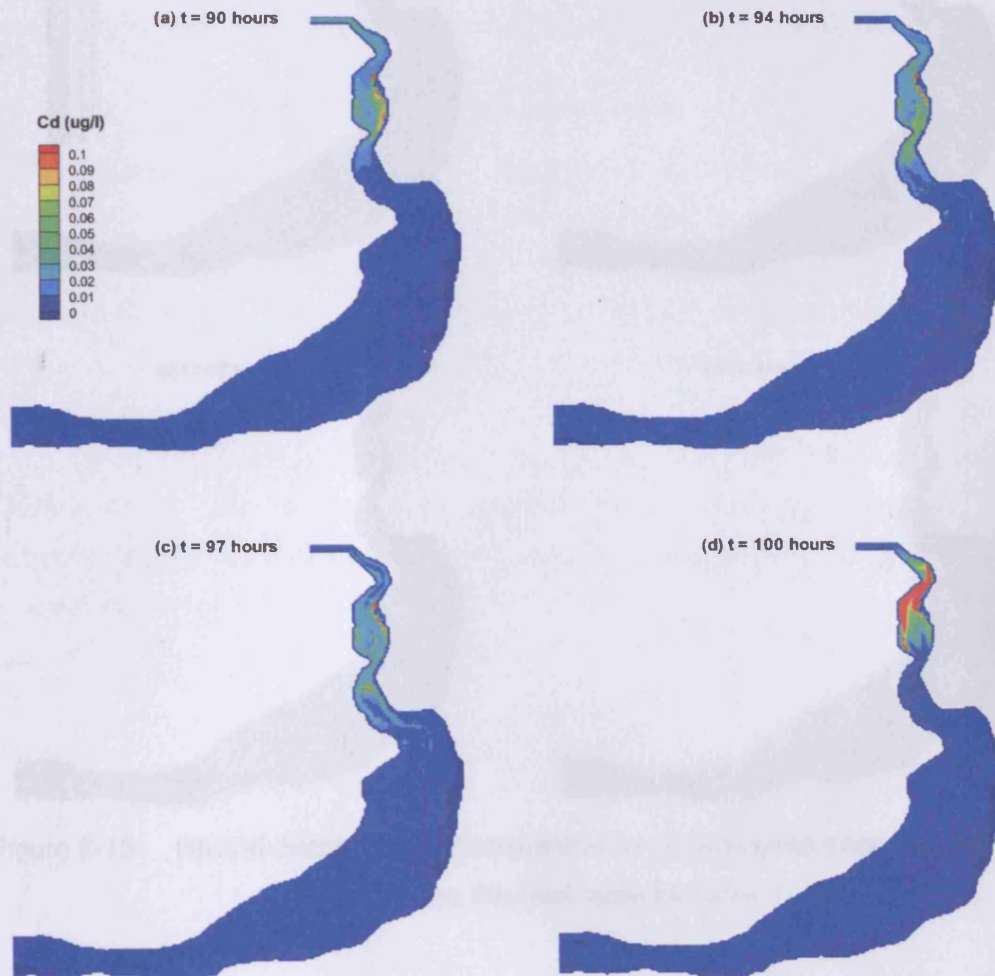


Figure 8-14 Spatial distributions of concentration of dissolved trace metal in water body during 8th tidal cycle for Case 1

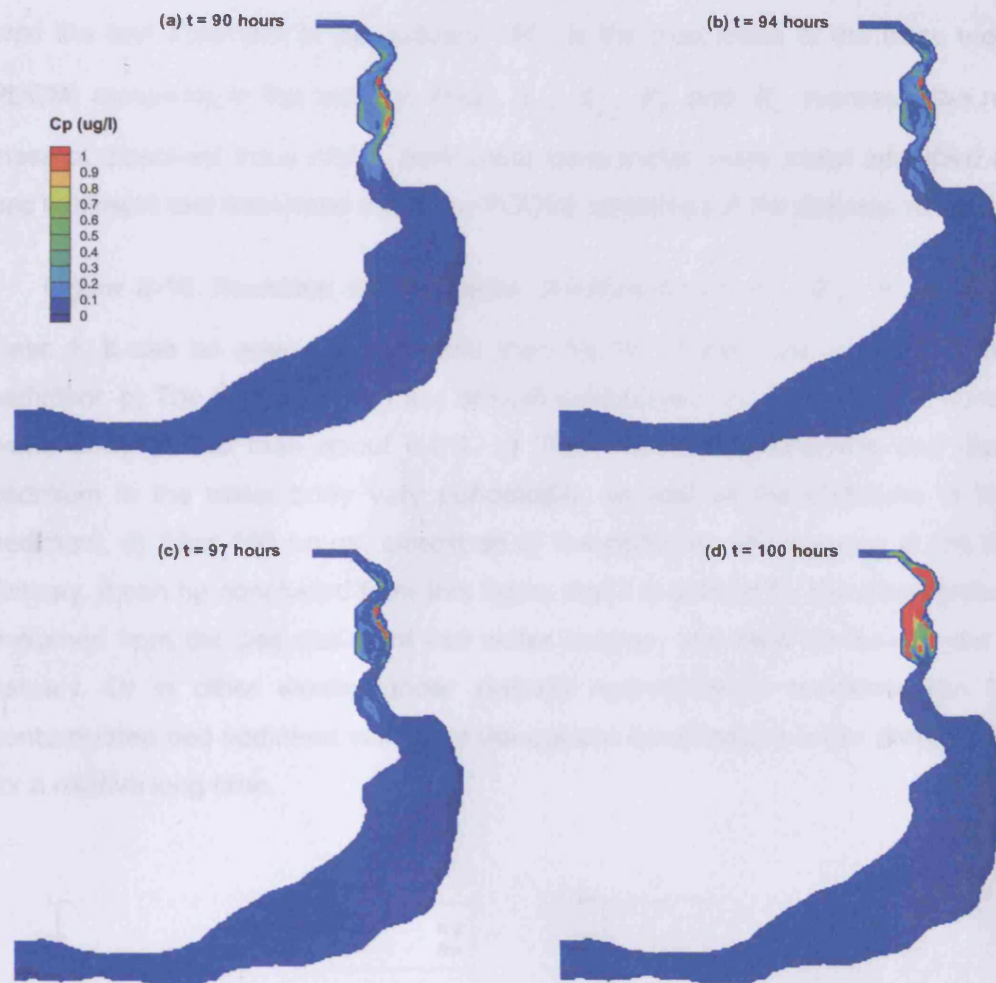


Figure 8-15 Spatial distributions of concentration of particulate trace metal in water column during 8th tidal cycle for Case 1

For the convenience of description, four definitions of relative mass will be used in this section, given as follows:-

$$R_d = \frac{M_d}{M_0}, \quad R_p = \frac{M_p}{M_0}, \quad R_b = \frac{M_b}{M_0}, \quad R_e = \frac{M_e}{M_0} \quad (8-44)$$

where M_d is the mass of the dissolved trace metal in the Mersey Estuary, M_0 is the total mass of the trace metal (or PDCM) being released into the domain (including that released at initial time), M_p is the mass of the trace metal adsorbed onto the

suspended sediment in the estuary, M_b is the mass of the trace metal adsorbed onto the bed sediment in the estuary, M_e is the total mass of the trace metal (or PDCM) remaining in the estuary. Thus R_d , R_p , R_b and R_e represent the relative mass of dissolved trace metal, particulate trace metal, trace metal adsorbed on the bed sediment and total trace metal (or PDCM) remaining in the estuary, respectively.

Figure 8-16 illustrates the temporal distributions of R_d , R_p , R_b and R_e for Case 1. It can be seen that: a) more than 99.5% of the trace metal is in the bed sediment. b) The total relative mass of both particulate and dissolved cadmium in the water body is less than about 0.5%. c) The masses of particulate and dissolved cadmium in the water body vary periodically, as well as the cadmium in the bed sediment. d) After 100 hours, almost all of the cadmium still remains in the Mersey Estuary. It can be concluded from this figure that it is difficult for the trace metal to be entrained from the bed sediment into water column, and then be flushed out of the estuary. Or in other words, under present hydrodynamic condition, the heavily contaminated bed sediment will affect the aquatic environment in the Mersey Estuary for a relative long time.

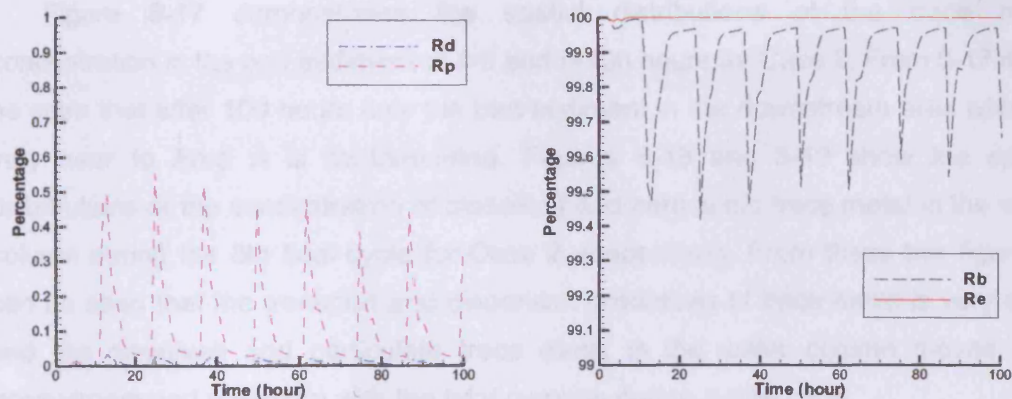


Figure 8-16 Temporal distributions of R_d , R_p , R_b and R_e for Case 1

8.6.4.2 Case2: Trace Metal Released due to Accidental discharges

In this case, it is imaged that a certain amount of cadmium spills out into the water column around Runcorn suddenly due to some accident. The initial concentration of total cadmium is set to $10\mu\text{g}/\text{l}$ in Area A (Figure 8-13a), and zero elsewhere. The initial cadmium concentration in the bed sediment is set to zero.

In order to aid analyzing the results of Case 1 and Case 2, another test case, namely Case 2-P is designed. The computational parameters, initial and boundary conditions are the same as that in Case 2, except cadmium being replaced by PDCM. In this case, it is not necessary to calculate sediment concentration and salinity.



Figure 8-17 Spatial distributions of concentration of trace metal in bed sediment at (a) $t=0$ and (b) $t=100$ hours for Case 2

Figure 8-17 demonstrates the spatial distributions of the trace metal concentration in the bed sediment at $t=0$ and $t=100$ hours for Case 2. From 8-17 it can be seen that after 100 hours only the bed sediment in the downstream area which is very near to Area A is contaminated. Figures 8-18 and 8-19 show the spatial distributions of the concentration of dissolved and particulate trace metal in the water column during the 8th tidal cycle for Case 2, respectively. From these two figures it can be seen that the transport and dispersion processes of trace metal is very slow, and the dissolved and particulate trace metal in the water column moves both downstream and upstream with the tidal currents during a tidal cycle.

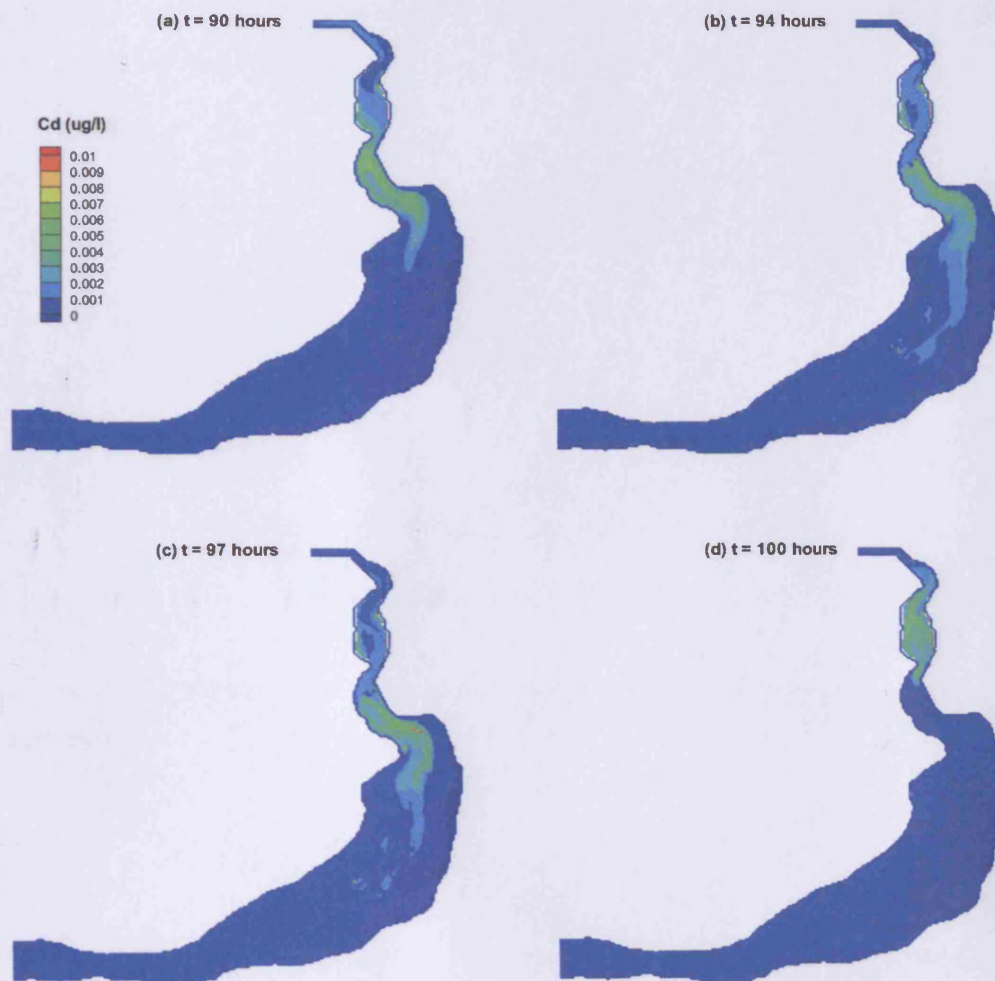


Figure 8-18 Spatial distributions of concentration of dissolved trace metal in water column during 8th tidal cycle for Case 2

Figure 8-18 illustrates the temporal distribution of Cd , Pb , Cu , and Zn in Case 2. It can be seen that, at the beginning, all of the trace metals are in the water body, and the concentration of the water column is high. By the middle of the tidal cycle, the concentration of the water body decreases rapidly to about 5% after two tidal cycles (20 hours), while the value of the sediment is about 50% and remains nearly constant. (b) the number of particles and dissolved substances in the water column, and the amount in the bed sediment vary periodically with tidal currents, and (c) after 100 hours, almost all of the particles and metals in the Muddy Bay are adsorbed onto the particles and settle down to the bed rapidly. Thus, the tidal flow has a significant effect on the

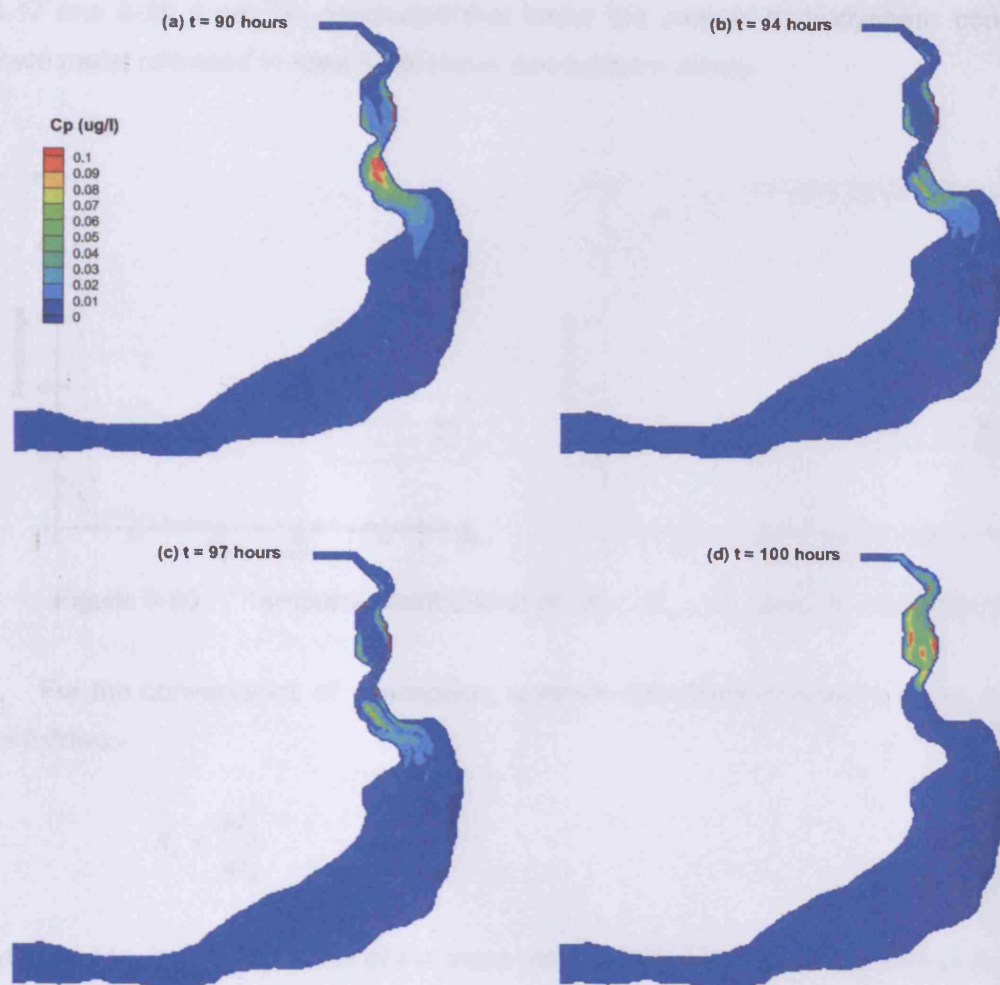


Figure 8-19 Spatial distributions of concentration of particulate trace metal in water column during 8th tidal cycle for Case 2

Figure 8-20 illustrates the temporal distributions of R_d , R_p , R_b and R_e for Case 2. It can be seen that: a) at the beginning, all of the trace metal is in the water body, and this is consistent with the given initial conditions, b) the masses of both particulate and dissolved cadmium in the water body decrease rapidly to about 5% after only two tidal cycles (25 hours), while the mass of the cadmium in the bed sediment increases rapidly to about 95%, c) the masses of particulate and dissolved cadmium in the water column, and the cadmium in the bed sediment vary periodically with tidal currents, and d) after 100 hours, almost all of the cadmium still remains in the Mersey Estuary. It can be concluded from this figure that most of the trace metal spills out into the upstream of the estuary will be adsorbed onto the sediment and settle down to the bed rapidly. Thus, the initial clean bed sediment could become a

huge storage for the trace metal released into the estuary. Considering both Figures 8-17 and 8-20 it can be concluded that under the present hydrodynamic condition, trace metal released in Area A will move downstream slowly.

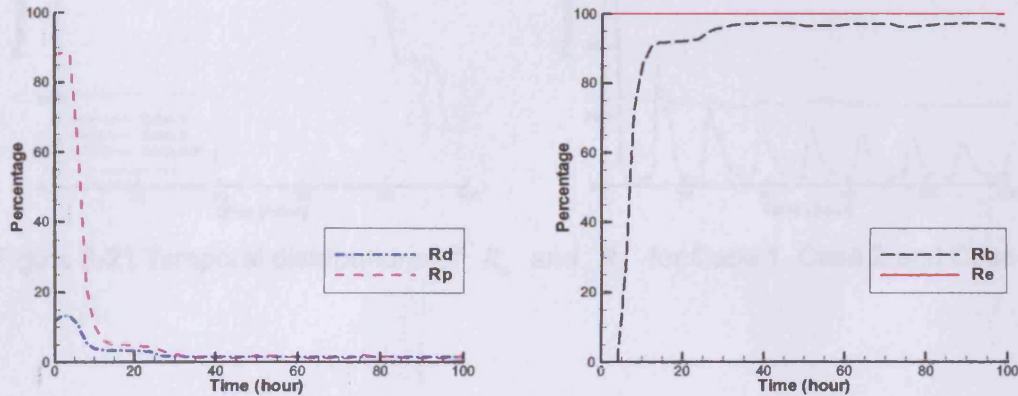


Figure 8-20 Temporal distributions of R_d , R_p , R_b and R_e for Case 2

For the convenience of description, another definitions of relative mass is given as follows:-

$$R_a = \frac{M_a}{M_0} \quad (8-45)$$

where, M_a is the total mass of the trace metal (or PDCM) remaining in Area A. Thus, R_a represents the relative mass of total trace metal (or PDCM) remaining in Area A.

Figure 8-21 compares the temporal distributions of R_e and R_a among Case 1, Case 2 and Case 2-P. It can be seen from Figure 8-21a that for Case 2-P R_e decreases to about 82% after 100 hours, while R_e almost keeps as 100% for Case 1 and Case 2. Figure 8-21b shows that R_a decreases slightly for Case 1. For Case 2, from the beginning to about 5 hour, R_a decreases from 100% to about 25% rapidly, and then from 5 to 100 hours, it decreases very slightly. For Case 2-P, R_a decreases obviously in an oscillating manner. It can be concluded from Figures 8-20 and 8-21 that due to the sorption to bed sediment, compared to PDCM, it will take a much longer time for trace metal to be flushed out of the estuary.

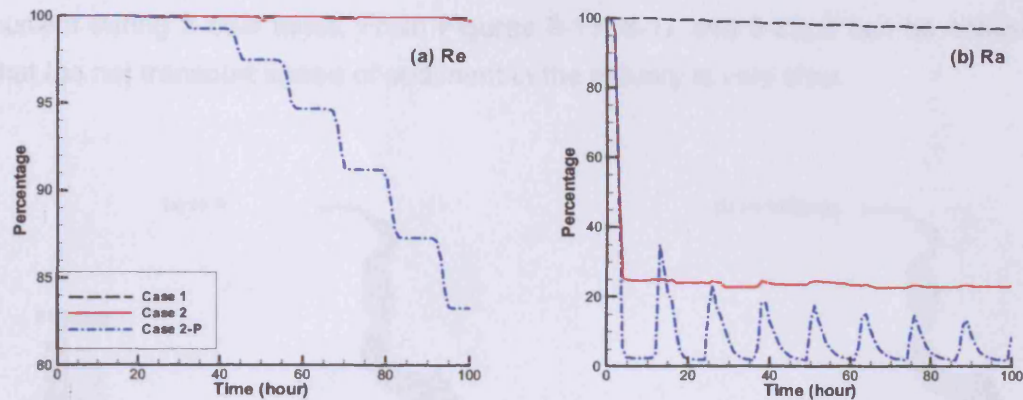


Figure 8-21 Temporal distributions of R_e and R_a for Case 1, Case 2 and Case 2-P

8.6.4.3 Case 3: Trace Metal Released Continuously from an Outfall with Clean Initial Water and Bed Sediment

Usually, most of the trace metals are released from the outfalls along the rivers. It is important to understand the transport and fate of the input trace metals, and how they pollute the bed sediment. In this case study, the initial concentration of cadmium adsorbed on bed sediment (P_b) is set to zero, and the concentration of total cadmium is also set to zero, i.e. both the bed sediment and the water column in the whole domain are clean at the initial time. Total cadmium is supplied at a rate of 1g/s dry weight at Randles Sluices (i.e. Point B in Figure 8-13a).

In order to aid in analysing the results of Case 3, another test case, namely Case 3-P, is also designed. The computational parameters, initial and boundary conditions are the same as that in Case 3, except cadmium being replaced by PDCM. In this case, it is not necessary to calculate sediment concentration and salinity.

Figure 8-22 demonstrates the spatial distributions of the trace metal concentration in the bed sediment at $t=0$ and $t=100$ hour for Case 3. It can be seen that after 100 hours the bed sediments in both the upstream and downstream parts to Point B are contaminated, and the areas being impacted is near to Point B. Figures 8-23 and 8-24 show the spatial distributions of the concentration of dissolved and particulate trace metal in the water column during the 8th tidal cycle for Case 3, respectively. From these two figures it can be seen that the transport and dispersion processes of trace metal are slow, and the dissolved and particulate trace metal in the

water column can reach both downstream and upstream to Point B with the tidal current during a tidal cycle. From Figures 8-13, 8-17 and 8-22, it can be concluded that the net transport speed of sediment in the estuary is very slow.

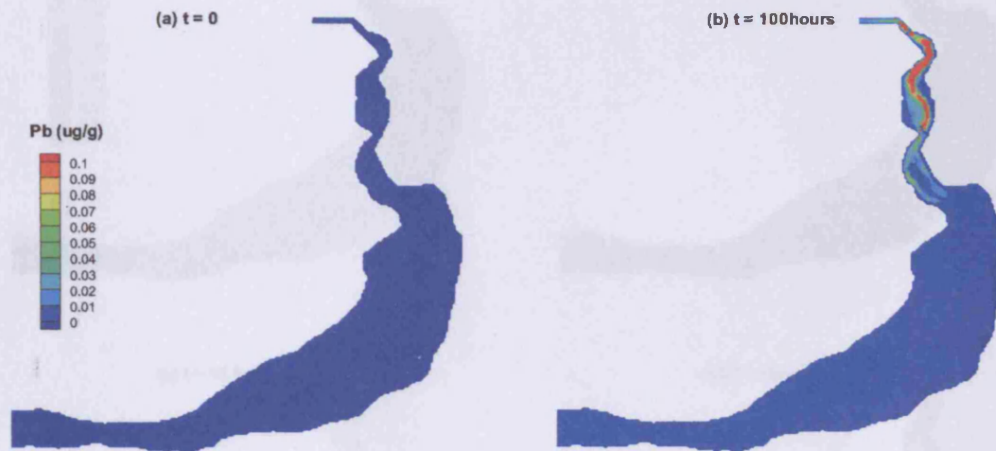


Figure 8-22 Spatial distributions of concentration of trace metal in bed sediment at (a) $t=0$ and (b) $t=100$ hour for Case 3

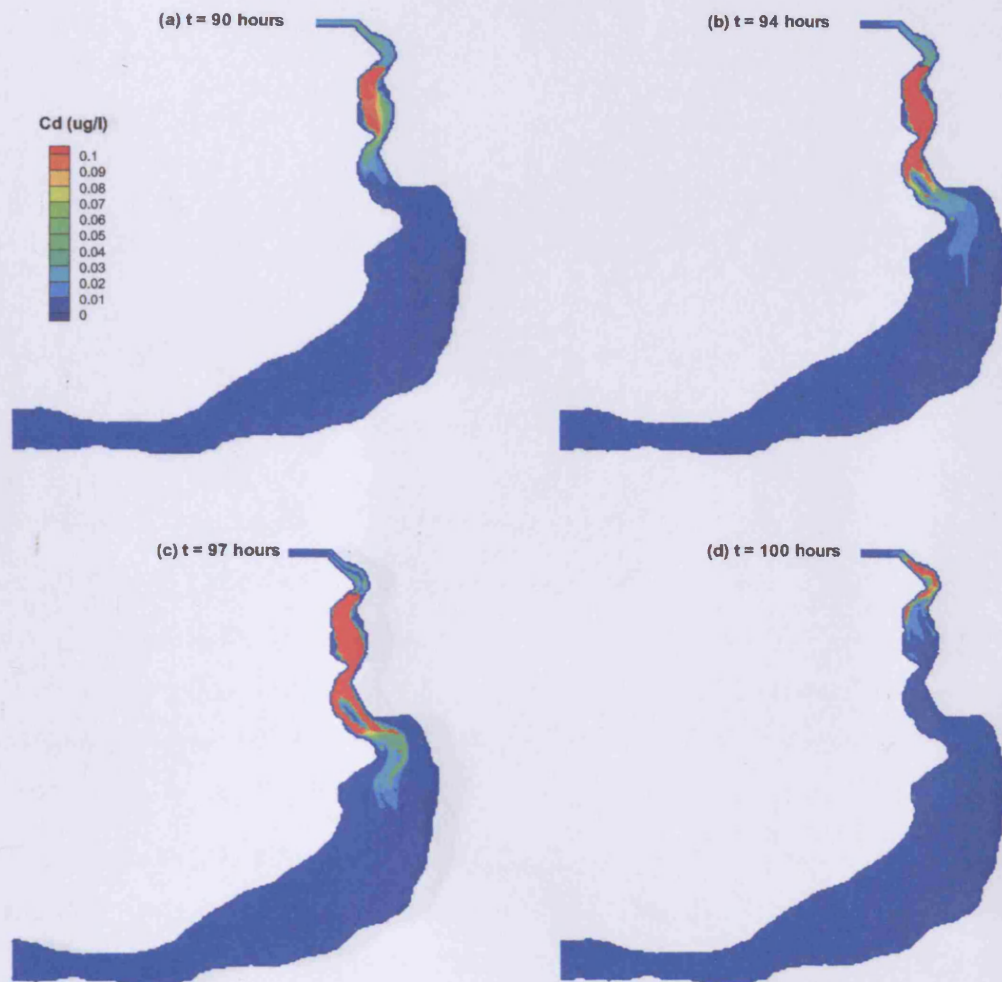


Figure 8-23 Spatial distributions of concentration of dissolved trace metal in water column during 8th tidal cycle for Case 3

Figure 8-23 illustrates the temporal distributions of R_{Cd} , R_{Cu} , R_{Pb} and R_{Zn} for Case 3. It can be seen that: (a) the proportions of both dissolved and particulate trace metals in the water mass increase gradually with time, while the proportion of trace metal particulates in the bed sediment increases with time; (b) R_{Cd} , R_{Cu} and R_{Zn} vary periodically due to the tidal current; (c) After 100 hours, more than 80% of the trace metals settle down to the bed with the sediments; (d) Almost 90% of the released trace metal is still in the column after 100 hours.

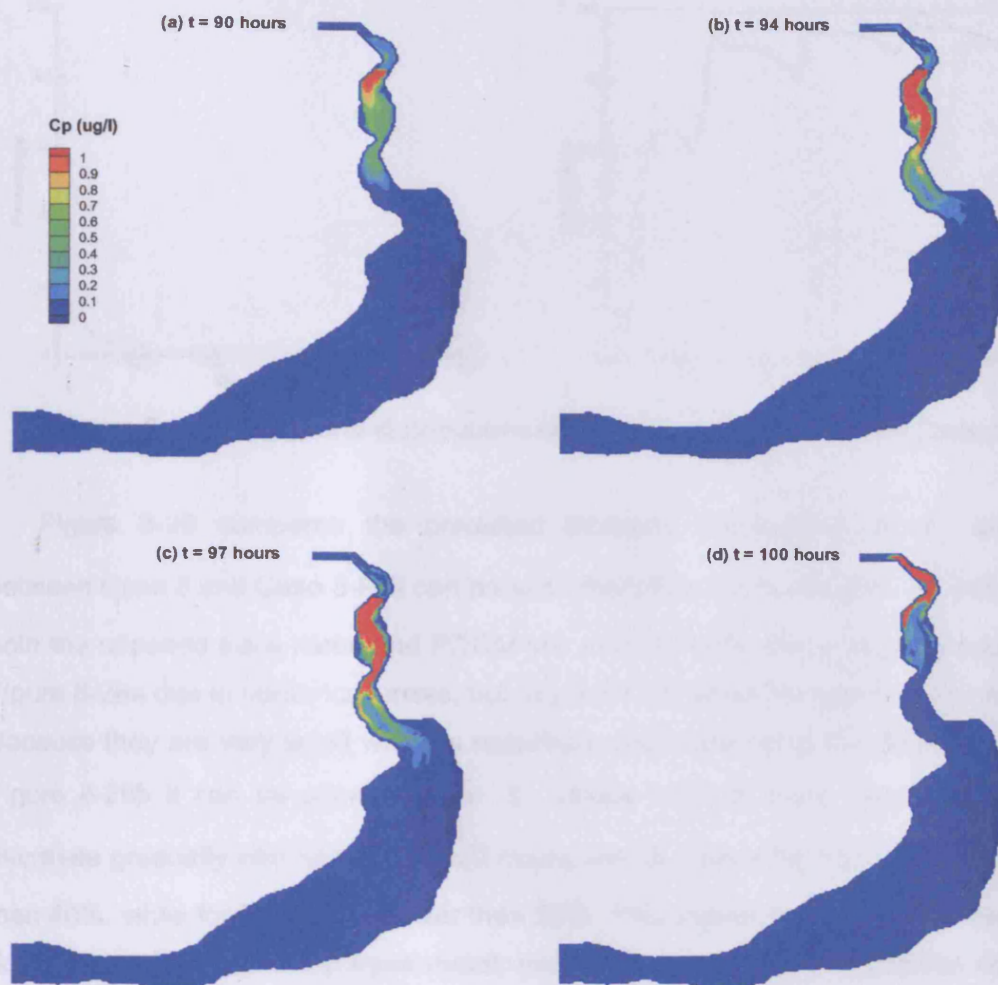


Figure 8-24 Spatial distributions of concentration of particulate trace metal in water column during 8th tidal cycle for Case 3

Figure 8-25 illustrates the temporal distributions of R_d , R_p , R_b and R_e for Case 3. It can be seen that: a) the proportions of both dissolved and particulate trace metal in the water body decrease gradually with time, while the proportion of the trace metal adsorbed onto the bed sediment increases with time. b) R_d , R_p and R_b vary periodically due to the tidal current. c) After 100 hours, more than 80% of the trace metal settles down to the bed with the sediment. d) Almost all of the released trace metal is still in the estuary after 100 hours.

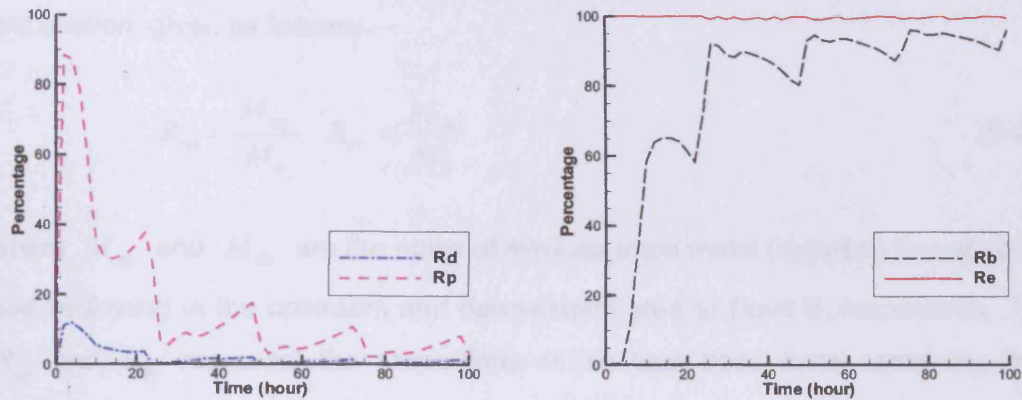


Figure 8-25 Temporal distributions of R_d , R_p , R_b and R_e for Case 3

Figure 8-26 compares the predicted temporal distributions of R_e and R_a between Case 3 and Case 3-P. It can be seen that after 100 hours, the R_e values for both the released trace metal and PDCM are almost 100%. Some wiggles appear in Figure 8-26a due to numerical errors, but this does not affect the quality of the results. Because they are very small with the maximum amplitude being less than 1%. From Figure 8-26b it can be seen that the R_a values for both trace metal and PDCM decrease gradually with time. After 100 hours, the R_a value for trace metal is higher than 40%, while for PDCM it is lower than 20%. This implies that: a) PDCM transport downstream faster than the trace metal, and b) a part of trace metal settles down to the bed and adsorbs onto the bed sediment.

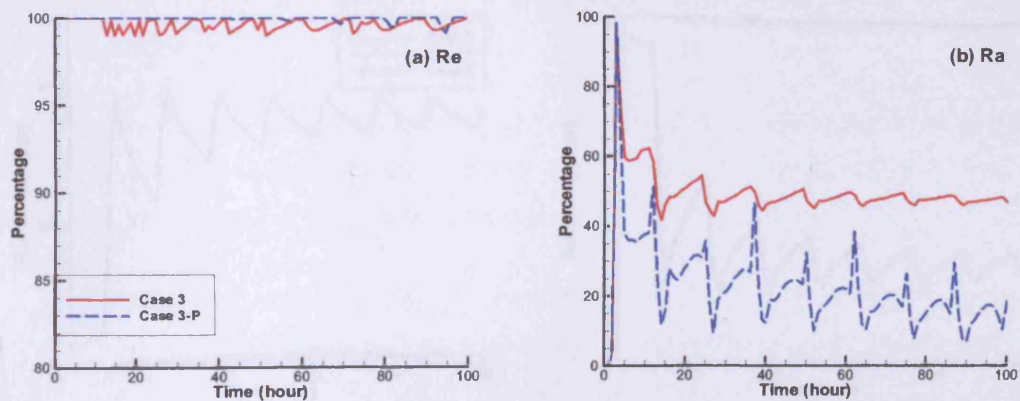


Figure 8-26 Comparison of temporal distributions of R_e and R_a between Case 3 and Case 3-P.

For the convenience of description, two definitions of relative mass will be used in this section, given as follows:-

$$R_{up} = \frac{M_{up}}{M_e}, \quad R_{dn} = \frac{M_{dn}}{M_e} \quad (8-46)$$

where M_{up} and M_{dn} are the mass of the total trace metal (including that adsorb on bed sediment) in the upstream and downstream area to Point B, respectively. Thus, R_{up} and R_{dn} represent the proportions of the total trace metal remaining in the upstream and downstream parts to Point B, respectively.

Figure 8-27 compares the temporal distributions of R_{up} and R_{dn} among Case 1, Case 2 and Case 3. For all of the three cases, R_{up} is less than R_{dn} , i.e. most of the trace metal will be transported downstream. For Case 1 and Case 2, no more than 5% of the trace metal being transported into the area upstream to Point B after 100 hours, while for Case 3, about 40% of the trace metal transports into the upstream part. The main reason for the difference between Case 3 and the other two cases is that in Case 3 the concentration of the total trace metal in the water column around Point B can keep a relative high level due to the continuous supply. Thus compared to Case 1 and Case 2, during flooding tide more trace metal can be transported into upstream area with the tidal currents, and more trace metal can settle down to the bed sediments in the upstream part (see Figures 8-13, 8-17 and 8-22).

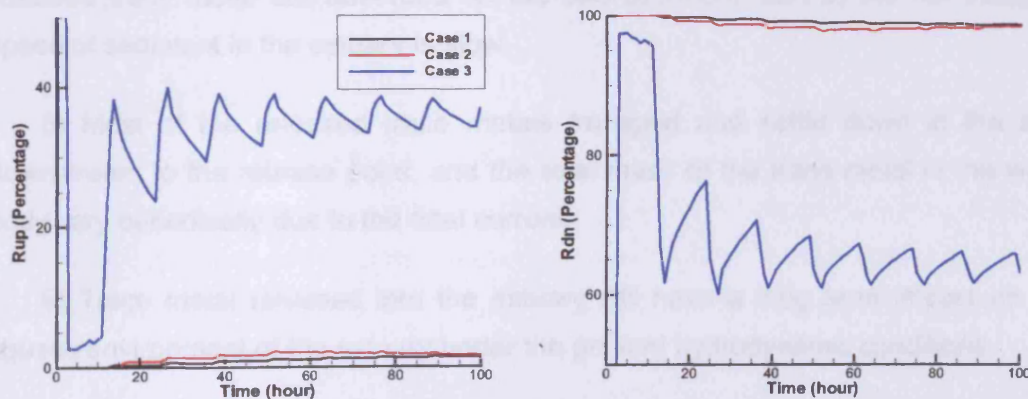


Figure 8-27 Comparison of the temporal distributions of R_{up} and R_{dn} among Case 1, Case 2 and Case 3.

8.7 SUMMARY

In this chapter the theoretical basis and mathematical manipulations for the trace metal transport model are described in detail. Analytical solutions have been derived for two idealised test cases where key trace metal transport processes are included. The model is first verified against the new analytical solutions. Then the model is verified and calibrated against the field survey data from the Mersey Estuary. Finally, three different scenarios are designed to investigate the transport and fate of trace metals in the Mersey Estuary. The main conclusions can be summarised as follows:-

1) With reasonable assumptions the complicated trace metal transport process is simplified and two new analytical solutions are obtained. It is convenient and effective to check the properties of the numerical model with the new analytical solutions.

2) The model predicted results agree very well with the analytical solutions for both deposition and erosion dominated transport process, i.e. the numerical model can give correct and accurate results for well controlled test cases.

3) The model predicted results agree reasonably well with the field measured data, i.e. the numerical model can give reliable results for a practical case with complex bathymetry.

4) Compared to PDCM, trace metal released into the upstream part of the estuary is more difficult to be flushed out of the estuary. This is because: a) most of the released trace metal are adsorbed on the bed sediment, and b) the net transport speed of sediment in the estuary is slow.

5) Most of the released trace metals transport and settle down in the area downstream to the release point, and the total mass of the trace metal in the water body vary periodically due to the tidal current.

6) Trace metal released into the estuary will have a long term impact on the aquatic environment of the estuary under the present hydrodynamic conditions.

CHAPTER 9

CONCLUSIONS AND RECOMMENDATIONS

9.1 CONCLUSIONS

An integrated hydro-environmental model has been developed in this study to simulate the hydrodynamic and solute, sediment and trace metal transport processes in estuarine and coastal waters. All of the sub-models for individual processes have been verified systematically against analytical solutions, published experimental and field survey data. The integrated model has been applied to study the water exchange and the fate of trace metals in a macro-tidal estuary, namely the Mersey Estuary, located in the north-western England. The main conclusions and achievements from this study can be summarised as follows:-

9.1.1 Model Development

Details are given of the governing hydrodynamic equations of fluid motion and the general form of solute transport equations in three- and depth-integrated two-dimensional frameworks for estuarine, coastal and ground waters. Numerical solution methods are briefly reviewed. The alternating direction implicit scheme technique which is based on the finite difference method is chosen to discretize the governing equations for both the hydrodynamics (continuity and momentum conservation) and solute transport equation.

A new method is developed to treat moving boundary problems implicitly, in which the surface water flow and groundwater flow are dynamically linked. In linking the surface and groundwater flow models, the discretized hydrodynamic governing equations for the processes are written in the same form thus to generate a whole tri-diagonal matrix.

The hydrodynamic and solute and mass transport numerical models have been systematically verified against analytical solutions and experimental data, with particular attention being paid to checking the ability of treating moving boundary with the linked hydrodynamic model. The test results show that:-

1) The model is capable of giving reliable and accurate results for both surface and groundwater flows, and the numerical methods are stable.

2) The model is capable of predicting the transport of a tracer in surface water accurately.

3) The linked surface and groundwater flow model is capable of treating the moving boundary problem effectively without causing any substantial problem for the conservation of mass and momentum.

4) Comparisons between the predicted water elevations and salinity against the field survey data in the Mersey Estuary shows that the integrated hydrodynamic and solute transport model developed in this thesis is capable of simulating the hydrodynamic and solute transport processes accurately even for a estuary with complex bathymetry.

In this study, the sediment transport equations proposed by van Rijn (1984a, b) is adopted in the numerical model. Details are given of the theoretic basis of the sediment transport model (including bed evolution), and the key coefficients used in the model.

Comparisons between the predicted suspended sediment concentrations and bed evolutions against the published analytical solution and experimental data show that satisfied results are obtained using the sediment transport model developed in this study. Furthermore, the model has been calibrated and verified against the measured data of suspended sediment concentration in the Mersey Estuary, and reasonably good results are obtained.

The trace metal transport model is developed based on total trace metal transport, including both dissolved and particulate metals as a combined flux, in contrast to previous model studies reported in the literature where the dissolved and particulate metal processes are treated independently. As a reasonable approximation, in this study the net sedimentation is ignored, i.e. only a single sediment layer with a given thickness is taken into account. It is also assumed in this study that the diffusive coefficient is infinite in the bed sediment (i.e. the deposit sediment and the bed sediment mix well immediately once the deposit sediment touches the bottom).

In order to verify the trace metal transport model accurately, two new test cases are designed with well defined boundary and initial conditions, and the corresponding analytical solutions are solved out. The numerical results show very good agreement

with the analytical solutions. Furthermore, the trace metal transport model is verified and calibrated against the field measured data from the Mersey Estuary and the numerical results agree reasonably well with the measured data.

9.1.2 Model Application

The integrated hydro-environment model has been applied to a practical case study to evaluate the residence time of a conservative tracer and the behaviour of trace metal in the Mersey Estuary.

9.1.2.1 Residence time

A series of numerical model simulations was undertaken to predict the residence time for various tidal and fresh water flow conditions. The main conclusions drawn from the model predictions can be summarised as follows:

1) The average residence time for the whole of the Mersey Estuary is relatively short for a large estuary, ranging from 17hr to 104 hours (i.e. from less than 1 day to about 4 days).

2) Due to the complex bathymetric features of the estuary, the deep channels at the upper part of the estuary play an important role in transporting the conservative tracer through the estuary. As a result of this impact, the local residence time varies significantly for different parts of the estuary. At the upper reaches of the estuary the residence time is much longer than that along the middle and lower reaches.

3) As a result of the large ratio of the tidal prism to the mean volume of water in the Mersey Estuary, the average residence time is sensitive to the water level at which the residence time integration is commenced. The value of the average residence time can vary significantly for starting integration at low or high water.

4) Generally speaking, the average residence time for the whole Mersey Estuary is affected more by the tidal range than the river discharge. However, if the tidal range is small, then the freshwater discharge can significantly affect the average residence time by changing the intensity of the residual tidal currents along the main channels.

9.1.2.2 Behaviour of trace metal

Three different scenarios were designed to investigate the behaviour of the trace metal in the Mersey Estuary, and the main findings can be concluded as follows:-

1) Compared to PDCM, it will take longer time for the trace metal released into

the upstream of the estuary to be flushed out of the estuary, due to the interaction between the trace metal, suspended sediment and bed sediment. The trace metal released into the estuary is likely to have a long term impact on the aquatic environment of the estuary.

2) Most of the released trace metal is adsorbed on the bed sediment due to the large partitioning coefficient, and most of the released trace metal is transported and settled down in the area downstream of the release point.

3) From 1) and 2) it can be concluded that in the Mersey Estuary the net flux of sediment transport is generally quite slow.

4) The total mass of the trace metal in the water body varies periodically, because a) the particulate trace metal settles down to the bed and then re-suspends to the water body with sediment, and b) the partitioning coefficient of the studied trace metal (Cadmium) is large in the Mersey Estuary.

9.2 RECOMMENDATIONS FOR FURTHER STUDY

In extending this research programme for further study, the following aspects are worthy of consideration:-

1) In this study a fully linked hydrodynamic model for both surface water flow and groundwater flow has been developed, while the solute transport model has not yet been extended to groundwater. In order to simulate the mass exchange between surface water and groundwater it is necessary to develop a linked solute transport model for both surface water and groundwater flows.

2) In modelling sediment transport using van Rijn's (1984a, b) theory, the two key coefficients namely γ and α (see Equation (7-63)) are determined by trial and error. Thus the calibration of the model for a practical engineering study is time consuming. Moreover, the constant values for γ and α as used in the current study may not be suitable for some other cases, because the values of γ and α are highly dependent the distributions of velocity and sediment concentration and the bed boundary condition. It is thus important to develop a method to estimate the values of γ and α more accurately and efficiently.

3) In modelling the trace metal transport, the bed sediment has been considered

as a single layer, and the net sedimentation in the bed sediment has been ignored. These assumptions are reasonable if the transport of the trace metal is only simulated for a short time period. However, if long term behaviour of the trace metal is to be predicted, a multi-layer bed sediment model should be applied, and the net sedimentation in the bed sediment should be taken into account. For more accurate simulation, the mass exchange of the dissolved trace metal between the water body and the interstitial water due to diffusive processes should also be included in the model. In the mean time new analytical solutions should also be derived for more sophisticated test cases for the purpose of model verification.

4) In order to improve the ability for the present model to fit the complicated geometry of estuarine and coastal basins, a curvilinear coordinate system could be introduced into the model.

REFERENCES

- Abbott, M.B., Basco, D.R., 1997. *Computational Fluid Dynamics: An Introduction for Engineers*. Addison Wesley Longman Limited, Edinburgh Gate, Harlow, England.
- Ahmed, A.A., Chen D., 2006. Effects of contamination age on phenanthrene desorption from aquifers. *Journal of Environmental Science and Health Part A: Toxic/Hazardous Substance & Environmental Engineering*, 41: 1-15.
- Akiyama, J., Fukushima, Y., 1986. Entrainment of non-cohesive sediment into suspension. *Proceedings of 3rd International Symposium on River Sedimentation*, S.Y., Wang, H.W., Shen and L.Z., Ding eds., University of Mississippi, 804-813.
- Anastasiou, K., Chan, C.T., 1997. Solution of the 2D shallow water equations using the finite volume method on unstructured triangular meshes. *International Journal for Numerical Methods in Fluid*, 24: 1225-1245.
- Bagnold, R.A., 1966. *An approach to the sediment transport problem for general physics*. Geological Survey Professional Paper 422-I, Washington, D.C.
- Balzano, A., 1998. Evaluation of methods for numerical simulation of wetting and drying in shallow water flow models. *Coastal Engineering*, 34: 83~107.
- Bao, X.W., Yan, J., Sun, W.X., 2000. A three-dimensional tidal model in boundary-fitted curvilinear grids. *Estuarine, Coastal and Shelf science*, 50: 775-788.
- Bedient, P.B., Huber, W.C., 1988. *Hydrology and Floodplain Analysis*. Addison-Wesley Publishing Company, New York.
- Bolin, B., Rodhe, H., 1973. A note on the concept of age distribution and transit time in natural reservoirs. *Tellus*, 25: 58-63.
- Burton, L.R., 2003. The Mersey Basin: a historical assessment of water quality from an anecdotal perspective. *The Science of the Total Environment*, 314-316: 53-66.
- Carstens, M.R., 1952. Accelerated motion of a spherical particle. *Transactions, American Geophysical Union*, 33(5): 713-720.
- Casulli, V., Walters, R.A., 2000. An unstructured grid, three-dimensional model based on the shallow water equations. *International Journal for Numerical Methods in*

Fluids, 32: 331-348.

Celik, I., and Rodi, W., 1984. A deposition-entrainment model for suspended sediment transport. Technical Report SFB 210/T/6, Sonderforschungsbereich 210, University of Karlsruhe.

Chatwin, P.C. and Allen, C.M., 1985. Mathematical models of dispersion in rivers and estuaries. *Annual Review of Fluid Mechanics*, 17: 119-149.

Chen Y., 1992. Numerical Modelling of Solute Transport Processes Using Higher Order Accurate Finite Difference Schemes. Ph.D. Thesis, University of Bradford, England.

Chien, N., Wan, C.H., McNown, J.S., 1999. *Mechanics of Sediment Transport*. American Society of Civil Engineering, pp913.

Cole, J.A., Whitelaw, K., 2001. Metal fluxes in the Mersey Narrows. *Hydrology and Earth System Science*, 5: 103-118.

Coleman, N.L., 1970. Flume studies of the sediment transfer coefficient. *Water Resources Research*, 6(3): 801-809.

Comber, S.D.W., Gunn, A.M., and Whalley, C., 1995. Comparison of the partitioning of trace metals in the Humber and Mersey Estuaries. *Marine Pollution Bulletin*, 30(12): 851-860.

Council of the European Communities, 1976. Council Directive 76/464/EEC of 4 May 1976 on pollution caused by certain dangerous substances discharged into the aquatic environment of the community. *Official Journal*, L129: 23-29.

Delhez, E. J.M., Heemink A.W. and Deleersnijder E., 2004. Residence time in a semi-enclosed domain from the solution of an adjoint problem. *Estuarine, Coastal and Shelf Science*, 61: 691-702.

Dong, L.X., Su, J.L., 1999a. Numerical study of the water exchange in Xiangshangang Bay. Part One: advection-diffusion tidal exchange model. *Oceanologia et Limnologia Sinica*, 30: 410-415 (in Chinese, with English abstract).

Dong, L.X., Su, J.L., 1999b. Numerical study of the water exchange in Xiangshangang Bay. Part Two: model application and water exchange study. *Oceanologia et Limnologia Sinica*, 30: 465-470 (in Chinese, with English abstract).

- Dou, G., 2003. Proceedings of Dou Guoren. China Waterpower Press, Beijing, pp976. (mainly in Chinese)
- Dronkers, J.J., 1964. Tidal Computations in Rivers and Coastal Waters. North Holland Publishing Co., Amsterdam.
- Einstein, H.A., 1942. Formula for the transportation of bed load. Trans., Amer. Soc. Civil Engrs, 107: 561-597.
- Einstein, H.A., 1950. The bed-load function for sediment transport in open channel flows. Department of Agriculture, Washington, D.C. Technical Bulletin 1026.
- Elder, J.W., 1959. The dispersion of marked fluid in turbulent flow. Journal of Fluid Mechanics, 5(4): 544-560.
- Engelund, F. and Fredsoe, J., 1976. A sediment transport model for straight alluvial channels. Nordic Hydrology, 7:283-306.
- Falconer, R.A., 1977. Mathematical Modelling of Jet-Forced Circulation in Reservoirs and Harbours. Ph.D. Thesis, University of London, London, England, 237p.
- Falconer, R.A., 1984. Temperature distributions in a tidal flow field. Journal of Environmental Engineering, 110(6): 1099~1116.
- Falconer, R.A., 1986. A water quality simulation study of a natural harbor. Journal of Waterway, Port, Coastal and Ocean Engineering, 112(1): 15~34.
- Falconer, R.A., 1994. "An Introduction to Nearly Horizontal Flows". Coastal Estuarial and Harbour Engineers Reference Book, edited by M.B. Abbott and W.A. Price, E&FN Son Ltd, Chapter 2: 27-36.
- Falconer, R.A., Chen, Y., 1991. An improved representation of flooding and drying and wind stress effects in a two-dimensional tidal numerical model. Proc. Instn Civ. Engrs, Part 2, 91: 659-678.
- Falconer, R.A., Lin, B., Wu, Y., and Harries, E., 1999. "DIVAST Model: Reference Manual". Environmental Water Management Research Centre, School of Engineering, Cardiff University, 17p.
- Falconer, R.A., Owens, P.H., 1987. Numerical simulation of flooding and drying in a depth-averaged tidal flow model. Proceedings of the Institution of Civil Engineers, 83(2): 161-180.
- Fisher, H.B., 1973. Longitudinal dispersion and turbulent mixing in open channel flow. Annual Review of Fluid Mechanics, 5: 59-78.

- Fischer, H.B., List, J., Imberger, J., Brooks, N., 1979. "Mixing in Inland and Coastal Waters". Academic Press, San Diego, 483p.
- Fletcher, C.A.J., 1991. Computational Techniques for Fluid Dynamics. Volume II: Specific Techniques for Different Flow Categories. Second Edition, Springer Verlag, Berlin.
- Forstner, U., Wittmann, G.T.W., 1979. "Metal Pollution in the Aquatic Environment (second edition)", Springer Verlag, New York.
- Fukumoto, T., Kobayashi, N., 2005. Bottom Stratification and Water Exchange in Enclosed Bay with Narrow Entrance. *Journal of Coastal Research*, 21: 135-145.
- Garcia, M. and Parker, G., 1991. Entrainment of bed sediment into suspension. *Journal of Hydraulic Engineering*, ASCE, 117(4): 414-435.
- Gibbs, R.J., Matthews, M.D. and Link, D.A., 1971. The relationship between sphere size and settling velocity. *Journal of Sedimentary Petrology*, 41(1): 7-18.
- Hallermeier, R.J., 1981. Terminal settling velocity of commonly occurring sand grains. *Sedimentology*, 28: 859-865.
- Harleman, D.R.F., 1966. Diffusion processes in stratified flow. In: *Estuary and Coastline Hydrodynamics*, A.T. Ippen (editor), McGraw-Hill Book Company, Inc., New York, pp575-597.
- Hartnett, M., Lin, B., Jones, P.D., Berry, A., 2006. "Modelling the Fate and Transport of Nickel in the Mersey Estuary" *Journal of Environmental Science and Health, Part A: Toxic/Hazardous Substances & Environmental Engineering*, 41: 825-847.
- Hatje, V., Payne, T.E., Hill, D.M., McOrist, G., Birch, G.F., Szymczak, R., 2003. Kinetics of trace element uptake and release by particles in estuarine waters: effects of pH, salinity, and particle loading. *Environment International*, 29: 619-629.
- He, S., Wang, L., 1986. Application of the slot method in the computation of two dimensional flow with transient boundary. *Journal of Hydraulic Engineering*, 12: 11-19. (in Chinese)
- Henderson, F.M., 1966. "Open Channel Flow". Macmillan Co. Ltd, 522p.
- Heniche, M., Secretan, Y., Boudeau, P., Leclerc, M., 2000. A two-dimensional finite element drying-wetting shallow water model for rivers and estuaries. *Advances in Water Research*, 23: 359-372.
- Hinze, J.O., 1975. "Turbulence (second edition)". McGraw-Hill Book Co., Inc.,

New York, 640-645.

- Ip, J.T.C., Lynch, D.R., Friedrichs, C.T., 1998. Simulation of estuarine flooding and dewatering with application to Great Bay, New Hampshire. *Estuarine, Coastal and Shelf Science*, 47: 119-141.
- Itakura, T. and Kishi, T., 1980. Open channel flow with suspended sediments. *Journal of the Hydraulics Division, Proceedings of ASCE*, 106(8): 1325-1343.
- Izquierdo, C., Usero, J., and Gracia, I., 1997. Speciation of heavy metals in sediments from salt marshes on the southern Atlantic Coast of Spain. *Marine Pollution Bulletin*, 34(2): 123-128.
- Jones, P.D., 2000. The Mersey Estuary – Back from the Dead? Solving a 150-year Old Problem. *J. Chart. Inst. Water Engrs Managers*, 14: 124-130.
- Kalinske, A.A., 1947. Movement of sediment as bed load in rivers. *Trans. American Geophysical*, 28(4): 615-620.
- Kennedy, A.B., Chen, Q., Kirby, J.T. and Dalrymple, R. A., 2000. Boussinesq modelling of wave transformation, breaking and runup. I: One dimension. *Journal of Waterway, Port, Coastal and Ocean Engineering*, 126: 39-47.
- Kitheka, J.U., 1997. Coastal tidally-driven circulation and the role of water exchange in the linkage between tropical coastal ecosystems. *Estuarine, Coastal and Shelf Science*, 45: 177-187.
- Koutitas, C., Cousidou-Koutita, M., 1986. A comparative study of three mathematical models for wind generated circulation in coastal areas. *Coastal Engineering*, 10: 127-138.
- Lane, A., 2004. Bathymetric evolution of the Mersey Estuary, UK, 1906-1997: causes and effects. *Estuarine, Coastal and Shelf Science*, 59: 249-263.
- Leendertse, J.J., 1970. A water-quality simulation model for well-mixed estuaries and coastal seas. Vol. 1, Principles of Computation. Rand. Sata Monica, February, RM-6230-RC.
- Li, L., Barry, D.A., Stagnitti, F., Parlange, J.-Y., Jeng, D.-S., 2000. Beach water table fluctuations due to spring-neap tides: moving boundary effects. *Advances in Water Resources*, 23: 817-824.
- Li, Y., Zhao, M. and Cao Zh., 2001. Two-dimensional Fluvial Flow and Sediment Transport Model. China Waterpower Press, Beijing, pp189. (in Chinese)

- Liggett, J.A., 1994. Fluid Mechanics. McGraw-Hill, Inc., Chapter 7: Turbulent Flow: 213-263.
- Lin, B., 1997. A depth-Integrated 2-D Coastal and Estuarine Model with Conformal Boundary-Fitted Mesh Generation. Ph.D. Thesis, Bradford University, 151p.
- Lin, B., 2001. Proceedings of Lin Bingnan. China Waterpower Press, Beijing, pp670. (mainly in Chinese)
- Lin, B. and Falconer, R. A., 1997. Three-dimensional layer-integrated modelling of estuarine flows with flooding and drying. *Estuarine, Coastal and Shelf Science*, 44: 737~751.
- Lin, B., Kashefipour, S.M., Harris E.L., Falconer, R.A., 2001. Modelling flow and water quality in estuarine and riverine waters: A dynamically linked 1-D and 2-D models approach. Proceedings of XXIX IAHR Congress, Theme B: Environmental Hydraulics, 469-475.
- Liu, P. L.-F., Wen, J., 1997. Nonlinear diffusive surface waves in porous media. *J. Fluid Mech.*, 347: 119-139.
- Luff, R., Pohlman, T., 1996. Calculation of water exchange times in the ICE-Boxes with an Eulerian dispersion model using a half-life time approach. *German Journal of Hydrography*, 47: 287-299.
- Lynch, D.R., Gray, W.G., 1978. Analytic solutions for computer flow model testing. *Journal of the Hydraulics Division, Proceedings of ASCE*, 14(HY10): 1409-1428.
- Martino, M., Turner, A., Nimmo, M., Millward, G.E., 2002. Resuspension, reactivity and recycling of trace metals in the Mersey Estuary, UK. *Marine Chemistry*, 77: 171-186.
- Mei, C.C., 2003. *The Applied Dynamics of Ocean Surface Waves*. World Scientific Publishing Co. Pte. Ltd., Singapore.
- Nece, R. E. and Falconer, R. A., 1989. Modelling of tide-induced depth averaged velocity distributions in a square harbour. Proceedings of the International Conference on Hydraulic and Environmental Modelling of Coastal, Estuarine and River Waters, 56-66.
- Ng, B., Turner, A., Tyler, A.O., Falconer, R.A. and Millward, G.E., 1996. Modelling contaminant geochemistry in estuaries. *Water Research*, 30(1): 63-74.

- Oey, L.Y., 2005. A wetting and drying scheme for POM. *Ocean Modelling*, 9(2): 133-150.
- Oliver, D.R., 1961. The sedimentation suspension of closely-sized spherical particles. *Chemical Engineering Science*, 15: 230-242.
- Owens, P.H., 1986. "Mathematical Modelling of Sediment Transport in Estuaries, Chapter 3: Mechanics of Sediment Transport". Ph.D. Thesis, University of Birmingham, Vol.1: 16-29.
- Parlange, J.-Y., Stagnitti, F., Starr, J.L., Braddock, R.D., 1984. Free-surface flow in porous media and periodic solution of the shallow-flow approximation. *Journal of Hydrology*, 70: 251-263.
- Preston, R.W., 1985. Representation of Dispersion in Two-dimensional Water Flow. Report No. TPRD/L/2783/N84, Central Electricity Research Laboratories, Leatherhead, England, 1-13.
- Raubenheimer, B., Guza, R.T., 1999. Tidal water table fluctuations in a sandy ocean beach. *Water Resources Research*, 35(8): 2313-2320.
- Richardson, J.F. and Zaki, W.N., 1954. Sedimentation and fluidization, part I. *Transactions of Institute of Chemical Engineering*, 32: 35-53.
- Roache, P.J., 1998. "Fundamentals of Computational Fluid Dynamics", second edition. Albuquerque, N.M.: Hermosa Publishers.
- Rodi, W., 2000. *Turbulence Models and their Application in Hydraulics*. A.A. Balkema, Rotterdam, Netherlands, 3rd Edition.
- Schlichting, H., 1979. *Boundary Layer Theory*, 6th edn. McGraw-Hill, New York.
- Schwartz, F.W., Zhang, H., 2003. *Fundamentals of Ground Water*. John Wiley & Sons, Inc, New York.
- Singamsetti, S.R., 1966. Diffusion of sediment in a submerged jet. *Journal of the Hydraulic Division, ASCE*, 92(HY2): 153-168.
- Smith, J.D. and McLean, S.R., 1977. Spatially averaged flow over a wavy surface. *Journal of Geophysical Research*, 82:1735-46.
- Soni, J.P., Garde, R.J., and Ranga Raju, K.G., 1980. Aggradation in streams due to overloading. *Journal of the Hydraulic Division, ASCE*, 106(1): 117-131.
- Soulsby, R., 1997. *Dynamics of Marine Sands*. Thomas Telford Publications, Thomas

Telford Services Ltd, 1 Heron Quay, London E14 4JD.

- Stelling, G.S., Wiersma, A.K., and Willemse, J.B.T.M., 1985. Practical aspects of accurate tidal computations. *Journal of Hydraulic Engineering, ASCE*, 112: 802-817.
- Sun, Y.L. and Zhang, Y.M., 2001. A three-dimensional variable boundary numerical tidal model for Jiaozhou Bay. *Oceanologia et Limnologia Sinica*, 32(4): 355~362. (in Chinese with English abstract)
- Tao, J., 1984. A numerical model of wave running up and breaking on a beach. *Acta Oceanal Sinica*, 6: 693-700. (in Chinese)
- Tao, J., Li, Q., Falconer, R.A. and Lin, B., 2001. Modelling and assessment of water quality indicators in a semi-enclosed shallow bay., *Journal of Hydraulic Research, IAHR* , 39: 611-618.
- Thacker, W.C., 1981. Some exact solutions to the nonlinear shallow-water wave equations. *Journal of Fluid Mechanics*, 107: 499~508.
- Thomann, R.V., Mueller, J.A., 1987. Principles of Surface Water Quality Modeling and Control. Harper Collins Publishers, New York. Chapter 8 Toxic Substance: 495-598.
- Takeoka, H., 1984. Fundamental concepts of exchange and transport time scales in a coastal sea. *Continental Shelf Research*, 3: 311-326.
- Thomas, C.G., Spearman, J.R., Turnbull, M.J., 2002. Historical morphological change in the Mersey Estuary. *Continental Shelf Research*, 22: 1775-1794.
- Turner, A., Martino, M., and Le Roux, S.M., 2002. Trace metal distribution coefficients in the Mersey Estuary, UK: evidence for salting out of metal complexes. *Environmental Science & Technology*, 36(21): 4578-4584.
- Turner, A. and Millward, G.E., 1994. The partitioning of trace metals in a macrotidal estuary: Implications for contaminant transport models. *Estuarine Coastal and Shelf Sciences* 39: 45-58.
- Turner, A., Millward, G.E., Bale, A.J., and Morris, A.W., 1993. Application of the KD concept to the study of trace metal removal and desorption during estuarine mixing. *Estuarine Coastal and Shelf Sciences* 36: 1-13.
- Turner, A., Millward, G.E. and Le Roux, S.M., 2001. Sediment-water partitioning of inorganic mercury in estuaries. *Environmental Science and Technology* 35:

4648-4654.

- Turner, A., Millward, G.E., Le Roux, S.M., 2004. Significance of oxides and particulate organic matter in controlling trace metal partitioning in a contaminated estuary. *Marine Chemistry*, 88: 179-192.
- USACE, Hydrologic Engineering Center, 2004. HEC-RAS Hydraulic Reference Manual. www.hec.usace.army.mil.
- Van Rijn, L.C., 1984a. Sediment transport, part I: Bed load transport. *Journal of Hydraulic Engineering*, ASCE, 110(10): 1431-1457.
- Van Rijn, L.C., 1984b. Sediment transport, part II: Suspended load transport. *Journal of Hydraulic Engineering*, ASCE, 110(11): 1613-1641.
- Van Rijn, L.C., 1993. "Principles of Sediment Transport in Rivers, Estuaries and Coastal Seas". Aqua Publications, Amsterdam.
- Wang, Z.B., Ribberink, J.S., 1986. The validation of a depth-integrated model for suspended sediment transport. *Journal of Hydraulic Research*, 24(1): 53-66.
- Wang, Z.J., 2000. A fast nested multi-grid viscous flow solver for adaptive Cartesian/quad grids. *International Journal for numerical Methods in Fluids*, 33: 657-680.
- Wang, Z.L., Tao, J.H., 1998. Numerical study of pollutant transport in the Sea-Bay with mild slope beach. *Acta Oceanologica Sinica*, 17(3): 399-408. (in Chinese with English abstract)
- Wu, Y., Falconer, R.A. and Lin, B., 2005. Modelling trace metal concentration distributions in estuarine waters. *Estuarine, Coastal and Shelf Science*, 64(4): 699-709.
- Yalin, M.S., 1972. *Mechanics of Sediment Transport*. Pergamm Press, N.Y., pp290.
- Zimmerman, J.T.F., 1976. Mixing and flushing of tidal embayments in the Western Dutch Wadden Sea, Part I: Distribution of salinity and calculation of mixing time scales. *Netherlands Journal of Sea Research*, 10: 149-191.

